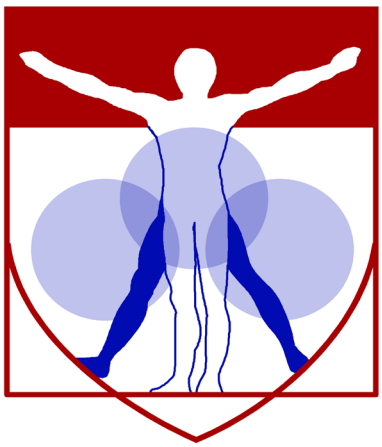

PENN
CENTER for
MUSCULOSKELETAL
DISORDERS

15th Annual Scientific Symposium/Retreat

Wednesday, November 7, 2018
Smilow Rubenstein Auditorium/Commons
8:30am-5:30pm
www.med.upenn.edu/pcmd/

Table of Contents

We gratefully acknowledge the financial support provided by the National Institute of Arthritis, Musculoskeletal and Skin Diseases of the National Institutes of Health and the University of Pennsylvania Perelman School of Medicine for our Center.

Penn Center for Musculoskeletal Disorders
Scientific Symposium Agenda

November 7, 2018

Smilow Rubenstein Auditorium ♦ University of Pennsylvania

08:30 – 09:30am **Registration and Poster Set-up**

09:30 – 09:50am **Welcome and Overview**
Louis J. Soslowsky, Ph.D.

09:50 – 10:50am **Session I: New Member Session** (Moderator: Ling Qin, Ph.D.)

- *Zoltan Arany, M.D., Ph.D., "From Pregnancy to Titin"*
- *Jordan Raney,Ph.D., "3D Printing Bioinspired Materials with Spatially-Controlled Fiber Alignment"*
- *Paris Margaritis, DPhil., "The Hemophilia A Rat as a Model to Study Hemophilic Arthropathy"*

10:50 – 11:50pm **Session II: Affiliate Member Session** (Moderator: Lachlan Smith, Ph.D.)

- *Noreen Hickok, Ph.D., Thomas Jefferson University, "Orthopaedic Implants and Infection: Surfaces, Synovial Fluid and the Joint Environment."*
- *John C. Elfar, M.D., Penn State Health, Milton S. Hershey Medical Center, "Peripheral Nerve Injury Adjunct Treatments for Classification"*
- *Michele Marcolongo, Ph.D., Drexel University, "Biomimetic Proteoglycans in Extracellular Matrix Regeneration"*

11:50 – 02:00pm **Poster viewing and lunch (provided) in Smilow Commons**
- **12:30-01:15pm Poster Session (Even numbered)**
- **01:15-02:00pm Poster Session (Odd numbered)**

02:00 – 03:00pm **Session III: Pilot Grantee Session** (Moderator: Maurizio Pacifici, Ph.D.)

- *Yejia Zhang, M.D., Ph.D., "ADAM8 in Intervertebral Disc Degeneration"*
- *Harvey Smith., M.D., "Novel Quantitative Assessment and Treatment Strategies for the Degenerated Inververtebral Disc"*
- *Joseph Baur, Ph.D., "NAD Metabolism in Muscles"*

03:00 – 04:00pm **Keynote Speaker** (Moderator: Kyu Sang Joeng, Ph.D.)

"Skeletal Dysplasias: Informing Skeletal Function & Homeostasis"

Brendan Lee, Ph.D., Robert and Janice McNair Endowed Chair in Molecular and Human Genetics, Professor and Chairman, Department of Molecular and Human Genetics
Baylor College of Medicine

04:00 – 04:10pm **Final Comments Preceding Poster Session and Reception**

04:10 – 05:30pm **Poster Session, Presentation of Poster Awards and Reception in Smilow Commons**

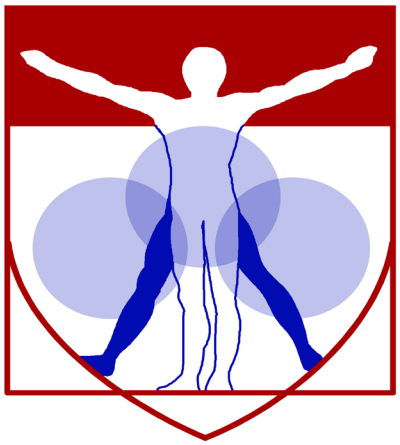

PENN

CENTER for

MUSCULOSKELETAL

DISORDERS

Center

Components

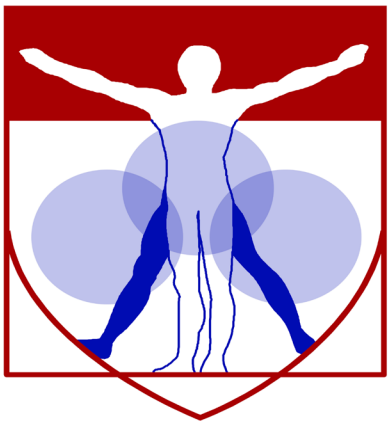

PENN

CENTER for

MUSCULOSKELETAL

DISORDERS

Center Overview

OVERVIEW OF THE PENN CENTER FOR MUSCULOSKELETAL DISORDERS

Director: Louis J. Soslowsky, PhD (soslowsk@upenn.edu)
Associate Director: Maurizio Pacifici, PhD (PacificiM@email.chop.edu)

Musculoskeletal-related conditions in the United States account for 132 million visits to physicians' offices, 29 million visits to emergency rooms, 15 million hospital outpatient visits, and cost over $850 billion each year. Further, musculoskeletal injuries in the United States cause workers to miss more than 440 million days of work annually. In fact, more than one in four Americans has a musculoskeletal impairment. With the widespread increase in athletic and recreational activities, and the increase of the elderly population at large, these numbers are expected to rise substantially. Musculoskeletal injuries represent a critical health concern which must be better understood and better treated. To do so, a dedicated and focused strategic effort is required that optimizes research translation from the bench to the bedside in an efficient and effective manner.

The Penn Center for Musculoskeletal Disorders (PCMD) will continue to enhance the research productivity of, and provide critical resources and programs to, investigators to address multidisciplinary research strategies for musculoskeletal problems. The overall goal of this Center is to promote cooperative interactions among investigators, accelerate and enrich the effectiveness and efficiency of ongoing research, foster new collaborations and new research, and ultimately, translate our research efforts into better and new therapies for musculoskeletal disorders. The central theme of the Center will continue to be "Musculoskeletal Tissue Injury and Repair". This theme is broad (as it includes all musculoskeletal tissue types, such as bone, cartilage, disc, ligament, meniscus, muscle, and tendon), focused (as takes advantage of commonalities in approaches across tissue types), and clinically significant (as it fosters development of assays, procedures and knowledge in preclinical animal and human models of translational relevance). It is important to note that our PCMD is not a "bone center" nor is it a "muscle center". Rather, it is truly a "musculoskeletal center" and has emerged as the recognized home for musculoskeletal research across the Penn campus and as a technical and intellectual resource for the broader Philadelphia musculoskeletal research community.

One focus of our Center is to translate research themes, approaches, and paradigms that are consistent across different tissues. Musculoskeletal tissues have much in common and their similarities are often overlooked when focus is restricted to a single tissue type. For example, the role of inflammatory cytokines is well studied in several tissue injury and repair scenarios; yet specific findings in one tissue-type are not always known and applied in other tissues. Similarly, the availability of technologies for imaging blood vessel formation in vivo to monitor healing in a given tissue is not always known and available to researchers focusing on other tissues. Given that approaches routinely used to evaluate mechanisms in one tissue could aid researchers in other areas, our Center will work to foster this critical cross-talk.

To provide a further focus for our Center, we will continue to develop programs with an emphasis on small animal models utilizing unique and sophisticated methods that can cross length scales to pre-clinical large animal models and human testing. Although large animal models for many human diseases exist and are essential for translational studies, small animals (e.g., mouse and rat) have become more commonly used for fundamental discovery of disease mechanism and initial therapeutic development due to availability of transgenic and knockout approaches and molecular tools, low cost, ease of handling and housing, and other practical issues. However, performing certain assays and experiments in mice and rats can be challenging and these difficulties often cannot be overcome in single investigator laboratories. The PCMD will provide unique expertise and sophisticated analytical tools to investigate musculoskeletal tissues across length scales.

Thus, the primary overall aims of this Center are to enhance and advance the research productivity of investigators in musculoskeletal tissue injury and repair by:

Aim 1: Providing innovation within critical resource core facilities in areas that cross disciplines, length scales, and hierarchies. These core facilities are μCT Imaging, Biomechanics, and Histology.

Aim 2: Developing a pilot and feasibility grant program for investigators, with direct mentorship, whereby new approaches, ideas, and collaborations can be developed prior to seeking extramural funding.

Aim 3: Developing educational and research enrichment programs spanning tissue types, research approaches, and paradigms, through which members can learn from national leaders and from each other.

High quality musculoskeletal research is currently being conducted by many groups at Penn. While many bring sophisticated approaches to bear on musculoskeletal problems, few groups have the required expertise and facilities to perform high quality and specialized assays in their own labs. Furthermore, most investigators are not aware of approaches utilized, and results obtained, in other tissues that may have direct relevance on their research questions. Ultimately, close cooperation, communication, and collaboration among researchers across musculoskeletal tissue types and from a wide variety of disciplines will significantly enhance the research of our members. The Center will provide opportunities to integrate multi-disciplinary techniques to determine mechanisms for tissue function, injury, degeneration, repair, and regeneration, with the ultimate goal of advancing the diagnosis, treatment, and prevention of diseases and injuries of the musculoskeletal system.

In addition to the specific features described in this proposal, there is an intangible feature of our Center that should not be overlooked. Although our musculoskeletal program is strong nationally, the Penn biomedical research community is large and diverse. As such, the Center serves as an essential mechanism to highlight our successes and the importance and excitement of musculoskeletal research across campus, as well as to institutional leadership. Having a strong voice for musculoskeletal researchers is critical to support our collective and individual research goals. In these ways, the Center - with essential support from the P30 - has become and remains an indispensable resource and advocate for our community.

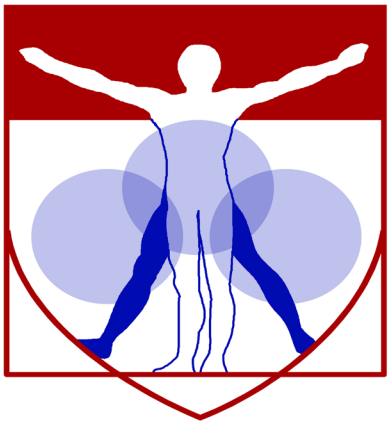

PENN

CENTER for

MUSCULOSKELETAL

DISORDERS

Core I

Biomechanics

Biomechanics Core

Core Director: Robert Mauck, Ph.D. (lemauck@pennmedicine.upenn.edu)
Technical Director: Snehal Shetye, Ph.D. (shetye@upenn.edu)

The overall objective of the Biomechanics Core is to develop and provide a wide range of innovative biomechanical approaches to evaluate musculoskeletal tissue function in the context of damage, repair, and regeneration, and to provide training and funding for new projects and collaborations utilizing these assays. Over the last decade, our Biomechanics Core at the Penn Center for Musculoskeletal Disorders (PCMD) has grown into a thriving resource for the University of Pennsylvania and Philadelphia area musculoskeletal research community. In this submission, we will further expand our services to meet the increased demand for specialized techniques and develop new and innovative methods that address the multi-scale mechanics of musculoskeletal tissues. These developments will provide customized services that enhance the research productivity of our members. The Specific Aims of the Biomechanics Core are:

- To provide guidance and training on the capabilities, advantages, and disadvantages of the various methodologies to assess musculoskeletal tissue biomechanical function through formal educational enrichment programs and one-on-one interactions

- To provide expertise and service for biomechanical assays of musculoskeletal tissues

- To develop innovative biomechanical testing techniques that will be applicable to Musculoskeletal research, and in particular those that provide information across tissue length scales

- To provide funding for the development of new projects and collaborations and to develop preliminary and/or feasibility data for investigators.

Successful completion of these aims will significantly enhance the environment and the capabilities of researchers at the University of Pennsylvania, leading to new approaches to address musculoskeletal disorders and new collaborations between Center faculties who may have not previously included biomechanical function approaches in their musculoskeletal research programs.

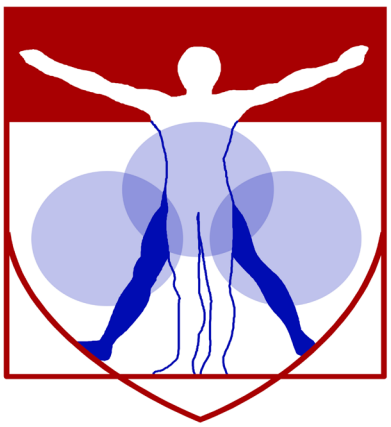

PENN

CENTER for MUSCULOSKELETAL DISORDERS

Core II

Histology

Histology Core

Overview and Mission

The mission of the Penn Center for Musculoskeletal Disorders (PCMD) Histology Core is to provide comprehensive, high quality histology services to musculoskeletal researchers at the University of Pennsylvania and the broader research community.

The Specific Aims of the core are:

- To provide guidance and training on the capabilities, advantages, and disadvantages of the various methodologies to assess musculoskeletal tissue structure and composition through formal educational enrichment programs and one-on-one interactions.
- To provide expertise and service for histological and histomorphometric assays of musculoskeletal tissues.
- To develop new histologically-based techniques that will be applicable to musculoskeletal research.
- To provide funding for development of new projects and collaborations and to develop preliminary and/or feasibility data for investigators.

Services Offered

The core offers a complete spectrum of services from sample preparation and processing, to sectioning, staining and analysis, with capabilities for paraffin, plastic and frozen histology. The core provides state of the art equipment in each of these areas, which can be accessed either on a self-service basis (upon completion of training) or a full-service basis through our full-time histology technician. Service fees are highly competitive, with significant subsidies offered for PCMD members.

- Consultation and protocol development (no charge for first 6 hours)
- Paraffin processing, embedding and sectioning
- Plastic processing and sectioning
- Frozen sectioning, including cryofilm method for undecalcified bone and teeth
- Routine histochemical staining
- Imaging and histoquantitation
- Training in histology techniques

If you are using the core for the first time, we highly recommend scheduling a meeting with one of the core co-directors and the core technician to discuss the scope of your project and specific needs.

We are very happy to provide letters of support for grant applications. To request a letter, please contact the core co-directors and provide the project title, a brief description of the project and core services you propose to use.

Please visit the core website for more information: www.med.upenn.edu/pcmd/histologymain.html

Co-Directors

Ling Qin, Ph.D. (Plastic and Frozen Histology)
Associate Professor of Orthopaedic Surgery
qinling@pennmedicine.upenn.edu
215 898 6697

Lachlan Smith, Ph.D. (Paraffin Histology)
Assistant Professor of Neurosurgery
lachlans@pennmedicine.upenn.edu
215 746 2169

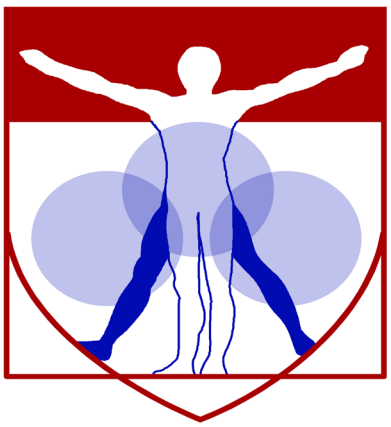

PENN

CENTER for MUSCULOSKELETAL DISORDERS

Core III

MicroCT

MicroCT Core

Director: X. Sherry Liu, Ph.D. (xiaoweil@pennmedicine.upenn.edu)

The development of high-resolution micro-CT (μCT) during the past two decades has revolutionized the quantitative assessment of calcified and X-ray dense tissue morphology. With the capability of non-destructive, three-dimensional (3D) visualization of tissue structure, μCT has largely supplanted traditional histomorphometry and become a gold standard for calcified tissue density and microstructure evaluation for many measures. Due to the low intrinsic X-ray contrast of non-mineralized tissues, traditional applications of μCT in musculoskeletal research have been limited to mineralized tissue. However, the development of contrast-enhanced imaging methods has greatly broadened applications of μCT to include musculoskeletal soft tissues as well. These cutting-edge image-based quantification methods not only enable characterization of soft-tissue morphology, but some also yield insight into tissue composition, such as glycosaminoglycan (GAG) density, which is associated with soft-tissue function and mechanics. Another important advance in the past decade is in vivo μCT imaging of living small animals. Research of musculoskeletal tissue injury and repair has been progressively utilizing animal models of human disease. Unlike many assays that require sacrificing the animal to extract tissues for analysis, in vivo μCT enables longitudinal evaluation of changes in a particular animal non-invasively over time. This new imaging strategy minimizes the number of animals required while enhancing statistical power. With these developments, μCT can now provide a deep and quantitative understanding of the genetic influences on the skeleton, as well as remodeling events in hard and soft tissues during repair, treatment, and with altered loading scenarios. Further, a μCT modality for clinical imaging of calcified tissue microstructure, called high-resolution peripheral quantitative CT (HR-pQCT), has recently been developed. This technology inaugurated a new era of non-invasive quantitative skeletal imaging, and has become a powerful tool for clinical research of musculoskeletal disorders. The overall objective of the μCTIC is to offer a wide range of μCT imaging approaches to evaluate musculoskeletal tissue injury and repair, and to provide training and consultation for new projects and collaborations utilizing these assays.

The Specific Aims for the μCTIC are:

- To provide guidance and expertise on the use of μCT imaging for musculoskeletal research through educational enrichment programs and one-on-one interactions
- To provide a range of μCT imaging resources, expertise, and services for the study of the structure, function and physiology of the musculoskeletal system in laboratory animals and humans
- To develop new μCT imaging-based techniques that will be applicable to musculoskeletal research
- 4) To provide funding for the development of new projects and collaborations and to develop preliminary and/or feasibility data for investigators.

Successful completion of these Aims will significantly enhance the environment and capabilities of researchers at the University of Pennsylvania, leading to novel and innovative approaches to address musculoskeletal disorders and to new collaborations between Core faculty who may not have previously included human and/or animal imaging in their musculoskeletal research programs.

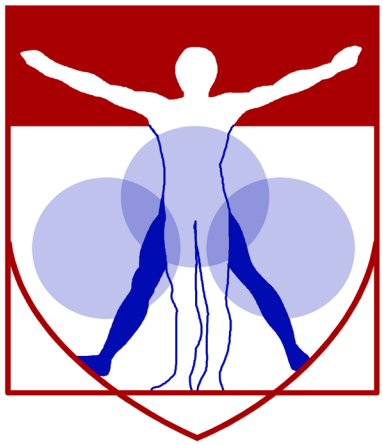

PENN

CENTER for

MUSCULOSKELETAL

DISORDERS

Pilot Grant Program

PENN CENTER FOR MUSCULOSKELETAL DISORDERS
PILOT AND FEASIBILITY GRANT PROGRAM

The Penn Center for Musculoskeletal Disorders has an ongoing Pilot and Feasibility Grant Program. Submissions should be related to musculoskeletal tissue injury and repair which is the broad focus of the Center and Grants are only eligible for Center members (if you are not a member but would like to become one, please contact pcmd@pennmedicine.upenn.edu). For more information on our Cores and Center in general, please see our web site at www.med.upenn.edu/pcmd . We are anticipating that the next Center grant submission deadline will be in Spring 2019.

Eligibility

- Only Full Center members are eligible. If you are not currently a member, please go to the link: http://www.med.upenn.edu/pcmd/memberinfo.shtml
- Categories of applicants include: 1) Established investigators with a proposal to test the feasibility of a new or innovative idea in musculoskeletal tissue injury and repair representing a clear and distinct departure from their ongoing research, 2) Established investigators with no previous work in musculoskeletal tissue injury and repair interested in testing the applicability of their expertise on a problem in this area, and 3) New investigators without significant extramural grant support as a Principal Investigator to develop a new project.
- Pilot and Feasibility Grants must use at least one of the Center's Research Cores.
- Pilot project awardees are eligible for one year, with a second year to be considered (budgets will be for $20-50,000 per year and timelines should be for one or two years). The second year of funding, the dollar amount of which would only be for up to half the year one budget, will be considered based on the progress report submitted after the first year of funding and funding availability in the Center. Please note that second year funding will often not be awarded, and when awarded, will be done so primarily to new investigators; second year funding to senior investigators will be quite rare.
- It is expected that these Pilot grants will lead to funding through other independent, extramural mechanisms. Therefore, the likelihood of future extramural funding will enter into the evaluation of these proposals.

Format

- Applications should be formatted loosely in the style of an NIH R03 grant (http://grants.nih.gov/grants/guide/pa-files/PA-18-488.html). The main body of the application (Specific Aims through Research Design and Methods-sections 4-7 below) is limited to five pages. The appli cation should be in a single pdf file. The format should be:

1) Cover Page (not NIH face page) with grant title, PI name (and co-PI name if applicable), affiliation, contact information
2) Budget and brief justification (note that equipment is not allowed) (Please use form PHS398, Page 4)
3) NIH Biosketch of PI (and co-PI if applicable) (in the new NIH format)
4) Specific Aims
5) Significance
6) Innovation
7) Approach
8) Brief Statement of Category of Investigator per guidelines above
9) Brief Statement of How this Funding will lead to other Extramural Funding
10) Human Subjects and/or Vertebrate Animal Subjects (if applicable)
11) Consultants (if applicable)
12) Literature Cited
13) Certification of Patient Oriented Research (if applicable)

Please do not hesitate to email pcmd@pennmedicine.upenn.edu with any questions or comments.

Penn Center for Musculoskeletal Disorders Pilot & Feasibility Grants
(all grants awarded since inception of Center)

Awarded 2018-2019
Miltiadis Zgonis, M.D., Assistant Professor of Orthopaedic Surgery, Perelman School of Medicine: "Development, Maturation, and Function of Meniscal Radial Elements"

Joel Boerckel, Ph.D., Assistant Professor of Bioengineering and Orthopaedic Surgery, Perelman School of Medicine: "Role of YAP/TAZ in osteoprogenitor cell-induced angiogenesis for vascularized bone repair"

Awarded 2017-2018
Nathaniel Dyment, Ph.D., Assistant Professor of Orthopaedic Surgery, Perelman School of Medicine: "Murine anterior cruciate ligament reconstruction model to understand the cellular origins and mechanisms of repair"

Yangqing Gong, Ph.D., Research Assistant Professor of Medicine, Perelman School of Medicine: "Role of plasminogen in mesenchymal stem cell function and post-injury bone regeneration"

Carla Scanzello, M.D., Ph.D., Assistant Professor of Medicine, Perelman School of Medicine: "Importance of Macrophage Responses in Osteoarthritis"

Susan Volk, V.M.D., Ph.D., D.A.C.V.S., Assistant Professor of Small Animal Surgery, School of Veterinary Medicine: "The Regulatory Roles of Type III Collagen in the Cartilage Collagen Network: Implications for Osteoarthritis Prevention and Treatment"

Awarded 2016-2017
Joseph Baur, Ph.D., Assistant Professor of Physiology Institute for Diabetes, Obesity and Metabolism, Perelman School of Medicine: "Targeting NAD metabolism in muscular dystrophy"

Yongwon Choi, Ph.D. Leonard Jarett Professor of Pathology and Lab Medicine, Perelman School of Medicine: "Cell adhesion regulation of multiple-myeloma induced bone destruction"

X. Sherry Liu, Ph.D., Assistant Professor of Orthopaedic Surgery and Bioengineering, Perelman School of Medicine: "Mechanical Consequences of Modeling- vs. Remodeling-Based Bone Formation" *(awarded extramural funding from the NSF Award #1661858)*

Hongtao Zhang, Ph.D., Research Assistant Professor, Department of Pathology and Lab Medicine, Perelman School of Medicine: "Novel cartilage-targeting Fc fusion proteins as novel and effective treatments for osteoarthritis"

Awarded 2015-2016
Yejia Zhang, MD, PhD, Department of Physical Medicine and Rehabilitation, "Inhibition of ADAM-8 to reduce intervertebral disc degeneration" *(Awarded extramural funding from the VA Pilot Grant; VA Competitive Pilot Fund)*

Oren Friedman, MD, Department of Otorhinolaryngology, Perelman School of Medicine: "Effect of injury to cartilage and recovery treatment with FGF-18"

Harvey Smith, MD, Department of Orthopaedic Surgery, "Impact of Pre-Culture and In Vivo Remobilization on Engineered Disc Replacement" *(Awarded extramural funding from the VA RX002274-01A1)*

Tejvir Khurana, MD, PhD, Department of Physiology, Perelman School of Medicine: "Role of the IL-15 / IL-15Rα axis in modulating muscle-tendon-bone adaptation and repair"

Awarded 2014-2015
Joshua F. Baker, MD, MSCE, Department of Rheumatology & Epidemiology/Perelman School of Medicine: *"Assessment of Intramyocellular Fat Accumulation in Rheumatoid Arthritis Using MR Spectroscopy*"

Russ P. Carstens, MD, Department of Renal-Electrolyte and Hypertension Division, Perelman School of Medicine: "Roles of Epithelial Splicing Regulatory Proteins in Craniofacial Development" *(awarded extramural funding NIH 1R56DE024749 and awarded R01 NIDCR)*

Foteini Mourkioti, PhD, Department of Orthopaedic Surgery/Perelman School of Medicine: "A Novel Molecular Mechanism in Chronic Skeletal Muscle Injury" *(supported in part from the IRM)*

Chamith Rajapakse, PhD, Department of Radiology/Perelman School of Medicine: "Biomechanics of Hip Fracture Assessed by MRI" *(Awarded extramural funding from the NIH R01 AR068382)*

Awarded 2013-2014
X. Sherry Liu, PhD, Department of Orthopaedic Surgery, Perelman School of Medicine: "Structure and Strength Recovery in Post-Lactation Bone" *(awarded extramural funding from the NIH R03 AR065145 and NSF Career Award #1653216)*

Ling Qin, Ph.D., Department of Orthopaedic Surgery, Perelman School of Medicine: "Novel Anabolic Treatment for Radiation-Induced Osteoporosis" *(awarded extramural funding from the NIH R01AR066098)*

Lachlan Smith, Ph.D. Department of Orthopaedic Surgery, Perelman School of Medicine: "Molecular Mechanisms of Failed Vertebral Bone Formation in Mucopolysaccharidosis VII" *(awarded extramural funding from the NIH R03 AR065142 and the MPS Society)*

Hansell H. Stedman, MD, Department of Surgery, Perelman School of Medicine: "Molecular Pattern Recognition in Acute and Chronic Injury to Muscle and Myotendinous Junction" *(awarded extramural funding from the NIH R01NS094705)*

Awarded 2012-2013
Jason Burdick, PhD, Department of Bioengineering, School of Engineering and Applied Science: "Acelluar Fibrous Scaffolds for Stem Cell Recruitment and Cartilage Repair" *(awarded extramural funding from the NIH R01 EB008722)*

James L. Carey, MD, MPH, Department of Orthopaedic Surgery, Perelman School of Medicine: "Development of a Large Animal Model of Osteochondritis Dissecans" *(awarded extramural funding from the NIH R01 EB008722)*

Andrew Kuntz, MD, Department of Orthopaedic Surgery, Perelman School of Medicine: "Effects of Intra-Articular Glenohumeral Injection of a Nonsteroidal Anti-Inflammatory Drug on Shoulder Joint Mechanics in a Rat Model"

Arjun Raj, PhD, Department of Bioengineering, School of Engineering and Applied Science: "Single Cell Analysis of Molecular and Micromechanical Heterogeneity in Mesenchymal Stem Cells and Engineered Tissues"

Awarded 2011-2012
Struan F.A. Grant, PhD, Department of Pediatrics, Children's Hospital of Philadelphia and Perelman School of Medicine: "Utilization of ChIP-seq to Identify Genes Regulated by Osterix"

Motomi Enomoto-Iwamoto, DDS, PhD, Department of Orthopaedic Surgery, Children's Hospital of Philadelphia and Perelman School of Medicine: "Tendon Repair by Retinoic Acid Receptor Agonists" *(awarded extramural funding from the NIH R21 AR062193)*

Ian N. Jacobs, MD, Department of Otorhinolaryngology: Head and Neck Surgery, Children's Hospital of Philadelphia and Perelman School of Medicine: "A Pilot Study for the Development of a Rabbit In-Vivo Tissue- Engineered Cartilage Graft for Pediatric Laryngotracheal Reconstruction" *(awarded extramural funding from The Triological Society)*

Awarded 2010-2011
Susan W. Volk, VMD, PhD, Dipl ACVC, Department of Small Animal Surgery, School of Veterinary Medicine: "The Role of Type III Collagen in Bone Repair and Regeneration"

Jaimo Ahn, MD, PhD, Department of Orthopaedic Surgery, Perelman School of Medicine: "Toward the Identification of Molecular Pathway Alterations in Aged Fracture Healing: A Pilot Study Utilizing a Genetic Model of Senescence" *(awarded extramural funding from the NIH R03 AG040670)*

Shannon Fisher, MD, PhD, Department of Cell and Developmental Biology, Perelman School of Medicine: "Requirement for Osterix in Skull Formation and Maintenance of Adult Bone in Zebrafish" *(awarded extramural funding from the NIH R21 DE021509)*

Awarded 2010-2011 (Jointly with IOA)
Olena Jacenko, PhD, Department of Animal Biology, School of Veterinary Medicine: "Aging of the hematopoietic niche" *(awarded extramural funding from the NIH R01 DK088334-01)*

Eileen M. Shore, PhD, Departments of Orthopaedic Surgery and Genetics, Perelman School of Medicine: "Modulation of Progenitor Cell Differentiation through BMP Signaling" *(awarded extramural funding from the NIH R01 AR041916-15)*

Kurt D. Hankenson, DVM, PhD, Department of Animal Biology, School of Veterinary Medicine: "Notch Signaling in Bone Regeneration" *(awarded extramural funding from the DOD CDMRP)*

Awarded 2009-2010
Ling Qin, PhD, Department of Orthopaedic Surgery, School of Medicine: "Mechanisms of EGFR Action on Bone" *(awarded extramural funding from the NIH R01 DK095803)*

Steven Scherer, MD, PhD, Department of Neurology, Perelman School of Medicine: "Are N-cadherin and L1 Adhesion Molecules Required for Recovery of Muscle Strength after Nerve Injury?"

Nader M. Hebela, MD, Department of Orthopaedic Surgery, Perelman School of Medicine: "A Pre-Clinical Rodent Model of Intervertebral Disc Autograft Transplant" *(awarded extramural funding from the DOD/CDMRP/PROP OR090090)*

Awarded 2008-2009
Sunday O. Akintoye, BDS, DDS, MS, Department of Oral Medicine, School of Dental Medicine: "Orofacial Bone Marrow Stromal Cells Promote Bisphosphonate-Associated Jaw Osteonecrosis" *(awarded extramural funding from the NIDCR R21 DE022826)*

Margaret M. Chou, PhD, Departments of Cell and Developmental Biology, Perelman School of Medicine: "Mechanisms of TRE17/USP6 Function in the Etiology of Aneurysmal Bone Cyst" *(awarded extramural funding from the NIH-NCI R01 CA168452 and R21-CA18601)*

Kenneth W. Leichty, MD, Department of Surgery, Perelman School of Medicine: "The Role of Inflammation in Regenerative Fetal Tendon Wound Healing" *(awarded extramural funding from the NIH DP2 DK083085)*

Kathleen M. Loomes, MD, Department of Pediatrics, Children's Hospital of Philadelphia: "The Role of Jag1 in Osteogenesis"

Eileen M. Shore, PhD, Departments of Orthopaedic Surgery and Genetics, Perelman School of Medicine: "Analysis of an ACVR1 Knock-in Mouse Model for FOP*" (awarded extramural funding from the NIH R01 AR041916-15S1)*

Awarded 2007-2008
Sherrill L. Adams, PhD, Department of Biochemistry, School of Dental Medicine: "Collagen III-deficient Mice as a Model for Musculoskeletal Wound Repair"

Kurt D. Hankenson, DVM, PhD, Department of Animal Biology, School of Veterinary Medicine: "Regulation of Bone Formation by Novel Activators of Canonical Wnt Signaling"

Awarded 2006-2007

Robert J. Pignolo, MD, PhD, Department of Medicine, Perelman School of Medicine: "Stem Cell Rescue of the Osteoporotic Phenotype in a Mouse Model of Accelerated Aging" *(awarded extramural funding from the NIH R01 AG028873)*

Robert L. Mauck, PhD, Department of Orthopaedic Surgery, Perelman School of Medicine "Meniscus Repair with a Novel Aligned Nanofiber Scaffold" *(awarded extramural funding from the NIH R01 AR056624 and the VA RR & D)*

Christopher S. Chen, MD PhD, Department of Bioengineering, School of Engineering and Applied Science: "Mechanotransduction in Mesenchymal Stem Cells" *(awarded partial funding as Co-Investigator on NIH P41 EB001046)*

Pedro K. Beredjiklian, MD, Department of Orthopaedic Surgery, Perelman School of Medicine: "Role of Hyaluronic Acid Receptors in Tendon Healing" (*awarded extramural funding from the NIH R21 AR052393*)

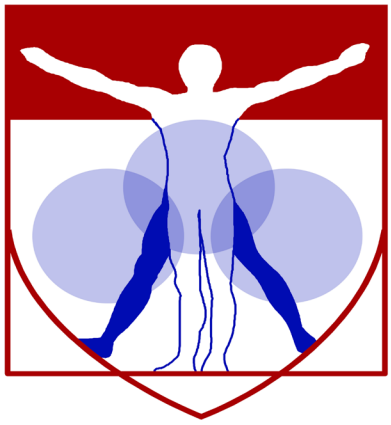

PENN

CENTER for

MUSCULOSKELETAL

DISORDERS

Visiting Professorship Series 2018-2019

PENN
CENTER for
MUSCULOSKELETAL
DISORDERS

Visiting Professorship Series-Academic Year 2018-2019

Tuesday, September 25, 2018, 1:30pm – 2:30pm, CRB Austrian Auditorium
Title: "Musculoskeletal Microbiology"
Christopher Hernandez, Ph.D.
Associate Professor, Sibley School of Mechanical and Aerospace Engineering Meinig School of Biomedical Engineering, Cornell University

Tuesday, October 23, 2018, 3:00-4:00pm/JMB Class of '62 Auditorium
Title: *Comparative and MRI Studies of Developmental Orthopedic Disease"*
Cathy Carlson, DVM, PhD, DACVP
Professor and Chair, Veterinary Clinical Sciences Department
College of Veterinary Medicine, University of Minnesota

ANNUAL SCIENTIFIC SYMPOSIUM (all day event)
Wednesday, November 7, 2018, 8:30-5:30pm/Smilow Rubenstein Auditorium/
Title: *"Skeletal Dysplasias: Informing Skeletal Function & Homeostasis"*
Brendan Lee, M.D., Ph.D.
Robert and Janice McNair Endowed Chair in Molecular and Human Genetics
Professor and Chairman, Department of Molecular and Human Genetics, Baylor College of Medicine

Tuesday, December 11, 2018, 1:30-2:30pm/ CRB Austrian Auditorium
Title: *A novel Hyaluronan-binding Peptide improves Cartilage Repair*
Thorsten Kirsch PhD
Professor, Vice Chair for Research and Director, Musculoskeletal Research Center, Department of Orthopaedic Surgery
New York University Langone Health

Tuesday, January 2019, 1:30-2:30pm/ CRB Austrian Auditorium
Title: TBD
Pura Munoz-Canoves, PhD
Professor of Cell Biology and Principal Investigator
Pompeu Fabra University (UPF), Barcelona, Spain
ICREA Research Professor, Joint appointment: Principal Investigator, Spanish National Cardiovascular Research Center, Madrid

Tuesday, February 12, 2019 1:30-2:30pm/ CRB Austrian Auditorium
Title: TBD
Karl Kadler, BSc, PhD
Professor of Biochemistry, Division of Cell Matrix Biology & Regenerative Medicine
University of Manchester, UK

Tuesday, March 12, 2019 1:30-2:30pm/ CRB Austrian Auditorium
Title: TBD
Johnna Temenoff, Ph.D
Professor, Department of Wallace H. Coulter Department of Biomedical Engineering
Georgia Tech, Emory University

Tuesday, April 30, 2019 1:30-2:30pm/ CRB Austrian Auditorium
Title: TBD
Michael T. Longaker, MD, MBA, DSc (hon) FACS
Deane P. & Louise Mitchell Professor
Vice Chair, Department of Surgery
Co-Director, Institute for Stem Cell Biology & Regenerative Medicine
Director, Program in Regenerative Medicine
Director, Children's Surgical Research
Stanford University School of Medicine

Tuesday, May 2019 TBD

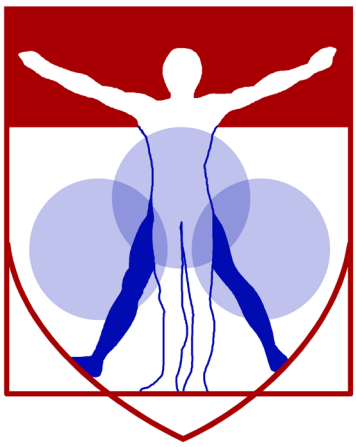

PENN
CENTER for
MUSCULOSKELETAL
DISORDERS

Symposium Participants

Name - First	Name - Last	Email	Affiliation
Kimberly	Agnello	kagnello@vet.upenn.edu	UPenn
Abass	Alavi	Abass.alavi@uphs.upenn.edu	U Penn
Robyn	Allen	roallen@vet.upenn.edu	UPenn
Marco	Angelozzi	angelozzim@email.chop.edu	CHOP
Golnaz	Anvari	tug10568@temple.edu	Temple Univ
Zoltan	Arany	zarany@pennmedicine.upenn.edu	UPenn
Beth	Ashinsky	beth.ashinsky@gmail.com	UPenn
Tala	Azar	talaazar@seas.upenn.edu	UPenn
Sonia	Bansal	soniab@seas.upenn.edu	UPenn
Mary	Barbe	mary.barbe@temple.edu	Temple Univ
Carrie	Barnum	cbarnum@pennmedicine.upenn.edu	UPenn
Joseph	Baur	baur@pennmedicine.upenn.edu	UPenn
Catherine	Bautista	cbaut@seas.upenn.edu	UPenn
Josh	Baxter	josh.baxter@uphs.upenn.edu	UPenn
Zak	Beach	zbeach@seas.upenn.edu	UPenn
Evangelia	Bellas	Evangelia.bellas@temple.edu	Temple Univ
Paul	Billings	BillingsP@email.chop.edu	CHOP
Joel	Boerckel	Boerckel@pennmedicine.upenn.edu	UPenn
Igor	Bogush	Igor.Bogush@pennmedicine.upenn.edu	UPenn
Paige	Boneski	Pxb083@jefferson.edu	Thomas Jefferson Univ
Eddie	Bonnevie	edbon@pennmedicine.upenn.edu	UPenn
Niambi	Brewer	nbrewer@pennmedicine.upenn.edu	UPenn
Jason	Burdick	burdick2@seas.upenn.edu	UPenn
James	Carey	james.carey@uphs.upenn.edu	UPenn
Jaclyn	Carlson	carlsonjaclyn@gmail.com	UPenn
Bob	Caron	rcaron@pennmedicine.upenn.edu	UPenn
Adnan	Cheema	adnan.cheema@uphs.upenn.edu	UPenn
Karthikeyani	Chellappa	kchel@pennmedicine.upenn.edu	UPenn
Chider	Chen	chenc10@upenn.edu	UPenn
Delia	Chen	dzchen@sas.upenn.edu	UPenn
Alessandra	Chesi	chesia@email.chop.edu	CHOP
Dennis	Chin	dchin1564@gmail.com	UPenn
Juliet	Chung	chungj7@email.chop.edu	CHOP
Rebecca	Chung	rebecca.chung@pennmedicine.upenn.edu	UPenn
Joseph	Collins	jmcollin@seas.upenn.edu	UPenn
Diana	Cousminer	cousminerd@email.chop.edu	CHOP
Jake	Cresta	jake.cresta@pennmedicine.upenn.edu	UPenn
Eric	Dai	ericnan@seas.upenn.edu	UPenn
Ryan	Daniels	rydan@pennmedicine.upenn.edu	UPenn
Andrew	Degnan	degnana@email.chop.edu	CHOP
Nikolas	Di Caprio	tuf97303@temple.edu	Temple Univ
Susan	Dinella	sdinella@pennmedicine.upenn.edu	UPenn
George	Dodge	gdodge@pennmedicine.upenn.edu	UPenn
Michael	Dodson	dodsonm@vet.upenn.edu	UPenn
Shilpa	Donde	Shilpa.Donde@uphs.upenn.edu	UPenn
John	Drazan	john.drazan@uphs.upenn.edu	UPenn
Nathaniel	Dyment	dyment@pennmedicine.upenn.edu	UPenn

John	Elfar	openelfar@gmail.com	Penn State Univ
Daniel	Farber	daniel.farber@uphs.upenn.edu	Upenn
Megan	Farrell	megan.j.farrell@gmail.com	UPenn
Melissa	Franklin	mef332@drexel.edu	Drexel Univ
Theresa	Freeman	theresa.freeman@jefferson.edu	Thomas Jefferson Univ
Chuanyun	Fu	chuanyf@upenn.edu	UPenn
Keitaro	Fujino	Keitaro.Fujino@pennmedicine.upenn.edu	UPenn
Ashley	Fung	afung@seas.upenn.edu	Upenn
Jonathan	Galarraga	jgala@seas.upenn.edu	UPenn
Rahul	Gawri	rahulgawri@hotmail.com	UPenn
Peeyush	Goel	pgoel@pennmedicine.upenn.edu	UPenn
Struan	Grant	grants@email.chop.edu	CHOP
Luigi	Grasson	luigi@navrogen.com	Navrogen
Sarah	Gullbrand	sgullb@pennmedicine.upenn.edu	UPenn
Biao	Han	bh462@drexel.edu	Drexel Univ
Lin	Han	lh535@drexel.edu	Drexel Univ
Abdul	Haseeb	haseeba@email.chop.edu	CHOP
Michael	Hast	hast@pennmedicine.upenn.edu	UPenn
Kimberly	Helbig	helbigkg@email.chop.edu	CHOP
Elizabeth	Henning	ehenning@pennmedicine.upenn.edu	UPenn
Su Chin	Heo	heosc@pennmedicine.upenn.edu	UPenn
Noreen	Hickok	Noreen.Hickok@jefferson.edu	Thomas Jefferson Univ
Brendan	Hilliard	hilliard@temple.edu	Temple Univ
Daniel	Himmelstein	daniel.himmelstein@gmail.com	UPenn
Md	Hossain	zubaer@udel.edu	Univ Delaware
Xiaobin	Huang	huangx1@email.chop.edu	CHOP
Julianne	Huegel	jhuegel08@gmail.com	UPenn
Todd	Hullfish	todd.hullfish@uphs.upenn.edu	UPenn
Meagan	Ita	meita@seas.upenn.edu	UPenn
Olena	Jacenko	jacenko@vet.upenn.edu	UPenn
Xing	Ji	JIX@EMAIL.CHOP.EDU	CHOP
Zhirui	Jiang	Zhirui.Jiang@pennmedicine.upenn.edu	Upenn
Xi	Jiang	jangxi@pennmedicine.upenn.edu	UPenn
Kyu Sang	Joeng	joeng@pennmedicine.upenn.edu	UPenn
Mitchell	Johnson	mitchell.johnson@pennmedicine.upenn.edu	UPenn
Shira	Johnston	shira.johnston@jefferson.edu	Thomas Jefferson Univ
Brandon	Jones	bcjones@seas.upenn.edu	UPenn
Timur	Kamalitdinov	timkam@seas.upenn.edu	UPenn
Ranjan	Kc	kcr@email.chop.edu	CHOP
Chris	Kegelman	ckeg@seas.upenn.edu	UPenn
Megan	Killian	killianm@udel.edu	Univ Delaware
Boa	Kim	boakim@upenn.edu	UPenn
Hyunsoo	Kim	hyunsoo3@pennmedicine.upenn.edu	UPenn
Dong Hwa	Kim	kimd1@pennmedicine.upenn.edu	UPenn
Jacob	Kocan	jkocan@sas.upenn.edu	UPenn
Eiki	Koyama	koyamae@email.chop.edu	CHOP
Andrew	Kuntz	andrew.kuntz@uphs.upenn.edu	UPenn
Mi	Kwon	miykwon@seas.upenn.edu	UPenn

Yian Khai	Lau	adrianlau02@gmail.com	UPenn
Thomas	Leahy	tpleahy@seas.upenn.edu	UPenn
Seoung	Lee	leesh2@wku.ac.kr	UPenn
Brendan	Lee	blee@bcm.edu	Baylor Univ
Yeonju	Lee	Yeonju.Lee@pennmedicine.upenn.edu	UPenn
Hyunyeol	Lee	hyunyeol@pennmedicine.upenn.edu	UPenn
Wen-Chih	Lee	leew2@email.chop.edu	CHOP
Veronique	Lefebvre	Lefebvrev1@email.chop.edu	CHOP
Ryan	Leiphart	rleip@seas.upenn.edu	UPenn
Scott	Levin	scott.levin@uphs.upenn.edu	UPenn
Yihan	Li	yihanl@seas.upenn.edu	UPenn
Ziqing	Li	ziqingli@upenn.edu	UPenn
Xinjua	Li	xinhuali@upenn.edu	Upenn
Dongming	Liang	dol@pennmedicine.upenn.edu	UPenn
Renata	Linardi	rlinardi@upenn.edu	UPenn
Sherry	Liu	xiaoweil@pennmedicine.upenn.edu	UPenn
Ryan	Locke	rlocke@udel.edu	Univ Delaware
Claudia	Loebel	loebelcl@seas.upenn.edu	UPenn
Fanxin	Long	longf1@email.chop.edu	CHOP
Vitali	Lounev	vlounev@pennmedicine.upenn.edu	UPenn
Veda	Madhu	vxm042@jefferson.edu	Thomas Jefferson Univ
Sai	Mandalapu	saimandalapu@yahoo.com	UPenn
Michele	Marcolongo	marcolms@drexel.edu	Drexel Univ
Paris	Margaritis	margaritis@email.chop.edu	CHOP
Anthony	Martin	armartin891@gmail.com	UPenn
Jerahme	Martinez	jerahme@udel.edu	Univ Delaware
Devon	Mason	dmason1@nd.edu	UPenn
Rena	Mathew	rm3325@drexel.edu	UPenn
Robert	Mauck	lemauck@pennmedicine.upenn.edu	UPenn
Rowena	McBeath	rowena.mcbeath@gmail.com	Thomas Jefferson Univ
Anna	McDermott	amcderm2@nd.edu	UPenn
Liane	Miller	liane.miller@uphs.upenn.edu	UPenn
Foteini	Mourkioti	fmour@pennmedicine.upenn.edu	UPenn
Victoria	Muir	vgmuir@seas.upenn.edu	UPenn
Christina	Mundy	matticolac@email.chop.edu	CHOP
Joey	Newton	josephbnewt@gmail.com	UPenn
Nicholas	Nicolaides	nick@navrogen.com	Navrogen Inc
Courtney	Nuss	cnuss37@gmail.com	UPenn
Kyla	Ortved	kortved@vet.upenn.edu	UPenn
Carlos	Osuna	cosuna@seas.upenn.edu	UPenn
Olivia	Ottone	oko002@jefferson.edu	Thomas Jefferson Univ
Nick	Pachuda	npachuda@its.jnj.com	Johnson & Johnson
Maurizio	Pacifici	pacificim@email.chop.edu	CHOP
Wei	Pan	weipan@pennmedicine.upenn.edu	UPenn
Na Rae	Park	Na.Park@pennmedicine.upenn.edu	Upenn
Saba	Pasha	pashas@email.chop.edu	CHOP
Jay	Patel	jaymilanpatel@gmail.com	UPenn
Sun	Peck	sunchung@pennmedicine.upenn.edu	UPenn

Ana	Peredo	anapperedo@gmail.com	UPenn
Nancy	Pleshko	npleshko@temple.edu	Temple Univ
Ling	Qin	qinling@pennmedicine.upenn.edu	UPenn
Min	Qiu	minqiu@upenn.edu	UPenn
William	Querido	william.querido@temple.edu	Temple
Julia	Quindlen-Hotek	juliaq@seas.upenn.edu	UPenn
Emilie	Rabut	erabut@pennmedicine.upenn.edu	UPenn
Chamith	Rajapakse	gotutor@lycos.com	UPenn
Jordan	Raney	raney@seas.upenn.edu	UPenn
Dean	Richardson	dwr@vet.upenn.edu	UPenn
Makarand	Risbud	makarand.risbud@jefferson.edu	Thomas Jefferson Univ
Douglas	Roberts	douglas2@upenn.edu	UPenn
Ashley	Rodriguez	ashley.b.rodriguez0391@gmail.com	UPenn
Danielle	Rux	ruxd@email.chop.edu	CHOP
Karanvir	Saini	karanvir@seas.upenn.edu	UPenn
Karanvir	Saini	karanvir@seas.upenn.edu	UPenn
Kamiel	Saleh	kamiel.saleh@gmail.com	UPenn
Jennifer	Sanville	sanvillejennifer@gmail.com	UPenn
Carla	Scanzello	cscanz@pennmedicine.upenn.edu	Upenn & CMC VA Medical Center
Elaine	Schmidt	schmidtelaine2@gmail.com	UPenn
Donna	Seravello	donnaser@upenn.edu	UPenn
Snehal	Shetye	shetye@pennmedicine.upenn.edu	UPenn
Yu	Shi	shiy1@email.chop.edu	CHOP
Eileen	Shore	shore@pennmedicine.upenn.edu	UPenn
Sagar	Singh	sagars@seas.upenn.edu	UPenn
Gail	Smith	smithgk@upenn.edu	UPenn
Harvey	Smith	Harvey.Smith@uphs.upenn.edu	UPenn
Lachlan	Smith	lachlans@pennmedicine.upenn.edu	UPenn
Kay	Smith	kaykesterson@yahoo.com	UPenn
Hee Kwon	Song	hsong@uphs.upenn.edu	UPenn
Chao	Song	songc2@email.chop.edu	CHOP
Lou	Soslowsky	soslowsk@upenn.edu	UPenn
Megan	Sperry	sperrym@seas.upenn.edu	UPenn
Sergei	Spitsin	spitsins@email.chop.edu	CHOP
Brendan	Stoeckl	bdstoeckl@gmail.com	UPenn
Michael	Struss	tuf19432@temple.edu	Temple Univ
Hao	Sun	sunhao2@pennmedicine.upenn.edu	UPenn
Noriko	Takegahara	tnoriko@pennmedicine.upenn.edu	UPenn
Waixing	Tang	waixing@pennmedicine.upenn.edu	UPenn
Brittany	Taylor	brtay@pennmedicine.upenn.edu	UPenn
Elisia	Tichy	etichy@pennmedicine.upenn.edu	UPenn
Azadeh	Timnak	azadeh.timnak@pennmedicine.upenn.edu	UPenn
Robert	Tower	rtower@pennmedicine.upenn.edu	UPenn
Oscar	Towler	otowler@pennmedicine.upenn.edu	UPenn
Wei-Ju	Tseng	weits@pennmedicine.upenn.edu	UPenn
Tonia	Tsinman	ttsinman@seas.upenn.edu	UPenn

Liyun	Wang	lywang@udel.edu	Univ Delaware
Wenzheng	Wang	docdoor1130@gmail.com	UPenn
Bin	Wang	bin.wang@jefferson.edu	Thomas Jefferson Univ
Mingkun	Wang	mw699@drexel.edu	Drexel
Felix	Wehrli	wehrli@pennmedicine.upenn.edu	UPenn
Yulong	Wei	yulongwei0121@gmail.com	UPenn
Stephanie	Weiss	weisssn@gmail.com	UPenn
Beth	Winkelstein	dsmarcus@upenn.edu	UPenn
Hetty	Wong	wonghe@pennmedicine.upenn.edu	UPenn
Boao	Xia	bxia9@seas.upenn.edu	UPenn
Meiqi	Xu	mqx@upenn.edu	UPenn
Yanmei	Yang	yanmei.yang@jefferson.edu	Thomas Jefferson Univ
Evan	Yang	yange3@email.chop.edu	CHOP
Feikun	Yang	feikun@vet.upenn.edu	UPenn
Lutian	Yao	lutian@pennmedicine.upenn.edu	UPenn
Yaping	Ye	YYPATPENN@GMAIL.COM	UPenn
Wei	Yu	whyuwei@gmail.com	UPenn
Chenghao	Zhang	Chenghao.zhang@pennmedicine.upenn.edu	UPenn
Deyu	Zhang	deyuz@pennmedicine.upenn.edu	UPenn
Yejia	Zhang	yejia.zhang@uphs.upenn.edu	UPenn
Xia	Zhao	zhaoxia@seas.upenn.edu	UPenn
Leilei	Zhong	zhongleilei8@gmail.com	Upenn
Cheng	Zhou	zhoucz@pennmedicine.upenn.edu	UPenn
Yilu	Zhou	yiluz@pennmedicine.upenn.edu	UPenn
Shannon	Zintner	smithsm@email.chop.edu	CHOP
Hannah	Zlotnick	zlotnick@seas.upenn.edu	UPenn

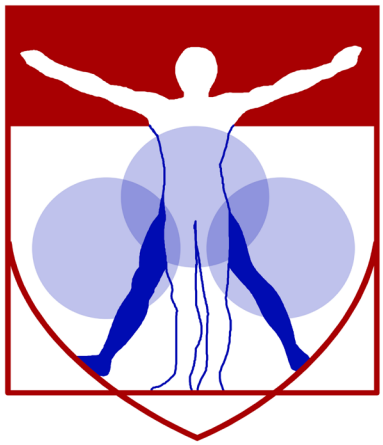

PENN

CENTER for

MUSCULOSKELETAL

DISORDERS

Speaker Abstracts

"From Pregnancy to Titin"

Zoltan Pierre Arany, MD, PhD
Professor of Medicine

Peripartum cardiomyopathy (PPCM) is a diseased marked by the unexplained onset of maternal systolic heart failure shortly before or after delivery. The disease affects approximately 1 in 2000 deliveries worldwide, with some racial and geographic variations. We have demonstrated in mouse models that the disease is likely triggered in part by late-gestational placental-derived hormones that harm cardiac vasculature. In addition, we've recently identified in human cohorts with PPCM an over-representation of loss-of-function variants in *TTN*, the gene encoding for the large sarcomeric protein Titin. Similar variants are found in idiopathic dilated cardiomyopathy (DCM), a disease with clinical similarities with PPCM. Examination of *TTN* LOFs in the UPenn Biobank revealed that the presence of TTN LOFs in patients with DCM predicts worse outcome. How *TTN* LOFs lead to PPCM and DCM remains unclear.

“3D printing bioinspired materials with spatially-controlled fiber alignment”

Jordan R. Raney, Ph.D.
Assistant Professor
Department of Mechanical Engineering & Applied Mechanics
University of Pennsylvania

Abstract.
The internal structural features of material systems used in engineering applications greatly affect their macroscopic mechanical properties. For example, natural structural materials such as wood possess highly heterogeneous mesoscale architectures, with hierarchical structure, spatially-varying fiber alignment, non-uniform density, and graded porosity. These features are the result of localized structural and compositional optimization, producing maximal bulk mechanical properties that greatly exceed those of the constituent materials. In contrast, due to the limitations of current manufacturing processes, synthetic engineering materials often lack optimized, carefully-defined mesoscale features. As a result, they lack the level of performance (strength, toughness, mass efficiency, etc.) that is ultimately possible. Additive manufacturing techniques have begun to enable more nuanced control of the internal structure of engineering materials, but many challenges remain, including notable process-intrinsic limits to the palette of printable materials. Here, direct write 3D printing is applied to the construction of architected engineering materials with the goal of enabling a new degree of control over mechanical properties in high-quality materials relevant to engineering applications. Epoxy-based and elastomer-based ink materials with fibrous fillers are developed, producing highly anisotropic materials during extrusion through a deposition nozzle. Using this approach, we control the fiber alignment to produce 3D printed parts with enhanced stiffness and damage tolerance, as well as novel instability-based shape change.

Jordan R. Raney is an assistant professor in the Department of Mechanical Engineering & Applied Mechanics at the University of Pennsylvania, where he operates the Architected Materials Laboratory. He received a B.S. in Physics and a B.S. in Computer Science from the University of Minnesota, before joining the staff at MIT Lincoln Laboratory. Subsequently, he attended Caltech for graduate school, where he received a M.S. and Ph.D. in Materials Science. Before joining Penn, he was a postdoctoral fellow in the John A. Paulson School of Engineering & Applied Sciences and the Wyss Institute for Biologically Inspired Engineering at Harvard. His research focuses on the mechanics and additive manufacturing of novel composites and material architectures, including hierarchical, heterogeneous, fibrous, and soft systems.

"The Hemophilia A Rat as a Model to Study Hemophilic Arthropathy"

Paris Margaritis, DPhil
University of Pennsylvania – Perelman School of Medicine
The Children's Hospital of Philadelphia - The Raymond G. Perelman Center of Cellular and Molecular Therapeutics

Hemophilia is an X-linked bleeding disorder caused by reduced levels/function of coagulation Factor VIII (FVIII, Hemophilia A [HemA]) or Factor IX (FIX, hemophilia B). Patients are effectively treated with infusion of FVIII or FIX. However, bleeding in the joint extravascular space (synovium) is the initiating event of hemophilic arthropathy (HAR), a major disease burden for patients with hemophilia. This complication involves diverse components such as changes in joint structure and iterative engagement of inflammation. This leads to deterioration and restriction in joint movement concomitant with severe pain. An additional complication is the development of anti-FVIII antibodies in ~30% of severe cases. These patients require the use of activated coagulation Factor VII (FVIIa) for bleed management. Limited clinical data on FVIIa prophylaxis demonstrate reduction of joint bleeds and no further deterioration of existing arthropathic joints. However, two essentials remain unclear in the setting of FVIIa prophylaxis. The first is the relationship of the therapeutic product's circulating level and clinical outcome (HAR). The second is the underlying molecular mechanism responsible for HAR. Advancing our knowledge in both aspects may potentially lead to novel therapeutic approaches. Our laboratory has been interested in hemophilia treatment of patients with anti-FVIII inhibitors. We have developed a gene-based approach using adeno-associated virus (AAV) to deliver a FVIIa *transgene* in vivo as a method of gene-based prophylaxis. Indeed, we have shown that stable expression of FVIIa can improve the bleeding defects in both mice and dogs with hemophilia. These data complement the clinical observations with FVIIa protein prophylaxis. More importantly, our approach provides a means to address essential questions in HAR and prophylaxis. Interestingly, FVIIa has a short plasmatic half-life (~2.7h) but extensive and rather long tissue distribution. A joint inflammatory milieu is a hallmark of HAR and FVIIa has been shown to engage in *direct* anti-inflammatory signaling via protease activated receptor 1 (PAR1). Additional anti-inflammatory effects may also be brought about via the endothelial protein C receptor (EPCR)-FVIIa interaction. Notably, we have also established that the EPCR-FVIIa interaction leads to reduced bleeding in hemophilic mice. It is currently unclear if the FVIIa anti-inflammatory effects come into play in HAR during FVIIa prophylaxis. Therefore, our research focuses on investigating the interplay of EPCR, PAR1 and FVIIa in modulating the joint state (structural and inflammatory) and HAR. Unfortunately, HemA mice lack spontaneous bleeds. Hemophilic dogs, while they exhibit bleeds, are prohibitive for sufficiently-powered studies. To address these issues, we have decided to utilize a novel rat model of HemA for our HAR studies. This model has unique advantages: (1) it captures the clinical symptoms of the disease; (2) it can be readily induced to develop HAR; and (3) large animal cohorts can be swiftly obtained. Using this model, FVIIa gene transfer followed by induction of HAR, will allow the study of FVIIa prophylaxis as it affects key aspects of HAR. Imaging methodology and measurement of joint biomarkers (protein and mRNA) can also aid in providing a comprehensive understanding of HAR and how it is affected by FVIIa. Overall, we believe that our studies will have mechanistic and potentially translational ramifications.

"Orthopaedic Implants and Infection: Surfaces, Synovial Fluid and the Joint Environment"

Noreen J. Hickok, Ph.D.[a], Sana Dastgheyb, Ph.D.[a], Samantha Knott, M.S.[a] and T.P.Schaer[b]
[a]Department of Orthopaedic Surgery, Thomas Jefferson University, Philadelphia, PA 19107;
[b]New Bolton Center, University of Pennsylvania School of Veterinary Medicine

With increases in numbers of biomaterial implantations, there is an urgent need to combat implant-associated infection. To better understand the factors that influence the recalcitrance of these infections, we have examined the role of growth media and specifically the synovial fluid and the hypoxic joint environment in the life cycle and antibiotic sensitivity of *Staphylococcus aureus*. Because synovial fluid contains a filtrate of blood, it is composed of many of the same proteins as blood, especially in the diseased joint, where the barrier between blood and synovium is altered. In synovial fluid and to a lesser extent in blood, *S. aureus* aggregate to form floating biofilms as well as forming biofilms on implant surfaces. We have asked whether fibrinogen, a protein that begins to appear in the synovial fluid in greater abundance during OA, is sufficient for the increased aggregation observed in synovial fluid. We have also examined the role of this aggregation in allowing the persistence of the bacteria within our ideal joint environment. Furthermore, we have asked if the bacterial aggregates are susceptible to disruption so that antibiotic sensitivity can be restored in the joint environment. Finally, we have started to explore how the low oxygen tension characteristic of the joint affects the bacteria.

"Peripheral Nerve Injury - Adjunct Treatments for Classification"

John C. Elfar, M.D.
Michael and Myrtle E. Baker Professor and Vice Chair Department of Orthopaedics and Rehabilitation
Director, Center for Orthopaedic Research and Translational Science (CORTS)
The Pennsylvania State University College of Medicine, Milton S. Hershey Medical Center

Traumatic peripheral nerve injury (TPNI) occurs in settings ranging from battlefield or motor vehicle trauma, to iatrogenic injury from surgical treatments of other serious conditions and beyond. The management of TPNI sits squarely with the orthopaedist who has tools to diagnose the extent of injury for almost all types of tissue except nervous tissue. This renders prognosis and treatment plan straightforward for all tissues except peripheral nerve.

The available classification schemes for TPNI have survived largely unchanged for 70 years and yet, for several reasons, they have never been very useful in the clinical setting. First, these schemes cannot easily be applied at the time of injury. Second, they often model the nerve as a single unit - not accounting for the fact that major peripheral nerves contain tens of thousands of axons that can be variably injured. Third, they are applied by guessing at the state of the nerve based on the little objective information available at the time of injury. Finally, no testing exists to confirm the classification of any particular nerve injury until six weeks after trauma when electrodiagnostic tests first become useable.

These shortcomings affect the critical utility of TPNI classifications in segregating out nerve lacerations. The determinant that most predicts outcome in severe limb trauma is nerve continuity. For example, a nerve that has been severed, say by a bullet, will never heal without surgical repair and yet, that same nerve, grazed by the bullet, or caught in the shockwave of a passing bullet, is indistinguishable from the nerve cut by the bullet. Both such nerves do not work, and yet the latter, unsevered nerve is best left to recover on its own without surgery.

In practice, two cardinal types of nerve injury exist in orthopaedic trauma, both yield nerves that are equally dysfunctional and yet one type requires urgent surgical repair whereas surgery is detrimental to the other. No tests exist to tell these types of TPNI apart until weeks have passed after the injury. After weeks have passed, we use electrodiagnostics (EDX) to tell which nerves were severed - and therefore which nerves should have undergone surgery weeks before. This is the state of the art in TPNI diagnosis.

Because continuity of the nerve is impossible to define for weeks after injury, the current standard treatment is waiting for spontaneous recovery in most patients we guess do not have a severed nerve. In every field of medicine, there are nerve injuries monitored in this way - without tools for definitive diagnosis, based only on our clinical suspicion.

We recently discovered that a current, FDA-approved drug (4-aminopyridine, 4AP), has the previously unknown effect of immediately allowing diagnosis of traumatically paralyzed nerves. Small doses can distinguish the severed nerve, which requires immediate surgery, from the non-severed nerve, which can be safely monitored. This novel property of 4AP, a drug already used in humans may be exploited to underpin a new classification based on the response to drug challenge. The repurposing of 4AP to diagnose nerve discontinuity may prove an avenue to avoid the guesswork currently used in orthopaedic and neurosurgical trauma.

“Biomimetic Proteoglycans in Extracellular Matrix Regeneration”

Michele Marcolongo, Ph.D.
Department Head and Professor
Materials Science and Engineering
Drexel University

Collagen is one of the leading components in extracellular matrix (ECM), providing durability, structural integrity, and functionality for many tissues. Regulation of collagen fibrillogenesis and degradation is important in the treatment of a number of diseases from orthopedic injuries to genetic deficiencies. In the body, this process is generally regulated by proteoglycans (PGs), a class of molecules that contain both pretentious and sugar components. Recently, novel, biocompatible, semi-synthetic biomimetic proteoglycans (BPGs) were developed, which consist of an enzymatically resistant synthetic polymer core and natural chondroitin sulfate (CS) bristles. It was demonstrated that BPGs affect type I collagen fibrillogenesis *in vitro*, as reflected by their impact delaying the kinetic formation of gels similar to native PGs. This indicates that the morphology of collagen scaffolds as well as endogenous ECM could also be modulated by proteoglycan mimics.

"Pathophysiological Role of ADAM8 (A Disintegrin and Metalloproteinase 8) in Intervertebral Disc Degeneration"

Yejia Zhang, MD, PhD; Zuozhen Tia, MS, Miersalijiang Yasen, MD, PhD; Robert Mauck, PhD, Maurizio Pacifici, PhD; Motomi Enomoto-Iwamoto, DDS, PhD.

Email address and telephone number of contact: *yejia.zhang@uphs.upenn.edu; Phone: 215-868-9951 (cell)*

INTRODUCTION: Chronic back pain related to intervertebral disc (IVD) degeneration is a significant problem, costing billions of dollars in the U.S. alone. Despite the staggering disease burden, there is no current effective treatment to retard IVD degeneration and reduce associated pain because the etiology of IVD degeneration remains unclear. IVD degeneration is characterized by increased extracellular matrix degradation and a variety of cellular responses. ADAM8 (A Disintegrin and Metalloproteinase 8) is a membrane-anchored proteinase that is involved in cell-matrix and cell-cell interactions in physiological and pathological processes. Our results led to the hypothesis that ADAM8 is a key enzyme in the degenerative cascade in IVD tissues and represents a major, novel and potentially far-reaching step ahead in understanding disease etiology.

METHODS: To examine expression and distribution of ADAM8 in IVD, degenerative annulus fibrosus and nucleus pulposus tissues were collected from patients undergoing surgery for back pain with appropriate institutional review board (IRB) approval. Degree of IVD degeneration was determined by MRI (grade V being the most degenerative). Distribution of ADAM8 in the IVD tissues was analyzed by immunostaining. ADAM8 and its specific proteolytic product, fibronectin fragments (FN-f; VRAA271), were quantified by Western blotting (n=3-4 for each grade). To examine the role of ADAM8 in IVD degeneration, we performed gain-of-function experiments in mice. Mature human ADAM8 ectodomain was generated in the HEK293T cell line (BioZyme, Apex, NC), labeled with the infrared dye (IRDye, Li-Cor Biosciences) and injected into the wild type mouse-tail IVD. The ADAM8 or vehicle-injected IVD tissue was harvested 1-4 weeks after injection and subjected to histological inspection and immunostaining with an antibody to VDPIEN (neoepitope of cleaved aggrecan, a generous gift from Dr. J. Mort). We have also performed loss-of-function experiments in mice. The ADAM8 gene-inactivation mutant mice that harbor a point mutation, replacing the Glutamic acid at position 330 with a Glutamine (ADAM8E330Q/E330Q mice, generously provided by Dr. Anne Marie Malfait), were used to examine requirement of ADAM8 for IVD. We dissected IVDs from wild type and ADAM8E330Q/E330Q mice at 9 months of age and examined the neoepitope of the fibronectin fragment (FN-f) (VRAA271) by Western blotting. Aggrecan cleavage was examined by immunostaining.

RESULTS: Immunostaining demonstrated that ADAM8 was expressed in human IVD tissues. Both ADAM8 and its proteolytic products (fibronectin fragments) were increased with IVD degeneration. These findings establish the clinical significance of ADAM8 in IVD degeneration. We observed that disorganized chondrocyte proliferation in IVDs was much more evident in the ADAM8-injected IVDs than in the PBS-injected IVDs in wild type mice. ADAM8-injected IVDs showed higher immunoreactivity to the antibody against the neoepitope of cleaved aggrecan, compared with the PBS-injected IVDs.

CONCLUSION: These findings suggest that the ADAM8 proteolytic domain stimulates IVD degeneration. Inhibition of ADAM8 may be a valid therapeutic option for IVD degeneration and related back pain.

ACKNOWLEDGEMENTS.: YZ has been supported by the Eunice Kennedy Shriver National Institute of Child Health and Human Development (NICHD, 1K08 HD049598). This work is supported, in part, by research grants from the North American Spine Society (NASS), a pilot grant from the Department of Veterans Affairs Healthcare Network-VISN 4, and a Penn Center for Musculoskeletal Disorders (PCMD) pilot grant (P30-AR050950-10 Pilot). Funding has been recently received from National Institute Of Arthritis & Musculoskeletal & Skin Diseases, NIH (R21 AR071623).

"Novel Quantitative Assessment and Treatment Strategies for the Degenerated Inververtebral Disc"

Authors: *Sarah E. Gullbrand[1,2], Beth G. Ashinsky[1,2,3†], Edward D. Bonnevie[1,2†], Dong Hwa Kim[1,2†], Lachlan J. Smith[1,2,4], Dawn M. Elliott[5], Thomas P. Schaer[6], Robert L. Mauck[1,2,7], Harvey E. Smith[1,2,4]*

Affiliations:

[1]Translational Musculoskeletal Research Center, Corporal Michael J. Crescenz VA Medical Center, Philadelphia, PA, USA

[2]McKay Orthopaedic Research Laboratory, Department of Orthopaedic Surgery, Perelman School of Medicine, University of Pennsylvania, Philadelphia, PA, USA

[3]School of Biomedical Sciences, Drexel University, Philadelphia, PA, USA.

[4]Department of Neurosurgery, University of Pennsylvania, Philadelphia, PA, USA

[5]Department of Biomedical Engineering, University of Delaware, Newark, DE, USA

[6]Department of Clinical Studies, New Bolton Center, School of Veterinary Medicine, University of Pennsylvania, Philadelphia, PA, USA

[7]Department of Bioengineering, University of Pennsylvania, Philadelphia, PA, USA

One Sentence Summary: Tissue engineered discs functionally matured and integrated *in vivo* in both small and large animal models demonstrating successful implantation at clinically relevant length scales, defining a path for clinical translation.

Abstract: The intervertebral disc (IVD) is an integral component of the spinal motion segment as it uniformly distributes load across vertebral bodies. Degenerative disc disease (DDD) has an economic burden that exceeds 100 billion dollars a year. Current treatments for DDD generally include fusion procedures that permanently alter the biomechanics and have been associated with adjacent segment degeneration and further surgeries. The goal of our research is to develop a tissue-engineered construct that can replace a degenerated disc and restore normal biomechanical properties to the motion segment: this would both alleviate pain as well as potentially decrease the incidence of degeneration at adjacent segments. We propose to achieve this through the development of a tissue-engineered construct including an engineered nucleus pulposus (NP) and annulus fibrosus (AF) to treat degenerative changes of the intervertebral disc (IVD). Our group has demonstrated preliminary success with engineered disc-like angle ply structures (DAPS) that recapitulate key micro-architectural features of the native tissue. We have established cell-seeded hydrogel NP-like regions as well as cell-seeded nanofiber-based organized AF regions. In order to transition to a larger animal model, we needed to optimize the DAPS implants in terms of the maturation of the cells that are seeded. With increasing time after cell seeding, the implants improve in terms of biomechanical properties, but there may be a trade-off between the maturity of the implant and its ability to integrate with the host tissue. We hypothesized that we can optimize culture conditions of the DAPS prior to implantation to achieve optimal integration into the host spinal motion segment.

We demonstrate functional maturation and integration of these eDAPS in a rat caudal disc replacement model, with compressive mechanical properties reaching native levels after 20 weeks *in vivo* and evidence of functional integration under physiologic loads. To further this therapy towards clinical translation, we implanted eDAPS sized for the human cervical disc space in a large animal cervical disc replacement model. Our results demonstrate maintenance of eDAPS composition and structure over 4 weeks *in vivo* in the goat cervical disc space, demonstrating the translational feasibility of replacement of the disc with a tissue engineered construct for the treatment of advanced degeneration.

"NAD Metabolism in Muscles"

David. W. Frederick[1], Timothy Luongo[1], Ling Liu[2], Will Quinn[1] Antonio Davila[1], Karthikeyani Chellappa[1], Marie Migaud[3], Joshua Rabinowitz[2], and Joseph A. Baur[1]

[1]Department of Physiology and Institute for Diabetes, Obesity and Metabolism, Perelman School of Medicine, University of Pennsylvania, Philadelphia, Pennsylvania, 19104
[2]Department of Chemistry and Lewis-Sigler Institute for Integrative Genomics, Princeton University, Princeton NJ 08544
[5]Mitchell Cancer Institute, University of Southern Alabama, Mobile, AL 36606

Nicotinamide adenine dinucleotide (NAD) is essential to life through its roles as a redox cofactor and an essential cosubstrate for many enzymes. NAD levels fall with age or due to disease in multiple tissues, and in most cases, the functional consequences of this change are unknown. Restoring or increase NAD in rodent models by supplementing with nicotinamide riboside or nicotinamide mononucleotide has resulted in substantial beneficial effects on health and physiology. However, many questions remain about the normal metabolism of NAD, how cells respond to deficiencies, and how supplemental NAD precursors are metabolized. Using mice overexpressing or lacking nicotinamide phosphoribosyl transferase, we have studied the consequences of chronic changes in NAD availability in muscle. While excess NAD has little effect in young mice, NAD deficiency triggers muscle weakness and degeneration. Taking advantage of isotopically labeled precursors, we have tracked the contribution of both NR and NMN to the NAD pools across tissues in mice. We further demonstrate that intravenous administration of NR can fully restore the intramuscular NAD content in mice lacking Nampt expression in skeletal muscle. Together, our results support the conclusion that physiologically relevant changes in NAD availability can affect tissue function and may play a role in mammalian aging.

"Skeletal Dysplasias: Informing Skeletal Function & Homeostasis"

Brendan Lee, MD, PhD. Department of Molecular and Human Genetics
Baylor College of Medicine

Over the past three decades, the study of Mendelian forms of human skeletal dysplasias have informed us on the genetic determinants of skeletal development and homeostasis. The delineation of genetic mutations that cause chondrodysplasias and osteodysplasias have respectively identified key transcription factors, signaling pathways, and regulatory mechanisms that govern cartilage and bone formation. For example, the study of brittle bone disease best represented by Osteogenesis Imperfecta (OI) has led to the identification of disease mechanisms that affect both the quality and quantity of bone. Similarly, the study of human dwarfisms have identified the role of Sox9 as the master transcription regulator of chondrogenesis and its downstream targets and regulatory components. These discoveries have been revolutionized by next generation sequencing and whole exome/genome analysis, and most recently the incorporation of multi-omic analyses. They have led to the discovery of enormous genetic heterogeneity that is becoming the rule for genetic phenotypes. In the case of OI, structural mutations in the most abundant components of matrix type I collagen, protein complexes that modify and chaperone collagen, and most recently components of signaling pathways have all been implicated. Together they underscore the factors the regulate mineralization of extracellular matrix and the differentiation and function of osteoblasts, osteoclasts, and osteocytes. In so doing they have also pointed to novel therapeutic strategies that may also need to be customized based on nature and consequence of mutation. Finally, the most recent data on the mutations that affect matrix-cell signaling and cell-cell signaling point to overlap with early onset osteoporosis phenotypes and ultimately to rare but strong effect variants in common disease.

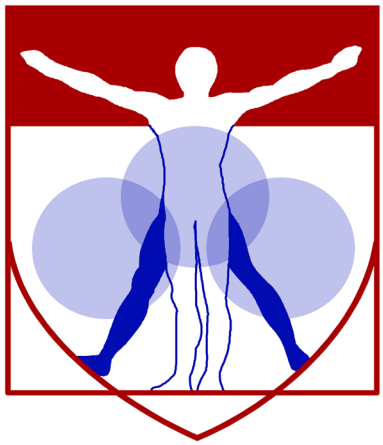

PENN

CENTER for

MUSCULOSKELETAL

DISORDERS

Biomechanics Abstracts

Effects of Pulsed Electromagnetic Field Therapy on Healing of Complete Achilles Tendon Tears in a Rat Model

Huegel J[1], Boorman-Padgett JF[1], Nuss CA[1], Minnig MCC[1], Kuntz AF[1], Waldorff EI[2], Zhang N[2], Ryaby JT[2], Soslowsky LJ[1]
[1]McKay Orthopaedic Research Laboratory, University of Pennsylvania, Philadelphia, PA [2]Orthofix Inc., Lewisville, TX

INTRODUCTION: The Achilles tendon, while the strongest and largest tendon in the body, is frequently injured. Even after surgical repair, patients risk re-rupture and typically have long-term deficits in function, with the rate of return to pre-injury level of activity reported to be as low as 16% [1]. To improve tendon healing outcomes, various non-invasive therapeutics have been utilized [2,3]. We have previously shown that pulsed electromagnetic field (PEMF) therapy improved tendon-to-bone healing in a rat rotator cuff model over a range of electromagnetic pulse frequencies and treatment durations [4]. Another study suggested that PEMF improves tendon strength after Achilles tendon rupture [5]. However, the effects of an FDA approved PEMF signal (Physio-Stim®, Orthofix Inc., Lewisville, TX) on joint function and tendon fatigue properties after complete Achilles tendon tear and repair have not yet been evaluated. Therefore, the objective of this study was to determine the effects of PEMF on Achilles tendon properties and ankle joint function after injury and repair. We hypothesized that PEMF exposure would improve tendon fatigue properties, increase collagen fiber organization, and alter in vivo joint function.

METHODS: 144 adult male Sprague-Dawley rats (400-450 g) were used in an IACUC approved protocol. Animals underwent acute, blunt complete transection and repair of the right Achilles tendon [6] followed by systemic Physio-Stim® PEMF for 1 or 3 hours daily. Control animals did not receive PEMF therapy (non-PEMF). All animals were immobilized in plantarflexion for the first week post-operatively, and sacrificed at 1, 3, or 6 weeks (n=16 per group per time point). Additionally, all animals in the 6 week group underwent longitudinal in vivo ambulatory and passive ankle joint mechanics [6] assessments throughout the experiment. At sacrifice, the Achilles-calcaneus complex was dissected out (n=6 per group per time point) and processed for histological analysis. All other animals (n=10 per group per time point) were frozen at -20C and thawed for dissection prior to tendon cross-sectional area measures using a custom laser device and mechanical testing using a load controlled fatigue testing protocol [6]. Statistical comparisons were made between the PEMF and non-PEMF groups at each time point. Comparisons for mechanics, functional assessments, and collagen fiber organization were made using one way ANOVAs with Bonferroni post-hoc tests. Histological comparisons were made using Kruskal-Wallis tests.

RESULTS: *Mechanical properties*: At 1 week, cross sectional area was larger for the 3 hour PEMF group and trended toward increased for 1 hour PEMF compared to control (data not shown). Tissue modulus was decreased at 1 week for 1 hour PEMF (data not shown). Stiffness was decreased at 1 and 3 weeks for 1 hour PEMF, and at 3 weeks for 3 hours PEMF (Fig 1A). Tanδ, a measure of force dissipation, was decreased for 3 hour PEMF at 6 weeks across tested frequencies (data not shown). Dynamic modulus was decreased for both PEMF groups at 3 weeks across tested frequencies (Fig 1B). Fatigue testing for the 6 week groups showed no differences in cycles to failure, initial peak strain, secant stiffness, tangent stiffness, or fatigue modulus. Normalized peak strain was increased for both PEMF groups at 50% fatigue life (Fig 1C), and hysteresis was increased for PEMF groups across all phases of fatigue (Fig 1D). At 1 and 3 weeks, many samples failed prior to load controlled fatigue testing. 1 hour PEMF groups failed at significantly lower loads than controls (Fig 1E). Note that at 1 week post-op, only quasistatic parameters were determined due to tendon fragility. Similarly, at 3 weeks, only quasistatic and viscoelastic parameters were reported due to failure during the ramp to 35N prior to fatigue testing. *Histological observations*: Semi-quantitative grading indicated increases in cellularity at 1 week for 1 hour PEMF groups (Fig 2A), and a difference in cell shape (more round) in both PEMF groups compared to control (Fig 2B). No differences were seen in collagen alignment. *Functional assessments*: Although the non-PEMF group had a greater ankle range of motion pre-operatively, range of motion was increased for 1 hour PEMF at all post-op time points compared to control (Fig 3A). This group also had increased joint stiffness in plantarflexion at 2 and 3 weeks post-op compared to control. No changes were found in dorsiflexion stiffness (data not shown). Operative limb loading rate was decreased for 1 hour PEMF at 3 and 6 weeks post-op, and for 3 hours PEMF at 6 weeks (Fig 3B). Additionally, stance time (total time foot is in contact with floor per gait cycle) was increased for both PEMF groups at both post-op time points compared to controls (Fig 3C).

DISCUSSION: This study investigated the effects of PEMF therapy on tendon healing after complete Achilles injury and repair. Although there were many parameters that did not indicate differences between treatment groups, other results suggest that PEMF had a negative effect on rat Achilles tendon healing for both treatment durations tested in this study. Tendon stiffness and modulus were significantly decreased and tendons failed at lower loads at early time points with PEMF treatment. Viscoelastic and fatigue properties at later time points were also decreased in PEMF groups compared to controls. Early differences in histological properties suggest that an increase in cell proliferation and/or infiltration in PEMF-treated tendons may be impacting tissue mechanical integrity. Increased joint range of motion in the 1 hour PEMF group may be due, at least in part, to increased tendon strain and hysteresis seen in the same group. Additionally, changes in loading rate and stance time of the injured limb indicate that PEMF-treated animals are altering ambulation patterns, which may be due to loss of function or pain [7]. Together, these results indicate that PEMF may be detrimental to the healing of complete Achilles tears after repair. Future studies will investigate matrix composition and structure to better define the effects of PEMF on healing Achilles tendons.

SIGNIFICANCE: Contrary to the consistent improvements seen in rotator cuff healing, PEMF therapy may be detrimental following surgical repair of a complete Achilles tendon tear in the rat model. This study identified numerous differences between non-PEMF and PEMF treated groups as early as 1 week post-injury. These data also support trialing potential treatment strategies across tendons before applying them generally.

REFERENCES: [1] Barfod KW et al. J Bone Joint Surg, 2014. [2] Ng CO et al. Ultrasound Med Biol, 2003. [3] Joensen J et al. Lasers Med Sci, 2012. [4] Tucker JJ et al. J Orthop Res, 2017. [5] Strauch B et al. J Hand Surg, 2006. [6] Freedman BR et al. J Orthop Res, 2016. [7] Caro AC et al. J Am Assoc Lab Anim Sci, 2014.

ACKNOWLEDGEMENTS: Funding was provided by Orthofix, Inc and the Penn Center for Musculoskeletal Disorders (P30 AR069619). The authors thank Stephanie Weiss, Daniel Gittings, and Mengcun Chen for assistance with surgical procedures.

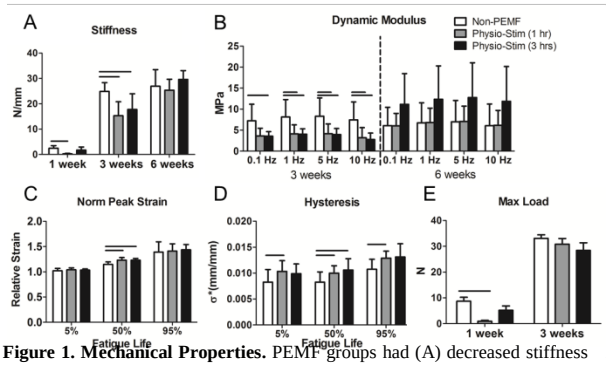

Figure 1. Mechanical Properties. PEMF groups had (A) decreased stiffness at 1 and 3 weeks, (B) decreased dynamic modulus at 3 weeks, (C) increased peak strain, (D) increased hysteresis during fatigue, and (E) decreased max load at 1 week. Solid lines: p<0.025.

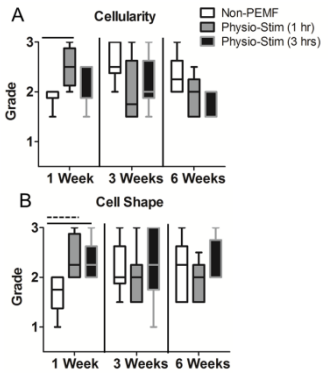

Figure 2. Histological Properties. (A) 1 hour of PEMF resulted in increased cell density at 1 week compared to controls. (B) PEMF groups had rounder cells in the injury region at 1 week compared to controls. Solid lines: p<0.025, dashed lines: p<0.05.

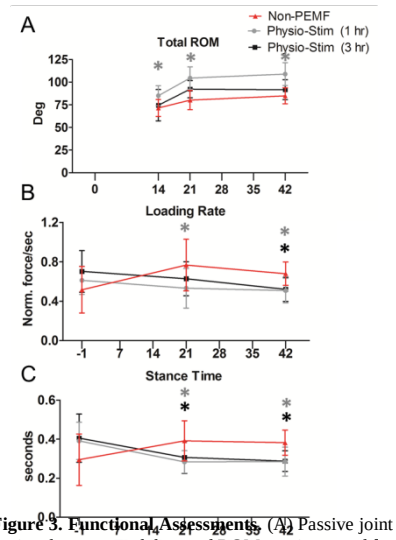

Figure 3. Functional Assessments. (A) Passive joint testing demonstrated that total ROM was increased for 1 hour PEMF group between 14 and 42 days post-op. (B) Ambulatory analysis showed that loading rate and (C) stance time were decreased for both PEMF groups post-op. Asterisks indicate significant differences from controls (p<0.025).

Rat Rotator Cuff Tendon Mechanical Properties Are Minimally Affected by Advancing Age

Joseph B. Newton, George W. Fryhofer, Snehal S. Shetye, Ashley B. Rodriguez, Andrew F. Kuntz, and Louis J. Soslowsky
McKay Orthopaedic Research Laboratory, University of Pennsylvania, Philadelphia, PA

DISCLOSURES: Joseph B. Newton (N), George W. Fryhofer (N), Snehal S. Shetye (N), Ashley B. Rodriguez (N), Andrew F. Kuntz (N), Louis J. Soslowsky (N).

INTRODUCTION: Rotator cuff tendinopathy is a common condition affecting a large portion of the population and can result in pain and joint dysfunction. Advancing age is directly correlated with increased incidence of rotator cuff pathology with over 90% involving injury to the supraspinatus specifically [1-4]. However, it is unclear if tendon-specific changes in mechanical properties with aging [5] may predispose the supraspinatus to injury relative to the other rotator cuff tendons. Therefore, the objective of this study was to define the age-related mechanical alterations in all four rotator cuff tendons to determine whether the supraspinatus is more susceptible to injury due to aging than the other rotator cuff tendons. We hypothesized that aging would preferentially affect supraspinatus tendon mechanics when compared to the subscapularis, infraspinatus and teres minor.

METHODS: *Experimental design and sample preparation:* 7-month juvenile (n=11-15), 18-month adult (n=11-15), and 27-month aged (n=11-15) male F344XBN rats were obtained from the National Institute of Aging (IACUC approved). After 3 weeks of acclimation, animals were sacrificed and shoulders were used for mechanical testing. Following sacrifice, lower and upper subscapularis (LS & US, respectively [6]), supraspinatus (SS), infraspinatus (IS), and teres minor (TM) muscle-tendon complexes were carefully dissected from the scapula and removed with the proximal humerus for mechanical testing (Fig. 1). Muscle and extraneous tissue was removed and cross-sectional area of each tendon was measured using a custom laser device [7]. The humeral shaft was potted in polymethyl-methacrylate, and the head of the humerus was secured with a self-tapping screw to prevent failure at the growth plate. *Mechanical testing:* The LS, US, SS, IS, and TM from each animal were mechanically tested independently on an Instron ElectroPuls E3000. The testing protocol consisted of a 0.1N preload, preconditioning (30 cycles, 0.125% to 0.375% strain, 0.25 Hz), stress relaxation at 3% strain magnitude for 600s, frequency sweep at 3% strain (+/- 0.1875% strain at 0.1 Hz, 1.0 Hz, 2.0 Hz, and 10.0 Hz), stress relaxation at 6% strain magnitude for 600s, frequency sweep at 6% strain (+/- 0.1875% strain at 0.1 Hz, 1.0 Hz, 2.0 Hz, and 10.0 Hz), 300s rest at 0% strain, and a ramp to failure at 0.15% strain/second. Tendon toe and linear stiffness was calculated using a bilinear fit. Insertion site linear modulus was determined via optical tracking of stain lines at the insertion site. A 1-way ANOVA with Bonferroni post-hoc tests was used to compare the different ages for each tendon with significance set to $p<0.05$.

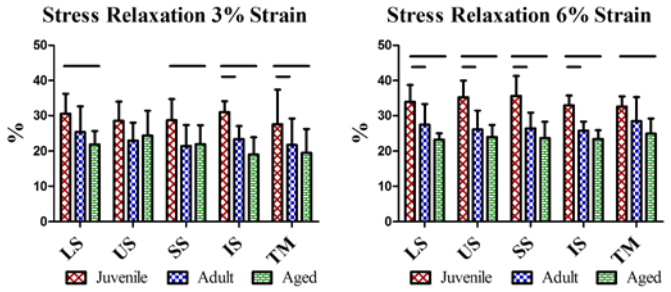

Figure 1. Percent relaxation of LS, SS, IS, and TM is decreased with aging at 3% strain (**A**). Percent relaxation of all tendons is decreased with aging at 6% strain (**B**).

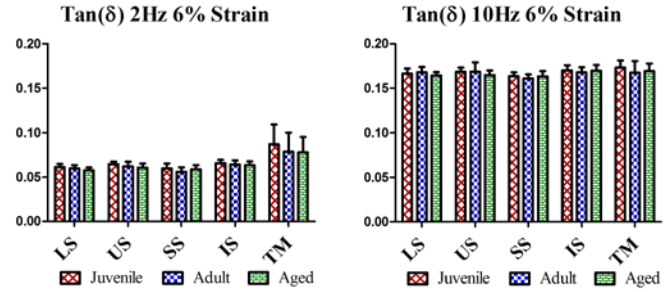

Figure 2. No changes were found in tan d across age groups for all tendons at 6% strain for 2Hz cycles (**A**) and 10Hz cycles (**B**) during the frequency sweeps.

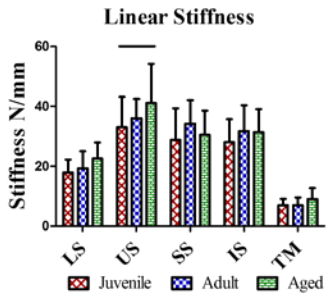

Figure 3. No significant changes were seen in linear stiffness except in the US.

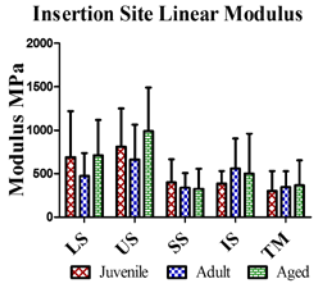

Figure 4. No changes were found in insertion site linear modulus across age groups for each tendon.

RESULTS: Consistent decreases in stress relaxation were seen with advanced aging in all rotator cuff tendons between juvenile and adult animals, and juvenile and aged animals (Fig. 1). Surprisingly, these changes were not exacerbated further into increasing age, as there were no differences between adult and aged tendons for any of the properties examined. No consistent significant differences were seen in tan delta (Fig. 2) or dynamic modulus (not shown) across all ages for each tendon. Only the US between juvenile and aged showed significant difference in linear stiffness (Fig. 3), and no changes were seen in insertion site linear modulus (Fig. 4).

DISCUSSION: In this rat study, the supraspinatus was not preferentially affected by aging, when compared to the other rotator cuff tendons. Therefore, it is not supported that aging is the primary factor causing the sharp increase in supraspinatus tears in the aged human population. Advanced aging had a limited effect on the mechanical properties of the five rotator cuff tendons in our rat model, indicating that aging itself may not be the primary factor causing the age-related increase of rotator cuff tears seen in humans. Instead other factors such as high cholesterol, overuse, and diabetes may play a more significant role later in life [8-10]. It is possible that the selected aged group (~63 year old human equivalent) is not old enough to see significant changes in mechanical properties, as the incidence of rotator cuff tears continues to increase with each decade past 60 [1-4]. Future work will investigate if there are differences in fatigue properties between juvenile, adult, and aged groups, and using older rats with human equivalent of 80+ years of age to fully describe the effect of aging on rotator cuff mechanics.

SIGNIFICANCE: This study suggests that aging alone may not be enough to explain the sharp increase in supraspinatus tears within the aged human population.

ACKNOWLEDGEMENTS: This study was supported by NIH/NIAMS (R01AR064216) and Penn Center for Musculoskeletal Disorders (P30AR069619).

REFERENCES: [1] Jempf JF et al., 1999. Arthroscopy, 15:56-66. [2] Minagawa H et al., 2013. J Orthop Res, 10:8-12. [3] Muto T et al., 2017. J Sports Med, 5476293. [4] Krishnan SG et al., 2008. Arthroscopy, 24:324-8. [5] Svensson RB et al., 1985. J Appl Physiol, 121:1237-1246 [6] Thomas S et al., 2013. JSES, 21:1687-1693. [7] Favata M et al., 2006. J Orthop Res, 24:2124-32. [8] Soslowsky LJ et al., 2000. JSES, 9:79-84. [9] Jungbluth K et al., 1999. Arch Orthop Trauma Surg, 119:280-4. [10] Sambandam SN et al., 2015. W J Orthop, 6:902-918.

Characterizing the Mechanical Effects of Bone Substitute Material and Far-Cortical Locking Techniques in Proximal Humerus Fracture Reconstructions: A Cadaveric Study

Michael W. Hast[1], Matthew Chin[1], Elaine C. Schmidt[1], Jennifer Sanville[1], G. Karl Van Osten[2], Samir Mehta[1]
[1]University of Pennsylvania, Philadelphia, PA, [2]North Mississippi Medical Center, Tupelo, MS
hast@pennmedicine.upenn.edu

Disclosures: M.W. Hast: 5; DePuy Synthes, Integra, Zimmer Biomet. M. Chin: None. E.C. Schmidt: None. J. Sanville: None. G.K. Van Osten III: 2; Zimmer. 3B; Zimmer. 5; Zimmer. S. Mehta: 2; AO North America, Smith and Nephew, Zimmer. 3B; Smith and Nephew, Synthes. 5; Amgen Co., Medtronic, Smith and Nephew, Zimmer. 8; Current Opinion in Orthopaedics, Wolters Kluwer Health. 9; Pennsylvania Orthopaedic Society.

INTRODUCTION: Proximal humerus fractures are one of the most common fractures in the elderly population [1]. When surgical intervention is required, locking plate fixation can be employed to provide support for the reconstructed bone as it heals. This technique is more susceptible to failure when bone quality is poor, and failure rates remain as high as 40% in some studies [2]. It has been posited that implant fixation may be improved in two ways. First, a far cortical locking (FCL) technique can be used to transfer energy away from the fragile humeral head and into the more robust shaft. In this case, the screw holes on the lateral side of the humerus are oversized, which permits controlled motion between the humeral head reconstruction and the humeral shaft (Fig 1). Second, bone substitute material (BSM) can be employed to reinforce the humeral head. Here, a bone substitute is injected through cannulated screws in an attempt to provide reinforcement to the native bone stock. It is understood that FCL "softens" the reconstruction and BSM "stiffens" it; however, it is unknown how these changes affect the fatigue life of the repair. Therefore, the purpose of this study was to make comparisons of the biomechanical properties of these techniques and to determine which fixation is most effective in reducing implant failure. We hypothesized that a combination of both techniques (ALL) will significantly improve the fatigue life of the implant.

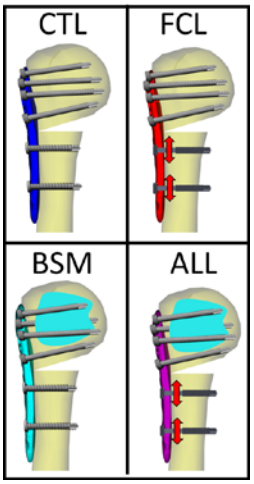

Fig 1: Computer-aided drawings illustrating the 4 groups tested in this experiment. The red arrows indicate motion provided by FCL screws and the cyan blob in the humeral head indicates BSM.

METHODS: This study was performed on sixteen matched pairs of fresh frozen cadaveric upper extremities (5 M, 11 F, mean age: 80.2 years). Lumbar DEXA scans were performed on donors to confirm that all specimens had osteopenia* or osteoporosis* on at least one vertebral body (mean min T-score: -2.96). Skeletonized humeri were osteotomized at the neck with a 30° wedge to represent a simple two-part fracture. Specimens were equally divided into CTL (traditional locking plate fixation), FCL, BSM, and ALL groups (n=8). Implants (Periarticular Proximal Humeral Locking Plate, Zimmer Biomet) were fixated per manufacturer guidelines by fellowship trained surgeons (SM and KVO). In the case of BSM and ALL groups, two screws in the humeral head were swapped out for cannulated screws (N-Force Fixation*, Zimmer Biomet), and up to 5cc of BSM (N-Force Blue*, Zimmer Biomet) was injected. After implantation, BSM and ALL groups were vacuum sealed and placed in a 98.5°F water bath for 24 hours to allow the calcium phosphate to cure. Non-destructive, quasi-static torsional (internal/external rotations) and axial (0°, +20°, -20° of abduction) stiffness tests were performed in a universal test frame (ElectroForce 3550, TA Instruments), similar to previous studies [3,4]. For fatigue testing, specimens were positioned at 0° of abduction and underwent a protocol that monotonically increased the magnitude of compressive loading by 0.25 N/cycle until failure. Relative displacement between the humeral head and shaft was calculated with optical 3-D motion tracking recordings (Optitrack, Natural Point, Inc.). One-way ANOVAs (α=0.05) were performed to determine differences between the 4 groups (SigmaStat 4.0, Systat Software, Inc.).

RESULTS: BSM exhibited significant differences between FCL and ALL in internal rotation torsional stiffness (Fig 2). Significant differences in 0° neutral and 20° adduction axial stiffness were seen between CTL and FCL, FCL and BSM, and BSM and ALL. In addition, there was a significant difference between CTL and ALL in 20° adduction axial stiffness. There were no statistically significant differences for number of cycles survived until 3 mm of permanent deformation, as measured by 3-D motion capture (CTL: 2051±501; FCL 1859±626; BSM 2284±811; ALL 2049±338).

DISCUSSION: As expected, the quasi-static torsional and axial tests suggests that BSM increases construct stiffness, while FCL and ALL provide lower stiffnesses. Results from the pooled data from this experiment suggest that the techniques used in the four groups provide similar implant fatigue life, which was contrary to our hypothesis. There are several limitations to this study that may be confounding the results. The screws used in this study were the same length for all specimens, which may have resulted in variable qualities of initial fixation. Additionally, variation in human anatomy and bone mineral density led to large data variability, which is inherent in cadaveric research. Future analyses will be performed on matched pairs of specimens to further assess the effects of these surgical techniques in a more controlled setting.

SIGNIFICANCE/CLINICAL RELEVANCE: This study shows that use of FCL and BSM by surgeons may directly change the mechanics of proximal humerus fracture repairs with locking plates, but the impact these changes have on fatigue life remains unclear. Cadaveric mechanical studies may not be indicative of clinical outcomes.

REFERENCES: [1] Lee SH, et al, Bone. 2002. [2] Owsley KC, et al, JBJS. 2008. [3] Mehta+, Injury, 2018. [4] Lescheid J, et al, J Trauma. 2010.

ACKNOWLEDGMENTS: This study was funded by Zimmer Biomet.

*N-Force Fixation Screws are not currently cleared/approved for use in a plate construct, and N-Force Blue is contraindicated for metabolic bone disease

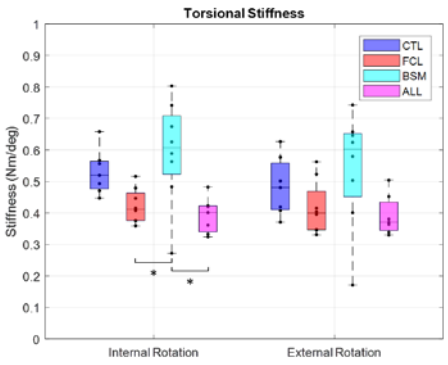

Fig 2: Plots of torsional stiffness in internal and external rotation. Significant differences between groups are marked with *.

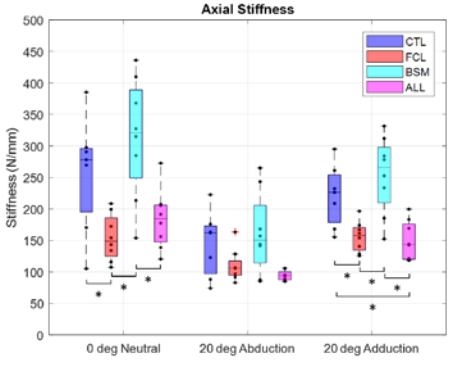

Fig 3: Plots of axial stiffness during 0 deg, -20 deg, and +20 degree tests. Significant differences between groups are marked with *.

Fluoroscopic Evaluation of Proximal Humerus Locking Plate Failure During Cyclic Loading

Jennifer Sanville[1], Liane Miller[1], Elaine C. Schmidt[1], Josh R. Baxter[1], Surena Namdari[2], Michael W. Hast[1]
[1]University of Pennsylvania, Philadelphia, PA, [2]Thomas Jefferson University, Philadelphia, PA
hast@pennmedicine.upenn.edu

Disclosures: J. Sanville: None. L. Miller: None. E.C. Schmidt: None. J. Baxter: None. S. Namdari: 1; DJ Orthopaedics, Miami Device Solutions. 2; DJ Orthopaedics, Miami Device Solutions. 3B; DJ Orthopaedics, Flexion Therapeutics, Miami Device Solutions, Synthes. 4; Force Therapeutics, MD Live, MD Valuate, Parvizi Surgical Innovations, Rubicon MD. 5; Arthrex, Inc, Integra, Zimmer. 7B; Saunders/Mosby-Elsevier. 8; American Journal of Orthopedics, Bone & Joint 360. 9; Philadelphia Orthopaedic Society. M.W. Hast: 5; DePuy Synthes, Integra, Zimmer Biomet.

INTRODUCTION: Fractures of the proximal humerus are common, particularly in the elderly population, making up approximately 10% of all fractures in this age group [1]. Additionally, the annual incidence is expected to rise with an increasingly aging population [2]. If the fracture is substantially displaced, surgical fixation with open reduction internal fixation techniques may be required. Locked plating constructs have shown immense promise in biomechanical testing and initial clinical results, however, long-term outcomes remain disappointing, with implant-related complication rates as high as 57% [3]. Reported complications include humeral head collapse, hardware failure, screw back out or cut out, nonunion/malunion, and loss of function, leading to revision surgery rates as high as 29% [4]. Thus, the overall cost and health care burden is high, necessitating a better understanding of mechanisms and characteristics involved in locked plating fixation failure.

While biomechanical studies are commonly employed to analyze fixation properties of proximal humerus locking plates, the association between failure modes and patterns observed biomechanically and clinically is unclear. In an effort to better characterize the cascade of events associated with implant failure, this study sought to evaluate implant failure of a locked plating construct in a 2-part proximal humerus fracture model undergoing cyclic fatigue. The movements of plates, locking screws, and humeral bone fragments were tracked using serial fluoroscopic assessments to identify what fails first and to determine the progressive steps to failure. This analysis may provide much needed clarity to the mechanism of failure seen in locked plating fixation of proximal humerus fractures and may elucidate novel solutions for future evaluation.

METHODS: This study was performed first as a pilot with Sawbones and again with cadaveric specimens. The Sawbones portion of the study used 4th generation proximal humeri (Pacific Research, Vashone, WA). In the cadaveric portion of the study, four matched pairs of upper extremities (3M, 1F, mean age: 83.75 years) with DEXA-confirmed osteopenia were used (Average T-Score -2.75±1.1). Humeri were potted and a two part fracture was simulated with a 30° wedge osteotomy at the humeral neck. Fractures were reconstructed with either Synthes (VA LCP Proximal Humerus; SYNs: n=2; SYNc: n=4) or Zimmer Biomet (Periarticular Proximal Humerus; ZIMs: n=2; ZIMc: n=4) locking plates.

Cyclic loading was performed in a testing frame (Electroforce 3300, TA Instruments) using a monotonically increasing waveform under displacement control. Each wave increased by 0.01mm at a rate of 0.2 Hz until failure occurred. Anteroposterior fluoroscopy was performed during a 10 second dwell that occurred at peak displacement of every tenth cycle. Fluoroscope images from each trial were compiled and the resulting movies were analyzed using a custom Matlab code. Onboard edge detection and centroid location algorithms were employed to track the relative 2-D displacements and rotations between the bone fragments, plate, and screws. Paired t-tests (α =0.05) were performed to assess differences in load, humeral head rotation, and plate bending for the SYNc and ZIMc groups. Due to limited sample size, no statistics were performed to compare SYNs and ZIMs.

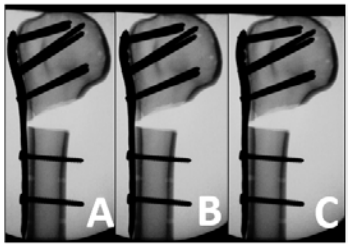

Fig 1: *Fluoroscopic images taken at (A) 0 mm, (B) 1.3 mm, and (C) 2.3 mm of actuator displacement in a SYNs trial, where bending of the plate can be visualized.*

RESULTS: Humeral head rotation, with respect to the humeral shaft, was found to be similar and relatively linear in nature for all groups (Fig 2A, Table 1). However, analysis of plate bending indicated there were statistically significant differences between ZIMc and SYNc after 0.2mm of displacement (Fig 2B, Table 1). This finding indicates that humeral heads were still fixed onto SYN plates throughout fatigue testing, whereas ZIM humeral heads were rotating independently from the implant. This result was confirmed visually and by analysis of the screw movements relative to the plate (not shown).

DISCUSSION: This study successfully characterized the mechanisms of failure that are seen in locking plates when cyclic fatigue loading is performed in Sawbones and cadavers. It was thought that this experiment would identify quantifiable and pragmatic thresholds (such as maximum load before humeral head loosening) which could be used ubiquitously, regardless of implant manufacturer. However, the findings suggest that, although the general design of locking plate implants may be similar, implant behavior varies substantially as displacement and load increases. This study is limited by cadaveric assumptions, which only assesses implant behavior in the absence of healing.

SIGNIFICANCE/CLINICAL RELEVANCE: The two locking plate implants tested in this study produced failure mechanisms that were significantly different. Regardless of implant design, conservative rehabilitative protocols should be used to avoid loading of the construct during healing.

REFERENCES: [1] Calvo E+, JSES. 2011. [2] Kim SH+, Arthritis Care Res. 2012. [3] Schnetzke, JBJS. 2016. [4] Burke NG+, Orthopedics. 2012.

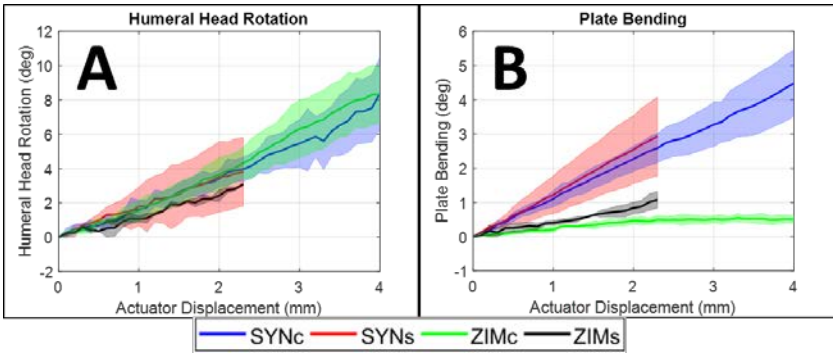

Fig 2: *(A) Plots of humeral head rotation with respect to the humeral shaft. There were no significant differences between groups with this analysis. (B) Bending of plates as a function of actuator displacement. Significant differences between SYNc and ZIMc start at 0.2mm of displacement. All data shown are means ± 1 standard deviation.*

Table 1: Linear Fits for Fig. 2A and 2B

Humeral Head Rotation		
	Slope (deg/mm)	R^2 Value
SYNs	1.72	0.992
ZIMs	1.24	0.972
SYNc	1.84	0.987
ZIMc	2.03	0.984
Plate Bending		
SYNs	1.27	0.999
ZIMs	0.42	0.979
SYNc	1.11	0.999
ZIMc	0.17	0.758

MRI-Based Assessment of Proximal Femur Compared to Direct Mechanical Testing

Daniel C. Kargilis, Gregory Chang, Jae S. Lee, Alexander R. Farid, Snehal S. Shetye, Michael Hast, Chamith S. Rajapakse

Half of the women who sustain a hip fracture would not have qualified for osteoporosis treatment by the current criteria, which are based on bone mineral density measurements by DXA. Thus, a better approach is needed to determine if an individual is at risk for hip fracture from a fall. MRI provides an ionizing-radiation free approach for assessing proximal femur microstructure in human subjects. The objective of this study was to determine the association between MRI-derived strength compared to direct mechanical testing of cadaveric femurs. This study used human femurs obtained from 6 male and 7 female donors aged 36-99 years. Specimen storage occurred at a temperature of -30° C before experimentation. Imaging was conducted on a clinical whole-body 3 Tesla MRI scanner (Siemens Prisma, Erlangen, Germany) using a sequence (flip angle 25°, TR/TE 27/3.8 ms, and voxel size 0.242 x 0.242 x 1.5mm 3).

Femora were dissected free of soft tissue and 4-120 ohm strain gauges (Omega Engineering, Norwalk, CT) were securely applied to the areas of interest on the bone with an adhesive (Figure 1). Strain gauges were arranged with 120 ohm resistors on a breadboard to form a Wheatstone bridge. The circuit was connected to custom software (Labview 2013, National Instruments, Austin, TX) capable of converting changes in resistance to changes in strain. The femora were securely fixed into a vise at a 10 degree angle relative to horizontal, similar to Keyak et al. (1998). The actuator of a universal test frame (Instron 8874, Norwood, MA) was equipped with a rigid, molded acetabular cup that conformed with the femoral head, and another rigid mold conformed to the greater trochanter. Bone strains (strain x 10 6) were recorded at a rate of 100Hz as the actuator pressed down upon the femoral head at a rate of 1.67mm/s until failure occurred.

The acquired MR images were processed to generate FE models. Simulations included forces that mimicked loading conditions for a side fall condition that replicated falling directly on the hip.

Computational bone stiffness showed strong correlation with experimental stiffness (R 2 = 0.82).

The findings from this study support the use of MRI-based FE analysis of the hip to reliably predict the mechanical competence of the human femur in clinical settings. Further work is needed to determine if post yield measures such as yield strength and ultimate strength could be accurately predicted using the MRI-based computational biomechanics approach.

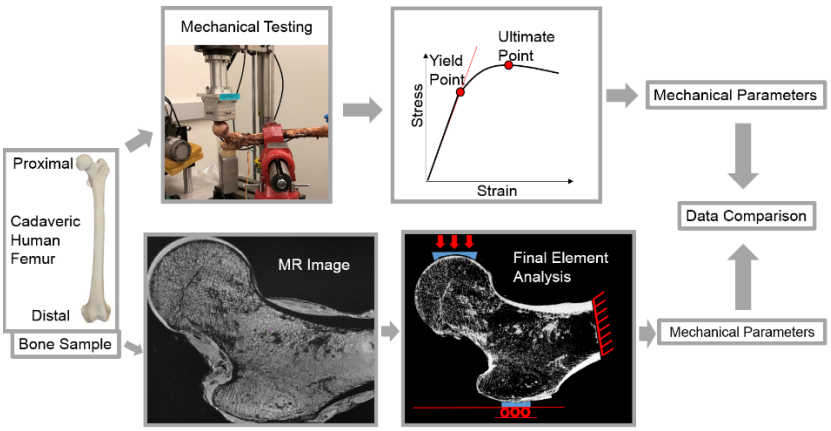

Figure 1: Illustration of work flow

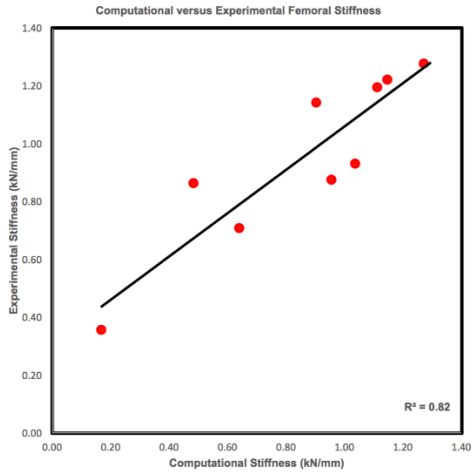

Multiscale and Multimodal Structure-Function Analysis of Intervertebral Disc Degeneration in a Rabbit Model

Beth G. Ashinsky[1,2,3], Sarah E. Gullbrand[1,3], Edward D. Bonnevie[1,3], Chao Wang[2], Dawn M. Elliott[4], Lin Han[2], Robert L. Mauck[1,3], Harvey E. Smith[1,3]
[1]University of Pennsylvania, Philadelphia, PA; [2]Drexel University School of Biomedical Engineering, Philadelphia; [3]Translational Musculoskeletal Research Center, CMC VA Medical Center, Philadelphia; [4]Department of Biomedical Engineering, University of Delaware, Newark, DE

Disclosures: R.L. Mauck (8, JOR Spine), no other disclosures

INTRODUCTION: Back pain, frequently associated with intervertebral disc (IVD) degeneration, is the leading cause of disability in the United States [1]. Despite the significant clinical burden of IVD degeneration, the underlying mechanism leading to end stage disease is poorly understood, hampering early clinical diagnosis and treatment [2]. Animal models can be used as a tool to understand disease progression, with the rabbit being the most common model system for studying spinal pathology [3]. This model also provides a platform through which structure-function relationships may be correlated with non-invasive imaging parameters from magnetic resonance imaging (MRI) [4]. Here, we utilize a rabbit annular injury model to characterize the time course of structure-function alterations to the IVD from the nanoscale to the macroscale, and correlate these changes with quantitative T2 MRI.

METHODS: Fifteen New Zealand White male rabbits underwent surgery to puncture four lumbar discs with a 16-gauge needle. At post-operative week 2, 4, 8, and 12, rabbits were sacrificed. Punctured motion segments (n=12-16/time point) and adjacent control motion segments (n=10), underwent MRI T2 mapping to quantify annulus fibrosus (AF) and nucleus pulposus (NP) relaxation time [4]. Following MRI, mechanical testing, consisting of 20 cycles of tension and compression (+21 N to -42N), was performed (n=5 punctured/time point and n=10 control). After this macroscale mechanical testing, motion segments were cryosectioned in the sagittal plane at 20μm thick using Kawamoto's film method [5]. AFM-nanoindentation (≥12 indents per region) was performed on these sections using microspherical tips ($R \approx 12.5$ μm, 10 μm/s rate) in PBS with protease inhibitors (n=5 punctured/time point and n=5 control). The indentation modulus, E_{ind} (in MPa), was calculated via the finite thickness-corrected Hertz model [6, 7]. μCT scans of intact motion segments (n=4 punctured/time point, n=4 control) were also acquired at 0N and under 42N of compression (~0.48 MPa) to quantify disc height and compressive strain. Additional motion segments (n=4 punctured/time point, n=2 controls) were processed for paraffin histology, and stained with Alcian blue and picrosirius red for proteoglycans and collagen, respectively. Immunohistochemistry was performed to detect the neo-epitope NITEGE, indicative of aggrecan enzymatic degradation [8]. Univariate regressions were calculated for all combinations of measured variables in R to generate correlation matrices of r and p values [9]. Multiple regressions were performed to determine the relative strengths and significances of contributors to NP and AF T2.

RESULTS: MRI T2 values of the NP region decreased following 2, 4, 8, and 12 weeks of puncture (Fig. 1A-B). AF T2 decreased at 2 weeks and then steadily increased to control values from 4-12 weeks (not shown). 2 weeks following puncture, motion segment mechanics were altered at the macroscale, as indicated by a decrease in neutral zone and compressive modulus (not shown), and an increase in range of motion (Fig. 1C-D). Whole motion segments subsequently stiffened at 4, 8 and 12 weeks, as measured by macroscale mechanical testing (Fig. 1D). Compressive strain measured via μCT compression testing mirrored findings from macroscale mechanical testing, with increased strain at 2 weeks (Fig.1E). In contrast, the nanoscale mechanical properties, measured by AFM, indicated softening of both the inner and outer AF at early time points, followed by stiffening at 12 weeks (Fig. 1H). At 4, 8 and 12 weeks, motion segments exhibited substantial anterior fibrotic remodeling and osteophyte formation, as well as a reduction in overall disc height, as visualized on histology (Fig. 1F). Immunohistochemical detection of NITEGE showed an increase in aggrecanase breakdown products in the NP at 4 and 8 weeks compared to controls (Fig. 1H). Multivariate regression analyses identified a linear model for NP T2 (r^2 =0.60, p=0.0009), with AF T2 (p=0.007), E_{ind} (p=0.0009), neutral zone modulus (p=0.02) and neutral zone range of motion (p=0.03) as parameters. For AF T2, NP T2 (p=0.002), E_{ind} (p=0.02) and compressive modulus (p=0.03), were included in the multiple regression model (r^2=0.44, p=0.003). Significant differences in quantitative outcome measures were assessed via two-way ANOVA with Tukey's post-hoc test.

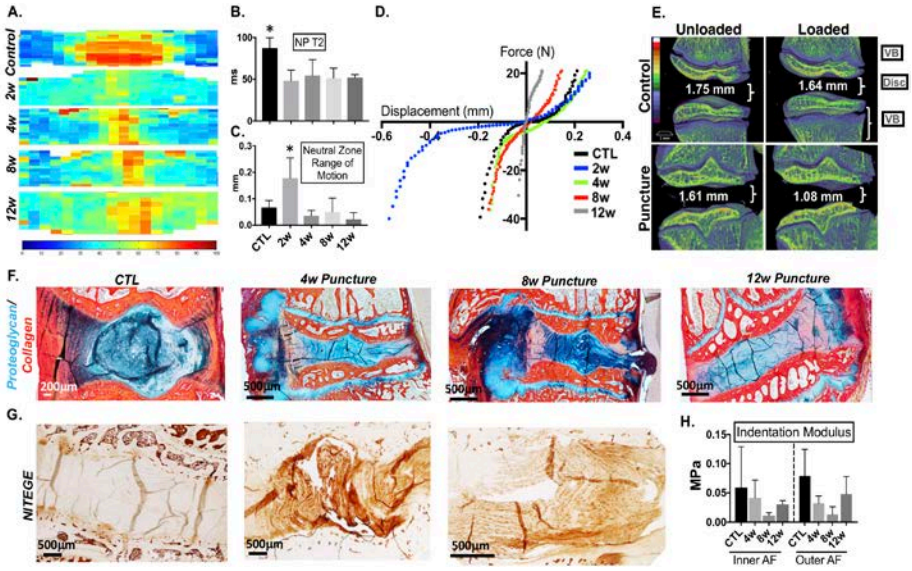

Figure 1. A) Average T2 MRI maps of control (CTL) and punctured groups. B) T2 values of the NP region. C) Neutral zone range of motion (mm) from whole motion segment mechanical testing. D) Representative force versus displacement curves for each time point. E) μCT scans of a control and a 2-week punctured disc before and after 42N of compressive load. Values in the disc space represent average disc height computed between the vertebral bodies (VB). F) Alcian blue and picrosirius red histology for proteoglycans and collagen. G) NITEGE staining of aggrecanase breakdown products in the disc space. H) AFM indentation modulus of the inner and outer AF regions. * = p<0.05

DISCUSSION: Needle puncture substantially altered disc structure and mechanics at multiple length scales and over time. Initial changes to disc (2 weeks post-puncture), such as reductions in NP T2 and compressive moduli, and increased motion segment strain under physiologic loads, are likely due to the acute depressurization of the NP due to needle puncture. At longer time points (4-12 weeks post-puncture), injury initiates a progressive degenerative cascade in the disc that results in a loss of disc height, annular disorganization and remodeling, anterior osteophyte formation, and fragmentation of aggrecan in the NP. These changes in disc structure resulted in progressive stiffening of whole motion segment mechanical properties at the macroscale. The micro-scale indentation modulus of the AF was reduced compared to controls at early post-puncture time points, but recovered towards control levels by week 12. This is suggestive of marked remodeling of the AF as a consequence of disc puncture. These structural and functional alterations to the disc were associated with significant changes to NP and AF T2 from non-invasive MRI. Multivariate regression identified that AF T2 was most influenced by whole motion segment compressive modulus, while the primary predictors of NP T2 were neutral zone mechanical properties. AF indentation modulus was included in both models, and AF and NP T2 were significantly correlated with one another, demonstrating the interplay between these two regions of the disc during degeneration.

SIGNIFICANCE: Here, we characterized structure-function alterations in the disc during degeneration across multiple length scales. Our results suggest that non-invasive quantitative MRI techniques may be sensitive to the mechanical changes occurring in the disc with degeneration at both the macro and micro-scale. This work will ultimately contribute to improved diagnosis and treatment of disc degeneration and associated back pain.

REFERENCES: [1] USBJI *BMUS* 2014 [2] Urban+ *Arthritis Res. Ther.* 2003 [3] Masuda+ *Spine* 2005 [4] Martin+ *J. Orthop. Res.* 2015 [5] Kawamoto+ *Stain Technology* 1986 [6] Li+ *Acta Biomater* 2017 [7] Dimitriadis+ *Biophys J.* 2002 [8]Ohtsuki+ *J. Orthop. Res.* 2018 [9] Gullbrand+ *J. Orthop. Res.* 2016

ACKNOWLEDGEMENTS: This work was supported by the NIH, Department of Veterans' Affairs, and Penn Center for Musculoskeletal Disorders.

Gender Dependent Alterations in the Mechanical Response of Collagen V Haploinsufficient Murine Tendons

Jaclyn A. Carlson, Snehal S. Shetye[1], Ashley B. Rodriguez[1], Jessica M. Johnston[1], Mei Sun[2], Sheila M. Adams[2], David E. Birk[2], Louis J. Soslowsky[1]
[1]McKay Orthopaedic Research Laboratory, University of Pennsylvania, Philadelphia, PA, [2]University of South Florida, Tampa, FL
Disclosures: Jaclyn A. Carlson (N), Snehal S. Shetye (N), Ashley B. Rodriguez (N), Jessica M. Johnston (N), Mei Sun (N), Sheila M. Adams (N), David E. Birk (N), Louis J. Soslowsky (N)

INTRODUCTION: Classic Ehlers-Danlos syndrome (EDS) patients, who commonly have mutations in the *COL5A1* gene, suffer from connective tissue hyperelasticity, joint instability, and skin hyperextensibility. The role of collagen V in fibrillogenesis in tissues such as skin, cornea, and tendon has been firmly established [1], wherein collagen V haploinsufficiency leads to abnormal tissue development and altered collagen assembly. Recent basic science studies suggest that differences in hormone physiology between sexes may be a factor influencing tendon health [2-4]. Given the joint laxity and tissue hyperelasticity in classic EDS patients, gender-specific changes in hormone levels, the different hormones produced, and their effect on body structure and composition, may further exacerbate the detrimental changes present in pathological tendons. Therefore, the objective of this study was to evaluate the role of gender in the mechanical response of normal and *classic* EDS tendons. We hypothesized that female *classic* EDS mice will have inferior tendon mechanical properties compared to male *classic* EDS mice, but there will only be differences in structural properties due to gender in wild type tendons.
METHODS: Adult male and female WT C57/BL6 and HET ***Col5a1***$^{+/-}$ EDS mice (n=60) at 150 days of age were used (IACUC approved). Uninjured patellar tendons were assessed to determine mechanical properties for both genders and genotypes. *Mechanics.* The patella-patellar tendon-tibia complexes were dissected and prepared for mechanical testing [5]. Tendons were subjected to a viscoelastic testing protocol [5, 6] consisting of 1) preconditioning, 2) stress relaxation at strain levels of 2%, 3% and 4%, 3) a sinusoidal frequency sweep (10 cycles at 0.1, 1, 5, and 10 Hz) at each strain level, 4) return to gauge length, and 5) ramp to failure. Tendon length was measured at nominal load prior to test initiation. Statistics. Two-way ANOVAs with post-hoc Tukey tests were used to assess the effects of genotype, gender, and their interaction on mechanical properties. Two-way repeated measures ANOVAs with post-hoc Tukey tests were used to assess the changes in viscoelastic properties. Significance was set at $p \leq 0.05$ and trends at $p \leq 0.1$.
RESULTS: WT male patellar tendons had significantly higher failure load and tissue stiffness when compared with WT females (Fig. 1A,B). WT male tendons also had significantly higher failure stress and tissue modulus when compared with WT females (Fig. 2A,B). The viscoelastic response followed similarly with WT males exhibiting significantly elevated dynamic modulus at 10Hz and across all strains when compared to WT females and trending increases at 0.1 Hz and 1 Hz (Fig. 3, only 3% data shown). HET male tendons had a significantly higher failure load when compared with HET females, with no difference observed in tissue stiffness (Fig 1A,B). HET males had significantly higher failure stress and a trending increase in modulus when compared with HET females (Fig 2A,B). HET male and female mice showed trending differences at 2% strain with frequencies of 0.1 and 1 Hz, and at 4% strain, 1 Hz (data not shown). Male HET tendons trended towards a decrease in stiffness compared to WT tendons, with no other difference between genotypes. Male WT and HET tendons had a significantly larger area than female mice of the same genotypes (data not shown).
DISCUSSION: WT male patellar tendons demonstrate superior material and structural properties compared to WT female patellar tendons. As female patellar tendons were significantly smaller than male patellar tendons, it is not surprising that their properties would be decreased. Conversely, it is surprising that although HET male patellar tendons were significantly larger in cross-sectional area than female patellar tendons, the same differences in structural properties seen in WT tendons were not present. This contrasting finding indicates that the structural properties of HET male tendons were affected by the reduction of type V collagen to a greater degree than the structural properties of HET female tendons, after considering the inherent gender-differences. We hypothesized a negative effect of female sex hormones on patellar tendon health, yet our results indicate the opposite. This finding is extremely interesting as previous studies have reported an influence of sex hormones on tendon health [2-4], without a clear determination of how hormones would affect tendon function. Furthermore, although HET ***Col5a1***$^{+/-}$ EDS mice have a 50% reduction in fibril number [1], this did not result in significant differences between HET and WT material, structural or viscoelastic properties. However, a trend toward a significant difference in stiffness between male WT and HET mice supports our conclusion that a reduction in type V collagen content affects male tendon mechanical properties to a greater degree than female properties. This indicates a gender specificity of the effects of collagen V on patellar tendon mechanical properties. Future work may include histological analysis of HET male and female patellar tendons to understand the cellular differences that could explain these mechanical differences.
SIGNIFICANCE: This study demonstrates that sex hormones and gender-specific effects of hormone expression play a tendon-specific role in tendon health, and can influence the degree to which tendon properties of *classic* EDS mice are affected.
REFERENCES: [1] Wenstrup RJ, et al. J Biol Chem. 279:53331-7, 2004. [2] Bridgeman JT, et al. Foot Ankle Int. 31:1081-4, 2010. [3] Liu SH, et al. J Orthop Res. 14:526:33, 1996. [4] Romani WA, et al. Eur J Appl Physiol. 113:2503-10, 2013. [5] Dunkman AA, et al. Matrix Biol. 32:3-13. 2013. [6] Miller KS, et al. J Biomech Eng. 134:031007. 2012
ACKNOWLEDGEMENTS: This study was supported by AR065995, AR044745 and the Penn Center for Musculoskeletal Disorders (P30 AR069619).

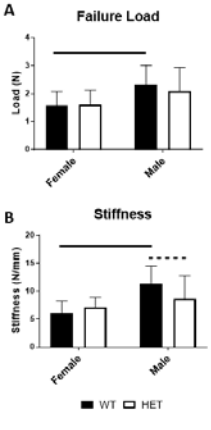

Figure 1. Structural properties of female and male WT and HET *Col5a1*$^{+/-}$ patellar tendons. WT male patellar tendons failed at higher loads (A) and had increased stiffness (B). Solid lines denote significant $p \leq 0.05$ and dashed lines denote trends at $p \leq 0.1$.

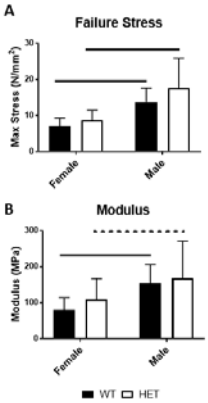

Figure 2. Material properties of female and male WT and HET *Col5a1*$^{+/-}$ patellar tendons. WT and HET male patellar tendons failed at higher stress (A) and WT male patellar tendons had an increased modulus (B). Solid lines denote significant $p \leq 0.05$ and dashed lines denote trends at $p \leq 0.1$.

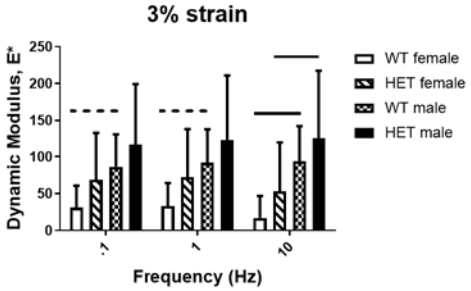

male WT and HET *Col5a1*$^{+/-}$ patellar tendons. At a frequency of 10 Hz and strain of 3%, WT and HET male patellar tendons dynamic moduli were significantly increased when compared to WT and HET female patellar tendons. Similar findings were seen at 2% and 4% strains across all frequencies. Solid lines denote significant $p \leq 0.05$ and dashed lines denote trends at $p \leq 0.1$.

Gastrocnemius fascicles are shorter and more pennate following acute Achilles tendon rupture

Todd J. Hullfish, Kathryn M. O'Connor, Josh R. Baxter
Department of Orthopaedic Surgery, University of Pennsylvania, Philadelphia, PA

INTRODUCTION: The incidence of Achilles tendon ruptures has increased 10-fold over the last three decades, disproportionally affecting adult athletic populations that participate in sports requiring sudden acceleration and jumping [1]. While advances in rehabilitation protocols have improved outcomes in patients treated either operatively or non-operatively, roughly 20% of patients without other complications are unable to return to their previous levels of athletic participation [2]. Deficits in plantarflexion function of the affected limb play a large role in preventing return to nominal levels of activity and have been shown to persist as far out as 2-years following injury [3]. These deficits have been attributed to the elongation of the affected tendon and the remodeling of the plantarflexors in response to the injury [4]. Changes in muscle structure have been shown to occur rapidly in animal models following surgical interventions [5], but it is unclear if and when these changes occur in humans. Therefore, the purpose of this study was to characterize and prospectively track the muscle structure of the medial gastrocnemius in patients that are undergoing non-operative treatment for an acute Achilles tendon rupture from time of injury through 4 weeks of treatment. We hypothesized that the medial gastrocnemius muscle of the injured Achilles tendon would have shorter and more pennate fascicles immediately following the injury and would persist throughout 4 weeks post-injury.

METHODS: Ten adults (9 males, Age: 44 ± 12; BMI: 28.6 ± 6.5) who suffered acute Achilles tendon ruptures and were treated non-operatively were enrolled in this IRB approved study. Ultrasound measurements of the medial gastrocnemius were performed at 3 clinical visits: time of injury when subjects were placed in a cast (week 0); time of cast removal when subjects were transitioned into partial weight bearing in a walking boot (week 2); and 2 weeks after transitioning into boot use (week 4). Images of the mid-muscle belly were acquired with an 8 MHz ultrasound transducer (LV7.5/60/128Z-2, SmartUs, TELEMED) while subjects lay prone on a treatment table with ankles supported by the edge of the table in the same position. Resting structure of the muscle was characterized by the length and pennation of the constituent fascicles as well as the thickness of the muscle belly using custom written software (**Fig. 1a**). Fascicle length was quantified as the distance between a single fascicle's insertions into the deep and superficial aponeuroses. Fascicle pennation was calculated as the angle between the fascicle and the deep aponeurosis. Muscle belly thickness was measured as the distance between the deep and superficial aponeuroses in the middle of the image. Measurements of the unaffected limb were made at time of injury and served as a control. To test our hypothesis that resting muscle architecture would change following injury, resting fascicle length, pennation angle, muscle thickness, and muscle quality measurements at weeks 0, 2, and 4 were each compared against the control values using paired one-way t-tests. Bonferroni corrections for multiple comparisons were applied, which set the threshold for statistical significance to $p = 0.0167$ (0.05 / 3), where 3 is the number of comparisons for each variable of interest.

RESULTS: Gastrocnemius muscle structure changed immediately following injury and remained structurally different over the first four weeks following injury (**Fig. 1b-d**). Fascicle length and pennation was 15% shorter and 21% greater at the presentation of injury (week 0), respectively ($p < 0.001$). These differences in fascicle length and pennation angle persisted throughout the 4 weeks after the injury ($p < 0.008$). Muscle thickness changes were not detected at any of the post-injury visits; however, a 3% decrease in muscle thickness at week 4 approached our threshold for significance when controlling for multiple comparisons ($p = 0.41$). Muscle quality measured, as mean echogenicity of the muscle belly, was 8 and 11% lower in the injured limb immediately and 2 weeks following injury, respectively ($P < 0.008$). At week 4 muscle quality had returned to within 1% of the contralateral limb ($p = 0.393$).

DISCUSSION: Differences in the structure of the medial gastrocnemius between the affected and unaffected limbs were apparent at time of injury and persisted throughout the 4 weeks the injury. These changes may be a biologic response to a sudden loss of intra-muscular tension, which is typically present with an intact tendon. When this tension is released by an acute rupture, the muscle retracts resulting in a shorter and more pennate fascicle. These findings are a preliminary set of data on a larger clinical cohort of patients that have been enrolled in a 1-year long prospective study. Ongoing work is focused on closely monitoring muscle and tendon structure at each clinical visit. Once cleared for activity, these patients will also undergo functional testing to characterize plantarflexor strength and power [6]. Our preliminary work also suggests that these structural changes in muscle are permanent and the magnitude of these changes may be predictive of long-term functional deficits [4].

Achilles tendon elongation has previously been linked to functional deficits in heel raise height [7]. When considered in this context, shorter and more pennate gastrocnemius fascicles indicate a coupled remodeling response with the healing tendon. Imaging studies of the healing Achilles tendon during the first 23 weeks after a rupture show continued tendon lengthening [8], which suggests that musculo-tendon adaptations continue for several months following the injury. The response of the muscle to changing loading conditions following injury is supported by animal models but has never been shown in humans. Understanding the progression of this remodeling process is crucial for the treatment of tendon rupture and can be used to inform clinical decisions as well as the prescription of rehabilitation protocols. Due to the loading restrictions in the weeks following the injury, this study was limited to imaging the muscle fascicles with the foot in maximal plantarflexion to ensure an unloaded tendon. Continued monitoring of this cohort will yield further insight into the link between tendon injury, muscle remodeling, and patient function.

REFERENCES: [1] Lantto+, *Scand JMed Sci Sports*, 2015; [2] Zellers+, *Br J Sports Med*, 2016; [3] Olsson+, *Knee Surg Sports Traumatol Arthosc*, 2011; [4] Baxter+, *JBiomech*, 2018; [5] Burkholder and Lieber, *JEB*, 1998; [6] Baxter and Piazza, *J Appl Physiol*, 2014; [7] Silbernagel+., *Am J Sports Med*, 2012; [8] Mortensen+, *JBJS*, 1999

ACKNOWLEDGMENTS: This work was supported by the Thomas B. McCabe and Jeannette E. Laws McCabe Fund.

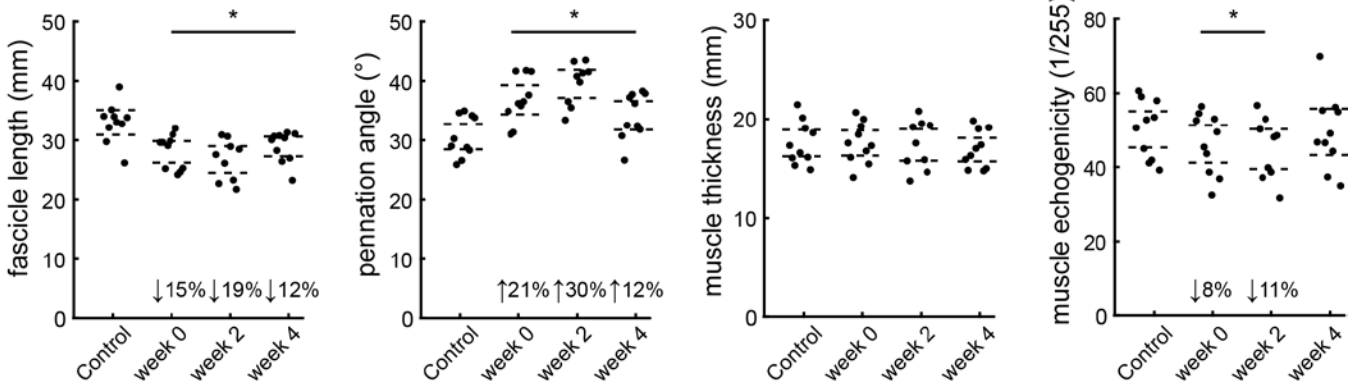

Figure 1: Medial gastrocnemius structure was altered following an acute Achilles tendon rupture. Resting fascicle length decreased while pennation angle increased in similar proportions after 4 weeks (12% change), which explained the stable muscle belly thickness following 4 weeks of injury. Muscle echogenicity was 8-11% reduced at week 0 and 2 before returning to non-injured values at week 4.

Automated Fascicle Tracking to Characterize Changes in Muscle Architecture During Isokinetic Contractions

John F. Drazan, Todd J. Hullfish, Josh R. Baxter
Department of Orthopedic Surgery, University of Pennsylvania, Philadelphia, PA

INTRODUCTION: Characterizing muscle architecture during functional movements provides important insight into the muscle mechanics underpinning musculoskeletal pathologies. Ultrasound imaging is a valuable tool to non-invasively observe changes in muscular structure for pennate muscles throughout a contraction. However, quantifying architectural parameters such as muscle fascicle length and pennation angle from ultrasound frames remains a challenge. Manually measuring these parameters are time and labor intensive. Conversely, automated tracking using computer vision offers efficient techniques improved research workflow and reliability. To address this research need, we have developed an automatic fascicle tracking algorithm that can be used by researchers to track fascicles and automatically extract pennation angle and fascicle length throughout a contraction. The purpose of this study was to quantify the reliability of this algorithm for quantifying medial gastrocnemius architecture during maximal effort plantarflexion contractions performed on a dynamometer.

METHODS: Five healthy-young adults performed maximal effort plantarflexion contractions and provided written informed consent in this IRB approved study. Images of the medial gastrocnemius of the right leg were acquired using an ultrasound transducer at 60 Hz at 8 MHz (LV7.5/60/128Z-2, SmartUs, TELEMED), which was secured in place using a custom-made molded cast secured by straps. Subjects were supine on a treatment table, which was secured to an isokinetic dynamometer (System 4, Biodex), with their right foot secured to the dynamometer footplate. Subjects performed maximal-effort isometric contractions at neutral ankle position and isokinetic contractions at 30, 120, 210, 300, and 500 degrees per second. We provided subjects with real-time feedback of plantarflexion torque using a computer monitor to encourage maximal effort. Subjects performed 3-4 contractions per condition until torque output plateaued over three trials. During each contraction, we synchronized ultrasound images with dynamometer angular position, velocity, and torque. We analyzed these videos using a three observation-three observer design to determine intra-rater and inter-rater reliability, respectively. To analyze each trial, users identified the deep and superficial aponeuroses and a muscle fascicle in the first frame of the video. Each of these structures were seeded with 100 tracking points, which were used to fit a line and define the aponeuroses and fascicle (Figure 1:A). Next, we tracked each one of these points frame by frame using affine optical flow in the MATLAB computer vision toolbox (Nanick MA, Mathworks) and automatically redrew the lines in each frame based on the movement of the seeded points to calculate fascicle length and pennation angle. Following the completion of automatic tracking for a given contraction, users identified the fascicle by drawing a line from the fascicle insertion in the deep aponeurosis in six evenly spaced frames across each contraction to serve as a comparison to the automatic tracking measurement (Figure 1). We used linear regression to evaluate the correlation between the manual and automatic measurements of fascicle length and pennation angle across all contractions for all subjects. We also calculated the reliability of both the manual and automatic tracking paradigms between days and examiners was using intraclass correlation coefficient (ICC). This test produced values ranging between 0 and 1 where values above 0.7 indicated “good” reliability between measurement methods.

RESULTS: Over 5,000 individual muscle fascicles were manually identified by the three examiners. The mean difference between manual and automatic fascicle length measurement was -4.49 ± 7.1 mm. The mean difference between manual and automatic pennation angle was 5.56 ± 7.6 degrees. These differences represent errors of 5.13% and 10.2 % of the dynamic range of fascicle lengths and pennation angle respectively. Manual and automatic fascicle length and pennation angle measurements were highly correlated across all contractions, subjects, examiners, and days (0.89 and 0.85, respectively). Both the manual and automatic fascicle length measurements had ‘good’ reliability between days for each examiner (0.75 and 0.92, respectively). Manual and automatic measurements of fascicle length also had ‘good’ reliability between all examiners (0.88 and 0.79, respectively).

DISCUSSION: We observed good measurement reliability across examiners between days and between examiners across all days for both manual and automatic tracking. Our findings indicate that this tool can be used by different users to reliably quantify fascicle architecture from ultrasound images acquired during maximal effort contractions. While the automatic measurements of fascicle geometry were on average longer and less pennate than manual measurements, especially at end-stages of contraction, there were many well-tracked fascicles as shown in (Figure 1:AB). We have observed that this under approximation (Figure 1:C) occurs when seeded points are initially selected over non-fascicle tissue such as veins which upon contraction do not move in concert with the rest of the muscle. These structures are often not evident in the first fame of the video and could be avoided by selecting a different fascicle if given another chance to initialize the program. This study used only the first attempt at tracking regardless of observed tracking quality. As such, these results represent a “worst-case-scenario” for tracking performance which we believe will drastically improve if users can reinitialize the program after observing a poorly tracked fascicle. Current work is focused on optimizing this automatic tracking paradigm to improve measurement fidelity.

CLINICAL RELEVANCE: Muscle function is dictated by the ability of muscles to change shape during contractions. However, the technical challenges of analyzing large data sets of ultrasound images limits the feasibility of implementing these measurements in a large scale. This work provides a reliable automated framework for extracting these architectural data from images of patient muscle.

ACKNOWLEDGEMENTS: This work was supported by the Thomas B. McCabe and Jeannette E. Laws McCabe Fund. We would like to thank Rena Mathew and Shilpa Donde for assistance in data collection and analysis.

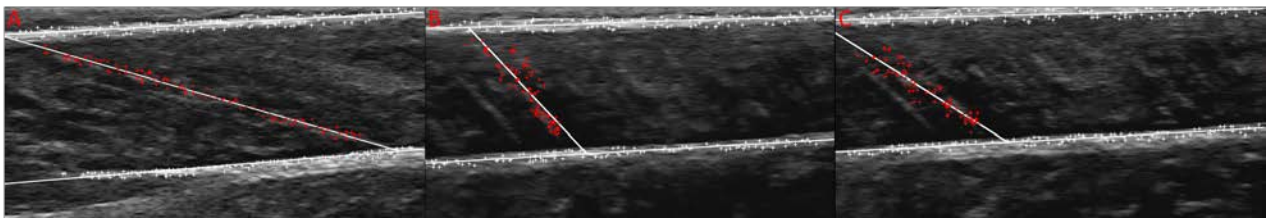

Figure 1. Dynamic ultrasound images of the medial gastrocnemius muscle while a patient performs a maximal plantarflexion contraction demonstrates the shortening dynamics of the muscle. To increase analysis speed and repeatability, users identify the deep and superficial aponeurosis as well as a single-continuous fascicle with the foot in dorsiflexion (A). Next, an affine optical flow paradigm tracks these structures through neutral position (B) and into peak plantarflexion (C). Our automated tracking algorithm has the strongest agreement with manual tracking when the muscle is actively shortening (AB) but tends to under-approximate fascicle pennation and over-approximate fascicle length when the muscle is fully shortened (C).

Bending-induced strain delays collagen degradation by collagenase

Karanvir Saini[1], Manu Tiwari[1], Jerome Irianto[1], Charlotte Pfeifer[1], Cory Alvey[1], and Dennis Discher [1,*]

[1] Biophysical Eng'g Labs, University of Pennsylvania, Philadelphia, PA 19104, USA
* Correspondence: discher@seas.upenn.edu

Abstract

Collagen is the predominant structural protein in mammals and is most abundant in stiff, solid tissues that sustain mechanical stress. Some studies have suggested tension stabilizes fibers against degradation, independent of cell activity, but strain-inhibited degradation and its mechanism(s) remain controversial. Here, strain gradients were generated in isolated tendon fascicle using three-point bending, with patterned photo-bleaching of fluorescent tendon used to measure strain. Deformed fascicles were exposed to collagenase, and degradation was tracked using the Second Harmonic Generation (SHG) signal produced by fibrillar collagen. Mechanical strains up to 5~8% magnitude maximize collagen fibril lifetime when exposed to collagenase, with higher and lower strains suggesting more rapid degradation. Fluorescent dextran permeation of the tendon further showed relatively uniform density, but Fluorescence Recovery after Photobleaching (FRAP) revealed increased mobility at high strain. Applied mechanical strain preserves collagen fibrils in tissue in the presence of collagenase. Our results suggest that, if collagen synthesis is constant, then collagen fibrils will accumulate most in regions of tissues that are strained by 5~8% during development, adaptation, and disease.

Keywords: Collagen; Strain; Degradation; Collagenase; Micro-bioreactor; Photo-bleaching; Kinetics

Increased Media Volume Enhances the Core Strength of MSC-based Engineered Cartilage

Zlotnick HM[1,2,3], Stoeckl BD[1,3], Henning EA[1,3], Steinberg DR[1,3], Mauck RL[1,2,3]
[1]Dept. of Orthopaedic Surgery, University of Pennsylvania, Philadelphia, PA, USA, [2]Dept. of Bioengineering, University of Pennsylvania, Philadelphia, PA, USA, [3]Translational Musculoskeletal Research Center, Philadelphia VA Medical Center, Philadelphia, PA, USA
zlotnick@seas.upenn.edu

Disclosures: Zlotnick HM (N), Stoeckl BD (N), Henning EA (N), Steinberg DR (N), Mauck RL (8, *JOR Spine*)

Introduction: Cartilage tissue engineering is promising for focal cartilage defect repair and potentially full anatomic joint resurfacing. For both applications, the optimal culture conditions that promote homogeneous tissue growth, cell viability, and native-like tissue mechanics from the sample edge to core have not yet been identified. Previous studies reported weaker mechanics and lower glycosaminoglycan and collagen content in the central region of mesenchymal stem cell (MSC) seeded constructs [1]. The introduction of nutrient channels can improve tissue construct homogeneity [2-3], however this approach may not be practical for all construct sizes and applications. It is possible that culture media volumes typically used for growth of engineered cartilage are insufficient to support tissue maturation, particularly in regions distant from the media source [4-5]. Cells on the exterior of constructs may consume the available nutrients, leading to malnourished and therefore weak construct cores. In this study, we varied the culture media volume supplied to MSC-seeded agarose constructs during maturation and assessed the overall and core mechanics and biochemical composition after 8 weeks of culture. We hypothesized that increasing the culture media volume would promote the development of more homogeneous mechanical and biochemical tissue properties.

Methods: Construct fabrication and culture: Juvenile bovine MSCs (P2) were encapsulated in 2% agarose (20x10^6 cells/mL) to create constructs (4 mm diameter, 2.25 mm thickness). Constructs were cultured for up to 8 weeks in 1V (1 mL), 3V (3 mL), and 5V (5 mL) of chemically defined media supplemented with 10ng/mL TGF-β3. Media was changed twice weekly. Construct orientation was maintained during culture, such that there was a defined sample top and bottom. Constructs were either left intact (Fig. 1Ai) or cored (Fig. 1Aii) with a 3mm biopsy punch for analyses. **Bulk mechanical testing:** Equilibrium and dynamic moduli were measured in uniaxial unconfined compression on total constructs (n=4) after 4 and 8 weeks of culture, and cored constructs (n=4) after 8 weeks of culture. **Local mechanical testing:** The depth dependent equilibrium modulus of the total constructs (n=4) and construct cores (n=4) was determined using a custom built microscope-based unconfined compression device. All constructs cultured for 8 weeks were halved diametrically and submerged in Hoescht dye to label cell nuclei. Samples were compressed through a series of 4% step strains with 7 minute relaxation periods. Images were taken post relaxation, and Lagrangian strains were calculated using Vic2D. 10 regions of equal size were marked across the depth (1=top and region 10=bottom). Local equilibrium modulus was calculated for each region from the recorded load and measured local strains at the 12% step. The top, middle, and bottom equilibrium moduli were obtained by averaging regions 2 & 3, 5 & 6, and 8 & 9, respectively. **Biochemical analyses:** Glycosaminoglycan (GAG) and hydroxyproline (OHP) assays were performed to quantify GAG and collagen content in the annulus top, center top, annulus bottom, and center bottom regions of the constructs (Fig. Aii). **Statistical analysis:** Significance ($p < 0.05$) was assessed by ANOVA with Tukey's post-hoc correction using STATA.

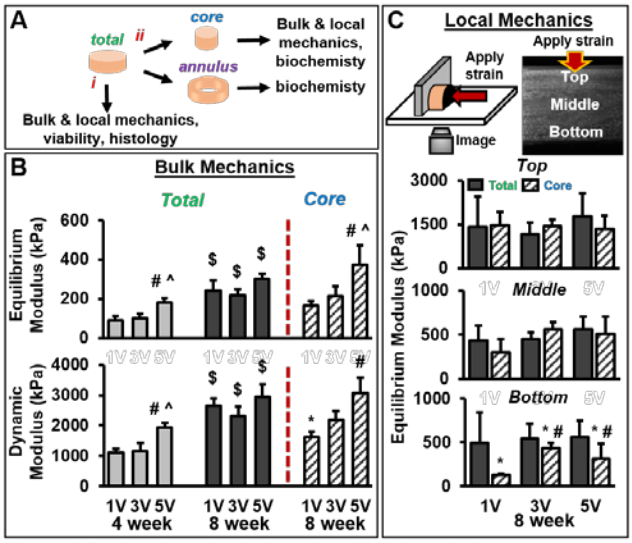

Figure 1. Regional mechanical testing of MSC-seeded agarose constructs. (A) Constructs were either left intact or cored for testing. (B) Bulk mechanical testing of the total constructs (4 weeks, 8 weeks) and cores (8 weeks). Symbols ($, #, ^, *) indicate significance ($p < 0.05$) compared to the same volume at 4 weeks, compared to 1V at the same time point, compared to 3V at the same time point, and compared to total construct at the same volume and time point, respectively. (C) Local mechanical testing of the total constructs and cores at 8 weeks. Symbols (#, *) indicate significance ($p < 0.05$) compared to the 1V core, and the total construct at the same volume, respectively. All bars represent mean ± std dev.

Results: The core strength of the constructs improved with increased media volume. Bulk mechanical analysis showed that the equilibrium modulus of the 5V cores (373.7 ± 97.2kPa) was significantly higher than the 1V (165.7 ± 23.2kPa) and 3V (214 ± 49.7kPa) cores (Fig. 1B). The dynamic modulus of the 5V cores (3071.1 ± 518.2kPa) was also significantly higher than the 1V cores (1627.5 ± 161.3kPa) (Fig. 1B). Local mechanical testing showed that the equilibrium modulus of the 3V (432.7 ± 58.3kPa) and 5V core bottoms (312.0 ± 168.2kPa) was significantly higher than the 1V core bottom equilibrium modulus (125.3 ± 18.5kPa) (Fig. 1C). For the biochemical analyses, at 4 weeks the 1V and 3V annulus top and center top, and 1V annulus bottom regions all have significantly less GAG than their 5V counterparts (Fig. 2A). The 1V annulus top, center top, and center bottom regions all had significantly less collagen than their 5V counterparts at 4 weeks.

Discussion: In this study, we hypothesized that increasing media volume would reduce the differences in mechanical and biochemical properties throughout the axial and radial directions of the constructs. At 4 weeks, provision of 5V media volume had a pronounced positive effect on bulk mechanics and biochemical content (Fig. 1A, 2A, 2B). These differences were less pronounced after 8 weeks of culture, however, indicating that while increasing the media volume did not eliminate long term axial and radial differences in mechanical and biochemical properties, it accelerated construct growth in the first 4 weeks of culture. Notably, even at 8 weeks, the core strength of constructs was improved in the 5V condition.

Significance: These findings suggest that increased culture media volumes can expedite the *in vitro* maturation and produce more homogeneous engineered cartilage tissue. These findings will improve the quality of cartilage tissue produced *in vitro* prior to *in vivo* implantation.

References: [1] Farrell+ ECM J 2012, [2] Cigan+ J Biomech 2016, [3] Kim+ Acta Biomaterialia 2017, [4] Henning+ ORS 2015, [5] Henning+ ORS 2016

Acknowledgements: This worked was funded by the National Institutes of Health (R01 EB008722) and the Department of Veterans Affairs (I01 RX00070).

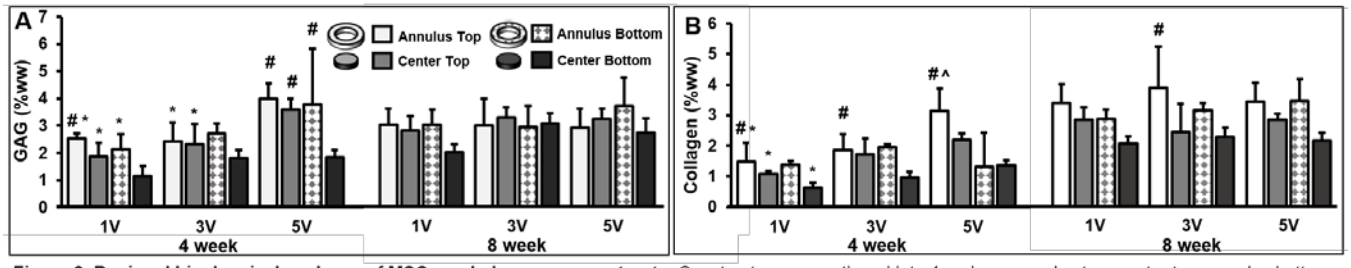

Figure 2. Regional biochemical analyses of MSC-seeded agarose constructs. Constructs were sectioned into 4 regions: annulus top, center top, annulus bottom, and center bottom. Symbols (#, ^, *) indicate a significant difference ($p < 0.05$) compared to the center bottom region at the same time point and media volume, the annulus bottom region at the same time point and media volume, and the same region at the same time point and 5V media volume.

Macro- and Micro-Scale Changes in Meniscus and Cartilage in a Large Animal Model of Meniscal Injury

Sonia Bansal[1,2], Jay M. Patel[*1,,2], Michael Eby[*1,,2], Kevt'her Hoxha[*3], Mackenzie L. Sennett[1,2], Kamiel S. Saleh[1], Brendan D. Stoeckl[1,2], Anthony R. Martin[1,2], Liane M. Miller[1,2], Dawn M. Elliott[4], Michael W. Hast[5], Lin Han[3], Miltiadis H. Zgonis[1,2], and Robert L. Mauck[1,2]
[1]McKay Orthopedic Research Laboratory, University of Pennsylvania, Philadelphia, PA [2]Translational Musculoskeletal Research Center, CMC VA Medical Center, Philadelphia, PA [3]NanoBiomechanics Laboratory, Drexel University, Philadelphia, PA [4]Multi-Scale Fiber-Reinforced Tissue Biomechanics Laboratory, University of Delaware, Newark, DE [5]Biedermann Laboratory for Orthopaedic Research, University of Pennsylvania, Philadelphia, PA
soniab@seas.upenn.edu
Disclosures: RL Mauck (8, *JOR Spine*).
INTRODUCTION: The meniscus is a complex and integral load-bearing tissue in the knee [1] that is commonly injured [2]. Depending on the type of injury, the ability of the meniscus to transfer and distribute loads is reduced to varying degrees. For example, with tears of the enthesis (root tears), free meniscal excursion occurs with joint loading, the mechanical equivalent meniscus removal (meniscectomy) [3]. Indeed, small animal (mouse and rat) models have used destabilization of the medial meniscus (DMM) to instigate controlled joint degeneration [4]. Even with smaller surgical excisions to treat radial or circumferential tears in the inner zone, the joint degrades over the longer term [5,6], as evidenced by the early onset of OA in humans. While degeneration of the articular cartilage is well established in small animal models of meniscus destabilization, and in human cohorts after meniscus surgery, progression of disease in the meniscus itself is not well studied, especially in larger animal models. Thus, the purpose of this study was to investigate how meniscus injury in a large animal model instigates pathologic remodeling of the meniscus itself and the joint as a whole, at the macro- and micro-scale.
METHODS: Juvenile (6 month old) Yucatan minipigs (n=12) underwent bilateral arthroscopic surgery and received two of the following four injuries to the medial meniscus - sham, DMM, a vertical longitudinal tear (1/3 arc length, red-white zone), or a radial tear (50% of meniscus width) (n=6/group). Animals were euthanized at one month and joints harvested for a series of macro- and micro-scale analyses. For macro-scale tests, intact joints were compressed to 1X body weight (400 N) at 15^{o} of flexion using a custom rig and universal test frame. Pressure sensors (TekScan #6900-110) were inserted into the joint to measure load transfer through the medial compartment [3]. Next, tissues were imaged for macroscopic changes to the meniscus and for cartilage wear (using India ink) [7]. Subsequently, medial menisci were harvested and sectioned (16 micron thickness, vertical plane, anterior and posterior horns) for atomic force microscopy (AFM) [8]. Additional sections were subjected to histological analysis of proteoglycan (PG) content (Safranin O/Fast Green) [9]. Osteochondral cylinders were isolated from the medial tibial compartment and indented using a 2 mm spherical indenter to determine cartilage mechanical properties in the region covered by the meniscus [10]. These samples then underwent microCT scanning followed by decalcification and paraffin processing for analysis of proteoglycan content (Safranin O/Fast Green) [11]. Histological outcomes were graded using the OARSI scoring method [7] by four blinded observers.
RESULTS: Sham operated menisci showed no macroscopic changes. Most vertical tears were no longer visible at 1 month, while radial tears were readily apparent. DMM menisci showed some healing with evidence of fibrous tissue at the anterior horn **(Fig 1A)**. However, this scar tissue was not mechanically competent, as the mean contact pressure was significantly higher in DMM joints compared to other groups **(Fig 1B)**. Menisci from sham limbs showed more intense staining for PGs compared to DMM menisci, with slight reductions in staining intensity radial and vertically defected menisci **(Fig 2A)**. AFM analysis revealed an increase in the indentation modulus of radial fibers in the inner zone of the anterior horn with radial defects, as well as a decrease in circumferential fiber modulus in the outer zone of the posterior horn with DMM **(Fig 2B)**. While no macroscopic signs of wear were visible on the tibial cartilage surface, PG staining was markedly reduced in DMM **(Fig 3A)** and slightly reduced in radial and vertical samples. OARSI scoring revealed changes in all groups, with significance for radial and vertical samples **(Fig 3B).** Cartilage indentation modulus was significantly decreased for DMM samples, and trended lower for vertical and radial samples **(Fig 3C).** There were no changes in the subchondral bone for any group at this time point (data not shown).
DISCUSSION: This is the first study, to our knowledge, to investigate meniscal remodeling in a minimally invasive (arthroscopic), large animal surgical model of meniscus injury. Despite the fibrous "healing" of the DMM in this model, load transfer to the underlying cartilage remained altered at 1 month post-surgery, with increases in contact pressure and decreases in cartilage PG staining and indentation modulus. This is consistent with outcomes from open surgical procedures in small [4,12] and large animal [13] models of DMM in the literature. Meniscus remodeling was also evident at this time point for DMM samples. Specifically, the PG content of the inner anterior horn was reduced, as was the indentation modulus of circumferential fibers in the outer posterior horn. This suggests that unloading caused by DMM results in remodeling of the meniscus. Vertical and radial tears did not alter load transmission at this time point, but both resulted in signs of cartilage degeneration (according to OARSI scoring) and radial tears increased micromechanics of the radial tie fiber network in the anterior horn of the meniscus. Future work will increase the sample size and extend the study duration to detail the temporal progression of meniscal injury-induced remodeling of the meniscus (and joint as a whole) at both the micro- and macro-scales in this large animal model.
SIGNIFICANCE/CLINICAL RELEVANCE: Understanding the progression of joint disease after meniscal injury in a large animal model will improve surgical decision making and inform novel repair strategies.
REFERENCES/ACKNOWLEDGEMENTS: [1] Makris+ 2011 [2] Mordecai+ 2014 [3] Bedi+ 2010 [4] Glasson+ 2007 [5] Roos+ 1995 [6] Lohmander+ 2007 [7] Little+ 2010 [8] Li+ 2018 [9] Pauli+ 2011 [10] Meloni+ 2017 [11] Sennett+ 2018 [12] Doyran+ 2017 [13] Waller+ 2017. This work was supported by the NIH and the Department of Veterans Affairs. *Authors contributed equally

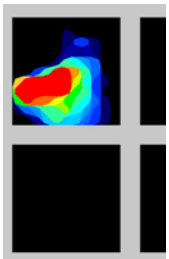

← **Figure 1** – Macroscopic images (A) of sham (upper left) and DMM (lower left) operated menisci, showing fibrous attachment formation in the DMM meniscus (white circle). Representative contact pressure maps shown from peak contact load point (right). Quantification of mean contact pressure (B) for all operative groups

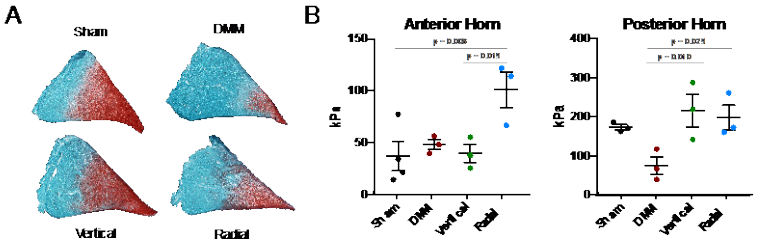

↑ **Figure 2** – Histological staining (A) of radial vertical sections from the anterior horn of the meniscus. Staining done with SafraninO/Fast Green for proteoglycan content. AFM indentation modulus (B) of the Anterior Horn, inner zone radial fibers (left) and Posterior Horn, outer zone circumferential fibers (right).

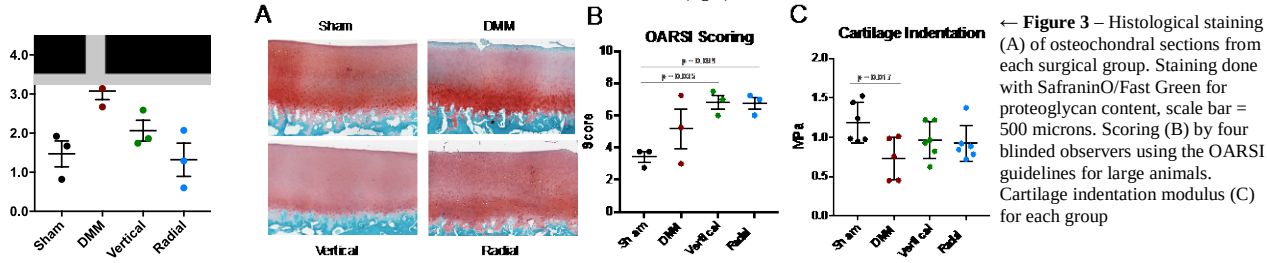

← **Figure 3** – Histological staining (A) of osteochondral sections from each surgical group. Staining done with SafraninO/Fast Green for proteoglycan content, scale bar = 500 microns. Scoring (B) by four blinded observers using the OARSI guidelines for large animals. Cartilage indentation modulus (C) for each group

Type II Diabetes Adversely Affects the Viscoelastic and Quasi-Static Properties of Supraspinatus Tendons

Snehal S. Shetye[1], Mengcun Chen[1], Ashley Rodriguez[1], Louis J. Soslowsky[1]
[1]McKay Orthopaedic Research Laboratory, University of Pennsylvania, Philadelphia, PA
shetye@pennmedicine.upenn.edu

Disclosures: Snehal S. Shetye (N), Mengcun Chen (N), Ashley Rodriguez (N), Louis J. Soslowsky (N)

INTRODUCTION: Type II diabetes mellitus (T2DM) is a metabolic disease affecting nearly 24 million people in the United States alone [1]. Along with hyperglycemia, nephropathy, increased risk of stroke and high blood pressure, T2DM can cause increased joint stiffness and limited mobility, which has been attributed to accumulation of AGE (advanced glycation end products)-derived crosslinks in collagenous tissues. Although multiple animal models of T2DM have been used to investigate tendon health, many have reported a decrease in tendon stiffness, which contrasts with that observed in the human population [2-4]. The University of California at Davis-type II diabetes mellitus (UCD-T2DM) model has been shown to more closely replicate the pathophysiology of human T2DM displaying polygenic obesity, later age of onset, and intact leptin signaling [5, 6]. Thus, the objective of this study was to investigate the elastic and viscoelastic properties of rat supraspinatus tendons in the UCD-T2DM diabetic rat model. We hypothesized that T2DM would result in increased tendon stiffness and modulus, with a concomitant decrease in stress relaxation.

METHODS: Six-month old lean Sprague-Dawley ("lean", n = 5), obese Sprague-Dawley ("obese", n = 5), and UCD-T2DM rats ("diabetic", n = 4) were studied. The age of diabetic onset was defined as the age where blood glucose concentration higher than 200mg/dl was detected in two consecutive measurements [6]. Supraspinatus muscle-tendon units were carefully dissected from the scapula of the left shoulder and removed with the proximal humerus for mechanical testing. Muscle, along with extraneous tissue was removed from each tendon and tendon cross-sectional area (CSA) was measured using a custom laser device [7]. Each humerus was potted in a custom acrylic cylinder secured with polymethyl-methacrylate around and over the humeral head to prevent failure at the growth plate. Stain lines were used to track strain optically. Stiffness was calculated as the slope of the linear region of the load-displacement curve during a ramp to failure at 0.01%/s. Modulus was calculated as slope of the linear region of the stress-strain curve. Stress relaxation (%) was calculated from a 300s stress-relaxation test at 6% strain. *Statistics:* Tendon mechanical properties were evaluated by one-way ANOVA followed by Bonferroni post-hoc tests. Significance for all statistical comparisons was set at $p \leq 0.05$ and trends at $p \leq 0.1$.

RESULTS: The UCD-T2DM rats were diabetic for 51.6±9.2 days based on blood glucose measurements. As expected, the obese and diabetic rats had significantly higher body weights than the age-matched lean controls (Fig. 1A). The obese rat supraspinatus tendons had a significantly higher cross-sectional area when compared with the lean controls (Fig. 1B). Diabetic rat tendons had significantly reduced stress relaxation as compared to the obese rats and a trend when compared to the lean controls (Fig. 2A). Diabetic rat tendons had significantly higher stiffness compared with the obese rats. The obese rat tendons had a significantly reduced stiffness compared to the lean controls, but no difference between the diabetic and lean animals (Fig. 2B). No differences were observed in tendon modulus for any of the groups (Fig. 2C).

DISCUSSION: This study evaluated the effects of type II diabetes on the mechanical response of supraspinatus tendons obtained from UCD-T2DM rats. We found that diabetes negatively affected almost all mechanical properties measured. Diabetic rats had a significantly reduced stress relaxation response. This is consistent with previous studies that have investigated the effect of AGEs on tendon mechanics [8]. Along with aging, diabetes is strongly correlated to altered mechanical response of connective tissues and reduced response to healing. An increase in non-enzymatic, oxidative reactions between glucose and collagen lead to accumulation of AGEs in collagen-rich tissues. These AGEs have been postulated to affect tendon collagen function in diabetes by altering shear load transfer between fibers, thus affecting its viscoelastic response. Further, numerous clinical studies on diabetic patients have reported the loss of joint function and increased stiffness of the shoulder joint, which is consistent with the increase in supraspinatus tendon stiffness observed here. Interestingly, in vitro studies have observed an increase in tendon stiffness and strength due to AGE cross-linking, however this has not been reliably observed in other animal models of type II diabetes, where both an increase [9] and decrease [2-4] in stiffness has been reported. Overall, the findings in this study more closely replicate the clinically observed adverse manifestations of T2DM on tendon mechanical health, and thus support the use of this UCD-T2DM diabetic rat model to further investigate the pathophysiology of diabetes on joint function, gait kinematics, and tendon healing response. This will help guide future therapeutic interventions to arrest the debilitating effects of diabetes on the musculoskeletal system.

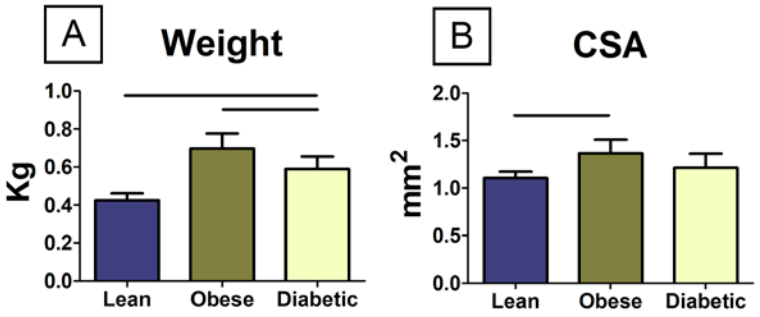

Figure 1 -(A) Body weights for the diabetic and obese rats were significantly higher when compared with the lean controls. **(B)** Obese rat tendons had significantly higher cross-sectional area when compared with the lean controls.

SIGNIFICANCE: This study demonstrates the adverse effects of diabetes on intact tendon tissue and highlights the necessity of appropriate animal models to study the effects of diabetes on the musculoskeletal system to ultimately develop innovative therapeutic solutions.

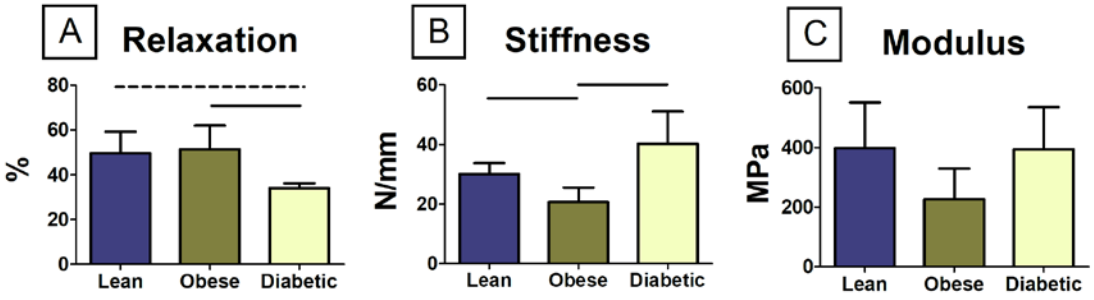

Figure 2 - (A) Diabetic rat tendons had significantly lower stress relaxation when compared with the lean and obese rats. **(B)** Obese rat tendons had significantly lower stiffness compared to the lean controls and the diabetic rats. **(C)** No differences were observed in modulus between any of the groups tested.

REFERENCES: [1] Mokdad et al., 2001. *JAMA*, 286:1195-1200 [2] Connizzo et al., 2014. Ann Biomed Eng 42:1880-1888 [3] de Oliveira et al., 2012. J Diabetes Complications 26:163-168 [4] Fox et al., J Orthop Res 2011. 29:880-885 [5] Cummings et al., Am J Physiol Regul Comp Physiol 2008. 295:R1782-R1793 [6] Fields et al., J Orthop Res 2015. 33:738-746 [7] Favata M, et al., 2006. JOR, 24(11):2124-2132. [8] Li et al., 2013 Matrix Biology. 32:169-177 [9] Andreassen et al., J Appl Physiol 2015 120:130-137

ACKNOWLEDGEMENTS: This study was supported by the Penn Center for Musculoskeletal Disorders (P30AR069619).

The Effects of Incremental Ulnar Styloid Osteotomies on Distal Radioulnar Joint Stability– A Biomechanical Cadaveric Study

Adnan N. Cheema MD[1], Agnes Dardas MD[1], Michael W. Hast PhD[2], Benjamin L. Gray, MD[1]

[1] University of Pennsylvania, Department of Orthopaedic Surgery, 3737 Market St, 6th floor
Philadelphia, PA 19104

5

[2] Biedermann Lab for Orthopaedic Research, University of Pennsylvania, 3737 Market St
10th floor, Suite 1050, Philadelphia, PA 19104

Funding: The authors would like to thank the Biedermann Lab for Orthopaedic Research at the University of Pennsylvania for providing funding for this project.

Introduction: Ulnar styloid fractures co-occur in about half of all distal radius fractures, but are often treated non-operatively. The exact location of ulnar styloid fractures at which stability of the DRUJ occurs is not clearly defined, nor does an algorithm exist for determining which ulnar styloid fractures should be repaired when performing open reduction and internal fixation of distal radius fractures. The purpose of this cadaveric study was to determine how different levels of ulnar styloid osteotomies affect radiographic measurements of instability, and to determine which radiographic views most reliably detect signs of DRUJ instability.

Materials and Methods: Six fresh-frozen cadavers underwent sequential ulnar styloid osteotomies: styloid tip, styloid base, and the subchondral surface of the ulnar head. PA and lateral stress-radiographs in both supination and pronation were obtained at each osteotomy level. Radiographic measurements of DRUJ gap and dorsal subluxation of the ulna were made and compared across specimens using one-way ANOVAs and post-hoc Tukey Honest Significant Difference tests.

Results: The supinated PA and pronated PA radiographs demonstrated a significant increase in the DRUJ gap after the ulnar styloid base osteotomy was made. On the lateral radiographs, no differences in dorsal ulnar subluxation were seen between any groups. Results are summarized in Figure 1.

Conclusions: This study provides radiographic evidence that only fractures at or proximal to the ulnar styloid base demonstrate a measurable increase in DRUJ instability. It also confirms that lateral radiographs are not reliable in measuring dorsal ulnar subluxation to detect DRUJ instability. Fractures proximal to and involving the ulnar styloid base should be seriously considered for fixation when performing open reduction and internal fixation of distal radius fractures.

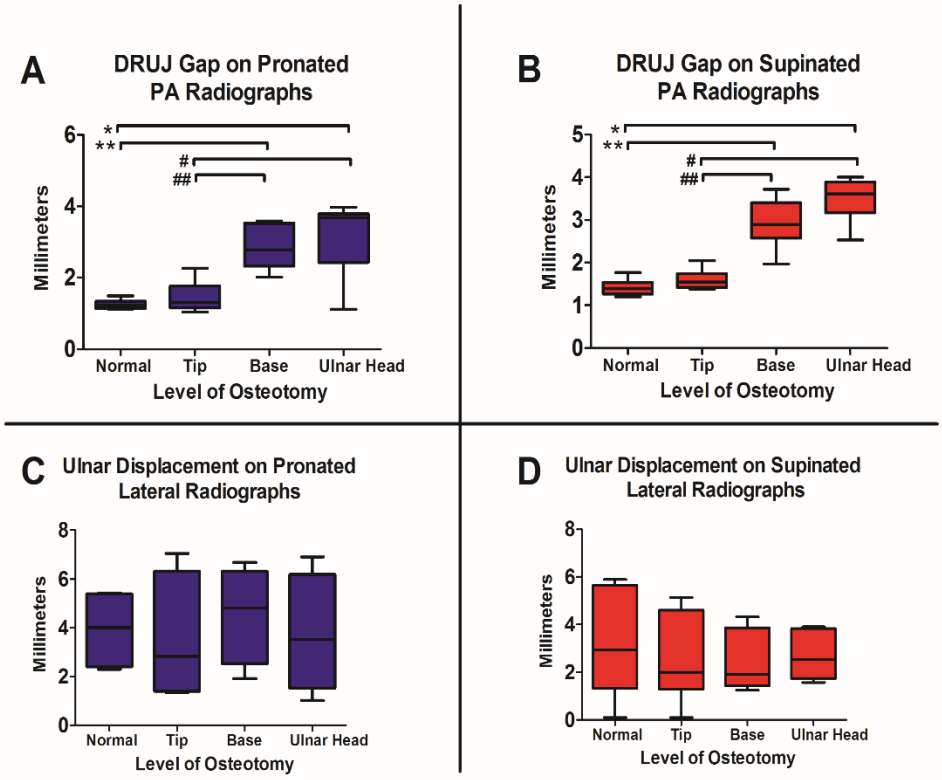

Figure 1. A) On pronated PA radiographs, significant differences in DRUJ gap were found between the following comparisons: normal-styloid base (**), normal-ulnar head (*), tip-styloid base (##), and tip-ulnar head (#). B) On supinated PA radiographs, significant differences in DRUJ gap were found between the following comparisons: normal-styloid base (**), normal-ulnar head (*), tip-styloid base (##), and tip-ulnar head (#). C) On pronated lateral radiographs and D) on the supinated lateral radiographs, no significant differences in dorsal displacement of the ulna were found. Whiskers denote maximum and minimum range, boxes denote interquartile (25%-75%) range, and lines denote the median.

Nicotine Impairs Intra-Substance Tendon Healing After Full Thickness Injury in a Rat Model

Adnan N. Cheema, MD, Joseph B. Newton, BS, James F. Boorman-Padgett, MS, Stephanie N. Weiss, BS, Courtney A. Nuss, AS, Daniel J. Gittings, MD, Daniel C. Farber, MD, Louis J. Soslowsky, PhD*

McKay Orthopaedic Research Laboratory
University of Pennsylvania
3450 Hamilton Walk, 110 Stemmler Hall
Philadelphia, PA 19104-6081
United States of America

Abstract

Nicotine is harmful to many bodily systems; however, the effects of nicotine on intra-substance tendon healing remain largely unexplored. The purpose of this study was to examine the functional, structural, and biomechanical effects of nicotine on the healing of Achilles tendons in rats after an acute full-thickness injury. Sixty Sprague-Dawley rats were enrolled in this study. Half were exposed to 0.9% saline and half to 61ng/mL of nicotine for 3 months via subcutaneous osmotic pumps. At 3 months, all rats underwent blunt full thickness transection of the left Achilles tendon and were immobilized for one week in plantarflexion. *In-vivo* assays were conducted prior to injury, at 21 days, and at 42 days post-injury and included the following: functional limb assessment, passive joint mechanics, and vascular evaluation. Rats were sacrificed at 21 and 42 days for biomechanical testing and histologic evaluation. Rats exposed to nicotine demonstrated decreased vascularity, greater alteration in gait mechanics, and increased passive ROM of the ankle joint. Biomechanically, the nicotine tendons failed at lower maximum loads, were less stiff, had smaller cross-sectional areas and had altered viscoelastic properties. Histologically, nicotine tendons demonstrated decreased vessel density at the injury site. This study demonstrates that nicotine leads to worse functional outcomes and biomechanical properties in tendons. The decreased vascularity in the nicotine group may suggest an underlying mechanism for inferior tendon healing. Patients should be counseled that using nicotine products increase their risk of poor tendon healing and may predispose them to tendon re-rupture.

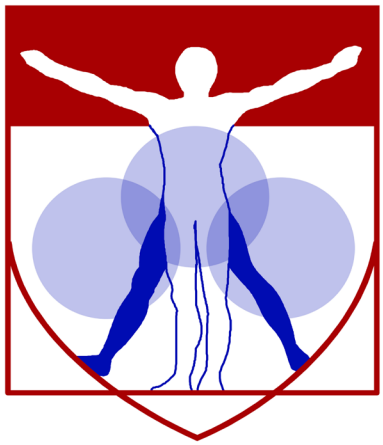

PENN

CENTER for

MUSCULOSKELETAL

DISORDERS

Histology Abstracts

Unique Subpopulation of Col1a1CFP Negative Tenocytes that Exhibit MMP Activity

Catherine A. Bautista[1], Xi Jiang[1], Nathaniel A. Dyment[1]
[1]University of Pennsylvania, Philadelphia, PA
cbaut@seas.upenn.edu

Disclosures: Catherine A. Bautista (N), Xi Jiang (N), Nathaniel A. Dyment (N).

INTRODUCTION: Tendon cells that are oriented in linear arrays within tendon fascicles are known as tenocytes (i.e., internal tendon fibroblasts). Tenocytes are thought to be a relatively homogenous population. Our lab utilizes transgenic lineage tracing and fluorescent reporter mice to define heterogeneity within this cell population in order to define markers that map the cell lineage and pathways that regulate tenogenic differentiation. Two such reporters include ScxGFP [1] and Col1a1(3.6kb)CFP, which display similar expression patterns within multiple tendons [2]. These reporters are expressed by the majority of cells within the tendon fascicle. However, there are always negative cells within linear arrays during postnatal growth. We hypothesized that these cells could either be proliferating, indicating a potential progenitor phenotype, or display MMP activity, indicating a distinct function within the tendon compared to Col1-expressing cells. The objective of this study was to determine proportion of proliferating cells or MMP-active cells within the tenocyte population.

METHODS: All animals and procedures were approved by UPenn's IACUC. Transgenic mice. One transgenic mouse line was used in this study: Col1a1(3.6kb)CFP mice containing 3.6kb of the Col1a1 promoter driving CFP expression [3]. Experimental design. Animals were injected with 3 µg/g EdU once daily for two days before day of sacrifice. Hindlimbs and tails were isolated from P5 and P28 mice for cryohistological analysis while tail tendons (**TT**) were isolated from P28 mice for explant culture (n=1-3 mice/time point). The patellar tendon (**PT**), Achilles tendon (**AT**), and **TT** were analyzed for histology. Cryohistology. Limbs and tails were fixed in formalin, embedded, sectioned, stained for EdU, counterstained with DAPI, and imaged on the Zeiss Axio Scan.Z1. TT explant culture and MMP14 immunolabeling. P28 TTs were cultured in individual channels of 6-channel slides (Ibidi µ-Slide VI) with 10% FBS 1% Pen Strep in DMEM containing 200 nM MMPSense 645 FAST Fluorescent Imaging Agent at 37˚C and 5% CO_2 for 4 days (n=5 TTs). MMPSense is a MMP-activated fluorescent dye. On Day 4, TTs were imaged on the Axio Scan and were serially digested enzymatically to remove cells on the surface of the TTs and obtain a single cell suspension. Suspended cells were incubated with mouse anti-MMP14 primary antibody (Millipore) followed by goat anti-mouse Alexa Fluor 647 secondary antibody, then imaged on the Zeiss Axio Observer. Image quantification. For cryohistological analysis, the CFP and EdU intensities were recorded for each cell within the tendon midsubstance; an equivalent minimum threshold was applied and the percentages of positive cells were computed across all tendons. For MMPSense analysis in TTs, the percentage of MMPSense(+) cells per linear array was calculated (n=10 arrays). For MMP14 immunolabeling analysis, the CFP, MMPSense, and MMP14 intensities were recorded for each cell and the percentages of CFP(+), MMPSense(+), and MMP14(+) cells were computed.

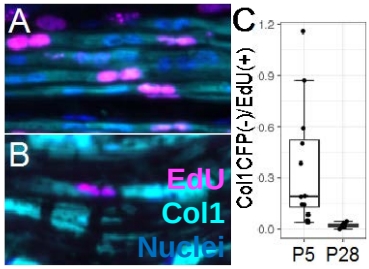

Fig. 1: EdU(+) cells are Col1CFP(-) by P28. EdU stained sections at P5 (A) and P28 (B). C) Number of EdU(+) cells that are Col1CFP(-) at both ages.

RESULTS: EdU(+) cells constitute 2% of Col1CFP(-) cells at P28. While Col1CFP is broadly expressed by tendon cells, 50.0% ± 27.7% and 65.1% ± 25.9% of cells in P5 and P28, respectively, were in fact negative for Col1CFP. As expected, EdU labeling showed a decrease in proliferating cells from P5 (10.8% ± 7.2% overall) to P28 (0.9% ± 0.8% overall). When normalized to the total number of CFP(-) cells, 14.1% ± 13.8% at P5 and 2.0% ± 1.6% at P28 were EdU(+) (Fig. 1C). MMPSense(+) cells constitute 20% of Col1CFP(-) cells at P28. TT explants maintained Col1CFP expression after 4 days in culture (Fig. 2; cyan). Intracellular localization of MMPSense (Fig. 2; red) revealed separate and distinct populations of Col1CFP(+) vs. MMPSense(+) cells with no cells exhibiting expression for both markers. MMPSense(+) cells accounted for 19.5% ± 6.8% of all cells in each array (Fig. 2; white arrows). MMPSense(+) cells on the surface (Fig. 2; yellow arrows) were excluded from this analysis. MMPSense(+) cells co-express MMP14. Quantification of isolated TT tenocytes revealed no overlap in Col1CFP and MMPSense signals (Fig. 3A). Conversely, 12% of cells were both MMPSense(+) and MMP14(+) (Fig 3B). Of the MMPSense(+) cells, 39% also expressed MMP14.

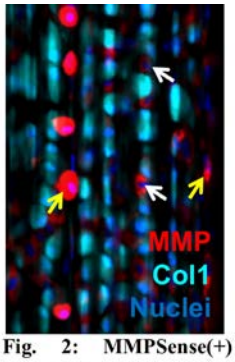

Fig. 2: MMPSense(+) cells are distinct from Col1CFP(+) cells. White and yellow arrows indicate MMPSense cells in linear arrays and on surface of tendon, respectively.

DISCUSSION: In order to better understand tendon pathologies and to develop improved repair strategies, we must first improve our understanding of the tendon lineage, including markers that define cells at multiple stages of the lineage and signaling pathways that regulate the differentiation of progenitors into mature tenocytes. Col1CFP, along with ScxGFP, may be expressed by cells at multiple stages of differentiation (e.g., tenoblast through tenocyte). Proliferating cells that are Col1CFP negative may be a resident progenitor population that will give rise to Col1-expressing progeny. In fact, the overall number of these cells reduces dramatically from P5 to P28, indicating that the progenitor pool may be diminishing. At P28, a larger percentage of these Col1CFP(-) cells are MMPSense(+) instead of EdU(+), which may identify a unique cell population with a separate function from cells expressing Col1CFP. Interestingly, 39% of MMPSense(+) cells co-express MMP14, which may give insight into their function. While MMP14 plays a role in ECM degradation, targeted KO of MMP14 in tendons resulted in fewer, smaller diameter collagen fibrils, suggesting that MMP14 may play a role in fibril secretion [4]. Our data suggest that separate cells display MMP-activity vs Col1-expression. Therefore, there may be a cross-talk between MMP-active and Col1-expressing cells during tendon fibrillogenesis. MMP14 and MMP2, which is also highly expressed in postnatal tendons, both can act on substrates within the cell and affect cell signaling pathways among other things [5]. Therefore, these cells may play a role beyond ECM assembly and degradation.

SIGNIFICANCE/CLINICAL RELEVANCE: An improved understanding of the cellular markers and signaling pathways that define and regulate the tendon lineage will be crucial to developing new therapies to attenuate the progression of pathologies and improve repair outcomes following injury. This study gives new insight into a potential cell population within tendon that may have a novel MMP-related function.

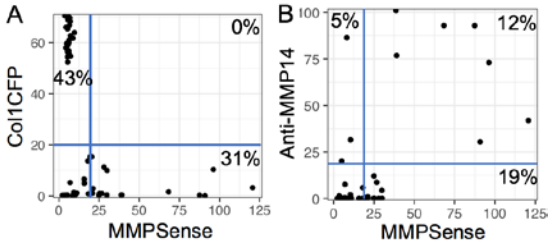

Fig. 3: MMPSense(+) cells express MMP14 but not Col1CFP. MMPSense vs. Col1CFP (A) and Anti-MMP14 (B) scatterplots. C) Representative images of Col1CFP only (top row) and MMPSense(+)/MMP14(+) (bottom row) cells.

REFERENCES: 1. Pryce BA, et al., *Dev. Dyn.*, 2007; 2. Dyment N, et al., *ORS Conference*, 2016; 3. Kalajzic I, et al., *JBMR*, 2001; 4. Taylor SH, et al., *Elife*, 2015; 5. Cauwe B, et al., *Crit. Rev. Biochem. Mol. Biol.*, 2010.

ACKNOWLEDGEMENTS: Work supported by NIH grants R00 AR067283, P30 AR069619, and startup funds from Dept. Orthopaedic Surgery at UPenn.

De novo gene transcription is required for persistent cell motility by controlling cytoskeletal dynamics

Devon E. Mason [1,2,3], James H. Dawahare[3], Trung Dung Nguyen[3], Yang Lin[4], Sherry L. Voytik-Harbin[5], Pinar Zorlutuna[3], Mervin C. Yoder[4], Joel D. Boerckel [1,2,3]
[1] McKay Ortho Research, Orthopedic Surgery, UPenn, Philadelphia, PA [2] Bioengineering, UPenn, Philadelphia, PA [3] Aerospace and Mechanical Engineering, ND, IN [4] Herman B. Wells Center, IU, IN [5] Biomedical Engineering, Purdue, IN

Introduction: Cell migration is crucial during development and is influenced by physical cues from both the extracellular matrix and surrounding cells. Mechanical signals drive cell motility through actomyosin-focal adhesion cross-talk, which produces a feed-forward loop where cytoskeletal tension drives force generation and adhesion reinforcement. Recent studies modeled this process as a mechanical molecular clutch, enabling cells to rapidly respond to extracellular stimuli without new gene expression. This lead us to ask whether new gene expression is required for directed migration.

We found that *de novo* gene expression is not required for the initial motile response, but is necessary for persistent migration. Surprisingly, rather than functioning to replenish depleted cytoskeletal machinery, transcription was required to modulate cytoskeletal tension, focal adhesion maturation, and polarization through YAP/TAZ-mediated regulation of myosin activation.

Methods and Results: Endothelial colony forming cells (ECFCs) were treated with low doses of transcriptional or translational inhibitors, actinomycin D (0.1 or 0.25 μg/mL) or puromycin (1 μg/mL), respectively, prior to induction of directed cell migration. Transcription/translation inhibition did not affect cell motility over two hours, but eventually caused migratory arrest (Fig. 1A). The amount of cytoskeletal or adhesion proteins remained unchanged, but stress fiber formation (Fig. 1B), actin polymerization (Fig. 1C), focal adhesion maturation, and myosin light chain phosphorylation (pMLC) (Fig. 1E) significantly increased. We then hypothesized that the mechanotransductive transcriptional co-activators yes-associated protein (YAP) and transcriptional activator with PDZ-binding domain (TAZ) play a role in transcription-dependent cytoskeletal tension.

YAP/TAZ depletion increased cytoskeletal rigidity measured by nano-indentation (Fig. 1D), and arrested cell motility in a cell-autonomous manner, comparable to transcription inhibition. Live cell imaging revealed progressive substrate anchorage through increased cytoskeletal polymerization and stress fiber formation (Fig. 1B&F), pMLC (Fig. 1E), and adhesion maturation (Fig. 1F), further phenocopying transcription inhibition. Blockage of the Rho-ROCK-myosin pathway, either through pharmacologic inhibition (Y-27632, Blebbistatin) or by depletion of the myosin light chain phosphatase inhibitor, NUAK2, rescued actin polymerization, focal adhesion morphology, and wound closure rate (data not shown), establishing feedback control of pMLC downstream of YAP/TAZ-dependent transcription.

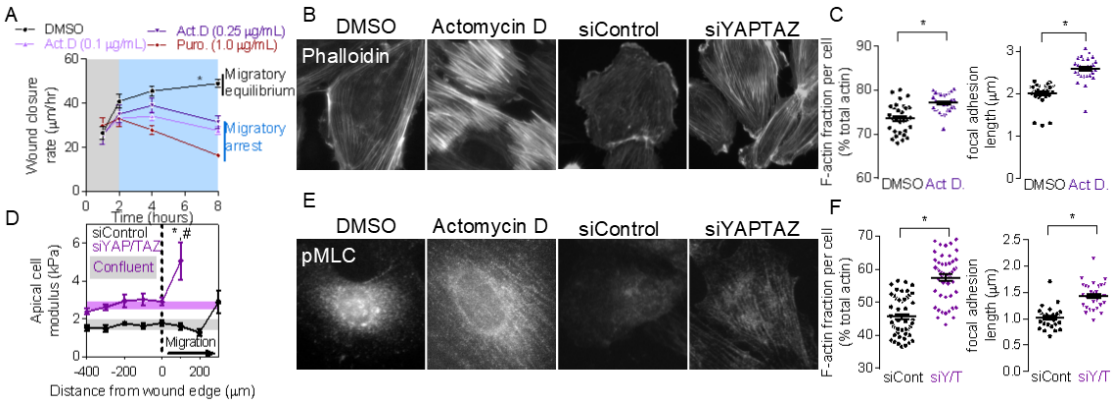

Fig. 1: **YAP and TAZ are molecular rheostats that mediate the transcriptional feedback control of cell motility mechanics**. (A) Wound closure rate in scratch migration assay. (B) Representative actin or (E) pMLC images. (C&F) Actin polymerization and focal adhesion length. (D) Cell stiffness as a function of distance from the leading edge of a migrating monolayer.

Discussion: Together, these data demonstrate that the pre-existing structural components of cellular motile machinery (actin, vinculin, myosin, etc.) are sufficient to build cytoskeletal tension in response to extracellular mechanical cues, but YAP/TAZ-mediated transcriptional feedback is required to modulate cytoskeletal tension and to permit persistent migration.

Plasminogen is Critical for Bone Fracture Repair by Promoting the Functions of Mesenchymal Progenitors

Luqiang Wang, Zhenqiang He, Duan Hao, Richard Mitteer, Yanqing Gong, Ling Qin

Plasminogen (Plg) is an inactive proenzyme that can be converted to the active serine protease plasmin for blood clot dissolution and plays a pivotal role in many physiological and pathological processes, such as embryogenesis, wound healing, fibrosis, tumor etc. To understand its function in bone regeneration, we compared the fracture healing process of Plg KO mice with their WT siblings and investigated the action of Plg on mesenchymal progenitors. MicroCT analysis revealed that Plg deficiency in 2-month old female mice causes 39%, 20%, 17%, and 15% decreases in tibial trabecular BV/TV, trabecular number, cortical area, and cortical thickness, respectively, and a 28% increase in trabecular separation (n=5/group). After a closed, transverse fracture on the tibial midshaft, Plg KO mice displayed drastically delayed fracture healing. In WT mice, callus formation normally peaks at 10 days and fracture site bridges at day 28. However, KO fractures displayed 66% and 57% decreases in callus volume and bone volume, respectively, and unchanged bone volume fraction compared to WT at day 7 post fracture (n=6 mice/group) and similar levels of decreases in callus and bone volumes at day 10 and 14 (n=6 mice/group/time point). KO fractures eventually reached a peak at 28 days but remained non-union at day 42. Histology showed that KO mice have 71% less cartilage formation at the early stage of healing, suggesting that Plg is required for the injury response of periosteal mesenchymal progenitors. In vitro, we found that 20 μg/ml Plg significantly increases the proliferation of periosteal mesenchymal progenitors by 1.5 fold and inhibits their cell death induced by ischemic condition (anoxia with low glucose). Plg also stimulated progenitor migration by activating MMP9 as shown by zymography analysis. To confirm the actions of Plg on mesenchymal progenitors in vivo, we injected Tomato+ WT mesenchymal progenitors into mice with hindlimb ischemia. Bioluminescence imaging showed that those cells were much less likely to survive and migrate at the injury site in Plg KO mice compared to those in WT mice. Taken together, we demonstrated a critical function of Plg in regulating mesenchymal progenitor proliferation, migration, and survival during the initiation stage of fracture healing. Our study also points out that drugs activating Plg might represent a novel direction for treating fracture non-union.

Development of an Extracellular Matrix-based Nanofibrous Scaffold for Meniscus Regeneration

Boao Xia[1], Dong-Hwa Kim[1], Robert L. Mauck[1], Su-Jin Heo[1]
[1]University of Pennsylvania, Philadelphia, PA

INTRODUCTION: The menisci are fibrocartilaginous tissues that stabilize and transfer load in the knee joint. Given their central function, menisci are commonly damaged, but have a limited self-healing capacity [**1**]. A number of extracellular matrix (ECM) based-tissue engineering approaches have been investigated to repair meniscus damage. For instance, Menaflex, a collagen-glycosaminoglycan (GAG) meniscus implant, enhances meniscus-like matrix production due to its similarity in composition to the native meniscus ECM [**2**]. Electrospun nanofibrous scaffolds have also been used to mimic the structure of the meniscus ECM [**3**]. Here, we investigated the combination of these two strategies by incorporating decellularized bovine meniscus ECM (MenECM) as a biomimetic component of a composite nanofibrous scaffold, and determined whether such a scaffold could support meniscus cell adhesion.

METHODS: *Tissue decellularization*: To avoid immune response, cell content in the tissues has to be removed. To this end, juvenile bovine meniscus was harvested, diced into cubes of approximately 1 mm^3, stirred in 1% SDS/PBS solution for 72 h (refreshed every 24 h), and then washed in 0.1% EDTA/PBS for 24 h, rinsed in DI water for 12 h, lyophilized for 72 h, and ground into powder (**Fig. 1A**) [**4**]. *Histology*: Cell removal was verified by counting nuclei after DAPI and hematoxylin & eosin staining. After decellularization, preservation of collagen and GAG content was visualized via picrosirius red and alcian blue staining, respectively. *Electrospinning solutions*: A 28% MenECM/PCL (50:50) mixture was prepared by stirring 1.4g of MenECM powder in 10mL of diluted acidic solution (Acetic Acid : Ethyl Acetate : DI Water = 3 : 2 : 1) at 50°C for 5 days. Next, 1.4g of PCL was added and stirred at 50°C continued for another 2 days [**5**]. *Scaffold fabrication*: Scaffolds were produced via electrospinning at a voltage of 15 kV, needle-to-collector distance of 14 cm, and flow rate of 2 mL/h, with fibers collected onto a grounded target. Scaffolds were crosslinked in 200 mM EDC with 200 mM NHS ethanol solution for 8 h, rinsed in DI, immersed in 100mM sodium phosphate aqueous solution for 3 h, rinsed again, and air dried. [**6**]. *SEM*: Surface morphology of the scaffold pre- and post-crosslinking was examined by SEM, and fiber thickness measured using BoneJ in FIJI [**7**]. PCL nanofibers served as a control. *Cell adhesion*: P2 juvenile meniscus cells were seeded onto 3 different scaffold types: (1) crosslinked composite MenECM/PCL nanofiber-coated glass slides (MenECM/PCL), (2) 20% PCL nanofiber-coated glass slides (PCL) and (3) non-coated glass slides (No fiber) for 1, 3, and 6 h, followed by fixation. Cells were visualized by actin staining, and cell area was quantified using ImageJ. (**Fig. 3A, 3B)** *Statistics*: Statistical analysis was performed using ANOVA (with Tukey's post hoc) or by Student's t-test ($p < 0.05$).

RESULTS: DAPI staining showed that cells were effectively removed from the tissue with the decellularization process, with only 0.5% of the nuclei remaining (**Fig. 1B, DAPI**). This was confirmed by H&E staining (**Fig. 1B, H&E**). Collagen content was preserved during decellularization, with the intensity of picrosirius red staining remaining similar. Conversely, the decrease in alcian blue staining indicated a loss of proteoglycan content with decellularization (**Fig. 1C**). When MenECM was spun, uncrosslinked scaffolds dissolved immediately when immersed in DI water, whereas EDC/NHS crosslinked scaffolds remained intact during rinsing and air drying. The crosslinking process also successfully preserved the fibrous morphology of the composite scaffold (**Fig. 2C, D**). PCL scaffolds electrospun from a 20% solution were closest across the group (16%, 20%, 24%) in terms of fiber thickness and morphology to the composite scaffold, and thus this formulation was selected for evaluating cell adhesion (**Fig. 2A, B**). *Cell adhesion*: The thickness of fibers spun onto glass slides was similar between the MenECM/PCL and PCL groups (**Fig. 3A**, $p < 0.05$). Cell area doubled for both the MenECM composite and PCL groups from 1 h to 3 h of incubation (**Fig. 3B, C**), indicating progressive interactions with the fiber substrate. However, cell area for the MenECM composite fiber group was more than double that of cells on PCL alone (and was comparable to cells on charged glass) for longer incubation times (3h and 6h, **Fig. 3B, C**).

DISCUSSION: In this study, we developed a process to fabricate a composite MenECM/PCL nanofibrous scaffold for meniscus regeneration using the meniscus matrix as a component of the polymeric fibers. Adhesion assays showed that this native bioactive content (i.e. MenECM) promoted meniscus cell adhesion, potentially through changing the hydrophilicity of the fibers or by making available adhesion motifs from the native ECM microenvironment for meniscus cell attachment. Ongoing studies are exploring the reinforcement of this scaffold via the addition of microfibers, to mimic the thick fibers present in the meniscus, and to increase the mechanical strength of the hydrated scaffold. Additional studies will evaluate how the presence of MenECM in the composite scaffold alters meniscus cell activity and phenotype to promote tissue formation and regeneration, both in long term *in vitro* culture and *in vivo*.

SIGNIFICANCE: This study developed a method to fabricate composite nanofibrous scaffolds containing MenECM and PCL in individual fibers. These scaffolds showed better meniscus cell adhesion than the PCL-only scaffolds. This novel combination of bioactive content with advanced scaffold fabrication techniques may generate material frameworks that can optimally promote meniscus tissue formation and regeneration.

REFERENCES: [1] Fox+ 2012 Sports Health [2] Bulgheroni+ 2016 Cartilage [3] Coburn+ 2012 PNAS [4] Wu+ 2015 Acta Biomaterialia [5] Binulal+ 2013 J Biomaterial Sci [6] Caruso+ 2005 J Biomed Mater Res A [7] Doube+ 2010 Bone.

ACKNOWLEDGEMENTS: This work was supported by the National Institutes of Health (R01 AR056624).

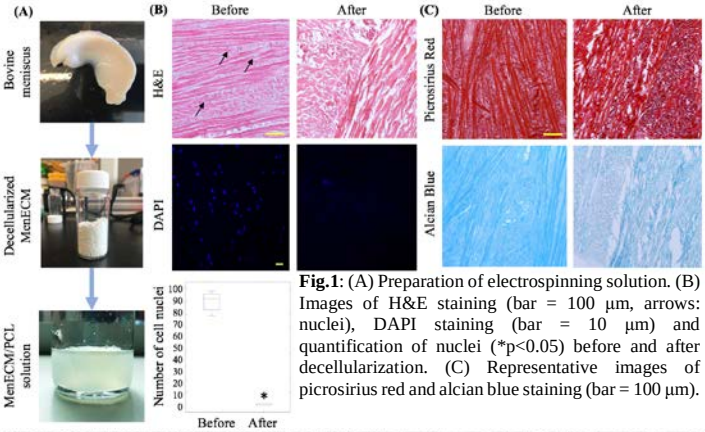

Fig.1: (A) Preparation of electrospinning solution. (B) Images of H&E staining (bar = 100 μm, arrows: nuclei), DAPI staining (bar = 10 μm) and quantification of nuclei (*p<0.05) before and after decellularization. (C) Representative images of picrosirius red and alcian blue staining (bar = 100 μm).

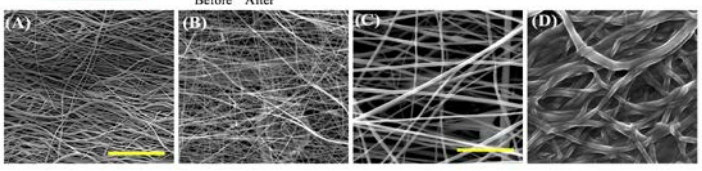

Fig.2: SEM of (A) 20% PCL and (B) 28% MenECM/PCL scaffolds (bar: 25μm). MenECM/PCL scaffold (C) pre- and (D) post-crosslinking (bar: 5μm).

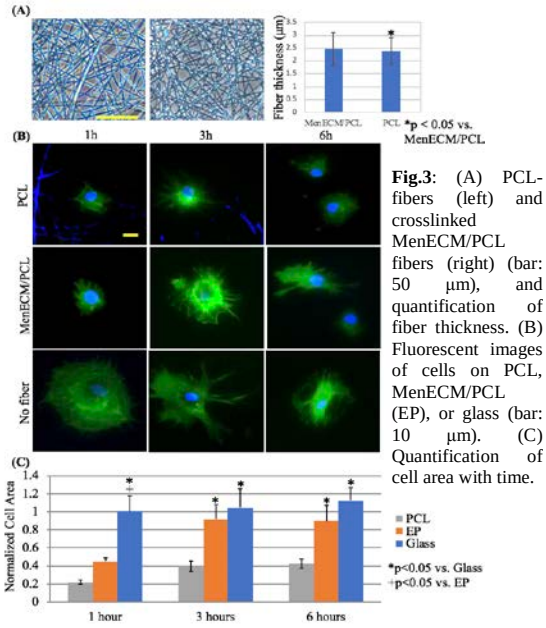

Fig.3: (A) PCL-fibers (left) and crosslinked MenECM/PCL fibers (right) (bar: 50 μm), and quantification of fiber thickness. (B) Fluorescent images of cells on PCL, MenECM/PCL (EP), or glass (bar: 10 μm). (C) Quantification of cell area with time.

$p16^{Ink4a}$ deletion in cells of the intervertebral disc affects their secretory phenotype without altering onset of senescence

Emanuel-Jose M. Novais, Brian O. Diekman, Irving M. Shapiro, Makarand V. Risbud

Abstract

Intervertebral disc degeneration is an important contributor to chronic low back and neck pain. Although many environmental and genetic factors are known to contribute to disc degeneration, age is still the most significant risk factor. Recent studies have shown that senescence may play a role in age-related disc degeneration in humans and mouse models. Clearance of $p16^{Ink4a}$-positive senescent cells reduces the degenerative phenotype in many age-associated diseases. Whether $p16^{Ink4a}$ plays a functional role in intervertebral disc degeneration and senescence is unknown. We characterized the senescence status of discs in young and old mice. Quantitative histology, gene expression and $p16^{tdTom}$ reporter mice showed an increase in $p16^{Ink4a}$, p21 and IL-6, with a decrease in Ki67. Accordingly, we studied the spinal-phenotype of 18-month-old mice with conditional deletion of $p16^{Ink4a}$ in the disc as driven by Acan-CreERT2 (cKO). The analyses of discs of cKO and control mice showed little change in cell morphology, tissue architecture, and overall collagen content. While cKO discs exhibited a small decrease in TUNEL positive cells, lineage tracing experiments using ZsGreen reporter indicated that the changes in cell fate or numbers were minimal. The cKO mice maintained expression of NP-cell phenotypic markers CA3, Krt19 and GLUT-1 along with Col-I and Col-II. Interestingly, in cKO discs there was a decrease in chondroitin sulfate levels and aggrecan turnover. Moreover, in cKO discs, levels of $p19^{Arf}$ and RB were elevated without alterations in Ki67, □H2AX, CDK4 and Lipofuscin deposition. In addition, the cKO discs showed lower levels of SASP markers, IL-1□, IL-6, MCP1 and TGF-□1. These results show that while, $p16^{Ink4a}$ is dispensable for induction and maintenance of senescence, $p16^{Ink4a}$ expression increases with age and conditional loss of $p16^{Ink4a}$ reduces apoptosis and limits the SASP phenotype of disc cells.

Mechanisms Regulating Articular Cartilage Growth and Morphogenesis

Danielle Rux[1], Kimberly Helbig[1], Eiki Koyama[1], Maurizio Pacifici[1]

[1]*Translational Research Program in Pediatric Orthopaedics, Children's Hospital of Philadelphia*

Synovial joints are essential for skeletal function and body movement. Unfortunately, joints - chiefly articular cartilage (AC)- are highly susceptible to congenital- and age-related diseases and exhibit poor repair capacity that current clinical strategies fall short of amending. To improve these strategies, more information is needed on mechanisms of AC development. AC acquires its mature, multizone functional organization postnatally, and consists of: flat, lubricant-producing surface zone cells; round, column-aligned intermediate zone cells that resist loads; and mineralized, deep zone cells that attach to bone. Little is known about mechanisms that drive this specific organization. Recent work from our lab tackled these central issues using genetic lineage-tracing tools in mice. Data showed that while cell proliferation plays a minimal role, cell translocation and realignment may be major drivers of tissue morphogenesis. To explore mechanisms, we ask here if primary cilia regulate this process. These mechanical- and morphogen-sensing cell surface organelles are crucial in morphogenesis of many mammalian tissues; studies show their involvement in chondrocytes contributing to skeletal elongation, however their roles in AC were unknown. We used a conditional loss-of-function approach (*Ift88-flox*) targeting joint-lineage progenitor cells (*Gdf5-Cre*) and monitored structural and functional consequences on AC growth. My current findings show that mutant tissue exhibits a drastic drop in proteoglycan levels essential for tissue resilience, and lack of columnar organization of intermediate zone cells with negative consequences on overall tissue organization. Ongoing studies aim to investigate mechanical and morphogenetic mechanisms accounting for these phenotypic effects.

A Novel Role for *Hox11* Genes During Postnatal Joint Morphogenesis

Kimberly Helbig, Danielle Rux, Maurizio Pacifici

Translational Research Program in Pediatric Orthopaedics, Children's Hospital of Philadelphia

Synovial joints are essential for body movement and function, yet are highly susceptible to injury- and age-related diseases for which current treatments fall short of ameliorating. In order to improve upon these treatments, more information on the developmental processes involved in joint morphogenesis is required. In our previous work, we showed that *Hox11* genes are essential for proper knee joint patterning during embryonic development. In this study, we expand upon these studies and report preliminary data that support a role for these *Hox* genes during postnatal joint morphogenesis. The *Hox* genes are critical transcriptional regulators of embryonic skeletal development and loss of function mutations of an entire paralogous group (*Hox1-13*) leads to regionally restricted malformations of the axial skeleton and the limbs. Specifically, complete loss of *Hox11* function results in severe patterning defects of the sacrum and of the limb zeugopod (tibia/fibula, radius/ulna). Interestingly, recent work also shows that the *Hox11* genes continue to function in postnatal/adult skeletal development/repair processes. To study the expression of *Hox11* genes during postnatal synovial joint morphogenesis, we used a *Hoxa11eGFP* knock-in allele and find that *Hox11* is expressed through critical stages of postnatal knee development to include the articular cartilage, meniscus, and synovium. Expression decreases after the joint is fully developed by about 4 weeks of age, but is maintained at lower levels in the adult. In order to understand a possible function for these genes, we analyzed a rare, viable 4-allele *Hox11* mutant (11aaCCdd). This animal displayed severe kidney and forelimb defects, but was able ambulate normally. Importantly, the hind limbs of this animal were shortened, but did not display the major patterning defects of the 6-allele mutant (11aaccdd) we described in our previous work. We examined the knee joint at 6 weeks of age and found that the articular cartilage showed no obvious morphological differences compared to controls, however meniscal chondrocytes failed to mature and the meniscus lacked ossification. In addition, the surrounding synovium displayed extensive hyper plasticity. Taken together, these preliminary findings suggest that *Hox11* genes continue to function during postnatal development of the knee joint. In our continued work we will collect additional compound mutants to observe penetrance of these described phenotypes and we will investigate the developmental mechanisms that require Hox11 function during synovial joint morphogenesis.

YAP and TAZ regulate the formation of the primary ossification center in embryonic limbs

Joseph M. Collins[1], Xi Jiang[1], Tonia Tsinman[1], Nathaniel Dyment[1] Joel D. Boerckel[1],
[1]University of Pennsylvania, Philadelphia, PA.
jmcollin@seas.upenn.edu

Disclosures: Joseph M. Collins (N), Xi Jiang (N), Tonia Tsinman (N), Nathaniel Dyment (N), Joel D. Boerckel (N)

INTRODUCTION: A critical step in endochondral ossification is the invasion of osterix-expressing osteoprogenitors from the surrounding bone collar into the hypertrophic zone (HZ), to establish the primary ossification center (POC)[1]. Despite its importance, a mechanistic understanding of osteoprogenitor mobilization in the embryonic limb remains unclear. We recently demonstrated that combinatorial deletion of yes-associated protein (YAP) and transcriptional coactivator with PDZ-binding motif (TAZ) in osterix+ osteoprogenitor cells resulted in perinatal lethality and bone fragility, and phenocopied human osteogenesis imperfecta[2]. While these data showed that YAP and TAZ play critical roles in skeletal development, the initiating cellular mechanisms that give rise to this phenotype are unknown. Here, we evaluated developing long bones in staged embryos, at the time points when osteoprogenitors first give rise to skeletal elements. First, to characterize the embryonic stages of the developing POC, we use Collagen-I/II/X triple transgenic fluorescent reporter mice to spatiotemporally characterize cell lineage progression in the developing limb. Second, we test the hypothesis that conditional ablation of YAP and TAZ in osterix-expressing osteoprogenitors would restrict primary ossification in embryonic long bones.

METHODS: We used two mouse models. First, a triple transgenic fluorescent reporter model which co-expresses fluorescent proteins under the control of promoters for three collagen genes: Collagen II, marked by CFP (Col2-CFP); Collagen X, by mCherry (ColX-mCherry); and the 3.6kb fragment of the Collagen1a1 promoter, by YPF (Col1-YFP). The Col1-YFP is expressed in both osteoprogenitor cells and committed osteoblasts[3]. Second, we generated embryos from a conditional loss-of-function mouse model with dual deletion of YAP and TAZ through cre-recombination under the control of the osterix1-promoter[4]. All procedures were performed under approved IACUC protocols. We used a breeding strategy that produced dual homozygous knockouts ($YAP^{fl/fl}$; $TAZ^{fl/fl}$; Osx1:EGFP-Cre, hereafter $cDKO^{osx}$) and littermate wild-type controls ($YAP^{fl/fl}$; $TAZ^{fl/fl}$, hereafter WT). Timed pregnant females were euthanized and embryos harvested at 15.5 days (E15.5) and 17.5 days (E17.5) post-conception. Embryonic hindlimbs (from the $YAP^{fl/fl}$;$TAZ^{fl/fl}$ model) or forelimbs (from the fluorescent reporter model) were processed by cryohistology, as previously described[5]. Sections were immunostained for anti-GFP, Phalloidin, anti-Collagen X and/or DAPI. Regions of interest were determined by tissue morphology and informed by endogenous fluorescent reporters. Image analysis was conducted in ImageJ. Cell number was determined from DAPI-labeled nuclei. Comparisons were made with one-way ANOVA and Tukey's HSD. A p-value of less than 0.05 was considered significant. Each limb was considered an independent sample.

RESULTS: Initiation of primary ossification at E15.5 coincided with a F-actin rich region at the center of the developing bone (Fig. 1). At E15.5 WT femurs displayed a robust primary ossification center, determined by F-actin intensity and tissue morphology (Fig 2A-B, red arrow). Primary ossification was delayed in $cDKO^{osx}$, with persistent hypertrophic chondrocytes, and a continuous ColX-positive hypertrophic zone (Fig. 2C-E). Despite failure of POC formation in $cDKO^{osx}$ limbs at E15.5, the distance between zones of proliferating cartilage (i.e., sum of POC+HZ length) was equivalent between WT and $cDKO^{osx}$ limbs (Fig. 3A-C). By E17.5, a POC emerged in $cDKO^{osx}$ femurs (Fig. 3B), but exhibited significantly decreased cell density and axial length compared to WT (Fig. 3A-E). Like E15.5, the distance between proliferating zones remained consistent (Fig. 3C). GFP localized to the HZ, bone collar, and the POC, indicating cre-expression/recombination in these regions of interest, in the $cDKO^{osx}$ group (Fig 2D). Unlike the POC region of interest, there were no detectable differences in morphology or cell density in the bone collar (data not shown).

DISCUSSION: Together, these data demonstrated a critical role for YAP and TAZ in osteoprogenitor cell-mediated embryonic primary ossification. Since the distance between the proximal and distal proliferating zones was consistent between groups at E15.5 and E17.5, the intermediate tissue was persistent hypertrophic chondrocytes embedded in ColX matrix, and we did not observe significant defects in the bone collar, we conclude that the role of YAP/TAZ in the osterix-positive cells of the developing limb was isolated to POC formation. Further, since primary ossification was delayed, and characterized by substantially decreased cell density, in $cDKO^{osx}$, these data suggest that YAP and TAZ play a critical role in osteoprogenitor recruitment and/or mobilization into the primary ossification center during embryonic bone development.

SIGNIFICANCE: A mechanistic understanding of how YAP and TAZ regulate osteoprogenitor behavior during embryonic bone development could yield new insights into developmental bone diseases such as osteogenesis imperfecta and may instruct future therapeutic strategies.

REFERENCES:[1] Maes+ Dev. Cell, 2010; [2] Kegelman+ FASEB J, 2018; [3] Kalajzic+ JBMR 2002 [4] Rodda+ Development, 2006; [5] Dyment+ JOVE, 2016.

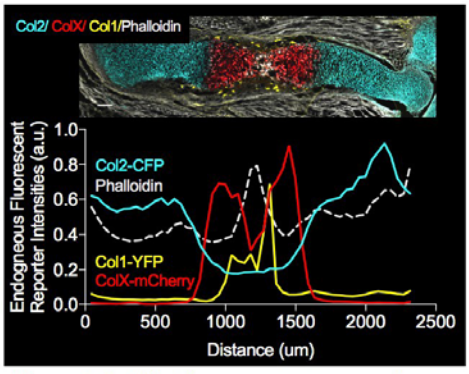

Figure 1. Relative fluorescent reporter and Phalloidin intensity along the longitudinal axis of the humerus (n=2).

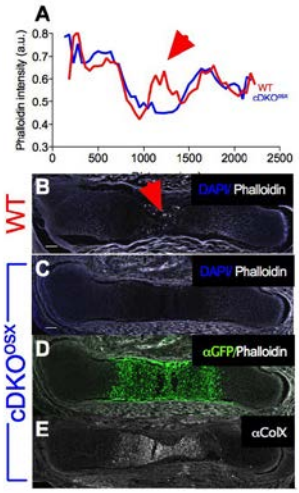

Figure 2 (left). **(A)** Axial Phalloidin intensity in E15.5 WT and $cDKO^{osx}$ femurs (n=2-3). **(B)** Representative 7um femoral section of E15.5 WT. **(C-E)**, Representative immunostained femoral sections of E15.5 $cDKO^{osx}$. Scale bar is 100μm

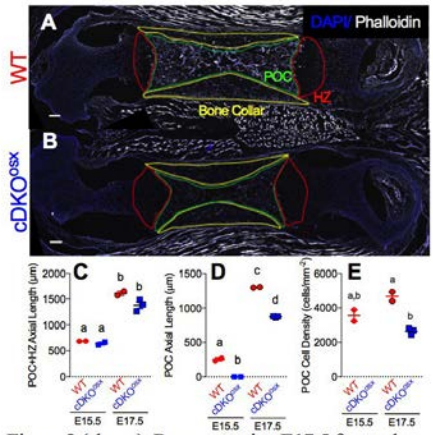

Figure 3 (above). Representative E17.5 femoral sections of **(A)** WT and **(B)** $cDKO^{osx}$ with defined ROIs. **(C, D)** total longitudinal distance of the (C) POC and HZ and (D) POC **(E)** Cell density of the primary ossification center. Scale Bar is 100μm.

Temporal evolution of cell phenotype and biophysical cues in the developing murine meniscus microenvironment

Tonia K. Tsinman[1], Chao Wang[2], Xi Jiang[1], Eiki Koyama[3], Lin Han[2], Robert L. Mauck[1], Nathaniel A. Dyment[1]
[1]McKay Orthopaedic Research Laboratory, University of Pennsylvania, Philadelphia, PA.[2]Nanobiomechanics Laboratory, Drexel University, Philadelphia, PA. [3]Children's Hospital of Philadelphia, Philadelphia, PA.

Disclosures: RL Mauck (8, *JOR Spine*), no other disclosures.

INTRODUCTION: The molecular composition and organization of the extracellular matrix (ECM) is essential for the load bearing function of the knee meniscus, and current treatments do not restore function after injury. Recent work in transgenic mice has better defined the molecular pathways important for meniscus formation during joint development in order to inform new regenerative strategies [1-3]. However, the mechanism by which interzone (meniscus precursor) cells assemble and ultimately generate a semi-lunar, fibrous, and mechanically viable tissue remains unclear. Additionally, how biophysical cues (stiffness, organization) from the evolving joint microenvironment impact cell phenotype and function have not yet been explored. We recently used a Col-1/Col-2/Col-10 transgenic reporter mouse to define the spatiotemporal changes in cellular expression of critical collagen types during meniscus postnatal maturation [4,5]. Here, we extend this analysis to include embryonic time points at key junctures of joint formation, and track concurrent changes in cellular phenotype and cyto-architecture, along with micro-mechanical properties of the evolving meniscus microenvironment.

METHODS: Mouse model: The study used triple transgenic reporter mice with promoters for Col1a1, Col2a1, and Col10a1 genes driving CFP, YFP, and mCherry reporter protein expression, respectively [4]. Animal use was approved by the UPenn IACUC. Sample preparation and staining: For immunofluorescence (IF) and reporter expression, E13.5, E15.5, E17.5, and P0 mouse knee tissues (n=3/timepoint) were harvested, fixed, cryo-embedded, and sectioned (7μm) in the sagittal, coronal and/or transverse planes through the interzone/meniscus [5]. For AFM, E15.5, P7, and P21 knees were cryo-embedded (without fixation) immediately post sacrifice and sectioned (30μm) in the coronal plane. Imaging: For IF, sections were digested with Proteinase K (1min) and incubated with antibody overnight. Lamin A/C (ab133256), actin (Phalloidin), and nuclei (DAPI) were visualized using confocal microscopy. Lamin A/C fluorescence intensity as a function of nuclear position was quantified using Fiji (n=10 nuclei/age). Col-1/Col-2 reporter expression was imaged as in [5]. To visualize fiber deposition, second harmonic generation (SHG) imaging of 7μm sections was performed at 20X using a multiphoton microscope. Nano-mechanical properties: Sections were thawed in PBS and immediately probed by AFM with a spherical indenter (R~5μm, *k*~0.1N/m, 30 points/animal, n=3 animals/age group). Data were analyzed using a custom written MATLAB script. One-way ANOVA with Tukey's post-hoc was used to determine differences between groups ($p<0.05$).

RESULTS: Col-2 reporter expression was lower in the interzone (IZ: E13.5, E15.5) and nascent meniscus (E17.5) compared to the neocartilage (NC), consistent with previous reports [2]. Col-1 reporter became detectable in the nascent meniscus by E17.5 (**Fig. 1, left**). Cells within the NC and IZ had a similar cytoskeletal organization at E13.5, but by E15.5, IZ cells had established a highly aligned actin cyto-architecture (compared to cortical actin in cells of the NC) (**Fig. 1, right**). E15.5 IZ cells also had established a meniscus-like circumferential alignment, though SHG imaging showed no detectable fibrous matrix deposition (**Fig. 2a**). By E17.5, along with sustained cellular organization in the nascent meniscus, collagen fibril deposition could be detected in the direction of cell alignment, consistent with the observed increase in Col-1 reporter expression. At P0, robust aligned collagen deposition was observed (**Fig. 2a**). In concurrence, AFM measurements showed a significant increase in tissue stiffness during postnatal growth (8±3 kPa at E15.5 compared to 47±9 kPa and 200±51 kPa at P7 and P21, respectively, **Fig. 2b**). Finally, the diffuse Lamin A/C observed at E13.5 became progressively enriched at the nuclear periphery at later time points (**Fig. 3**).

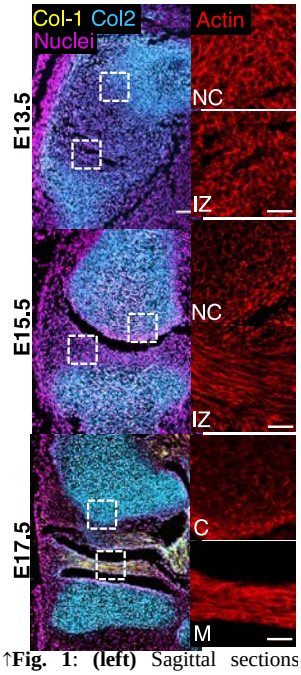

↑**Fig. 1**: **(left)** Sagittal sections showing Col-1/Col-2 reporter expression at E13.5, E15.5, and E17.5. **(right)** Actin staining within indicated boxed regions. NC: neocartilage; IZ: interzone; C: cartilage; M: meniscus. SB: 20μm.

DISCUSSION: This study demonstrates that circumferential organization of interzone cells *precedes* joint cavitation/meniscus formation and Col-1 expression. The distinct organization of these meniscus precursors may provide a template for the subsequent deposition of Col-1 and other ECM components during the rapid post-natal tissue growth that follows [6]. Our findings also support the concept of an evolving cellular microenvironment during tissue formation and maturation, characterized by organized fibrous matrix deposition and tissue stiffening. These time-varying biophysical cues are reflected in the cyto-architecture of meniscus precursors, with the development of a highly organized actin cytoskeleton and enrichment of Lamin A/C at the nuclear envelope during tissue maturation. Given published data showing that mesenchymal stem cells increase contractility and nuclear Lamin A/C with increasing microenvironmental stiffness [7,8], our data on Lamin A/C (**Fig. 3**) additionally supports a role for mechano-adaptation of meniscus precursors during embryonic development, which may contribute to their adult fate and function.

SIGNIFICANCE: This work provides new insight into the process by which the critical component of the meniscus - its circumferentially aligned collagen network - is initially formed. Importantly, alterations in cellular contractility and nuclear architecture highlight mechanobiologic adaption in these precursors, suggesting a role for biophysical cues in developing microenvironment that may impact cell fate in conjunction with other molecular pathways.

REFERENCES: [1] Gamer+ 2017. [2] Hyde+ 2008. [3] Pazin+ 2012. [4] Dyment+ 2015. [5] Tsinman+ ORS 2018. [6] Hayes+ 2001. [7] Swift+ 2013. [8] Heo+ 2016.

ACKNOWLEDGEMENTS: This work was supported by the NIH (R01 EB002425 and R00 AR067283) and the NSF (CMMI: 15-48571).

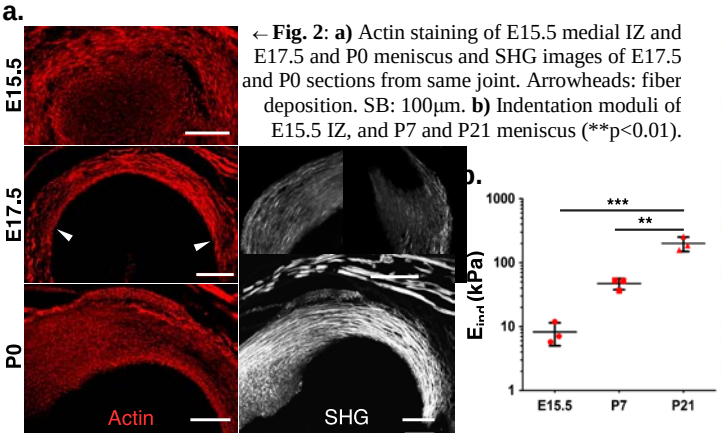

← **Fig. 2**: **a)** Actin staining of E15.5 medial IZ and E17.5 and P0 meniscus and SHG images of E17.5 and P0 sections from same joint. Arrowheads: fiber deposition. SB: 100μm. **b)** Indentation moduli of E15.5 IZ, and P7 and P21 meniscus (**p<0.01).

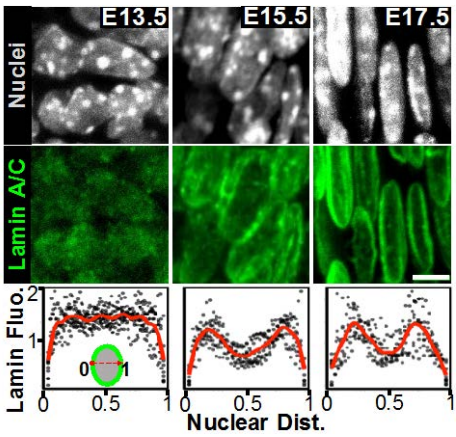

← **Fig. 3**: Top: Lamin A/C in nuclei of IZ cells (E13.5, E15.5) and meniscus cells (E17.5). SB: 5μm. Bottom: Nuclear Lamin A/C distribution (scaled to average intensity). Dots: values from n=10 nuclei/age. Red line: average value.

Inhibiting Hedgehog Signaling Leads to Reduced Chondrogenesis and Osteochondroma Formation: A Potential Therapy for HME

Juliet Chung[1], Christina Mundy[1], Till Bechtold[2], Eiki Koyama[1] and Maurizio Pacifici[1]

[1] Translational Research Program in Pediatric Orthopaedics, Division of Orthopaedic Surgery, The Children's Hospital of Philadelphia, Philadelphia, Pennsylvania, [2] Department of Orthodontics and Orofacial Orthopedics, University Hospital Tuebingen, Tuebingen, Germany

Hereditary Multiple Exostoses (HME) is a pediatric skeletal disorder characterized by benign cartilaginous tumors called exostoses or osteochondromas (OC). They form along the perichondrial border of growth plates in several skeletal elements. The majority of cases are caused by loss of function mutations in the heparan sulfate (HS)-synthesizing enzymes EXT1 or EXT2, resulting in systemic HS deficiency. The HS chains are components of cell surface and extracellular matrix-associated proteoglycans (HSPGs). HSPGs interact with numerous HS- binding proteins, such as hedgehog proteins and regulate protein distribution, bioavailability and target of action. Our lab and others have shown that hedgehog signaling plays a prominent role in early chondrogenesis and skeletal development. Indeed, in the case of HME, a deficiency in HS in growth plates allows for broader distribution and distribution of indian hedgehog that could diffuse into the perichondrium, activate signaling in chondroprogenitor cells and result in OC formation. Given the findings from these studies, we asked whether the clinically relevant Hh antagonist – LDE225- could 1) block chondrogenesis in vitro and 2) reduce OC formation in vivo. LDE225 suppressed chondrogenesis as monitored by alcian blue positive cartilage nodule formation and gene expression of cartilage marker genes in our micromass cultures. More importantly, LDE225 effectively reduced OC formation in long bones, rib cartilage and cranial base in our conditional *Ext1*-mutant mice. Collectively, our data indicate that targeting the hedgehog signaling pathway could be an ideal therapeutic approach to treat patients with HME.

Biocompatibility and Bioactivity of an FGF-Loaded Microsphere-Based Bilayer Delivery System

Dong Hwa Kim[1,2], Julianne Huegel[1,2], Courtney Nuss[1,2], Stephanie Weiss[1,2], Louis J. Soslowsky[1,2], Robert L. Mauck[1,2], and Andrew F. Kuntz[1,2*]
[1]University of Pennsylvania, Philadelphia, PA, [2]Philadelphia VA Medical Center, Philadelphia, PA

Disclosures: DH Kim (N), J Huegel (N), C Nuss (N), S Weiss (N), LJ Soslowsky (N), RL Mauck (N), AF Kuntz (N)

INTRODUCTION: Biodegradable micro-particle systems have attracted increasing interest for use as delivery vehicles for drugs, proteins, and other factors [1-2]. Several new strategies have been developed to improve protein stability within such biodegradable polymer matrices [3]. For instance, sustained release of basic fibroblast growth factor (bFGF) from microspheres can promote proliferation and differentiation processes in a wide range of cells [4]. Albumin is commonly included in such formulations, both as a model protein to monitor release and as a carrier to preserve growth factor activity and prolong shelf-time [5]. In this study, we developed microspheres (MS) containing both Alexa-tagged BSA and bFGF and incorporated them into a Bilayer Delivery System (BiLDS) [6]. This system was designed to sequester MS in a defined pocket between two nanofibrous scaffolds, where the scaffold provides a template for new tissue formation while enabling independent and local release from the co-delivered MS. The objective of this study was to evaluate the biocompatibility and bioactivity of an FGF-loaded BiLDS system in vitro and in vivo.

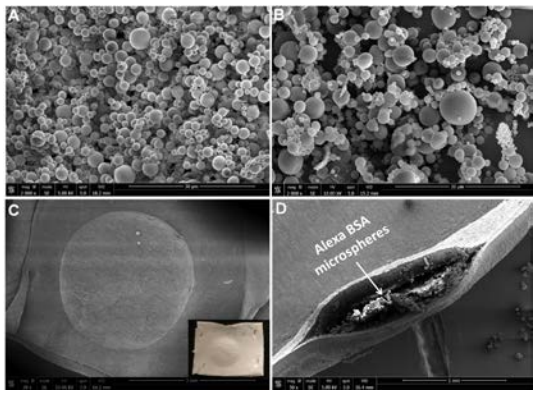

Figure 1. SEM of (A) Alexa-BSA and (B) Alexa-BSA/bFGF MS. (C) Top view and (D) cross-section showing MS within BiLDS (scale = 1mm).

METHODS: *Microsphere and BiLDS fabrication:* Microspheres were produced by combining 75:25 PLGA (0.15 g/mL, Mw=70 kDa) with/without 200 µg recombinant human bFGF and Alexa-BSA in dichloromethane. The external phase of the emulsion consisted of 5 mL of aqueous 1% poly(vinyl alcohol). To generate the bilayered delivery system (BiLDS), each MS formulation (Alexa-BSA MS and Alexa-BSA/bFGF MS) was suspended in 50 µl of PBS and placed onto the center of an aligned poly(ε-caprolactone) nanofibrous scaffold (6×8 mm) [6]. A second layer was placed on top and the two layers were sealed together by heat-annealing in a circular pattern around the microspheres using a custom heating device. *Direct/indirect tenocyte culture*: For direct culture, rat tenocytes (5000 cells/BiLDS) were seeded onto the BiLDS and cultured for 18 days in 1% FBS containing DMEM. For indirect culture, each BiLDS was incubated in basal media for 1 week at 37ºC. Tenocytes were seeded (3×10^3 cells/well) into a 24-well plate and the conditioned media from each BiLDS was added. At regular intervals, cell viability (via MTT assay, n=4-5) and MS and cell morphology (via actin staining and SEM, n=3) was evaluated. *BiLDS release in-vivo*: BiLDS containing no MS, Alexa-BSA-MS, and Alexa-BSA/bFGF-MS (n=4/group) were fabricated and implanted into the rat's dorsal subcutaneous space. At 1, 2, and 4 weeks, samples were recovered and fluorescence images were taken to identify MS within the BiLDS and frozen sections were processed for hematoxylin and eosin (H&E) staining. Statistical analysis was performed by 2-way ANOVA with Tukey's post-hoc test.

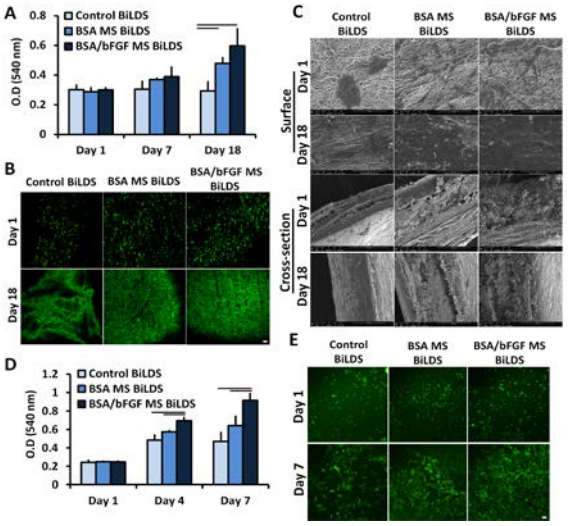

Figure 2. (A) Viability, (B) actin staining, and (C) SEM over 18 days with direct culture of tenocytes on BiLDS. (D) Viability and (E) actin staining over 7 days with indirect culture of tenocytes in media from BiLDS (Scale = 10 µm).

RESULTS: SEM images demonstrated that MS were spherical with a smooth surface. Alexa-BSA and Alexa-BSA/bFGF MS ranged in diameter from 1.5-3 µm and 1.5-4.5 µm, respectively (not shown) **(Fig. 1A, B)**. SEM images also showed a seal along the margin that effectively localized MS within the BiLDS **(Fig. 1C)** and cross-sectional views of the BiLDS showed large quantities of MS within the BiLDS **(Fig. 1D)**. In direct culture, cell viability and proliferation of Alexa-BSA and Alexa-BSA/bFGF BiLDS increased during culture and were significantly higher than control at day 18 **(Fig. 2A)**. Cells attached and spread along the BiLDS **(Fig. 2B)**. SEM images confirmed this finding, and cross-sectional views showed that MS remained entrapped after 18 days **(Fig. 2C)**. In indirect culture, after 4 and 7 days, proliferation in media from Alexa-BSA/bFGF BiLDS was higher than from no MS and Alexa-BSA BiLDS **(Fig. 2D, E)**. After implantation, fluorescent images showed that MS remained within the BiLDS **(Fig. 3A)** and H&E staining revealed increased cellularity at the periphery with greater infiltration into nanofiber layers of the Alexa-BSA/bFGF BiLDS **(Fig. 3B)**.

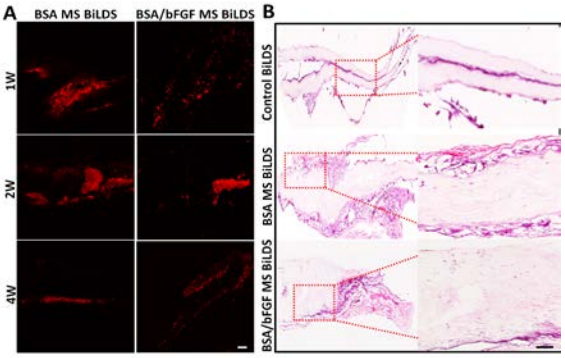

Figure 3. (A) Fluorescent images of Alexa tagged MS in BiLDS after implantation. (B) H&E staining after 4 weeks in vivo (scale = 200 µm).

DISCUSSION: In this study, we developed a bilayered delivery system to deliver bFGF in a local manner using a clinically relevant and previously validated scaffold system. We previously showed that MS entrapped within the BiLDS system showed a somewhat attenuated release profile compared to free MS, and that protein release was sustained and continuous for up to 30 days [6]. Importantly, our new data show that cell viability and proliferation were enhanced in the context of Alexa-BSA/bFGF BiLDS, both in vitro and in vivo. MS delivered via the BiLDS system persisted in a localized area after implantation for at least 4 weeks, and bFGF release increased colonization of the implant. These data establish the BiLDS technology as a sustained in vivo drug delivery platform that can localize protein and other growth factor release to a surgical site. In future studies, we will explore the ability of this BiLDS technology to deliver growth factors to promote repair in a small animal model of rotator cuff injury.

SIGNIFICANCE: This work establishes the biocompatibility and bioactivity of a MS-loaded bilayered delivery system (BiLDS) for sustained release in a localized and clinically relevant fashion for tissue repair and regeneration.

REFERENCES: [1] Rafati+, 2012 J Control Release. [2] Ambrosch+, 2012 Acta Biomater. [3] Emma+, 2007 Biomaterials. [4] Rouch+, 2016 J Pediatr Surg. [5] Kratz+, 2008 J Control Release. [6] Kim+, 2017 ORS Proceedings.

ACKNOWLEDGEMENTS: This work was supported by the Department of Veterans' Affairs (O0979-R and RX001764) and the Penn Center for Musculoskeletal Disorders (P30 AR050950).

Engineering the Microenvironment of the Damaged Cartilage Interface to Direct Stem Cell Localization and Mechano-Response

Jay M. Patel[1,2], Claudia Loebel[1], Hannah M. Zlotnick[1,2], Kamiel S. Saleh[1], Liane M. Miller[1], James L. Carey[1], Jason A. Burdick[1], Robert L. Mauck[1,2]
[1]University of Pennsylvania, Philadelphia, PA, [2]Corporal Michael J Crescenz VA Medical Center, Philadelphia, PA.
Disclosures: RL Mauck (8, JOR Spine)

Introduction: Cartilage injuries are common, and while current surgical treatments provide short-term symptomatic relief, defects often progress to joint-wide degeneration. Intra-articular mesenchymal stem cell (MSC) injections have become an increasingly common treatment, with some data suggesting improved outcomes [1]. However, injection into the synovial space does not localize MSCs to the injury site [2], limiting the efficacy and consistency of outcomes. Moreover, the fate and function of these cells is not controlled post-injection, further limiting their regenerative potential. To address this, we developed a tunable biomaterial designed to attract and retain MSCs at the damaged cartilage interface and regulate their subsequent activities in order to enhance cartilage repair. The purpose of this study was to: 1) establish the ability of the biomaterial to bind and form an integrated microenvironment at the damaged cartilage interface *in vitro*, 2) determine the mechano-biological response of MSCs attaching to the modified tissue-biomaterial composite, and 3) translate the biomaterial in a proof-of-concept large animal model and evaluate its implementation and retention.

Methods: Biomaterial Synthesis and Attachment: Methacrylated hyaluronic acid (MeHA; 75kDa, ~35% modification) was conjugated with fluorescent (FITC) and cell-adhesive (RGD) peptides. The material was oxidized with sodium periodate to modify adjacent hydroxyl groups into aldehydes (~30% substitution), chemical groups that can form covalent linkages with exposed amines in damaged tissue [3]. To investigate biomaterial attachment to native tissue, the superficial zone was removed from 5mm-diameter cylindrical cartilage plugs (juvenile bovine femoral condyle) to expose "damaged" cartilage. These plugs were then sectioned into 100µm thick discs. The material was applied, discs were rinsed in PBS, and fluorescence was quantified (n=4). Material attachment and diffusion into the tissue was evaluated as a function of application time (5, 10, 30 minutes) by confocal microscopy.

MSC Mechano-response: Additional 100µm cartilage discs were used to study stem cell attachment and mechano-response. Samples were maintained as naïve samples or were digested in collagenase (0.01% for 30 minutes) to mimic degenerated cartilage. Biomaterial was applied with 5 or 15 minutes of UV cross-linking, followed by PBS washes to remove non-adhered biomaterial. Cartilage discs (both non-degraded and degraded) without biomaterial served as controls. Cartilage discs were seeded with juvenile bovine MSCs (P2-P3, 500 cells per disc) for 24 hours. Samples were fixed in 10% buffered formalin, followed by staining for F-actin with phalloidin (to quantify cellular spread area) and for the nuclear co-factors YAP/TAZ (to quantify cell mechano-response) [4]. YAP/TAZ signal intensity in the nucleus and cytoplasm were quantified in Fiji to obtain a measure of nuclear localization.

Large-Animal Study: As a pilot study, one juvenile Yucatan minipig (~6 months old, 30kg) was used to test the implementation and retention of the biomaterial. Through a medial patellar arthrotomy in each hind limb, four partial-thickness trochlear groove defects were created with a surgical curette (**Fig 3A-B**) [5]. Biomaterial was applied to three of the defects (one empty defect served as control), and cross-linked for either 0, 5, or 15 minutes with UV light (**Fig 3C**). Defects were visualized with a fluorescent dissecting microscope, and processed for histology.

Results: *In vitro*, the biomaterial showed preferential attachment to defected cartilage compared to the intact superficial cartilage surface (**Fig 1A**). Material attachment increased with duration of application (**Fig 1B**), with 30-minute application showing ~50% greater fluorescence intensity than 10-minute application. Confocal microscopy showed that the biomaterial infiltrated ~30-50µm into the tissue prior to cross-linking, forming an integrated microenvironment at the defect edge, around and in between chondrocytes in the cartilage matrix (**Fig 1C**). The biomaterial also promoted MSC adhesion (**Fig 1C, Fig 2A**) to the tissue-biomaterial interface, increasing cell area (**Fig 2B**) and adhesion. Biomaterial application and cross-linking increased YAP/TAZ nuclear localization (**Fig 2C**) of MSCs on both non-degraded and degraded cartilage, consistent with the increased MSC spread area (**Fig 2B**) and substrate mechanical properties (**Fig 2D**, assessed by AFM) with biomaterial augmentation. Finally, in the 1-week pilot animal study, biomaterial was retained in 3 of 4 defects that were cross-linked (**Fig 3D**). Time of cross-linking did appear to influence retention of the biomaterial.

Discussion: The results of this study detail the development of a modified biomaterial that 1) attaches and forms an integrated microenvironment at the damaged cartilage interface, 2) controls initial cellular mechano-response based on the extent of cross-linking, and 3) is retained in a large-animal load bearing cartilage defect model. These findings support the promise of creating tunable microenvironments to home and retain stem cells at the defect interface, and ultimately control their biologic response.

Significance/Clinical Relevance: A tunable biomaterial microenvironment at the cartilage defect interface may enhance the efficacy of intra-articular MSC injections for cartilage repair and regeneration.

References: [1] Jo et al, Stem Cells, 2014. [2] Kim et al, Amer J Sports Med, 2015. [3] Wang et al, Nat Mater, 2007. [4] Dupont et al, Nature, 2011. [6] Fisher et al, Tissue Eng A, 2015.

Acknowledgements: This work was supported by the NIH and AOSSM. The authors thank Minwook Kim, Sonia Bansal, Edward Bonnevie for their help.

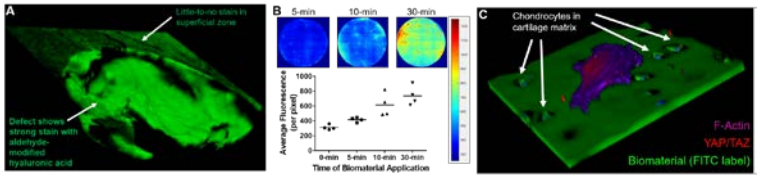

← **Fig 1.** (A) FITC-MeHA-Ald conjugates to a cartilage defect (*in vitro*). (B) Biomaterial adherence increases over a range of clinically-relevant application times. (C) Cartilage with biomaterial coating forms integrated environment around chondrocytes in the native tissue matrix, and allows stem cells (purple) to attach.

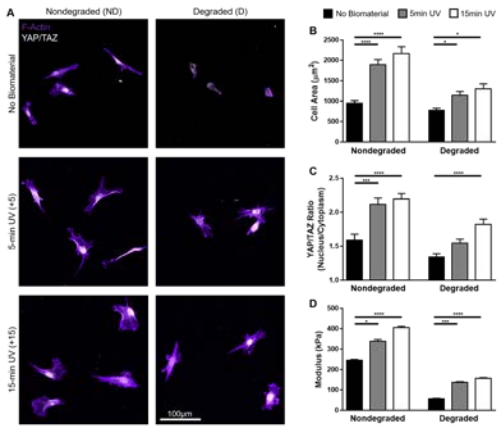

← **Fig 2.** (A) Representative cells after 24 hours of culture on nondegraded and degraded samples, control or with biomaterial (5 and 15 min UV crosslinking). F-Actin shown in purple, YAP/TAZ shown in white. Scale bar = 100µm. (B) Cell area, (C) YAP/TAZ ratio (nuclear : cytoplasmic) and (D) AFM modulus of samples. Mean ± SEM. *, **, ***, **** represent p<0.05, 0.01, 0.001, and 0.0001, respectively.

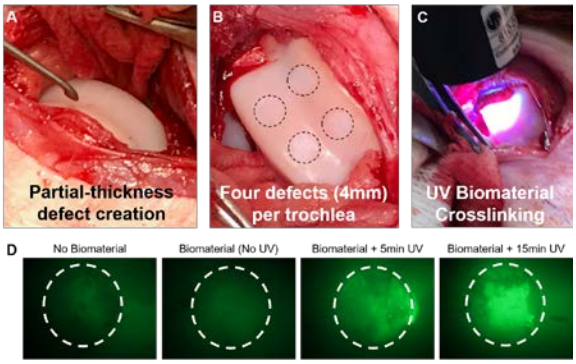

↑ **Fig 3.** Pilot Animal Study. (A/B) Partial thickness trochlear defects (4mm diameter) created, biomaterial applied, and (C) cross-linked via UV light. (D) Biomaterial is retained at 1 week in cross-linked groups.

Intramembranous bone formation critically relies on SOXC transcription factors to control progenitor cell maintenance and osteoblastic differentiation

Angelozzi M, Ashraf S, Bhattaram P, Pellegrino R, Gonzalez M, Lefebvre V

Division of Orthopaedic Surgery, Children's Hospital of Philadelphia, Philadelphia

Most of our bones develop through endochondral ossification, while the others, including the skull vault, form through intramembranous ossification. Both processes require adequate specification and amplification of progenitor cells before commitment to differentiation into either chondrocytes (endochondral ossification) or osteoblasts (intramembranous ossification). To date, the mechanisms underlying chondrocyte and osteoblast differentiation are fairly well understood, whereas those involved in controlling progenitor cells remain incompletely deciphered. Uncovering these mechanisms is paramount to understanding the regulation of skeleton patterning and growth in normal development and in disease. We previously showed that SOXC transcription factors, i.e., SOX4, SOX11 and SOX12, ensure proper delineation, articulation, and growth of cartilage primordia during limb development. They namely promote survival of chondroprogenitor cells and deter joint and perichondrium cells from adopting a chondrogenic fate. We here asked whether SOXC proteins have roles in skull development. Gene expression analyses in vivo and in vitro indicated that *Sox4* and *Sox11* are highly expressed in skull progenitor cells and that *Sox4* but not *Sox11* expression is maintained at a significant level throughout osteoblast differentiation. Mice in which the SOXC genes were conditionally inactivated in skull progenitor cells (*Sox4*$^{fl/fl}$*Sox11*$^{fl/fl}$*Sox12*$^{fl/fl}$*Prx1CreER* mice) died at birth. Skeletal preparations revealed a severely underdeveloped calvarium. Histology analysis showed the tissue had a reduced number of cell layers, and that its mineralization was strongly delayed. Single-cell RNA-seq analysis in young fetuses indicated a selective deprivation of the progenitor cell pool and a relative increase in the populations of pre-osteoblasts and mature osteoblasts. A SOX11-gain-of-function experiment in primary calvarium cells further supported an important role for SOXC proteins in delaying osteoblastic differentiation of progenitor cells. Mechanistic experiments are underway to identify the target genes and molecular network whereby SOXC transcription factors participate in skull development. In conclusion, the SOXC transcription factors are critical regulators of both endochondral and intramembranous ossification. They are most highly expressed in progenitor cells and regulate the pace at which these cells develop into either chondrocytes or osteoblasts. Changes in their expression or molecular network could contribute to the development of various types of skeletal dysplasias in humans.

Direct 3D-Printing of Thiol-ene Crosslinked HA Hydrogels for Cartilage Repair

Jonathan H. Galarraga, Liliang Ouyang, Christopher B. Highley, Mi Y. Kwon, Jason A. Burdick
Department of Bioengineering, University of Pennsylvania, Philadelphia,

Statement of Purpose: 3D-printing is a promising approach for the engineering of tissues; however, the identification of bioinks with the requisite printability, cytocompatibility, and bioactivity remains an ongoing challenge.[1] To this end, we recently developed a 3D-printing approach that permits the extrusion and deposition of non-viscous, photocrosslinkable materials with high fidelity and encapsulated cell viability.[2] Specifically, we directly cured bioinks *in situ* with light during extrusion to print hyaluronic (HA)-based hydrogels into 3D structures. This approach allowed the printing of a wide range of photocrosslinkable hydrogel bioinks. We hypothesize that direct 3D-printing of rationally designed bioinks will enable the fabrication of constructs towards the repair of cartilaginous tissue.

Methods: *Material Synthesis:* HA (75 kDa) was modified with norbornenes (NorHA, 20% mod.) and crosslinked in the presence of dithiothreitol (DTT), 0.05 wt% photoinitiator (lithium phenyl-2,4,6-trimethylbenzoylphosphinate or Irgacure 2959) and either UV or visible light (λ=320-390 nm or 400-500 nm, respectively) to yield NorHA hydrogels. *Mechanics:* Rheological testing (AR2000, TA Instruments) and dynamic mechanical analysis (Q800, TA Instruments) were performed on hydrogels to characterize mechanics. *3D-Printing:* Constructs were printed using a 3D FDM printer (K8200).[2] *Cell Viability:* Live/Dead assays were performed on encapsulated juvenile bovine chondrocytes (CHs) (P1, 20 x10^6 cells/mL) using calcein AM and ethidium homodimer stains. *Histology:* Printed constructs were stained with Alcian blue or anti-collagen type II (COL II) antibodies to observe glycosaminoglycan (GAG) and COL II content, respectively. *Biochemical Assays:* Dimethylmethylene Blue (DMMB) assays were performed to quantify GAG content.

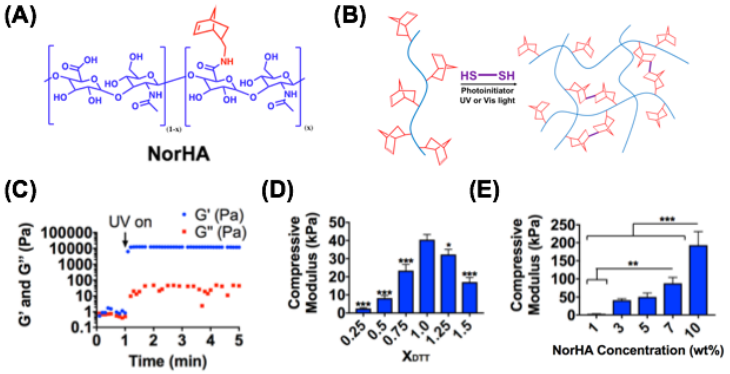

Figure 1. (A) Chemical structure and (B) schematic of crosslinking of norbornene-modified hyaluronic acid (NorHA). (C) Time sweep (0.5% strain, 1 Hz) of NorHA crosslinking with exposure to UV light. Compressive moduli as a function of (D) thiol-to-norbornene ratio (X_{DTT}) at 3 wt% and (E) concentration of NorHA at X_{DTT} = 1.0.

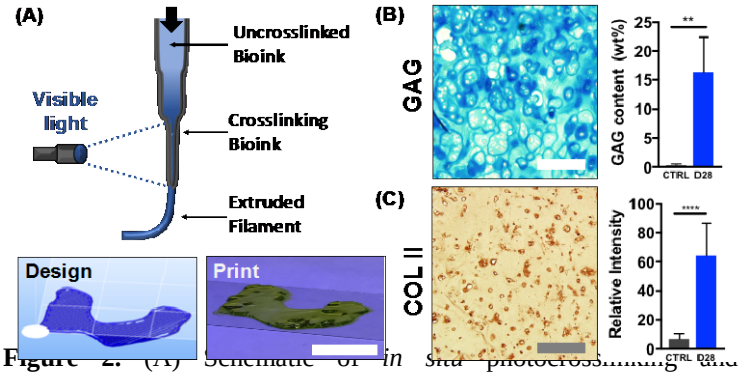

Figure 2. (A) Schematic of *in situ* photocrosslinking and representative printed construct. Scale bar = 10 mm. (B) Alcian blue staining and GAG content of printed constructs at D28 (20x10^6 cells/mL, acellular control constructs). Scale bar = 200 μm. (C) COL II staining and quantification of printed constructs at D28 (20x10^6 cells/mL, control constructs labeled with secondary antibody only). Scale bar = 100 μm. **p ≤ 0.005, ****p ≤ 0.00005.

Results: NorHA is a bioink that crosslinks with a thiol-ene reaction (Fig. 1A,B), as gelation occurs rapidly once the ink is exposed to light (Fig. 1C). The bulk mechanics of NorHA hydrogels may be readily altered by changing the amount of crosslinker (Fig. 1D) or NorHA concentration (Fig. 1E). We recently developed an *in situ* curing process for non-viscous materials (Fig. 2A), where curing occurs immediately before extrusion rather than after, to improve printability, cell viability and resolution.[2] *In situ* photocrosslinking of bioinks involves the extrusion of non-viscous polymer solution through a photopermeable capillary with simultaneous light exposure. The residence time of bioinks within the extrusion capillary and the rate of polymerization of NorHA hydrogels are tunable, such that a simple model was developed to identify permissible printing regimes. Filaments containing encapsulated CHs were printed with high viability (92.6± 4.0% at D1) that persisted with 7 days of culture in chondrogenic media (89.3± 7.1% at D7). This printing approach allowed the design and printing of 3D anatomical constructs, illustrated through the printing of a portion of the femoral condyle (Fig. 2A). After long-term culture, printed constructs contained an abundant amount of GAG and COL II (Fig. 2B,C), indicating that these constructs support neocartilage formation.

Conclusions: NorHA hydrogels were synthesized with a range of properties and 3D-printed via *in situ* photocrosslinking. The process was cytocompatible and used to print cell-laden hydrogels for cartilage engineering. The ability to print different bioink formulations and to pattern printed constructs with bioactive peptides will be useful for numerous applications, including for stem cell chondrogenesis.[3] Ultimately, this approach will be useful towards designing patient-specific implants for the treatment of focal defects and eventually osteoarthritis.

References: [1]Kyle et al. Adv. Healthcare Mater. 2017; 6 (16). [2] Ouyang et al. Adv. Mater. 2017, 29, 1604983. [3] Vega et al. Nat. Commun. 2018, 9, 614.

Regulation of phalangeal joint development by ACVR1 in fibrodysplasia ossificans progressiva

Authors: O. Will Towler, Frederick S. Kaplan, & Eileen M. Shore

Abstract: Fibrodysplasia ossificans progressiva (FOP; MIM #135100) is a genetic disease of heterotopic ossification accompanied by short, laterally deviated great toes, caused by an activating mutation in the BMP receptor ACVR1/ALK2. To investigate the skeletal developmental phenotype of FOP, we used a conditional knock-in mouse model (MGI:5763014) with the FOP ACVR1 R206H mutation to examine digit and joint formation. Mice expressing the FOP mutation globally or in limb mesenchymal cells (Prrx1+) exhibited stunted hindlimb first digits similarly to FOP patients and revealed generalized delayed digit development. Three-dimensional whole-mount pSmad1/5 immunohistochemistry and imaging of embryonic mouse limbs revealed unrestricted BMP signaling throughout the developing digit rays of mutant animals, supporting that BMP pathway activity from the mutant receptor was insufficiently inhibited in the joint space. Expressing the mutation only in joint progenitor cells using Gdf5-Cre showed that mutation activity in these cells was sufficient to induce the joint and digit phenotype. Histological analyses revealed disorganized, interphalangeal chondrocyte proliferation in both Prrx1-Cre and Gdf5-Cre models, supporting the hypothesis that the phenotype is due to improper spatiotemporal activation of chondrogenic pathway signaling in the joint space that is precipitated by increased BMP pathway signaling through the mutant ACVR1 receptor during skeletal development.

Collagen GFP Reporter Mice Reveal Unique Subsets Of Cells Within The Tendon Midsubstance

Xi Jiang[1], Courtney Thompson[2], Pegah Abbasnia[1], Nicholas Oyster[1], Nathaniel A Dyment[1]
[1]University of Pennsylvania, Philadelphia, PA, [2]Univeristy of Notre Dame, South Bend, IN
Email of Presenting Author: jiangxi@pennmedicine.upenn.edu

Disclosures: None.

INTRODUCTION: Heterogeneity within tendons and ligaments has traditionally been defined at the tissue level. Although, cells residing within the tendon fascicle, known as internal tendon fibroblasts or tenocytes, have classically been regarded as a homogenous population. Recent work has suggested that cells at multiple stages of the lineage exist within the internal population [1]. *In vivo* tools are needed to identify the progenitors and more mature cell types to better understand this lineage. To this end, our lab has identified lineage tracing and GFP reporter mouse lines that map to certain subset of cells within the tenocyte population. We previously reported that Col1a1(3.6kb)-CFP mice containing a 3.6kb fragment of the Col1a1 promoter display similar expression to Scx-GFP within multiple tendons and ligaments [2]. In addition, we demonstrated that Col1a1(2.3kb)-GFP, with a truncated 2.3kb region of the Col1a1 promoter, and Col6a1-GFP transgenic mice display expression in only a subset of cells within the tendon fascicle. The objectives of the current study are 1) to quantify the number of Col1a1(2.3kb)-GFP+ and Col6a1-GFP+ cells within multiple tendons and ligaments at different stages of growth and 2) to measure endogenous gene expression profiles of laser captured GFP+ cells using a microfluidic qPCR array to further define the level of cellular heterogeneity.

METHODS: Transgenic Mice. All animals and procedures were approved by UPenn's IACUC. Two transgenic mouse lines were used in this study: 1) **Col2.3GFP** - Col1a1(2.3kb)-GFP mice contain 2.3kb of the Col1a1 promoter driving GFP expression [3] and 2) **Col6GFP** – BAC containing Col6a1 promoter driving GFP expression (acquired from MMRRC). Experimental Design. Fore- and hindlimbs were isolated from P4, P14, and P28 mice for cryohistological analysis while knees from P14 mice were isolated for LCM and qPCR. The patellar tendon (**PT**), cruciate ligaments (**ACL/PCL**), Achilles tendon (**AT**), and supraspinatus tendon (**ST**) were analyzed for histology (n=4-5/group). For LCM, **Col2.3+** and **Col6+** cells were isolated from the PT and compared to **ACL/PCL**, articular cartilage (**AC**), and *whole* PT midsubstance controls from Col2.3GFP (**Col2.3PT**) and Col6GFP (**Col6PT**) sections (n=4/group). Cryohistology. Limbs were fixed in formalin, embedded, counterstained with DAPI, and imaged on the Zeiss Axio Scan.Z1. Laser capture microscopy (LCM). Knees were fixed in 4% PFA, embedded, and sectioned using CryoJane system. Slides were dehydrated and GFP+ cells or larger regions of tissue were isolated using the ArcturusXT laser capture microscope. Microfluidic qPCR Array. RNA was extracted from LCM samples, converted to cDNA, and preamplified for 93 targets and 3 housekeeping genes. qPCR reactions for 96 samples and 96 genes were run on Fluidigm's 96.96 Dynamic Array IFC yielding 9,216 individual Ct reactions. Image Quantification. The GFP intensity was recorded for each cell within the tendon/ligament midsubstance. An equivalent minimum threshold was applied and the percentage of GFP+ cells was computed. Statistics. One-way ANOVAs with either tissue type or age as fixed factors were used to analyze the number of GFP+ cells in the histological sections. Principal component analysis and hierarchical clustering were used to summarize the qPCR data.

RESULTS: Age and tissue dependence of fluorescent reporters. Both tissue type and age had an effect on Col2.3GFP and Col6GFP expression (Fig. 1; $p<0.05$). Col2.3GFP expression increased in both the AT and PT with age (Fig. 1A). Conversely, Col2.3GFP was higher in the ACL/PCL and ST at P4 and P14 but significantly dropped at P28 ($p<0.05$). Col6GFP expression was highest in the cruciate ligaments (ACL/PCL) at all three ages (Fig. 2B). There was an increasing trend in Col6GFP expression in the ACL/PCL with age while the three tendons all decreased with age. Interestingly, the AT showed a regional variation in both reporter lines (data not shown). The region of the AT midsubstance proximal to the enthesis but adjacent to the calcaneus displayed elevated Col2.3GFP expression at P4 and P14 with a significant drop at P28, similar to the ACL/PCL. Additionally, this region of the AT had the highest Col6GFP expression at all time points. Endogenous gene expression indicates Col2.3GFP+ cells are more unique than Col6GFP+ cells in the PT. Principal component analysis of the 93 target genes and 6 cell/tissue types (Col2.3+, Col6+, Col2.3PT, Col6PT, ACL/PCL, and AC) revealed that 92% (57+26+9%) of the total variance was accounted for in the first 3 principal components. PC scores indicated that AC was the most different (Fig. 2A). However, Col2.3+ cells were more unique from *whole* PT samples than Col6+ cells (Fig. 2A). In fact, Col2.3+ cells expressed higher levels of cell cycle genes (Pcna, Gmnn, Cdt1) (Fig. 2B). The tendon samples expressed higher levels of tenogenic markers (Tnmd, Scx, Mkx, Col1a1, Tgfb3) while the ACL/PCL expressed higher levels of other collagens (Col3a1, Col5a1, Col6a1, Col6a2). Finally, the AC samples had the highest levels of cartilage-related genes (Col2a1, Prg4, Acan, Sox9).

DISCUSSION: In order to better understand tendon pathologies and to develop improved repair strategies, we must first improve our understanding of the tendon lineage, including markers that define cells at multiple stages of the lineage and signaling pathways that regulate the differentiation of progenitors into mature tenocytes. We utilized two GFP reporter strains in this study to demonstrate a level of cellular heterogeneity within the internal tendon fibroblast (i.e., tenocyte) population that has not been appreciated previously. The Col2.3+ cells may be of particular interest as they display significant changes in expression with age (Fig. 1A) as well as larger differences in endogenous gene expression compared to *whole* PT controls than the Col6+ population (Fig. 2). Col2.3GFP's age-related expression changes correlate with changes in mineral apposition rate in these tissues during growth [4]. In addition, these cells also express higher levels of cell cycle genes. Therefore, we hypothesize that Col2.3GFP is a marker of an actively growing cell phenotype with increased proliferation, metabolic activity, and ECM production. A hypothesis that we will test in future studies.

SIGNIFICANCE: An improved understanding of the cellular markers and signaling pathways that define and regulate the tendon lineage will be crucial to developing new therapies to attenuate the progression of pathologies and improve repair outcomes following injury. The anatomical and temporal differences in GFP expression found in this study indicate that cells within the tendon midsubstance are not as homogeneous as previously thought. Using these model systems, we aim to identify the phenotype and function of these cells during normal processes of growth, homeostasis, and repair.

REFERENCES: 1. Dyment N, et al., PLOS One, 2014; 2. Dyment N, et. al., ORS, 2016; 3. Kalajzic I, et al., JBMR, 2001; 4. Dyment N, et al., Dev Biol, 2015.

ACKNOWLEDGEMENTS: Work supported by NIH grants R00 AR067283, P30 AR069619, and startup funds from Dept. Orthopaedic Surgery at UPenn.

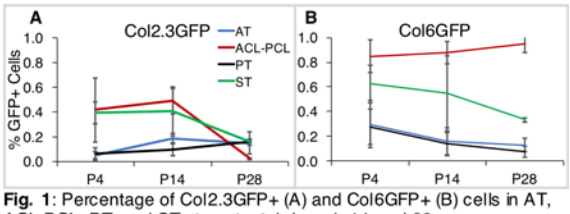

Fig. 1: Percentage of Col2.3GFP+ (A) and Col6GFP+ (B) cells in AT, ACL-PCL, PT, and ST at postnatal days 4, 14, and 28.

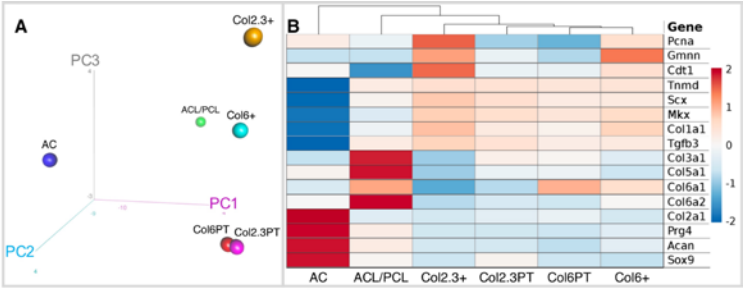

Fig. 2: Principal component scores (A) of 6 tissue/cell groups and hierarchical clustering of groups (B) for subset of genes from dCt values of Fluidigm 96.96 dynamic array.

Hand-Spun Gelatin Noodles Provide Tunable Diameter and Elasticity for Engineering Fibro-Cartilaginous Tissues

Mingkun Wang[1], Su-Jin Heo[2], Robert L. Mauck[2], Li-Hsin Han[1]
[1]Drexel University, [2]University of Pennsylvania, Philadelphia, PA

INTRODUCTION: Regenerating the meniscus is a challenging topic for tissue engineering, as it involves the replication of the inner, central and outer zones of the meniscus, which contain different cell phenotypes, biochemical compositions, and matrix orientations to produce the distinct load-bearing function of the native tissue. Polymer microfibers with diameters that are comparable with the size of meniscal cells are a promising template for such regeneration, as the microfibers, resembling collagen bundles, may be assembled into three-dimensional (3D) scaffolds of specific microstructures to stimulate the cell activities associated with the different meniscal zones. However, how the properties of these microstructures, including fiber elasticity and matrix pore size and anisotropy, affect cell activities is not yet well defined. Efforts to bridge this knowledge gap is also challenged by technological hurdles, as cell-size fibers of the same composition are difficult to fabricate and assemble into different 3D scaffolds. Inspired by the culinary art of hand-pulled noodles, here we develop a novel technology to spin a single biopolymer into discrete cell-size fibers with easily tunable elasticity, diameters, and alignment. These fibrous materials can be generated in large quantity and at an unprecedented speed. Using this novel platform, we explored the available parameter space to determine the optimal scaffold designs for meniscus regeneration.

METHODS: (1) Stretch-and-Fold spinning. Microfibers were fabricated by repeatedly folding and stretching a polymer rod that contained a core and a sheath compartment (Fig.1A-D). The core contained hydrated gelatin, and the sheath was made of a solvent-soluble thermoplastic that kept the cores separated. The number of stretch-and-fold cycles (n) increased the core number (N) exponentially ($N = 2^n$) while decreasing the core diameter exponentially ($D = D_0 / 2^{0.5n}$) (Fig.1G). After stretch and folding, gelatin microfibers were released by dissolving the cladding, and were aldehydes-fixed, methacrylated, washed, and freeze-dried for subsequent use. Fiber diameter was determined by the number of cycles and alignment of fibers was achieved by the repeated stretching and could be randomized when needed. The elasticity of fibers was tuned by the degree of methacrylation of the gelatin. (2) Cell study. Meniscal cells were harvested from the central zone of juvenile bovine menisci and expanded for one passage before use. Freeze-dried microfibers were hydrated with PBS at a fixed weight ratio, and the resulting paste-like material was uniformly mixed with the cells, molded to 2 mm thick samples, and photo-crosslinked. To form different types of microstructures, the microfiber diameter was varied from 2 µm to 20 µm, with the fiber elasticity varied from 0.2 kPa to 20 kPa. The scaffolds were cultured in chondrogenic medium supplemented with TGF-β for 4 weeks and collected on day 1, 14, and 28. Cell production of ECM, e.g. collagens , proteoglycan (GAG), and aggrecan were examined by histology and immunofluorescence staining. The instantaneous and equilibrium moduli of the scaffold were measured by compressive tests using 0-15% strain and 15 mins wait-time.

RESULTS: All scaffold formulations generated engineered constructs that were viable through 4 weeks of culture, with the following trends noted: (1) Softer fibers promoted collagen and proteoglycan production (Fig.2 A, B). By four weeks, cells in the soft scaffolds produced with 0.2 kPa fibers elaborated dense networks of collagen and GAG matrix filling the empty spaces of the scaffolds. In contrast, cells in stiff scaffolds (comprised of 20 kPa fibers) formed negligible amount of collagen and GAG, with most residing in the pericellular spaced. (2) Thinner fibers promoted dense matrix formation. The neo-ECM formed in scaffolds made of 2µm fibers had a significantly higher density than the neo-ECM formed in scaffolds generated from 20µm fibers. (3) Fiber alignment led to ECM anisotropy. Collagen produced by cells in aligned scaffolds was anisotropic and aligned in parallel with microfibers (Fig.2C), while the collagen produced in randomized fibers was less ordered. (4) Matrix composition. Scaffolds made of soft-fibers had significantly higher staining for type-I collagen than the scaffolds formed of stiff-fibers (Fig. 2D). Collagens type II and X, and aggrecan showed a similar trend. (5) Compressive properties. Compressive moduli measured for each group were consistent with ECM formation (Fig.2E). For all groups of different fiber diameters and aliments, the instantaneous and equilibrium moduli of soft groups increased significantly more than the stiff groups ($p < 0.01$).

DISCUSSION: Our results suggest the optimal choice for engineering the outer zone of meniscus would be 2 µm aligned soft fibers (to maximize collagen production), while for the inner zone the best formulation would be 2 µm or 20 µm randomized fibers (to maximize collagen and proteoglycan production). The above results also showed that meniscal cells are highly sensitive to changes of fiber diameter, elasticity, and alignment, which altered the mechanical cues, pore size, and matrix organization the cells sensed within the scaffolds. Given that the microfibers from all groups provided similar biochemical cues (from gelatin), this suggests that the dramatic differences in ECM production in different groups arose from differential mechanosensing in these distinct microenvironments, in which biophysical cues, e.g. shape and stiffness of the microstructure of ECM, impact cell morphology, cytoskeletal organization, and gene expression, as reported elsewhere. Porosity may also play an important role, as scaffolds with smaller pores, which were formed by thinner fibers, may provide more contact area to support cell engraftment and might have accelerated ECM production. In comparison with the 2D models commonly used for studying mechanosensing, this 3D platform enables a better understanding of how 3D ECM cues impact cell fates and tissue formation, while providing more clinically relevant results for meniscus regeneration.

SIGNIFICANCE/CLINICAL RELEVANCE: This work develops a novel fibrous scaffold that may be promising for the clinical repair of the meniscus, as well as other fibro-cartilaginous tissues. It also offers a versatile platform for fundamental studies to decipher the relationship between cell-size microstructures, biophysical cues, and mechanosensing pathways that direct cell activities and ECM production.

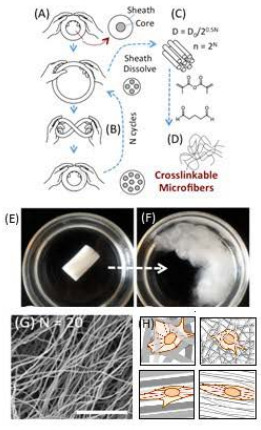

Fig. 1 Schematic of stretch-and-fold spinning, and photos of samples. (A-D) Stretch-and-fold Procedure. (E-F) Fiber releasing. (G) Fibers under SEM. (H) Cell encapsulation Scheme. Scale bar: 100 µm.

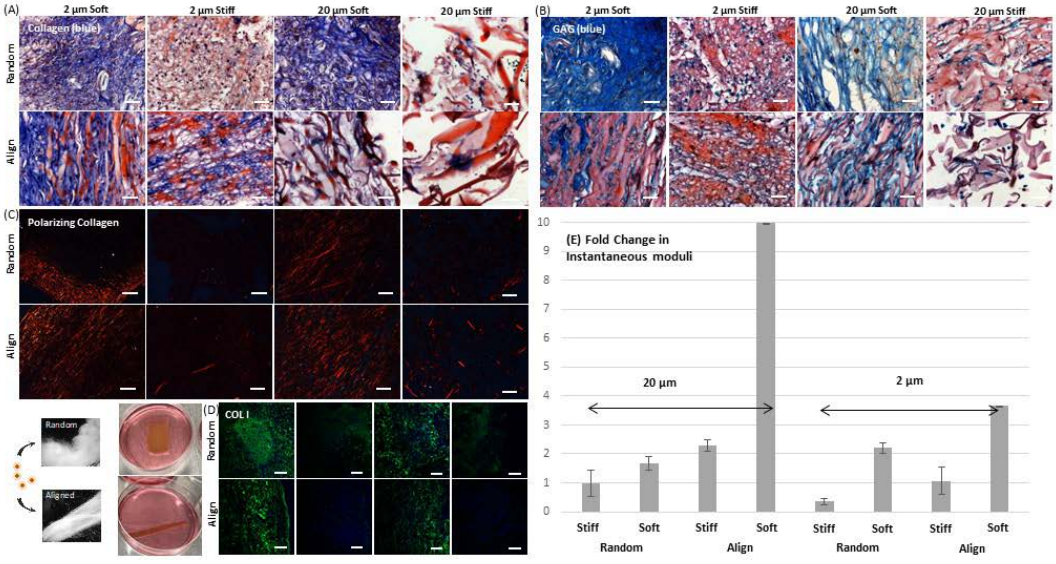

Fig. 2 Day 28 (A) trichrome staining (blue: collagen, red: fibers). (B) Alcian blue/picrosirius red staining (blue: proteoglycan, red: fibers). (C) polarizing imaging of picrosirius red staining (red: collagen). (D) Immunofluorescence of collagen type I. (H) Instantaneous moduli from compression test.

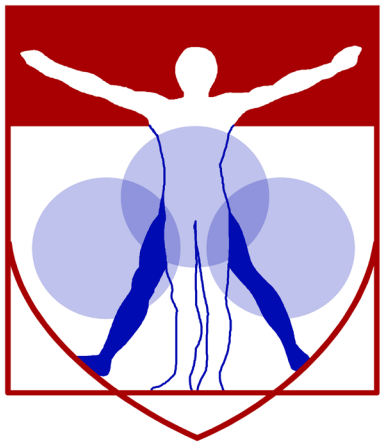

PENN

CENTER for

MUSCULOSKELETAL

DISORDERS

MicroCT Abstracts

Disc Degeneration Alters Endplate Morphology and Mechanics and Reduces Disc Nutrition in a Rabbit Model

Beth G. Ashinsky[1,2,3], Edward D. Bonnevie[1,3], Stephen Pickup[1], Chao Wang[2], Lin Han[2], Robert L. Mauck[1,3], Harvey E. Smith[1,3], Sarah E. Gullbrand[1,3]
[1]University of Pennsylvania, Philadelphia, PA; [2]Drexel University, Philadelphia, PA; [3]Corporal Michael J. Crescenz VA Medical Center, Philadelphia, PA
Disclosures: BGA (N), EDB (N), SP (N), CW (N), LH (N), RLM (8, JOR Spine), HES (N), SEG (N)

INTRODUCTION: Intervertebral disc degeneration is associated with a cascade of cellular, compositional and structural changes to the nucleus pulposus (NP), annulus fibrosus (AF) and boney and cartilage vertebral endplates (EP), and is frequently associated with back pain. Low back pain is the most common cause of disability in the United States, and has a prevalence greater than heart conditions, stroke and cancer combined [1]. The disc is the largest avascular structure in the body; cells within the disc therefore rely on diffusive and convective transport via the vasculature in the EP to receive nutrients and eliminate waste products [2]. For this reason, it has long been hypothesized that compromised trans-endplate transport plays a role in the initiation and progression of disc degeneration. Despite the critical role of trans-endplate transport in disc homeostasis, the relationships between endplate structure, function and disc nutrition remain poorly understood. Here, we utilize an *in vivo* rabbit puncture degeneration model to study these interactions, and hypothesize that increasing degeneration of the boney and cartilaginous EP, characterized by increased stiffness and bone density, and reduced vascularity, reduce small molecule transport into the degenerating disc.

METHODS: Following IACUC approval, 9 male New Zealand white rabbits underwent a surgical procedure to puncture 4 lumbar spine levels per animal. The adjacent, non-punctured levels were utilized as healthy controls. Three animals were euthanized at each time point 4, 8 and 12 weeks post puncture, and a subset of the punctured discs were utilized in this study. At each time point, animals (n=1-2 per time point) were administered the small molecule, non-ionic MRI contrast agent gadodiamide intravenously 30 minutes prior to euthanasia [2]. Quantitative MRI T1 mapping of the lumbar spinal levels was performed immediately after euthanasia using an inversion-recovery sequence. Gadodiamide is a T1 shortening agent, and thus the percent reduction in T1 (discs without gadodiamide versus those with gadodiamide at each time point) provides a quantitative measure of small molecule diffusion into the disc. Motion segments (n=4 per group) were subjected to µCT scanning at 10µm isotropic resolution to quantify bone volume fraction and trabecular morphometry parameters in the vertebral endplate between the growth plate and disc. Following µCT, motion segments were cryosectioned in the sagittal plane using Kawamoto's tape method to 20µm thickness [3]. AFM-nanoindentation (≥12 indents per region, n=2-3 per group) was performed on sections at the AF-EP and NP-EP interfaces using microspherical tips ($R \approx 12.5$ µm, 10 µm/s rate). The effective indentation modulus, E_{ind} (in MPa), was calculated via the finite thickness-corrected Hertz model [4, 5]. Additional motion segments (n=2-3 per group) were processed for paraffin histology, sectioned to 10µm thickness, and stained with Mallory-Heidenhain trichrome stain to visualize the vasculature in the vertebral endplate, or with alcian blue and picrosirius red to visualize overall degenerative changes to the disc. Second harmonic generation imaging (SHG) was also performed on paraffin sections to visualize collagen organization at the AF-EP and NP-EP interfaces. Significant differences ($p<0.05$) in quantitative out comes were assessed via Kruskal-Wallis with Dunn's multiple comparison testing.

RESULTS: In the rabbit puncture model, degeneration progressed with time post-injury, and was characterized by loss of disc height, disorganization of the annulus fibrosus, anterior osteophyte formation, and reductions in NP water and proteoglycan content. T1 mapping demonstrated reduced gadodiamide diffusion into the NP in the 12 week puncture-degenerated group compared to healthy controls, while transport into the AF of degenerative discs increased compared to controls (Figure 1A). Preliminary AFM analysis suggested progressive increases in indentation modulus of the AF-EP interface, as well as the cartilaginous endplate adjacent to the NP, with increasing time post-puncture (Figure 1B). µCT showed significant increases in bone volume fraction of the vertebral endplate compared to healthy controls (Figure 1D) at 8 and 12 weeks post-puncture, as well as significant increases in trabecular thickness at 4, 8 and 12 weeks (Figure 1E). Mallory-Heidenahin staining, which stains erythrocytes in the vasculature orange, revealed a marked reduction in vessel density and size in the vertebral endplate adjacent to the NP at 8 and 12 weeks (Figure 2, black arrows). Finally, SHG showed progressive disorganization of lamellae at the AF-EP interface as well as increases in organized collagen deposition within the cartilage endplate at 4 and 8 weeks, compared to controls (Figure 2, white arrows).

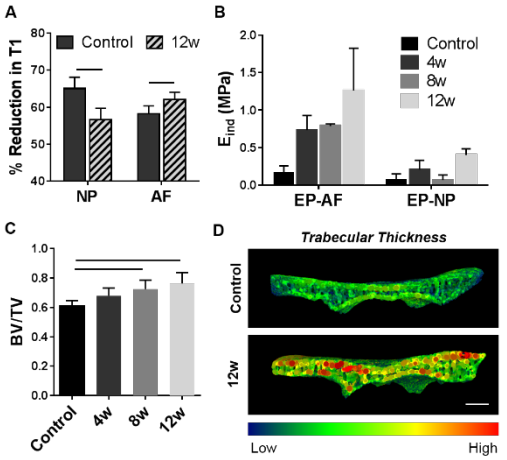

Figure 1. (A) Quantification of small molecule diffusion into the disc via post-contrast enhanced T1 mapping. (B) AFM indentation modulus of the intervertebral disc interfaces. (C) Endplate (EP) bone volume fraction and (D) trabecular thickness maps (red = higher trabecular thickness). Scale = 1 mm. Bars indicate $p<0.05$ between groups.

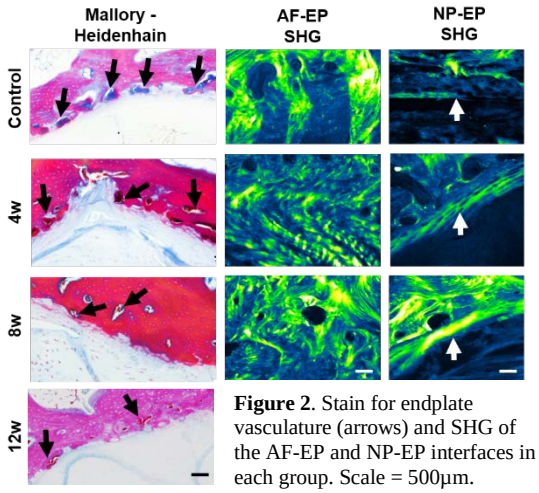

Figure 2. Stain for endplate vasculature (arrows) and SHG of the AF-EP and NP-EP interfaces in each group. Scale = 500µm.

DISCUSSION: Degeneration of the disc in the rabbit annular puncture model resulted in significant alterations to the adjacent vertebral endplate and disc interfaces. Bone volume fraction and trabecular thickness increased and vascularity decreased in the boney endplate, while the interfaces between the bone and disc progressively stiffened with increasing severity of degeneration. These structural and functional changes were concomitant with reductions in small molecule diffusion into the NP. As NP cells rely entirely on diffusive transport for nutrient and waste product exchange, the reduction in disc nutrition may promulgate the progression of degeneration in the NP. Interestingly, diffusion into the AF region increased compared to controls, which may be due to neovascularization in the anterior osteophytes and peripheral annulus fibrosus local to the puncture. Ongoing work will provide a comprehensive analysis of interface micromechanics via AFM, and the changes to trans-endplate transport over the time course of degeneration.

SIGNIFICANCE: The role of small molecule trans-endplate transport in degeneration is a debated topic in the field. This work demonstrates that small molecule diffusion into the disc is compromised during degeneration, and is associated with alterations to endplate mechanics and composition. This work furthers our knowledge of the role of diffusive transport in disc degeneration, and may be leveraged towards the improved diagnosis and treatment of patients with disc degeneration and back pain.

REFERENCES: [1] Mokdad+ *JAMA* 2018 [2] Gullbrand+ *Spine* 2015 [3] Kawamoto+ *Stain Tech* 1986. [4] Li+ *Acta Bio*2017. [5] Han+ *BiophysJ.* 2011.
ACKNOWLEDGEMENTS: This work was supported by the NIH, the Department of Veterans' Affairs, and the Penn Center for Musculoskeletal Disorders.

Scleraxis Targeted Collagen V Deletion Affects Bone Morphology with Altered Skeletal Loading

Ashley B. Rodriguez[1], Snehal S. Shetye[1], Brianne K. Connizzo[1], Julianne Huegel[1], Wei-Ju Tseng[1], David E. Birk[2], Louis J. Soslowsky[1]
[1]McKay Orthopaedic Research Laboratory, University of Pennsylvania, Philadelphia, PA
[2]Department of Molecular Pharmacology & Physiology, University of South Florida, Tampa, FL

Disclosures: Ashley B. Rodriguez (N), Snehal S. Shetye (N), Brianne K. Connizzo (N), Julianne Huegel (N), David E. Birk (N), Louis J. Soslowsky (N)

INTRODUCTION: Classic Ehlers-Danlos syndrome (EDS) is characterized by abnormalities in connective tissue due to mutations in collagen V, with the most common mutation being haploinsufficiency in COL5A1. This syndrome is characterized by hypermobility, instability, hyperextensible skin, and abnormal wound healing [1-2]. Scleraxis-driven collagen V null ($Col5a1^{\Delta ten/\Delta ten}$) mice have been developed to determine the role of collagen V in tendon [3-4]. In addition to differences in tendon, $Col5a1^{\Delta ten/\Delta ten}$ mice demonstrate decreased body size and exhibit reduced cortical bone polar moment of inertia (pMOI) [5-6], despite the fact that the role of collagen V in bone is believed to be limited [7]. The cause of this change in pMOI in these mice is unlikely, given the specificity of scleraxis, and as such, the cause of alterations in cortical bone morphology is unknown. Therefore, the objective of this study was to determine whether the observed bone morphological changes could be due to reduced skeletal loading. We hypothesized that any changes in bone morphology in the $Col5a1^{\Delta ten/\Delta ten}$ would be due to decreased skeletal loading.

METHODS: Humeri from day 60 $Col5a1^{+/+}$ (WT, n=8) and $Col5a1^{\Delta ten/\Delta ten}$ (NULL, n=13) mice, and ribs from day 120 $Col5a1^{+/+}$ (WT, n=10) and $Col5a1^{\Delta ten/\Delta ten}$ (NULL, n=8) mice (IACUC approved) were prepared for high-resolution micro-computed tomography (μCT). Rib bone was chosen as a skeletal structure that is relatively load-independent and therefore its structure would not be affected by decreased mechanical loading. *High-Resolution μCT.* All samples were scanned using a μCT 35 (Scanco Medical AG). The epiphyseal and metaphyseal regions of the humeri, defined as proximal and distal to the growth plate, respectively, as well as the ribs at the cortical midshaft, were scanned at an isotropic resolution of 6μm. Standard cortical and trabecular morphometry parameters (trabecular number (Tb.N), trabecular thickness (Tb.Th), trabecular spacing (Tb.Sp)), were measured for all humeri, while ribs only underwent cortical evaluation. Samples were kept hydrated with phosphate buffered saline (PBS) during scanning. *Data Analysis:* The maximum pMOI for the cortical regions was calculated using custom code (MATLAB) and standard cortical and trabecular evaluations provided by Scanco were used to obtain all other parameters. *Statistics* Unpaired t-tests ($p<0.05$) were used to compare between WT and NULL mice for both humeri and ribs.

RESULTS: Body weight was significantly decreased in the NULL mice when compared to the WT mice for both the day 60 and day 120 mice (**Fig.1A-B**). *Cortical regions.* pMOI in the WT mice was significantly greater than in the NULL mice for the humeri (**Fig.2A)**; however no changes were detected in pMOI in the ribs between groups (**Fig.2B)**. There were no changes found for the other cortical parameters (data not shown). *Trabecular regions.* Tb.N was greater in the WT mice than the NULL mice in the epiphyseal region, (**Fig.3A)**, and greater in WT mice than NULL mice in the metaphyseal region (**Fig.3B**). Tb.Th was greater in WT mice than the NULL mice in the epiphyseal region (**Fig.3C**) and in the metaphyseal region (**Fig.3D**). Tb.Sp in WT was decreased compared to NULL in both the epiphyseal region (**Fig.3E**) and metaphyseal region (**Fig.3F**).

DISCUSSION: This study investigated whether changes in bone morphology in $Col5a1^{\Delta ten/\Delta ten}$ were caused by reduced loading due to body weight. The WT mice had greater body weight than the NULL mice and therefore exhibited greater mechanical loading on load-bearing skeletal structures resulting in more numerous, thicker trabeculae in WT mice when compared to NULL mice. The only differences in cortical bone were observed in pMOI in the humeri, but not in the ribs. This indicates that altered skeletal loading due to a decrease in body weight is a strong contributing factor to the differences observed between the WT and NULL mice. In addition to reduced body weight, these mice exhibit altered mobility and diminished activity [7], which may also contribute to reduced mechanical loading. These results are also in agreement with previous studies demonstrating that increased volume of mineralized tissue is induced by increased loading, and that mechanical unloading leads to trabecular bone loss [8-9]. Previous research in EDS patients has shown a reduction in bone mineral density (BMD) and lower trabecular bone scores (TBS) [10]. Although we found no differences in BMD, we did observe reduction in trabecular morphological parameters. In conclusion, results indicate that bone loss consistent with EDS may be due to mechanical unloading of load-bearing skeletal structures. However, other influences such as level of physical activity or aging might also contribute to this bone loss and future studies will investigate these potential influences further.

SIGNIFICANCE: This study highlights the importance of monitoring bone integrity in patients suffering from *classic* EDS especially with reduction in physical activity and body weight during aging.

ACKNOWLEDGMENTS: We thank H. Zhao and B. Taylor for their assistance. This study was supported by NIH/NIAMS AR065995, AR044745 and the Penn Center for Musculoskeletal Disorders (NIH/NIAMS, P30 AR050950, P30 AR069619).

REFERENCES: [1] Malfait F et al. Hum Mutat. 25:28-37, 2005. [2] Symoens S et al. Hum Mutat. 33:1485-1493, 2012. [3] Wenstrup RJ et al. J Biol Chem. 79:53331-7, 2004. [4] Connizzo BK et al. J Orthop Res. 33:882-8, 2015. [5] Connizzo BK. Ph.D Thesis. University of Pennsylvania; 2015. [6] Sun M et al. AJP. 185(5):1436-47, 2015. [7] Roulet et al. Cell Tissue Res. 2007. [8] Anderson MJ et al. J Orthop Res. 34:1680-1687, 2016. [9] Fritton JC et al. Bone. 36:1030-1038, 2005. [10] Eller-Vainicher C et al. Osteoporos Int. 27:2525, 2016.

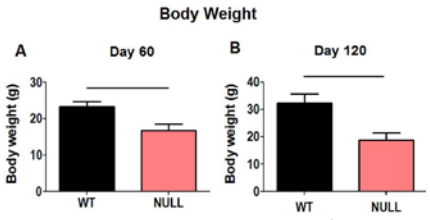

Figure 1: Body weight in WT was significantly greater than NULL at **(A)** day 60 and **(B)** day 120

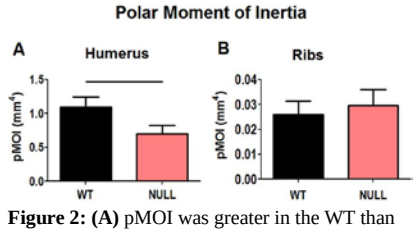

Figure 2: (A) pMOI was greater in the WT than the NULL for the humeri but **(B)** no changes were shown in the ribs.

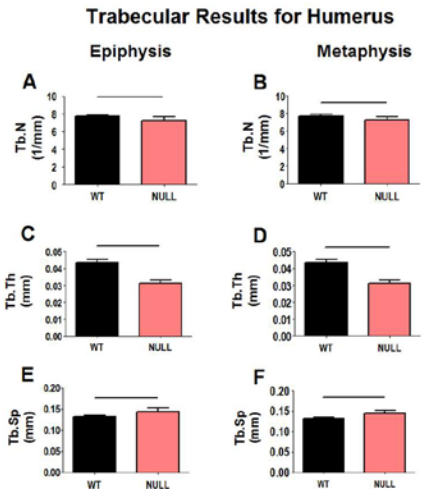

Figure 3: Tb.N was significantly greater in WT than NULL in both the **(A)** epiphysis and **(B)** metaphysis. Tb.Th was significantly greater in WT than NULL in both the **(C)** epiphysis and **(D)** metaphysis. Tb.Sp. was decreased in WT compared to NULL in both the **(E)** epiphysis and **(F)** metaphysis.

Alternating Parathyroid Hormone (PTH) and Alendronate Treatment Regimens Further Improve the Efficacy of Daily and Cyclic PTH Regimens in Osteoporosis Therapy

Hongbo Zhao, Wei-Ju Tseng, Tien-Jung Lee, Wonsae Lee, Yihan Li, Chantal de Bakker, Thomas Leahy, X. Sherry Liu
[1]McKay Orthopaedic Research Laboratory, Department of Orthopaedic Surgery, University of Pennsylvania, Philadelphia, PA; zhhongbo@upenn.edu

Disclosures: Nothing to disclose for all authors.

INTRODUCTION: As the only FDA-approved anabolic agent for treating osteoporosis, intermittent PTH can only be used 18-24 months in clinical practice. However, bone mineral density rapidly decreases upon withdrawal from PTH treatment despite its potent effect of promoting new bone formation [1]. In our previous study, μCT results showed a continuous anabolic window during the first week of PTH discontinuation in ovariectomized (OVX) rats [2]. During this anabolic window, no change occurs in osteoblast and osteoclast number while bone mass and microarchitecture continue to improve. However, after a 2-week discontinuation of PTH, osteoblast number starts to decline and osteoclast number increases significantly. To fully utilize this anabolic window, a cyclic treatment regimen with repeated cycles of on and off daily injection of PTH may be able to maximize the efficacy of PTH and extend treatment duration [3]. Furthermore, adding the anti-resorptive treatment during the off-PTH period may prevent the increased osteoclast activities and further improve the treatment benefit. Therefore, the objective of this study is to test the effect of cyclic and sequential treatment regimes alternating PTH and alendronate (ALN, an anti-resorptive agent) on bone microarchitecture and mechanical competence.

METHODS: Animals:29 female SD rats received bilateral OVX surgery at age 4 months and developed osteoporosis for 4 weeks. These rats were assigned to VEH (n=6, saline for 18 weeks), PTH-VEH (n=6, PTH 40μg/kg 5x/wk for 9 weeks followed by saline for 9 weeks), cyclic PTH-VEH (n=7, PTH for 3 weeks followed by saline for 3 weeks, repeat for 3 cycles), cyclic PTH-ALN (n=5, PTH for 3 weeks followed by ALN 20mg/kg 2x/wk for 3 weeks, 3 cycles) and cyclic ALN-PTH (n=5, ALN for 3 weeks followed by PTH for 3 weeks, 3 cycles). In vivo μCT Imaging: Sequential scans of the proximal tibiae were performed by in vivo μCT (Scanco Medical) at 10.5 μm voxel size at week -4 (OVX surgery),0, 3, 6, 9, 12, 15 and 18. The same volume of interest (VOI, Fig 1A) was identified by 3D image registration [4] in all scans and subjected to trabecular bone microstructural analysis. Ex vivo μCT Imaging: The center 2 mm of the vertebral body of lumbar vertebra L2 was imaged by μCT at 10.5 μm voxel size, and cross-sectional area (CSA) and trabecular bone microstructure were assessed. Uniaxial compression test of L2: A 4-mm-thick section of the vertebral body with processes removed [5] were compressed to failure at a displacement rate of 1.8 mm/minute by using Instron 5542. Load-displacement curves were used to calculate peak load, stiffness, and energy to failure. Apparent-level properties, including ultimate stress, elastic modulus, and toughness, were estimated by normalizing extrinsic properties by μCT-derived total CSA, as described in [6]. Statistics: Longitudinal comparisons were made using a 2-way, repeated-measures ANOVA, adjusted for baseline values, and cross-sectional comparisons were made using 1-way ANOVA. Bonferroni corrections were applied to all post hoc tests.

RESULTS: 4-week osteopenia development in tibiae caused 51% and 11% decrease in bone volume fraction (BV/TV) and trabecular thickness (Tb.Th) respectively, and a 105% increase in structure model index (SMI, Fig 1 B-D). Bone microarchitecture deterioration continued in VEH rats for 18 weeks. Meanwhile, in PTH-VEH group, 9-week PTH treatment led to greater BV/TV, Tb.Th and lower SMI than all the other groups. However, these improvements were abolished upon 9-week discontinuation from PTH treatment. On the other hand, cyclic PTH treatment efficiently maintained the benefit of 3-week PTH treatment in BV/TV and SMI from the 1st cycle of treatment, and further increased Tb.Th over the next 2 cycles of PTH on and off treatment. Furthermore, both alternating PTH-ALN and ALN-PTH regimens further improved the benefit of PTH treatment in BV/TV and SMI when compared to cyclic PTH-VEH regime (Fig 1B and D). Interestingly, only cyclic PTH-ALN regime, but not cyclic ALN-PTH regime, led to greater Tb.Th than cyclic PTH-VEH group. Moreover, results of lumbar vertebra L2 suggested greater BV/TV and Tb.Th in both cyclic PTH-ALN and ALN-PTH groups than all the other groups, respectively (Fig 2 A-C). Additionally, peak load, energy to failure, and apparent-level toughness were 29%, 45%, and 43% greater in cyclic PTH-ALN vs. cyclic PTH group (Fig 2 D, E and H), and 29%, 48%, and 46% greater in cyclic ALN-PTH vs. cyclic PTH-VEH group, respectively. In contrast, there were no difference in any of the L2 mechanical properties among VEH, PTH-VEH, and cyclic PTH-VEH groups (Fig 2 D-I).

DISCUSSION: Similar to previous clinical findings [1], this study showed that significant bone loss and bone microarchitecture deterioration occurred in OVX animals after discontinuation of PTH treatment. The cyclic PTH-VEH treatment regime alleviated bone deterioration and extended the total duration of treatment. However, despite continuous increases in Tb.Th, the cyclic PTH-VEH regime did not further improve BV/TV or SMI during the 2nd and 3rd cycles of treatment, neither did it improve any of the L2 mechanical properties by the end of the 3rd cycle. By adding antiresorptives (ALN) during the off-PTH period, both cyclic PTH-ALN and ALN-PTH regimes showed greater improvement in bone microarchitecture at the proximal tibia and lumbar vertebra when compared to cyclic PTH treatment regimen. Furthermore, cyclic treatment regime with alternating PTH and ALN injections led to greater bone strength at both whole bone and apparent levels. In conclusion, cyclic and sequential treatment of PTH and anti-resorptive agent can further improve the treatment efficacy of daily and cyclic PTH treatment regime and extend PTH treatment duration.

SIGNIFICANCE: By testing various cyclic and sequential treatment regimes alternating PTH and anti-resorptive agents, this study provided important insight into the clinical design and optimization of pharmacological treatment strategies to maximize the duration and efficacy of osteoporosis treatment.

REFERENCES: [1] Black DM et al. N Engl J Med, 2005; [2] Tseng W-J et al. ASBMR 2017; [3] Cosman F et al. N Engl J Med, 2005; [4] Lan S et al. Bone, 2013; [5] Pendleton MM et al. SB3C 2016; [6] Altman-Singles AR et al. J Bone Miner Res, 2017.

ACKNOWLEDGEMENTS: Funding: NIH/NIAMS P30-AR050950 and NIH/NIAMS K01-AR066743.

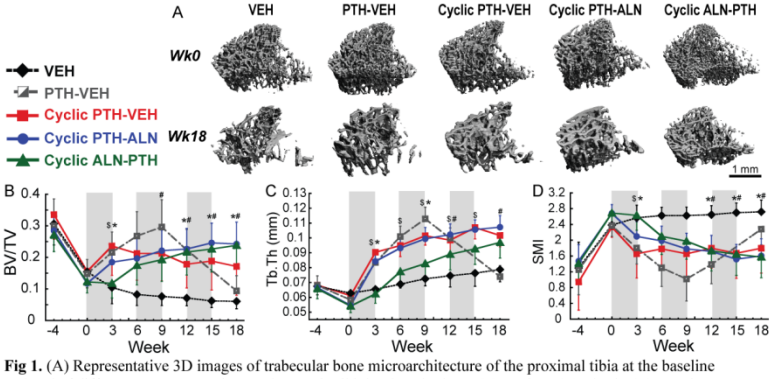

Fig 1. (A) Representative 3D images of trabecular bone microarchitecture of the proximal tibia at the baseline and end of different treatment regimes. Changes in tibial trabecular bone (B) BV/TV, (C) Tb.Th, (D) SMI in different treatmet groups. Significant difference between groups at each time point ($p<0.05$): $: cyclic PTH-ALN *vs.* ALN-PTH, # : cyclic PTH-ALN *vs.* cyclic PTH-VEH, * : cyclic ALN-PTH *vs.* cyclic PTH-VEH.

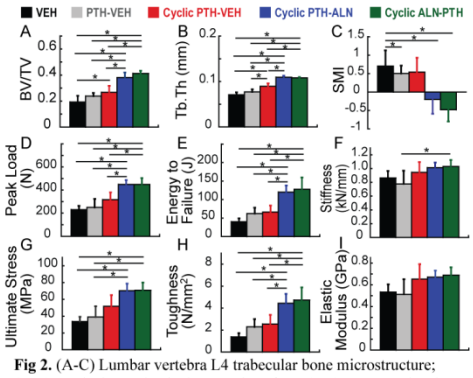

Fig 2. (A-C) Lumbar vertebra L4 trabecular bone microstructure; (D-F) Extrinsic mechanical properties of L4; (G-I) Apparent level properties, derived by normalizing extrinsic properties by total cross-sectional area. * $p<0.05$.

Effects of Reproduction and Lactation on Maternal Bone Mechano-Sensitivity

Yihan Li [1], Chantal de Bakker [1], Tan Meng [1], Wei-Ju Tseng [1], Hongbo Zhao [1], Ashutosh Parajuli [2], Liyun Wang [2], X. Sherry Liu [1]
[1] McKay Orthoapedic Research Laboratory, Department of Orthopaedic Surgery, University of Pennsylvania, Philadelphia, PA; yihanl@seas.upenn.edu
[2] Department of Mechanical Engineering, University of Delaware, Newark, DE.

Disclosures: Nothing to disclose for all authors

INTRODUCTION: The maternal skeleton undergoes dramatic bone loss during pregnancy and lactation [1]. Despite the significantly elevated bone formation after weaning, the bone mass is only partially recovered [2]. However, multiple clinical studies have suggested that the reproduction and lactation exert no adverse effect on long-term fracture risk [1]. Our previous study found that rats that had undergone three repeated cycles of pregnancy and lactation had attenuated estrogen-deficiency-induced bone loss compared to age-matched virgins [3]. This finding implies that the history of reproduction and lactation may lead to functional adaption of the maternal bone microarchitecture and mechano-sensitivity, which may protect the skeleton from future estrogen-deficiency-induced bone loss. A few recent studies suggest that the osteocyte can actively remodel its peri-lacunar matrix during lactation [4, 5], which may alter the local osteocyte microenvironment, and thus affecting skeletal mechano-sensitivity. Therefore, we hypothesize that the history of reproduction and lactation primes the microenvironment of osteocytes, which leads to enhanced mechano-sensitivity to confer protective effects against estrogen deficiency. The overall objective of this study is to investigate the long-term effects of reproduction and lactation history on bone's mechano-sensitivity and osteocyte microenvironment when subjected to estrogen deficiency.

METHODS: *In vivo dynamic loading:* Female, SD rats were assigned to Virgin (n=7), and Reproductive (n=6) groups. Reproductive rats underwent two reproductive cycles consisting of pregnancy, 3-week lactation and 6-week post-weaning recovery. All rats underwent OVX surgery at age of 10 months and were subjected to a 2-week dynamic, compressive loading protocol 6 weeks post-OVX [6]. A peak load of 45N, corresponding to ~1250 με at the tibial shaft as determined by strain gauges, was applied to the left tibia at 2 Hz (i.e., 0.15s ramp up, 0.15s ramp down, and 0.2s dwell time), at 5 min/session for 2 weeks (5 days/week), while the right tibia remained unloaded. *In vivo μCT imaging:* μCT scans were performed on both tibiae at day 0 and day 14 using VivaCT 40 (Scanco Medical AG, voxel size 10.5μm). 3D image registration was performed to track structural changes within a constant trabecular volume of interest (VOI) at the proximal tibia (Fig 1C) and the tibial midshaft [7]. Percent changes between day 0 and day 14 for non-loaded and loaded tibiae were calculated. *Dynamic histomophometry:* Rats were injected with calcein green and alizarin red 11 days and 2 days before sacrifice. Double-labeled histology images of the tibial midshaft were taken by confocal microscope (Zeiss LSM7) (Fig 2C-F). *Lacunar size analysis:* The tibial cortex (n=4/group) was subjected to scanning electron microscope in backscatter mode (bSEM, Zeiss Supra 50VP) to assess lacunar structure. *Statistics:* A two-way ANOVA with baseline parameters as covariate and Bonferroni corrections were used to compare loading responses between virgin and reproductive rats.

RESULTS: All rats underwent significant reduction in bone volume fraction (BV/TV) over 6 weeks post-OVX. Two weeks of dynamic loading attenuated OVX bone loss in virgin rats and abolished the OVX bone loss in reproductive rats (Fig 1A). Loading also led to 7% increased trabecular thickness (Tb.Th) in virgin rats and abolished the OVX-induced reduction in Tb.Th in reproductive rats (Fig 1B). However, the extent of loading responses (loaded *vs.* non-loaded) was not different in trabecular bone between virgin and reproductive rats. On the other hand, loading increased the polar moment of inertia (pMOI) of tibial midshaft by 7% in virgin rats and 13% in reproductive rats (Fig 2A). Similarly, cortical area (Ct.Area) increased by 3% in virgin rats and by 6% in reproductive rats (Fig 2B). Moreover, ANOVA test indicated greater responses in pMOI and Ct.Area to loading (loaded *vs.* non-loaded) in reproductive rats than those in virgin rats. Representative dynamic histology images showed higher double-labeled bone formation in the loaded than the non-loaded tibia in both virgin and reproductive rats (Fig 2C-F). Lastly, results from bSEM images indicated a trend toward 11% greater lacunar area in reproductive rats than that in virgin rats (p=0.07, Fig 3).

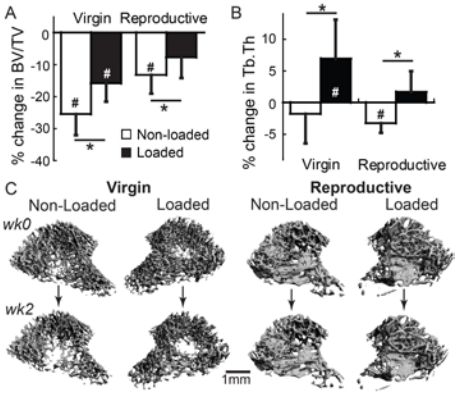

Fig 1. (A-B) Comparisons of % changes in trabecular bone between the non-loaded and loaded tibia in virgin and reproductive rats. p<0.05: # difference between wk0 and wk2 and * between responses in the non-loaded and loaded tibia. (C) Representative 3D tibial trabecular bone images.

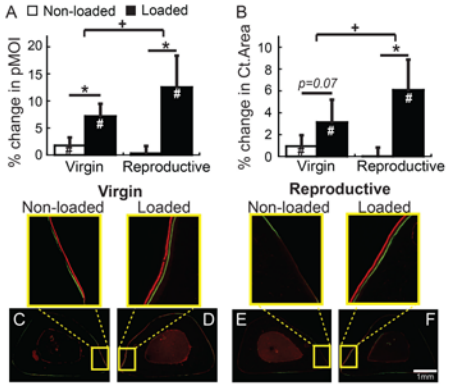

Fig 2. (A-B) Comparison of % changes in midshaft cortex between the non-loaded and loaded tibia in virgin and reproductive rats. p<0.05: # difference between wk0 and wk2; * between responses in the non-loaded and loaded tibia; + between loading response of virgin and reproductive rats. (C-F) Representative histology images of tibial midshaft.

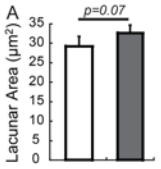

Fig 3. (A) Comparisons of lacunar area and (B) bSEM images between virgin and reproductive rats.

DISCUSSION: This study investigated the long-term effects of reproduction and lactation on bone's mechano-sensitivity and osteocyte micro-environment to estrogen deficiency later in life. The *in vivo* tibial loading dramatically reduced the extent of OVX bone loss and led to thickened trabeculae in virgin rats, and abolished OVX bone loss and trabecular thinning in reproductive rats. At tibial midshaft cortex, reproductive rats had greater extent of bone formation responses to loading than virgins. The above results suggested that rats with a reproductive history had an elevated mechano-sensitivity than virgins when subjected to estrogen deficiency, especially in cortical bone. Furthermore, we found that the reproductive rats tended to have greater osteocyte lacunar size compared to virgins post-OVX. As the presumed mechano-sensor in bone, the osteocyte and its process form an extensive lacunar-canalicular system (LSC) in bone matrix for signaling transportation and bone homeostatic regulation. Our results suggested that the osteocytes could directly modulate the peri-lacunar bone tissue, which could lead to enlarged lacunae after multiple reproductive cycles. According to the LCS fluid flow model established by Weinbaum *et al.* [8], the enlarged lacuna and canaliculi could contribute to the pericellular fluid space, leading to increased fluid flow on osteocytes when subjected to loading. This functional adaptation in osteocyte LCS micro-environment could enhance the mechano-sensitivity, which may protect the maternal skeleton from postmenopausal bone loss later in life. Thus, further tests with direct measurements of load-induced fluid flow in LCS [6] are necessary to establish the roles of osteocyte perilacunar remodeling on modulating bone's mechano-sensitivity in rats with different reproductive histories.

SIGNIFICANCE: Reproduction and lactation may exert long-term effects on bone's mechano-sensitivity to protect bone from estrogen deficiency. The osteocyte and its processes can actively remodel the peri-lacunar bone matrix to alter its microenvironment, thus regulating bone's mechano-sensitivity. This investigation provided new insight into osteoporosis prevention and treatment for postmenopausal women by considering their reproduction histories.

REFERENCE: [1] Kovacs CS, *Physiol Rev.*, 2015; [2] de Bakker CM *et al.*, *J Bone Miner Res.*, 2017; [3] de Bakker CM *et al.*, ORS 2017; [4] Qing H *et al.*, *J Bone Miner Res.*, 2012; [5] Kaya S *et al.*, *J Bone Miner Res.*, 2017; [6] Wang B *et al.*, *J Bone Miner Res.*, 2014; [7] Lan S *et al.*, *Bone*, 2013; [8] Weinbaum S *et al.*, *J Biomech.*, 1994.

ACKNOWLENDGEMENTS: NIH/NIAMS P30-AR050950, R03-AR065145, and R01-AR071718.

Lithium Treatment Improves Vertebral Trabecular Bone Architecture in Mucopolysaccharidosis I Dogs during Postnatal Growth

Sun H. Peck[1], Yian Khai A. Lau[1], Justin R. Bendigo[1], Megan Lin[1], Toren Arginteanu[1], Jessica H. Bagel[1], Patricia O'Donnell[1], Neil R. Malhotra[1], Peter S. Klein[1], Eileen M. Shore[1], Margret L. Casal[1], Lachlan J. Smith[1]
[1]University of Pennsylvania, Philadelphia, PA
sunchung@pennmedicine.upenn.edu

Disclosures: S. H. Peck (N), Y. K. A. Lau (N), J. R. Bendigo (N), M. Lin (N), T. Arginteanu (N), J. H. Bagel (N), P. O'Donnell (N), N. R. Malhotra (N), P. S. Klein (N), E. M. Shore (N), M. L. Casal (N), L. J. Smith (5-Ultragenyx; 9-ORS Spine Section)

INTRODUCTION: Mucopolysaccharidosis (MPS) I is a lysosomal storage disease characterized by deficient alpha-L-iduronidase activity, which leads to abnormal accumulation of incompletely degraded dermatan and heparan sulfate glycosaminoglycans (GAGs) [1]. MPS I patients present with severe spinal deformity, due in part to impaired vertebral bone formation during postnatal growth, which decreases quality of life and increases mortality [2]. Enzyme replacement therapy (ERT), the current clinical standard of treatment for MPS I, has been shown to attenuate progression of spine disease in MPS I dogs [3,4]. However, ERT is expensive, requires frequent and regular administration throughout the duration of the patients' lifetimes, and does not fully normalize bone formation even when commenced at birth [5]. Thus, it is important to identify alternative therapies that specifically target and enhance bone formation. Our previous work in other MPS subtypes with similar bone manifestations showed that impaired bone formation is due to failed hypertrophic differentiation of vertebral epiphyseal chondrocytes during postnatal development [6], which is associated with decreased Wnt signaling [7], an important regulator of endochondral ossification during postnatal growth. Therefore, we hypothesized that stimulating the Wnt signaling pathway would result in improved bone formation in MPS I. Lithium activates the Wnt pathway by inhibiting GSK-3β and is already FDA-approved for human use for treating bipolar disorder [8]. Thus, the objectives of this study were to 1) establish a lithium dosing and monitoring regimen and 2) investigate whether treatment with lithium can enhance bone formation during postnatal growth in MPS I in the naturally-occurring canine model.

METHODS: For this study, we used the naturally-occurring MPS I canine model, which mimics both the progression and pathological phenotype of the skeletal abnormalities found in human patients [9]. With IACUC approval, MPS I dogs (n=3) were treated orally with lithium carbonate daily from 14 days to 6 months-of-age. Following an initial 1 week period of low dose acclimation, the dose was gradually increased to 30-50 mg/kg in order to maintain serum lithium levels in the putative therapeutic range (0.5-1.5 mmol/L) [10]. Throughout the study, lithium doses were adjusted twice a week based on animal weight and serum analyses. At 6 months-of-age, serum was collected from the three lithium-treated MPS I dogs as well as age-matched unaffected control dogs (n=4) and untreated MPS I dogs (n=5) in order to measure bone-specific alkaline phosphatase (BAP) activity using a commercially available ELISA kit. All animals were euthanized following serum collection, and thoracic vertebrae were excised postmortem and analyzed using micro-computed tomography (μCT). Significant differences in BAP levels between all groups were determined using 1-way ANOVA with post-hoc Bonferroni test ($p<0.05$). Significant differences in μCT measurements between lithium-treated and untreated MPS I animals were determined using unpaired t-tests ($p<0.05$).

RESULTS: After the acclimation period, lithium treated MPS I dogs generally maintained serum lithium levels within the desired therapeutic range (Fig 1). While control dogs had significantly higher serum BAP than either the untreated or treated MPS I dogs, BAP levels were significantly higher in lithium-treated than untreated MPS I dogs (Fig 2). While bone volume fraction, bone mineral density, and trabecular thickness were not significantly different in lithium-treated MPS I dogs compared to untreated MPS I dogs, connectivity density and trabecular number were significantly higher, and trabecular spacing was significantly lower (Fig 3A, B). Preliminary cortical bone analysis showed no differences between groups. Upon clinical examination, forelimb and hindlimb joints of the MPS I lithium-treated animals presented with less swelling, less fluid retention, and better mobility than untreated MPS I animals.

DISCUSSION: Overall, these findings suggest that activating the Wnt pathway with lithium can alter bone turnover in MPS I animals. Our dosing regimen maintained serum lithium levels in the therapeutic range. Higher serum BAP levels in lithium-treated animals suggest increased bone formation, potentially due to increased osteoblast numbers or activity with treatment. Higher connectivity density and trabecular number and lower trabecular spacing in the lithium-treated animals also suggest improvements in bone microarchitecture. Importantly, these findings demonstrate that bone cells in MPS I are still able to respond to activating stimuli despite significant GAG storage and that Wnt pathway agonists may represent a potential therapeutic strategy for stimulating bone formation in MPS I. Furthermore, measuring BAP levels is a non-invasive method to detect increases in bone formation in patients as a result of therapeutic intervention. Decreased swelling and improved mobility of joints suggest that lithium treatment may be able to alleviate other related musculoskeletal symptoms of MPS I. Ongoing work will establish the underlying cellular basis of improved bone formation with lithium treatment in MPS I dogs and whether these alterations in trabecular bone architecture are associated with improved mechanical properties.

SIGNIFICANCE/CLINICAL RELEVANCE: MPS I is associated with debilitating skeletal disease stemming from impaired bone formation for which there is no effective treatment. Our results suggest that Wnt activation is a potential therapeutic strategy for stimulating bone formation in MPS I patients.

REFERENCES: [1] Scott+ Hum Mutat 1995; [2] White Rheum 2011; [3] Chiaro+ J Bone Min Res 2014; [4] Dickson+ Mol Gen Met 2010; [5] Yasin+ Spine 2014; [6] Peck+ Mol Gen Met 2015; [7] Peck+ ORS Trans 2016; [8] Hedgepeth+ Dev Biol 1997; [9] Haskins+ Pediat Res 1984; [10] Rosenthal + J Vet Pharmacol Therap 1983.

ACKNOWLEDGEMENTS: NIH (R03AR065142, R01AR071975, F32AR071298, R01DK054481, P40OD010939), Penn Orphan Diseases Center, National MPS Society Penn Center for Musculoskeletal Disorders. The authors thank the veterinary staff and students at the Penn School of Veterinary Medicine.

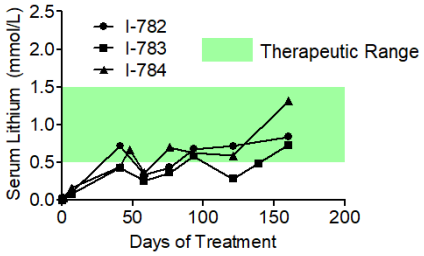

Figure 1. Serum lithium levels in treated dogs. Lithium-treated MPS I animals generally maintained serum lithium levels in the therapeutic range throughout the duration of the study under our dosing regimen. N=3, each line represents a lithium-treated MPS I animal.

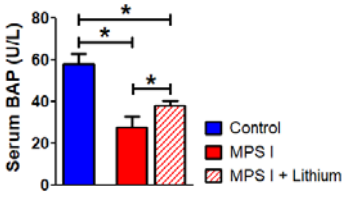

Figure 2. Serum bone-specific alkaline phosphatase (BAP) activity levels. Lithium-treated MPS I animals exhibited higher levels of BAP activity compared to untreated animals. Control (n=4), MPS I (n=5), MPS I lithium treated (n=3). *p<0.05.

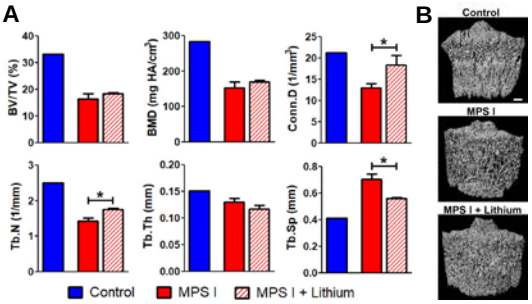

Figure 3. Micro-computed tomography (μCT) measurements of T12 vertebrae showed improvements in trabecular bone microarchitecture. A. Bone volume fraction (BV/TV), bone mineral density (BMD), connectivity density (Conn.D), trabecular number (Tb.N), thickness (Tb.Th), and spacing (Tb.Sp) from control (representative baseline), MPS I (n=3), and lithium-treated animals (n=3). *p<0.05. **B.** Representative 3D reconstructions of vertebral trabecular bone. Scale bar = 2 mm.

CD14 Deficiency Alters Bone Remodeling in a Murine Model of Osteoarthritis

Cheng Zhou[1, 2], Vu Nguyen[1, 2], Ryan R. Smalley[1], Nisha Sambamurthy[1, 2], Kurt Hankenson[4], George R. Dodge[1, 3], Carla R. Scanzello[1, 2]
[1]Translational Musculoskeletal Research Center, VA Medical Center, Philadelphia, PA, [2]Division of Rheumatology, [3]Deopartment of Orthopaedic Surgery, University of Pennsylvania Perelman School of Medicine, Philadelphia, PA; [4]University of Michigan, Ann Arbor, MI.

INTRODUCTION: Pathogenesis of osteoarthritis (OA) is accompanied by chronic inflammation. We previously reported high levels of soluble CD14, which is expressed by monocyte/macrophage lineage cells, and is a pattern-recognition receptor that facilitates Toll-like receptor (TLR) signaling. Upon binding, the CD14/TLR complex can activate cytokine production and promote chronic inflammation. Given that CD14 is expressed by osteoclast precursors, and TLR signaling influences osteoclast development and activation, we hypothesized that CD14 may play a role in bone remodeling after joint injury in a murine post-traumatic knee OA model.

METHODS: 10-12 week old male mice from CD14$^{-/-}$ and congenic C57BL/6 (WT) controls were subjected to destabilization of medial meniscus (DMM), sham surgery or left un-operated (Animal research was conducted with the approval of the IACUC of University of Pennsylvania and the CMCVA Medical Center). Mice were sacrificed at 6 and 19 weeks post-surgery, knees isolated, and cartilage and bone histopathology evaluated with the modified OARSI score. Micro-CT was used to measure subchondral bone mineral density (BMD) and trabecular thickness (TbTh). In separate experiments, bone marrow was isolated from tibias and fibulas of WT and CD14$^{-/-}$ mice at 10-12 weeks of age. Non-adherent cells were isolated after 24-hour initial culture, and then media containing M-CSF (35 ng/ml) was used to generate osteoclast precursors for 3 days. RANKL (100 ng/ml), along with M-CSF, was further added to promote osteoclast differentiation. After 5 days, TRAP+ (tartrate-resistant acid phosphatase) staining was assessed, and mRNA expression of calcitonin receptor and cathepsin K were measured using real time quantitative PCR. In the meantime, adherent bone marrow cells were subjected to osteoblastogenic differentiation with media containing β-glycerophosphate (10 mM), L-Ascorbic Acid (50 μg/ml), and dexamethasone (0.1 μM) for 21 days, mineralization deposit was assessed by Alizarin Red staining and quantification.

RESULTS: 6 weeks after DMM surgery cartilage histology was similar in the two strains, but at 19 weeks degeneration was significantly less in CD14$^{-/-}$ mice compared to WT (7.125 vs 16.22, p=0.0002). Micro-CT analysis showed age-related increases in BMD and TbTh in WT mice (12.8% increase at 19 weeks compared to baseline, p=0.006) but not in CD14$^{-/-}$ mice. CD14$^{-/-}$ mice were protected from surgery-related increases in BMD, which were observed in WT mice 6 week post-DMM: (7.3% increase in WT BMD DMM vs. naïve, p=0.04; 2.0% increase in CD14$^{-/-}$ BMD DMM vs. naïve, p=ns) (Fig 1, A-F). In response to M-CSF and RANKL, cells from CD14$^{-/-}$ mice showed less TRAP staining, reduced numbers of multi-nucleated cells, and lower expression of calcitonin receptor and cathepsin K compared to WT mice (Fig 2, A-F). No significant difference was seen in osteoblastic differentiation capacity in these two strains (data not shown, n=4).

DISCUSSION: CD14 deficiency significantly protected mice from subchondral bone changes after joint injury, and reduces the capacity of precursors to differentiate into osteoclasts. This was observed with both TRAP staining and quantitative gene expression of osteoclastic markers. Bone remodeling is dependent on both bone resorption and anabolism, therefore it is possible that the defect in osteoclastogenesis may inhibit the ability of the subchondral bone to remodel in response to age and joint injury. Further work is being pursued to determine if there are also differences in osteoclast resorption capacity function between these two strains that could explain the observation in this OA model.

SIGNIFICANCE/CLINICAL RELEVANCE: This study provides novel information to the pathologic bone remodeling in osteoarthritis models, and these results suggest a possible new therapeutic target to explore that could alter the clinical course of OA and joint health. The effect of CD14 on osteoclastogenesis may be relevant to other musculoskeletal disorders characterized by abnormal bone remodeling.

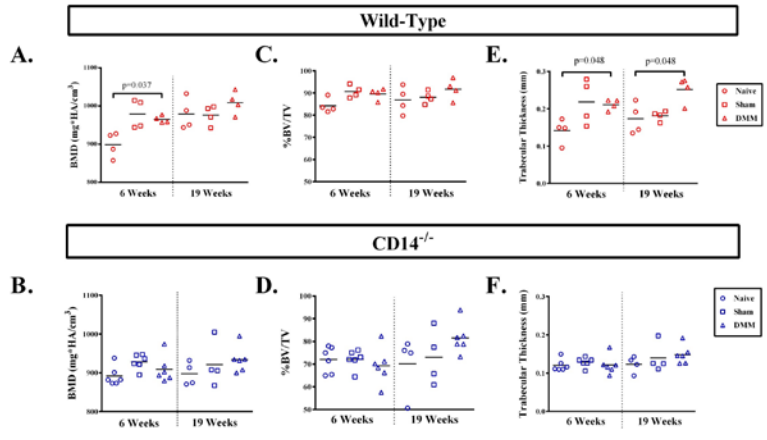

Figure 1. Micro-CT analysis of surgery-related changes in subchondral bone after joint injury.
A, C and E) depict trends in BMD, %BV/TV and Tb.Th respectively in WT mice. **B, D and F)** indicate trends in CD14$^{-/-}$ mice. (n=4-6 mice per group). P-values (multiplicity adjusted) obtained by Kruskal-Wallis multiple comparison test followed by Dunn's post-test.

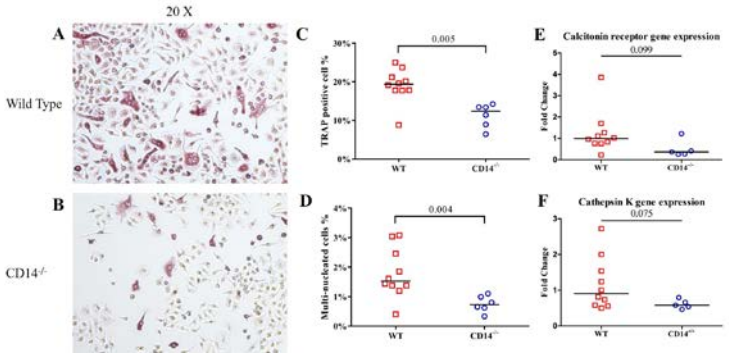

Figure 2. CD14 deficiency dampens osteoclastogenesis of bone marrow cells.
A-C) In response to M-CSF and RANKL, bone marrow cells from CD14$^{-/-}$ mice demonstrated decreased percentages of TRAP positive cells (Median = 12.40%) compared to WT (Median = 19.38%). **D)** Percentage of multi-nucleated cells were also reduced (CD14$^{-/-}$: Median = 0.73%, WT: median = 1.53%). **E-F)** CD14$^{-/-}$ osteoclast cultures exhibited lower expression of both calcitonin receptor and cathepsin K (median: 0.36- and 0.58-fold change, respectively) compared to WT mice in response to M-CSF and RANKL treatment.

Multi-Modal Image Registration and Spatial Analyses to Unravel Angiogenic-Osteogenic Coupling

Robert J Tower and Ling Qin
Department of Orthopaedics, University of Pennsylvania, Philadelphia, PA
rtower@mail.med.upenn.edu

Disclosures: All authors declare no conflicts of interest

INTRODUCTION: A close association has previously been observed between bone forming osteoblasts and angiogenesis during bone development, fracture healing and under normal remodeling conditions. This coupling of angiogenesis and osteogenesis, combined with an age-dependent decline in the bone marrow vasculature observed in both human and animal models, has suggested that disruption of this coupling may play a role in the onset and progression of metabolic bone disorders such as osteoporosis. Our goal was to develop 3D, multi-modal image registration techniques and spatial analyses to investigate the relationship between the bone surface and the recruitment of bone marrow vasculature under physiological and anabolic treatment conditions.
METHODS: *Animals*- All animal work performed was approved by the Institutional Animal Care and Use Committee (IACUC) at the University of Pennsylvania. C57BL/6 female 10-week-old mice, as well as mice injected 3 days or 14 days with the osteoanabolic agent parathyroid hormone (PTH), were injected with 15 mg/kg calcein 24 h prior to sacrifice 12 weeks. N=3 per treatment group. *Immunofluorescence*- Samples were fixed in 4 % PFA for 4 h, then embedded in OCT media. Femurs were bisected using a Leica cryostat, rinsed of OCT and stained for the blood vessel marker endomucin. *Tissue Clearing*- Stained, bisected bones were then subjected to tissue clearing using Murray's clear to permit deep tissue imaging up to ~300um. Samples are dehydrated using an ethanol gradient followed by treatment with benzyl alcohol and benzyl benzoate (BABB). *Imaging*- Cleared and stained samples were placed in small dishes with coverslip bottoms, using fresh BABB to mount. A ~4 mm^2 region encompassing the secondary spongiosa was imaged by a Zeiss LSM7 confocal microscope. *Micro-CT*- Bones were scanned *in vivo* at 10 weeks prior to treatment using the VivaCT 40 (Scanco Medical AG) at a resolution of 10.5 µm and after sacrificing and following bisection on the µCT 35 (Scanco) at a resolution of 6 µm. *Analysis*- Bone surface was established using calcein labeling and endogenous bone autofluorescence. Points spaced every ~6um were placed along the bone and blood vessel surfaces and a minimum distance analyses was carried using ImageJ to determine bone surface-blood vessel interactions. Confocal scans and micro-CT images were resampled, registered and transformed using Amira v5.3 (FEI). Time-lapse micro-CT was used to determine sites of bone formation and resorption. *Statistics*- All analyses were conducted by 1-way ANOVA with a bonferroni's post-test for multiple comparisons using Prism (GraphPad).
RESULTS: Rigid registration was conducted to identifying forming and resorbing bone regions (time-lapse micro-CT) (Fig 1A), as well as to do non-rigid registration between calcein surfaces, imaged by confocal microscopy, and micro-CT scans. Segmentation based on the labeling intensity of calcein, with highly active surfaces at the time of calcein injection labeled with a high intensity, less active or recently active surfaces labeling medium to low and non-active surfaces showing no notable calcein labeling (neg) was used to evaluate the bone metabolic activity. Time-lapse micro-CT and confocal registration following segmentation revealed that higher calcein intensity surfaces preferentially associate with formed bone determined from micro-CT, while resorbed surfaces preferentially associated with lower calcein intensity surfaces ($p<0.001$) (Fig 1B). Minimum distance analyses were next conducted on segmented confocal images (Fig 2A). Outer bone and blood vessels surfaces were extracted and measured points placed along the surface lengths (Fig 2B). Minimum distance spatial analyses showed that blood vessels were significantly closer to high and medium intensity bone surfaces than negative bone surfaces ($p<0.05$) (Fig 2C). Distance analyses were then conducted on mice treated for 3 or 14 days of PTH (Fig 2D). Micro-CT and confocal analyses confirmed the anabolic effects of PTH, with 14 day treatment resulting in a significant 38.1% increase in BV/TV ($p<0.05$) and 172% increase in calcein high surfaces ($P<0.05$) compared to control mice. Results revealed a significant redistribution of blood vessels to the bone surface following 14 days PTH treatment (Fig 2E), resulting in the average distance between the bone surface and the nearest blood vessel being reduced by 54.7% compared to control mice ($p<0.01$) and 46.5% compared to 3-day PTH treated mice ($p<0.01$).
DISCUSSION: Here we show the use of multi-modal image registration using *in vivo* and *ex vivo* micro-CT, along with deep tissue confocal imaging of cleared bones. Success of the registration is supported by a strong correlation between time-lapse micro-CT based forming and resorbing surfaces and high and low calcein intensities, respectively, determined by confocal microscopy. Furthermore, image segmentation was successfully used for both bone and blood vessel surfaces. These results support the preferential association of blood vessels with actively mineralizing surfaces rather than inactive, calcein-negative surfaces. Modulation of bone surface activity through treatment with the anabolic agent PTH was also able to show a significant redistribution of the bone marrow vasculature to the bone surfaces. Further works exploiting these image registration techniques will be used to unravel the spatial and temporal relationship between and angiogenic and osteogenic coupling.
SIGNIFICANCE/CLINICAL RELEVANCE: It is well established that the processes of angiogenesis and osteogenesis are coupled, though little remains known of the temporal and spatial characteristics of this coupling. By furthering our understanding of this coupling process with special emphasis on the temporal relationship, we may be able to utilize existing or develop novel therapeutics which could enhance angiogenic-osteogenic coupling useful in the treatment of a variety of metabolic bone disorders such as osteoporosis and in the treatment of non-union fractures.

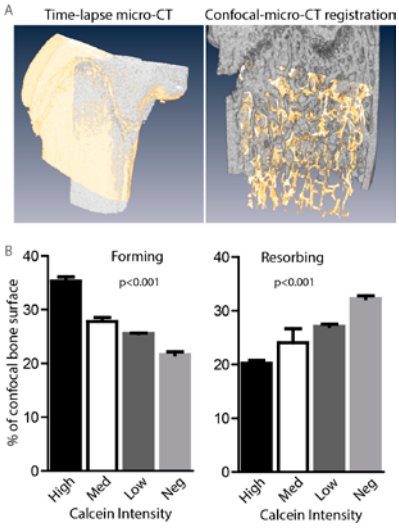

Figure 1 **Forming and resorbing surfaces, identified by time-lapse micro-CT, correlate with calcein intensities, determined by confocal microscopy**. (A) Amira was used to register *in vivo* micro-CT scans at 10 wks (left panel) or 12 wk confocal images (right panel) (orange) with the bisected bone scanned at 12 wks (grey). (B) Analyses show significant associations between formed bone and high calcein intensity, as well as resorbed bone with low calcein intensity. Values represent the average values of 3 animals ± SD, each measured at 3 separate regions. Statistics were calculated using 1-way ANOVAs

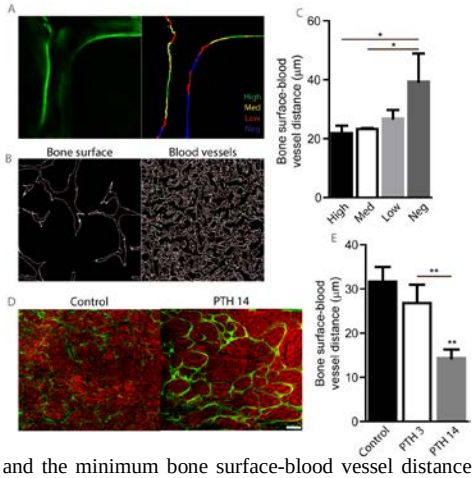

Figure 2 **Blood vessels are recruited to sites of active bone mineralization**. Calcein intensity was thresholded based on intensity (A). Bone and blood vessel surfaces (white outline) were labeled with individual measurement points (red points) (B) and the minimum bone surface-blood vessel distance calculated (C). Bisected and cleared femurs injected 24 h before sacrifice with calcein (green) were stained for the blood vessel marker endomucin (red) (D). Bar=100 µm. (E) Bone surface-blood vessel distance calculations following 3 days or 14 days PTH treatment. Values represent the average values of 3 animals ± SD, each measured at 3 separate regions. *p<0.05, **p<0.01, ***p<0.001

YAP and TAZ mediate osteocyte perilacunar/canalicular remodeling

Christopher D. Kegelman[1], Jennifer C. Coulombe[2], Kelsey M. Jordan[1], Daniel J. Horan[3], Alexander G. Robling[3], Virginia L. Ferguson[2], Teresita M. Bellido[3], and Joel D. Boerckel[1]

[1]University of Pennsylvania, Philadelphia, PA; [2]University of Colorado, Boulder, CO; [3]Indiana University School of Medicine, Indianapolis, IN

ckeg@seas.upenn.edu

Disclosures: Christopher D. Kegelman (N), Jennifer C. Coulombe (N), Kelsey M. Jordan (N), Daniel J. Horan (N), Alexander G. Robling (N), Virginia. L Ferguson (N), Teresita M. Bellido (N), Joel D. Boerckel (N)

INTRODUCTION: As the most abundant cell type in bone, osteocytes are critical mediators of skeletal mass and material quality. They reside in lacunae surrounded by a mineralized matrix through which an interconnected network of canaliculi exist that allows for cellular communication[1]. Through this widespread network, osteocytes mediate their effects on bone by regulating mineral homeostasis, facilitating skeletal mechanotransduction, and coordinating osteoblast-osteoclast coupled remodeling[2]. In addition to these functions, osteocytes direct resorption and deposition of bone surrounding their lacunae, a process called perilacunar/canalicular remodeling (PLR)[1-3]. Osteocyte PLR is critical for preserving bone matrix quality by permitting lacuno-canalicular network connectivity, organization of collagen, and matrix mineralization[3]. Extracellular matrix-degrading proteases (e.g. Mmp13 and cathepsin K, Ctsk) facilitate pericellular resorption while extracellular matrix forming genes like collagen (e.g. Col1a1) enable matrix deposition during PLR[3]. We recently found that conditional ablation of yes-associated protein (YAP) and transcriptional co-activator with PDZ-binding motif (TAZ) from osteoblast lineage cells caused neonatal lethality and reduced bone formation with severely impaired collagen content, organization, and expression[4]. However, we could not distinguish between the effects of YAP/TAZ deletion in osteoprogenitor cells from osteocytes as our model targeted deletion in both of these cell types. As skeletal cell YAP and TAZ play critical roles in regulating bone quality, we next tested their role in osteocyte-mediated processes including PLR by ablating YAP and TAZ from 8kb-DMP1-Cre expressing cells (i.e. from osteocytes).

METHODS: We generated a conditional loss-of-function mouse model with dual deletion of YAP and TAZ through Cre-recombination under control of the 8kb-DMP1 promoter. All animal experiments were approved by the IACUC. We employed a breeding strategy to produce allele-dosage dependent deletion of YAP and/or TAZ, but only double homozygotes ($YAP^{fl/fl}$;$TAZ^{fl/fl}$;DMP1-Cre, hereafter cDKO) had a significant deficit in long bone growth. These were further compared with $YAP^{fl/fl}$;$TAZ^{fl/fl}$ (WT) littermates. At 12 weeks of age, long bones (i.e., femurs and tibiae) from both WT and cDKO were harvested for analysis. The right femur was scanned by microCT (vivaCT80) and tested in three-point bending to failure. Femurs were then decalcified, processed for histology and second harmonic generation imaging, and immunostained for MMP13 and Cathepsin K. Messenger RNA was isolated from contralateral limbs and evaluated by qPCR. Right tibiae were used to visual the osteocyte-network via Ploton silver nitrate staining. Left tibiae underwent non-destructive X-ray microscopy imaging (Zeiss 520 Versa; 0.6 μm voxels) to quantify osteocyte lacunar shape and orientation. Methyl-methacrylate-embedded bones from a separate cohort of 3-week-old mice, injected with Calcein and Alizarin Complexone at 26 and 28 days, respectively, were processed for dynamic bone histomorphometry. Comparisons were made using Student's t-tests, with data log-transformed to achieve homoscedasticity, when necessary. A p-value less than 0.05 was considered significant.

RESULTS: DMP1-conditional YAP/TAZ deletion reduced femoral bone accrual in both cancellous and cortical compartments (Fig. 1A), reduced osteoblast number (Ob.N/BS) and bone formation rate (BFR/BS), and increased osteoclast surface (Oc.S/BS) (data not shown). YAP/TAZ deletion impaired matrix collagen content and organization, (Fig 1B,C; N=8) and reduced collagen 1a1 gene expression (Fig. 1D; N= 6), which significantly contributed to bone matrix mechanics (Fig. 1E,F;N=8). X-ray microscopy demonstrated that YAP/TAZ deletion reduced lacuna number and increased lacuna oblateness, an indication of more plate-like lacunae (Fig. 2A-C; N=4). YAP/TAZ deletion increased the percentage of empty lacunae (data not shown), reduced mean osteocyte process length (Fig. 3A,B; N=8), and reduced osteocyte expression of MMP13 and Ctsk at both protein and message levels (Fig. 3C-F; N=8).

DISCUSSION: Here, we show that YAP/TAZ deletion from DMP1-expressing cells impairs bone quantity and quality by both osteocyte coordination of osteoblast-osteoclast bone remodeling and by osteocyte perilacunar-canalicular remodeling. Osteocyte YAP/TAZ regulated bone mechanical behavior in part through collagen matrix content, organization, and gene expression. In addition, osteocyte YAP/TAZ mediated local perilacunar-canalicular remodeling by regulating matrix protease expression, altering lacuna number and shape and canalicular length. We conclude that YAP/TAZ promote expression of extracellular matrix formation (collagen) and degradation enzymes (Mmp13, Ctsk) by osteocytes to enable canalicular network connectivity and preserve bone matrix quality. Taken together, these data identify YAP/TAZ signaling as a novel pathway mediating the critical effects of osteocyte PLR on bone quality during skeletal growth and homeostasis.

SIGNIFICANCE/CLINCAL RELEVANCE: A mechanistic understanding of how YAP/TAZ signaling regulates osteocyte PLR could guide future therapeutic strategies for diseases associated with bone fragility, including osteogenesis imperfecta and osteoporosis.

REFERENCES: [1] Tokarz+ *JBMR*, 2017; [2] Qing+ *JBMR*, 2012; [3] Dole+ *Cell Press*, 2017; [4] Kegelman+ *FASEB J*, 2018

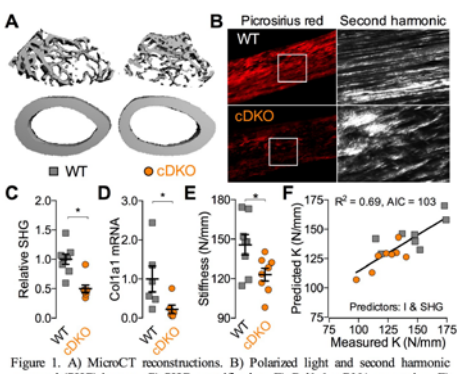

Figure 1. A) MicroCT reconstructions. B) Polarized light and second harmonic generated (SHG) images. C) SHG quantification. E) Col1a1 mRNA expression. E) Bending stiffness. F) Multivariate model of bending stiffness (K) with signficant predictors moment of inertia (I) and SHG.

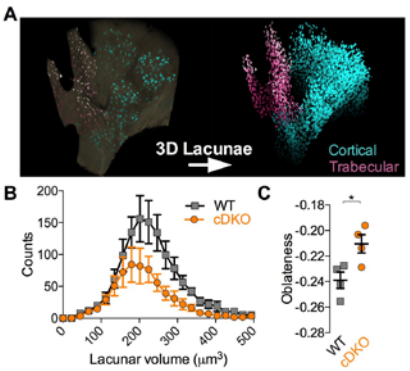

Figure 2. A) X-ray microscopy imaging of 3D osteocyte lacunae. B) Lacunae volume distributions in trabecular bone. C) Lacunae oblateness (-1 is perfectly rod-like and +1 is perfectly plate-like).

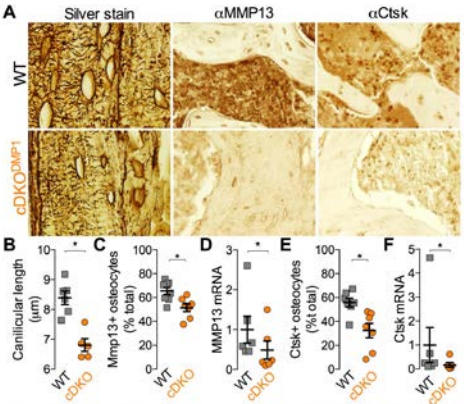

Figure 3. A) Silver staining and immunostaining for MMP13 and Ctsk. B) Mean canalicular length, C) Percent MMP13-positive osteocytes. D) MMP13 mRNA expression. E) Percent Ctsk-positive osteocytes. F) Ctsk mRNA expression.

Bioactive Factor Release from Acellular Hyaluronic Acid Scaffolds Enhances Articular Cartilage Repair in a Large Animal Model

Anthony R. Martín[1,2], Jay M. Patel[1,4], Michael R. Eby[1,2], Mackenzie L. Sennett[1,4], Andrew H. Chang[2], Hannah M. Zlotnick[1,3], Matthew D. Davidson[3], James L. Carey[1,2], Jason A. Burdick[3], Robert L. Mauck[1,3,4]

[1]McKay Orthopedic Research Laboratory, University of Pennsylvania, Philadelphia, PA; [2]Perelman School of Medicine, University of Pennsylvania; [3]Department of Bioengineering, University of Pennsylvania; [4]Translational Musculoskeletal Research Center, Philadelphia VA Medical Center

Disclosures: RL Mauck (8, *JOR Spine*), no other disclosures.

Introduction: Articular cartilage is often damaged during extreme impact or torsional joint loading[1]. Large focal cartilage injuries often progress to osteoarthritis, a costly epidemic affecting over 30% of adults in the United States[2]. To treat these patients, cartilage repair therapies often use cell-seeded scaffolds, which require preliminary cartilage biopsies and are limited by donor site morbidity, high costs, and poor efficacy in patients with mechanical or medical comorbidities[3–5]. To address these limitations, we developed a cell-free hyaluronic acid (HA) scaffold with two embedded signaling proteins designed to enhance cartilage repair: Stromal Cell-Derived Factor-1α (SDF-1α) chemokine to increase the recruitment of mesenchymal stem cells (MSC)[6] and Transforming Growth Factor-β3 (TGF-β3) to enhance cartilage regeneration[7]. The objective of this study was to evaluate the effect of SDF-1α and TGF-β3 incorporation into electrospun nanofibrous HA scaffolds on cartilage regeneration in a large-animal full-thickness chondral defect model. We hypothesized that SDF-1α and TGF-β3 release from the scaffold would synergistically improve cartilage defect repair.

Methods: Scaffold Fabrication: To study the interactivity of the bioactive factors, four scaffold groups were tested: 1) Scaffold (without signaling proteins), 2) SDF-1α, 3) TGF-β3, and 4) SDF-1α + TGF-β3. HA (76 kDa) was methacrylated (MeHA, 45% modification) and conjugated with RGD to promote better cell attachment. A solution of MeHA (4% w/v), polyethylene oxide (PEO, 900 kDa, 2% w/v), and photoinitiator (Irgacure 2959, 0.05% w/v) in ddH20 was electrospun into nanofibrous scaffolds[7], with or without growth factor. Samples (4.5mm diameter) containing protein had a theoretical maximum of 21.25 ng SDF-1α (0.002361%mass) and/or 106.29 ng TGF-β3 (0.011805%mass), embedded within the electrospun nanofibers. Scaffold Characterization: Scaffold micro-structure was visualized using scanning electron microscopy, and fiber diameter was measured using ImageJ (n=10). Scaffold degradation was measured using a uronic acid assay after incubation in PBS at 37ºC for 1, 7, 14, and 35 days (n=8). To determine *in vitro* bioactivity, scaffolds were co-cultured with bovine MSC pellets (300,000 cells) for 4 weeks (n=4). Pellets were sectioned and stained for proteoglycan content (Safranin O/Fast green). Scaffolds were seeded with labeled bovine MSCs (100,000 cells), cultured for 1 week (n=5) in chondrogenic media, and imaged on a confocal microscope to measure infiltration. Animal Model: Six male juvenile Yucatan Minipigs (5-6 months, 30-40 kg) underwent bilateral stifle joint surgery[7]. In each knee, four full-thickness trochlear cartilage defects were created using a 4mm-diameter biopsy punch, and all defects were subject to microfracture (MFx). Three defects per joint were filled with scaffolds from the same group to prevent protein cross-contamination, and one defect per joint was left without scaffold, as a MFx control (**Fig 1A**). All defects were coated with fibrin sealant (TISSEEL) to provide initial fixation. Animals received bisphosphonate therapy (alendronate, 40 mg/day) from 2 weeks prior to surgery through euthanasia to reduce subchondral bone remodeling[8]. Animals were euthanized 12 weeks post-op and underwent second-look arthroscopy (**Fig 1B**) for ICRS Cartilage Repair Assessment by 3 blinded reviewers[9] (n=3 knees per group, 3 replicates per knee). Defect sites and healthy control regions (**Fig 1C**) were harvested as osteochondral blocks and mechanically tested using a 2 mm spherical indenter on an Instron 5848. Four steps of 10% strain (0.1%/s) and equilibration (600s) were applied, and the data was analyzed with a custom MATLAB algorithm to determine equilibrium modulus (n=3 x 3 replicates).

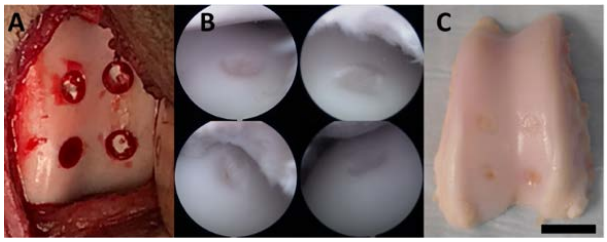

Figure 1. Cartilage defects in a minipig trochlea. (A) Scaffolds implanted in 4mm defects at the time of implantation. (B) Second-look arthroscopy 12 weeks post-op. (C) Gross trochlea harvested 12 weeks post-op (scale bar = 10mm).

Results: Fiber diameter was not significantly different between the four scaffold groups fabricated and averaged 190.43 ± 5.67 nm. Scaffold groups swelled uniformly overtime from 0.49 ± 0.01 mm to 1.41 ± 0.05 mm at 24 hrs. The minipigs had varying cartilage thickness at baseline, ranging from 1.38 to 2.00 mm. Scaffold groups degraded uniformly over time with roughly 50% degradation at 5 weeks. MSC pellets cultured with scaffolds releasing TGF-β3 showed increased proteoglycan staining (**Fig 2 Left**). MSCs seeded onto scaffolds releasing SDF-1α and/or TGF-β3 showed greater infiltration into scaffolds (**Fig 2 Right**). Second look arthroscopy revealed that TGF-β3 and SDF-1α+TGF-β3 groups trended towards out-scoring Scaffold and SDF-1α groups, but not MFx (**Fig 3A**). Indentation testing of cartilage repair sites revealed that all scaffold groups outperformed MFx, but groups with signaling proteins were not different from each other or control (**Fig 3B**).

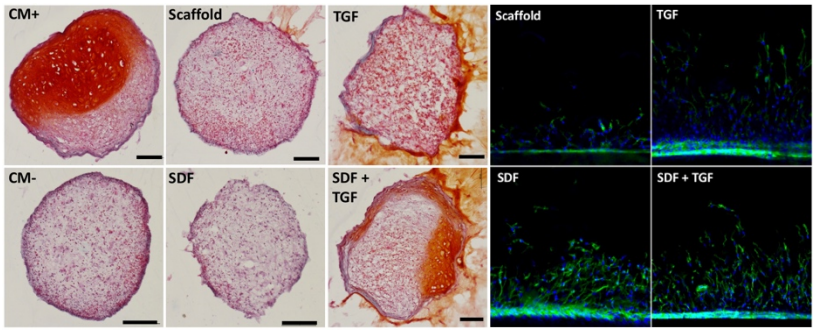

Figure 2. In vitro evaluation of bioactive factor activity. (Left) MSC pellets cultured for 4 weeks in chondrogenic media with (CM+) or without (CM-) soluble TGF-β3 or scaffold (others), Safranin O /Fast Green. Scale bar = 100 um. (Right) MSCs cultured on scaffolds for 1 week and imaged with confocal microscope with Hoechst (blue, nuclei) and Phalloidin (green, actin) stains to measure infiltration.

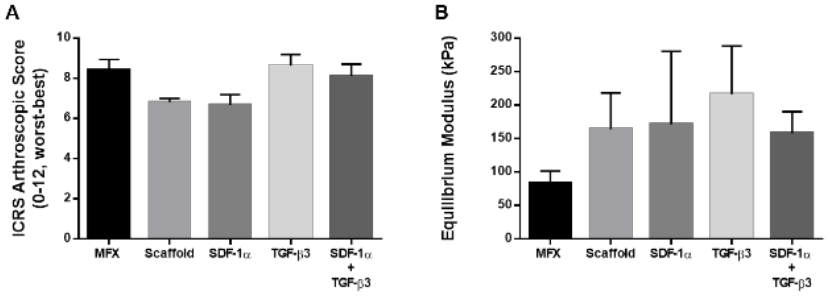

Figure 3. In vivo evaluation of cartilage repair. (A) ICRS Arthroscopic Repair Assessment scoring 12 weeks post-op. (B) Indentation testing of repaired cartilage 12 weeks post-op.

Discussion: This study demonstrates the ability to incorporate more than one signaling protein into electrospun HA scaffolds, which could serve as a platform for a variety of regenerative medicine applications. Preliminary data suggests that TGF-β3 released from scaffolds improves cartilage repair, but that the addition of SDF-1α does not augment this effect as hypothesized. Future data analysis includes dual protein release profiles, quantification of pellet chondrogenesis and MSC infiltration, microCT of osteochondral samples to measure defect fill, and defect repair histological scoring.

Significance: The incorporation of bioactive factors into novel scaffold technologies has the potential to improve tissue repair and regeneration.

References: 1) Buckwalter+ 2002 CORR, 2) Jafarzadeh+ 2018 Arth Rheum, 3) Mistry+ 2017 Health Tech Asses, 4) Wylie+ 2016 Arthroscopy, 5) Filardo+ 2013 AJSM, 6) Purcell+ 2012 Biomaterials, 7) Kim+ 2015 Tissue Eng, 8) Muehleman+ 2009 J Orth Res, 9) Smith+ 2005 AJARS

Acknowledgments: This work was supported by the AOSSM and the NIH NCATS.

Ciliary IFT20 and IFT80 are required for intervertebral disc development and maintenance

Xinhua Li[1], Jormay Lim[1], Zuozeng Tian[2], Yejia Zhang[2], Shuting Yang[1], Lin Han[3] and Shuying Yang[1]*

[1]Department of Anatomy and Cell Biology, School of Dental Medicine, University of Pennsylvania; [2]Department of Physical Medicine & Rehabilitation, Perelman School of Medicine, University of Pennsylvania, Philadelphia, PA; [3]School of Biomedical Engineering, Science and Health Systems, Drexel University, Philadelphia; *Corresponding author: Dr. Shuying Yang, shuyingy@upenn.edu

Rationale: Intervertebral disc disease (IVDD) is one of most common musculoskeletal diseases in the world. Pathological mechanism of this disease remains unknown, which restricts the effective treatment. Cilia are microtubule-based organelles extend from the cell surface into the extracellular environment. There are two types of cilia, motile cilia and primary cilia. Primary cilia play important roles in polarity maintenance and mechano and chemical signaling sensing and cell behaviors to affect organ development and pathological changes including musculoskeletal system. However, it is largely unknown whether and how cilia and IFT proteins are involved in intervertebral disc (IVD) development and maintenance.

Methods: To address these unknown questions, we first detected cilia formation in IVD by using the cilia-GFP transgenic mice, and in bovine tail and human lumbar IVD. We further utilized the mice IVD tail injury model to characterize whether cilia were affected in the injured IVDD mouse by performing immunofluorescence staining for acetylated tubulin, which marks the cilia. To determine how ciliary IFT80 and IFT20 affect IVD development, we generated the mice with cartilage and annular fibrosus (AF) specific tamoxifen induced deletion of IFT80 and IFT20 by crossing Collagen type II (Col2CreERT) and Collagen type I Cre (Col1CreERT) with the $IFT80^{f/f}$ and $IFT20^{flf}$ mice respectively. The phenotype of two mice strains were analyzed by performing MicroCT, histology and scanning electron microscope (SEM). The IVD, annual fibrosis cell(AFC) and nucleus pulposus cell (NPC) from the tail were isolated for gene expression level analysis in vitro.

Results: we found that cilia length was significantly different in NP and AF. About 15-30% cells were ciliated in the mouse, and the cilia length varied 0.5-4 μm in the mouse, bovine and human AF. Whereas, in mouse NP, about 15-48% cells were ciliated and the cilia length were varied 1.5-15μm. The cilia number significantly reduced in the injured IVD when comparing with the control. The trabecular bone markedly decrease in the vertebral of $IFT20^{flf}$Col1CreERT or $IFT80^{f/f}$ Col1CreERT mice comparing to the control cre. HE and sarfarnin o fast green staining revealed a noticeable and similar phenotype in IVD in $IFT20^{flf}$Col2CreERT or $IFT80^{f/f}$ Col2CreERT mice : the chondrocytes were disorganized in growth plate; the annular fibrosus were disorganized and fissured; the endplate cartilage was thinner and the cells were underdeveloped and smaller. In the $IFT20^{flf}$Col1CreERT and $IFT80^{f/f}$ Col1CreERT mice, the outer annular fibrosus were disorganized. The cilia number in the IVD were significantly reduced compared to that in the control mice. SEM results showed that the collagen fibers in AF were disorganized, and the average diameter of fiber decreased from 75.9±14.7nm in $IFT80^{flf}$ (74.5±15.0 in $IFT20^{flf}$) to 41.1±15.1nm in $IFT80^{flf}$Col1CreERT (43.5±10.5nm in $IFT20^{flf}$Col1CreERT) mice ($P<0.001$). The expression level of collagen I in AF and sox9, aggrecan, colagen2 in NP were significantly decreased in both IFT20 or IFT80 mutant mice and in vitro cell culture compared to those in control groups.

Conclusion: Our data revealed that ciliary IFT80 and IFT20 are important for IVD development and collagen fiber formation and orientation in mice.

Significance: Revealing the function and mechanism by which IFT80 and IFT20 regulate IVD development, and maintenance will provide new insights into the etiologies, diagnosis, and new prevention and treatment strategies of IVD and related diseases.

Acknowledgments: This work was supported by a National Institute of Health grant DE023105 (S. Yang) and AR061052 (S. Yang)

Atrophic Non-union Fracture is Caused by Severe Damage on Periosteal Mesenchymal Progenitors and Fibrosis Derived from Non-osseous Tissue

Luqiang Wang, Robert Tower, Abhishek Chandra, Yejia Zhang, Xiaowei Liu, Joel Boerckel, Xiaodong Guo, Jaimo Ahn, Ling Qin

Fractures represent a substantial economic burden to our society. The atrophic non-union of a fracture is especially challenging, as it often requires additional surgeries to overcome the lack of inherent biology in a regenerative healing process gone awry. Using a focal irradiator for rodents, we reproducibly created a nonsurgical atrophic non-union model in mice. 2-month-old male mice received radiation (8 Gy, day 1 and 3) at the mid-shaft of right tibiae (5 mm long) followed by bilateral, transverse tibial fractures on day 15. MicroCT and mechanical testing at day 57 (n=9) revealed that, in sharp contrast to bone healing in contralateral tibiae, fractures in irradiated tibiae did not show any bony bridging, resulting in 100% non-union. Histology at days 22, 29, 43, and 57 (n=6-9/time point) revealed that irradiated tibiae show less robust endochondral healing at the proximal side (region close to the knee) and a clear biologic non-union response on the distal side (region close to the ankle) with exclusive fibrotic cells and type I collagen matrix. These fibrotic cells did not stain for osteogenic (osterix and osteocalcin) and chondrogenic (Sox9 and type II collagen) markers, nor did they express VEGF. Thus, histology and microfil perfusion showed no vessel infiltration in this region. Characterization of tissues from clinical human atrophic non-union paralleled our mouse findings. Mechanistically, radiation blunted the injury response of periosteal mesenchymal progenitors at 3 days post fracture, resulting in a 67% reduction in their proliferation rate and an 83% reduction in periosteum thickness (n=6). In vitro, radiation hindered osteogenic differentiation of periosteal mesenchymal progenitors but did not affect hypoxia-induced chondrogenesis of these cells. Lineage tracing using mouse models that specifically labeled bone mesenchymal cells (Col2-Cre, aSMA-CreER, and Gli1-CreER in combination with Rosa-Td) revealed that non-union fibrotic cells did not originate from periosteal progenitors but from progenitors residing in non-osseous tissues. In addition, we surgically removed periosteum at either side or both sides of the mouse tibial fracture site and found that it eventually leads to atrophic non-union with fibrosis formation only at the surgery side(s). In summary, we demonstrate that atrophic non-union fracture is caused by severe damage to the periosteal mesenchymal progenitors with fibrosis formation that is derived from non-osseous tissue.

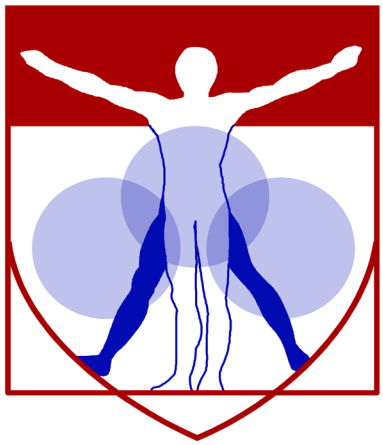

PENN

CENTER for

MUSCULOSKELETAL

DISORDERS

Miscellaneous Abstracts

Osmotic Annealing Generates a Suite of Mechanically-Activated Microcapsules for Tunable Drug Delivery

Ana P. Peredo[1,2], Gang Duan[1], Bhavana Mohanraj[1,2], Daeyeon Lee[1], George R. Dodge[1,2], Robert L. Mauck[1,2]
[1] Department of Orthopaedic Surgery, University of Pennsylvania, [2] Translational Musculoskeletal Research Center, CMC VAMC, Philadelphia, PA
anapperedo@gmail.com

DISCLOSURES. GR Dodge (4, 6, 8, 9), RL Mauck (8), all others none.

INTRODUCTION. Drug delivery systems that employ physiological stimuli to trigger release (e.g. temperature, pH, etc.) allow for precise control and on-demand provision of biological factors in a physiologic setting [1]. However, to date, few systems have employed the mechanical environment as a means for such activation [2]. Many tissues, especially in the musculoskeletal system, experience significant loading during the activities of daily living. Moreover, with injury or degeneration, normal loading patterns can shift to aberrant, supra-physiological states, which can intensify damage and promote degeneration [3]. Delivering therapeutic molecules in response to normal loading (and overloading) as well as loading regimens during post-surgical therapy, could provide precise spatiotemporal control of the release of biomolecules to maintain tissue homeostasis and/or promote tissue repair. To that end, we recently developed mechanically-activated microcapsules (MAMCs) [4-5]. In that work, differing thresholds for mechano-activation were achieved by changing polymer formulations and fabrication parameters. To extend the range of possible mechanical activation profiles, this study used osmotic annealing (**Fig 1A**) during fabrication to tune capsule size and shell thickness, and characterized MAMC activation in 2D and 3D environments (with static and cyclic loading) as well as their stability in a physiologically relevant synovial fluid setting.

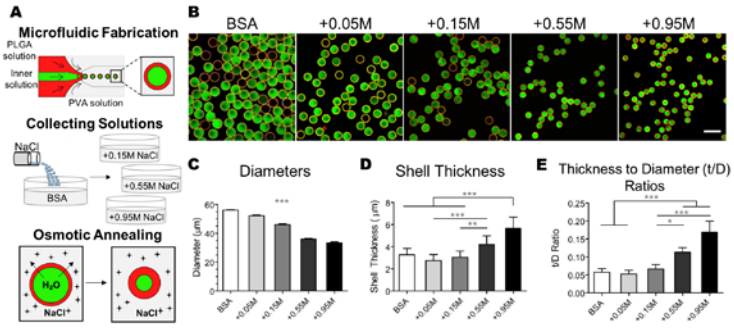

Figure 1. (A) Osmotic annealing was achieved by varying the osmolarity of the collecting solutions. **(B)** This generated MAMCs with a range of sizes and shell thicknesses. **(C)** Increased osmolarity decreased MAMC diameter and increased shell thickness (**D**), resulting in an increased t/D ratio (**E**). (Scale bar=100μm; *p≤0.05, **p≤0.01, ***p≤0.001).

METHODS. MAMCs were fabricated using a glass capillary microfluidic device [6]. The inner phase contained bovine serum albumin (BSA) and Alexafluor488-BSA, while the middle phase contained poly(lactic co-glycolic) acid (PLGA) 85:15 (with Nile Red for visualization). Osmotic annealing was performed by collecting MAMCs into NaCl solutions of different osmolarities prior to hardening. Final MAMC dimensions were measured by confocal microscopy (**Fig 1C-E**). To determine mechano-activation thresholds, MAMCs were compressed between parallel plates at 0.5% strain/sec to different loads and imaged after overnight incubation (**Fig 2A**). To evaluate response in 3D, MAMCs were embedded in 500kPa PEGDA hydrogels (19%w/v). Using a custom confocal mounted compression device [7], MAMC-containing hydrogels were compressed from 0-30% strain at 5% strain steps. Gels were imaged at each step to evaluate MAMC deformation (**Fig 2B**). To determine durability under cyclic loading, MAMC-containing hydrogels were loaded between parallel plates from 2-20% strain at 5Hz for different loading durations, and imaged (**Fig 2C**). Finally, to investigate MAMC stability in a more physiologic 'synovial-like' setting, MAMCs were incubated in PBS, basal media (with 10% FBS), or bovine synovial fluid at 37ºC for up to 2 weeks, with imaging on 1, 7, and 14 days. Normally distributed data was analyzed by one-way ANOVA followed by Tukey's post-hoc; non-normally distributed data was analyzed via Kruskal-Wallis test with Dunn's Multiple Comparison or Bonferroni post-hoc.

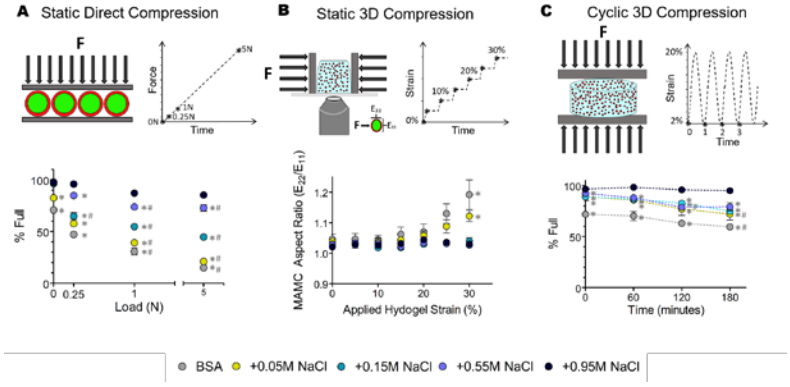

Figure 2. (A) Direct compression of MAMCs showed increased resistance to compressive load (F) with osmotic annealing. In 3D environments, osmotically annealed capsules deformed less with higher degree of annealing (higher NaCl content) **(B)** and resisted cyclic compressive loading to a greater extent **(C)**. (* p≤0.05 vs. +0.95M NaCl, # p≤0.05 vs. 0 Load, Strain or Minutes.)

RESULTS. Osmotic annealing decreased MAMC diameter and increased shell thicknesses as a function of osmolarity of the collecting solution (**Fig 1**). MAMCs did not form at 1.2 M, suggesting an upper limit for osmotic annealing. Direct compression testing showed that higher collecting osmolarities increased MAMC resistance to load (**Fig 2A**). In 3D environments, annealing at higher osmolarity decreased MAMC deformation during compression and increased resistance to rupture under cyclic loading (**Fig 2B-C**). Annealed MAMCs were stable in synovial fluid for over 2 weeks in comparison to MAMCs maintained in PBS and media (**Fig 3**).

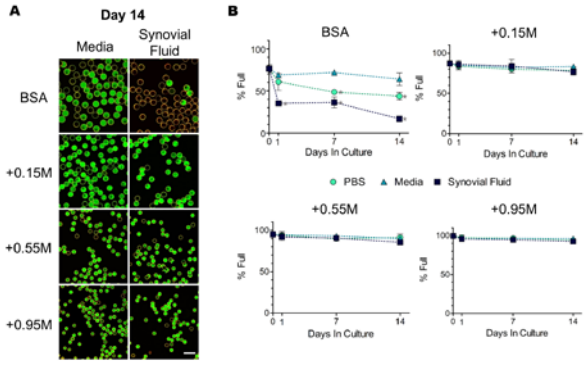

Figure 3. (A) Osmotically annealed MAMCs incubated for 14 days in media and synovial fluid showed increased stability and retention of contents compared to BSA MAMCs. **(B)** Quantification of percent full MAMCs over time. (Scale bar=100μm; * p≤0.05 vs. Day 0, # p≤0.05 vs. Media.)

DISCUSSION. Osmotic annealing expands the range of mechanical activation profiles that can be achieved with MAMCs, generating microcapsules with a greater resistance to static and dynamic compressive load in 2D and 3D environments and improved stability in synovial fluid. This modification does not require alteration of microfluidic parameters or polymer composition, providing a straightforward means for generating a number of MAMC types in one run. The large suite of MAMCs developed in this study will allow for their combination to provide sequential on-demand delivery of molecules to musculoskeletal tissues in response to loading, allowing for programmed mechano-regulation of biomolecule presentation for tissue regeneration as well as therapeutic interventions to treat infection and inflammation.

SIGNIFICANCE. This novel fabrication method generates a suite of MAMCs with differing mechano-activation profiles in a single fabrication run, efficiently generating capsules with varying resistance to load and stability in synovial fluid. This delivery platform is easily tuned to physiologic and therapeutic loading patterns (and injury thresholds) to promote healing of musculoskeletal tissues.

REFERENCES. [1] Kost+ Adv Drug Deliv Rev 2001, [2] Korin+ Science 2012, [3] Sun+ Ann NY Acad Sci 2010, [4] Mohanraj+ 2016 ORS #282, [5] Mohanraj+ 2017 ORS #1405, [6] Tu+ Langmuir 2012, [7] Farrell+ Eur Cells & Mat 2012.

ACKNOWLEDGEMENTS. This work was supported by the National Institutes of Health (R01 AR071340).

Collagenase in the spinal facet joint induces pain & alters genes in the DRG absent any cartilage destruction

Meagan E. Ita[1], Christine L. Weisshaar[1], Beth A. Winkelstein[1,2]
[1]Bioengineering, [2]Neurosurgery, University of Pennsylvania, PA
meita@seas.upenn.edu

AIM OF INVESTIGATION: Joint degeneration causes pain, degrades tissues, initiates inflammation, and alters joint structure. Bacterial collagenase (BC) has been used in models of knee degeneration and induces cartilage damage, nociceptive protein increases, and pain. Although intraarticular BC induces cartilage degeneration in the lumbar facet joint, pain was not evaluated despite facets being implicated in painful spine disorders. This study tested whether intraarticular purified BC can induce pain in spinal facet joints, and investigated degenerative and nociceptive pathways in the peripheral and central nervous systems. Dorsal root ganglia (DRG) and spinal cord (SC) were assayed at day 7 for genes including substance P (SP), glial fibrillary acidic protein (GFAP), proinflammatory cytokines (IL1β, CCL2), matrix metalloproteinases (MMP8, MMP14) since they contribute to tissue degradation, their inhibitor TIMP1, and the ECM proteins thrombospondins (TSP1, TSP4) given their role in trauma and joint-mediated pain. Cartilage structure was also evaluated.

METHODS: Under IACUC-approval and inhalation isoflurane anesthesia, male Hotzman rats received a bilateral C6/C7 intraarticular facet injection (10μL) of purified BC (60U; CLSPANK) (n=11) in saline or saline vehicle (n=3). Mechanical hyperalgesia was measured using bilateral paw withdrawal threshold (PWT) at baseline and until day 7 or day 21. Differences in PWT were compared with a repeated-measures ANOVA and post-hoc Tukey tests. Gene expression in the C7 DRG and SC was measured at day 7, using real-time qPCR for target genes and calculated as fold-changes over the housekeeping gene CyA. Separate t-tests compared each gene. Structure of C6/C7 joints was assessed at day 21 (n=3) using coronal-sections (16μm), and stained with Safranin-O/Fast Green. A modified Mankin score was used to grade articular surfaces: normal (0) to maximally degenerate (10). Scores were averaged and compared by a Student's t-test.

RESULTS: Intraarticular BC in the spinal facet is sufficient to induce pain within 1 day that persists for at least 21 days; BC significantly lowers ($p<0.01$) PWT from baseline and compared to a vehicle injection through day 7, and the PWT remains below baseline through day 21 ($p\leq0.01$). All genes were assayed in the DRG (n=3/group) at day 7, with gene expression of SP in the DRG ($p=0.03$) decreasing, but IL1β ($p=0.03$) and TIMP1 ($p=0.04$) in the DRG increasing. Of the subset of genes assayed in the SC (SP, GFAP, IL1β) at day 7, none showed differences from vehicle control. Although pain persists at day 21 after BC, those joints do not exhibit signs of cartilage degeneration (2.9±0.5 Mankin score) compared to controls (3.3±0.0 Mankin score).

CONCLUSIONS: The increased IL1β, but not SP, gene is consistent with findings from DRG neurons exposed to BC in vitro and painful joint degeneration in vivo. Since cytokine-induced neuronal excitability is implicated in osteoarthritis, IL1β may contribute to pain. The decrease in SP may reflect joint afferent injury since SP decreases in DRG neurons after nerve injury. Although TIMPs regulate ECM degradation and TIMP1 increases, the lack of degeneration suggests its upregulation may reflect BC is a neural stimulus. Although sustained pain from unpurified BC has been attributed to joint destruction, pain persists here in the absence of any such evidence, further supporting that other mechanisms may be involved in pain maintenance. This corroborates clinical findings of negative associations between extent of structural degeneration and pain. Additional studies are needed to fully elucidate the molecular pathways driving onset of and sustained BC-induced pain, and whether that regulation is pre- or post-translational.

ACKNOWLEDGEMENTS/DISCLOSURES: This study was supported by the NIBIB (U01EB016638). The authors have nothing to disclose.

In Vivo Bone ^{31}P Relaxation Measurement and Its Implications on Mineral Quantification

Xia Zhao, Hee Kwon Song, Felix W. Wehrli
Department of Radiology, Perelman School of Medicine, University of Pennsylvania

Introduction

Although accurate knowledge of the relaxation times is critical to proper quantification of bone mineral phosphorus with solid-state ^{31}P MRI, the T_1 of bone ^{31}P is particularly difficult to measure[1-4]. Here we measured T_1 of bone ^{31}P in a cohort of healthy subjects with wide age range at 3 T, and the possible implications of errors in T_1 on ^{31}P quantification. The accuracy of the technique was analyzed by simulation and the measured T_1 and T_2* were subsequently used to estimate bone mineral density from ^{31}P zero echo time (ZTE) images. Repeatability was also evaluated in three subjects.

Methods

The tibial mid-shafts of ten healthy subjects (26 to 76 y/o) were scanned on a Siemens 3 T Trio system with a ^{1}H/^{31}P dual frequency birdcage calf coil. T_1 of bone ^{31}P was measured with a saturation recovery (SR) sequence. Bone ^{31}P spectrum was isolated from that of muscle metabolites via spectra subtraction, which was subsequently fitted to a Lorentzian. The fitting of integral of the Lorentzian lines obtained from different saturation recovery delays to a mono-exponential model yields T_1. Errors in T_1 estimation due to interference from metabolite signals was evaluated via simulation using literature value of relaxation times [5], taking into account B_1 inhomogeneity of the coil measured with the Bloch-Siegert method [6]. ^{31}P images were acquired with a custom-made ZTE-PETRA sequence [7, 8] and [^{31}P] was quantified relative to a calibration sample [9]. Three subjects underwent three scans each for test-retest repeatability evaluation.

Results

Figure 3a plots percent error in quantified [^{31}P] as a function of the error in relaxation times. Effects of relative contributions from metabolites to total signal on the relaxation times measured are shown in **Figure 3b**. **Table 1** summarizes the relaxation times measured for all ten subjects as well as bone [^{31}P] quantified from ZTE images using the measured relaxation values. Repeatability experiments yielded average coefficients of variation of 1.53% for T_1, 2.64% for T_2* and 4.77% for [^{31}P]. Neither the relaxation times nor [^{31}P] was found to be significantly correlated with age.

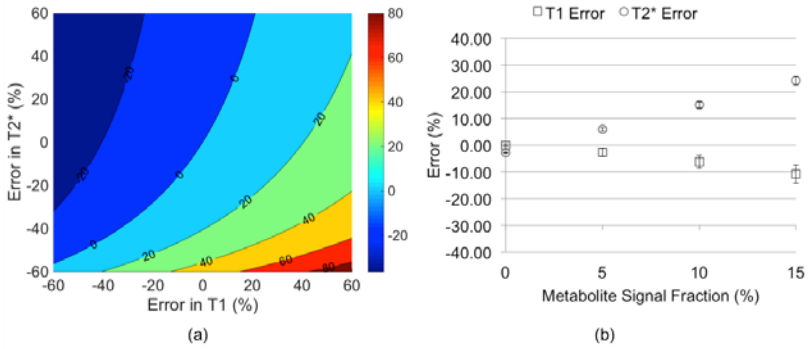

Figure 3. (a) Error in quantified [^{31}P] as a function of error in T_1 and T_2*. (b) Error in relaxation times measured with the method shown in **Figure 2,** versus metabolite signal fraction.

Table 1. Measured relaxation times and quantified bone ^{31}P concentrations.

	Measured T_1 (s)	Measured T_2* (μs)	Quantified [^{31}P] (mol/L)
26 M	36.1	185.7	5.56
30 F	35.7	202.7	6.45
33 M	34.7	213.9	5.97
44 M	38.7	190.1	7.57
51 F	37.9	190.5	6.55
58 F	37.6	188.6	5.92
60 F	36.7	185.7	5.70
61 F	35.0	206.4	5.62
65 F	36.9	206.5	5.61
76 F	38.5	198.4	6.02
Mean	36.8	196.9	6.10
SD	1.4	10.1	0.62

Discussion and Conclusions

Simulation suggests a progressive underestimation in T_1 with increasing fraction of metabolite ^{31}P in the total signal. Using typical muscle metabolite concentrations [10], bone [^{31}P] measured *ex vivo* [1] and muscle volume measured from gradient echo images, a rough estimate done on a few subjects indicated that over 90% of *in vivo* ^{31}P total signal actually originates from bone, limiting the measurement error for T_1 and T_2* to within -6% and 15%, respectively. According to the simulation, this magnitude of relaxation time error translates into an error in estimated [^{31}P] of less than 6.3% if relaxation is the only error source. The variation in T_1 across subjects observed in this study is very small (36.8±1.4 s), which parallels the relatively small variation in T_1 (96.7±10.8 s measured at 7 T) for a group of 16 tibia specimens from donors aged 27 to 97 years at death [1], and no correlation with age was observed in that study as well. In addition, mean [^{31}P] quantified using measured relaxation times in the present study (6.10±0.62 mol/L) is close to measurements *ex vivo* (6.74±1.22 mol/L) [1], where the experiment was free from interference of metabolites signal. In conclusion, the finding of the current study might obviate the need to measure individual bone ^{31}P T_1 altogether, using instead estimated values, thereby shortening the scan protocol.

References: 1. Seifert, A.C. et al. NMR Biomed (2014). 2. Seifert, A.C. NMR Biomed (2013). 3. Robson, M.D. et al. MRM (2004). 4. Wu, Y. et al. Calcif Tissue Int (1998). 5. Zhao, X. et al. PLoS One (2017). 6. Meyerspeer, M. et al. MRM (2003). 7. Sacolick, L.I. et al. MRM (2010). 8. Grodzki, D.M. et al. MRM (2012). 9. Li, C. et al. MRM (2016). 10. Kemp, G.J. et al. NMR Biomed (2007)

Acknowledgement: NIH R01-AR50068

Building a single-cell transcriptome atlas of mouse bone marrow mesenchymal lineage cells for analyzing MSC heterogeneity

Robert J Tower, Leilei Zhong, Jihwan Park, Luqiang Wang, Rojesh Shrestha, Katalin Susztak and Ling Qin

Stem cell heterogeneity and plasticity are common features of mammalian tissues. However, owing to a lack of investigative tools, whether bone marrow MSCs are made of heterogenic subpopulations has long been suspected, but never proven. The *Col2-Cre Rosa-tdTomato* (*Col2/Td*) specifically labels all mesenchymal lineage (MLin) cells, thus providing a perfect system to comprehensively analyze subpopulations of MLin cells in vivo. In this project, we enzymatically digested endosteal bone marrow from 1-month-old Col2/Td mice and sorted for the top 1% Td+ cells, which contained all the CFU-F forming cells found in unsorted cells. Cells were subjected to single-cell RNA sequencing using the 10X Genomics drop-seq platform. After rigorous quality control and exclusion of contaminating hematopoietic and endothelial cells, we identified 2,489 MLin cells expressing ~2500 sequenced genes per cell. Unsupervised clustering with Seurat divided those cells into 8 clusters (Fig. 1A). According to known markers, they are early MSCs (Sca1, CD34), late MSCs, chondrocytes (Col2a1, Col10a1), mesenchymal bi-potent progenitors (MBPs), osteoblasts (osteocalcin, Col1a1), osteocytes (SOST), adipoprogenitor (AP) 1, and AP2 (adiponectin, Lpl, Pparg). Interestingly, plots suggest that these cells exist in a continuum, rather than in discrete states. Cell cycle analysis based on the expression levels of >90 cell cycle-related genes revealed that early MSCs are quiescent; osteocytes are the least proliferative cells; AP1 and late MSCs are the most proliferative cells. Monocle trajectory analysis generated three differentiation directions with the first branch separating chondrocytes from MBPs and the second branch bi-pronged into osteoblasts and APs (Fig. 1B). Cells in AP clusters, particularly those in AP2, highly and specifically express Cxcl12 and LepR, resembling the previously identified CAR/LepR+ MSC population. Fluorescence imaging confirmed that in Col2/Td mice, Td+ stromal cells have reticular shape and that almost all LepR+ bone marrow cells were Td+. Interestingly, sequencing data suggests that these AP cells are a major source of cytokines and chemokines such as Scf, RANKL, VEGFs, Il6, Cxcl12, etc, indicating that they play important roles in regulating the bone marrow environment. Taken together, our work demonstrates the heterogeneity of bone marrow MSCs by identifying their novel subpopulations and delineating their relative positions along the MSC tri-differentiation axes.

Aberrant muscle tissue repair by mutant ACVR1 FOP muscle stem cells

Alexandra Stanley, Elisia Tichy, Foteini Mourkioti, and Eileen M. Shore
Perelman School of Medicine, University of Pennsylvania, Department of Orthopaedic Surgery, Cell and Developmental Biology, 3450 Hamilton Walk, Philadelphia, PA 19104, USA.

In the rare genetic disease fibrodysplasia ossificans progressiva (FOP), progenitor cells are mis-regulated to differentiate to heterotopic extra-skeletal bone in connective tissues. Mutations in the BMP type I receptor ACVR1/ALK2 cause FOP, with the R206H mutation as the most prevalent. Our lab previously identified that *ACVR1*^{R206H} increases both BMP ligand-dependent and ligand-independent signaling and promotes increased downstream chondro-/osteogenic gene expression and heterotopic ossification (HO) in FOP patients. HO formation in FOP is often initiated by injury within skeletal muscle. The regenerative potential of skeletal muscle is dependent on the function of muscle stem cells (MuSCs). Quiescent MuSCs are activated within 1-2 days after injury, quickly followed by proliferation, and then differentiation of cells until muscle architecture is restored. We developed an *Acvr1*^{R206H} mouse model that forms HO after cardiotoxin (CTX) injury to skeletal muscle. By 14 days, while muscle of CTX-injured WT animals is fully repaired, muscle tissue from *Acvr1*^{R206H} mice is fibrotic and has not repaired, indicating that muscle healing is impaired by the *Acvr1*^{R206H} mutation. Impaired muscle regeneration is accompanied by a substantial amount of HO within *Acvr1*^{R206H} muscle. BMP signaling has been shown to promote MuSC proliferation and repress their differentiation, leading us to hypothesize that *Acvr1*^{R206H} in MuSCs impairs their ability to regenerate muscle after injury. We examined the effect of the *Acvr1*^{R206H} mutation on MuSC proliferation specifically by isolating MuSCs using fluorescent activated cell sorting. No significant differences between proliferation of MuSCs from WT and FOP injured muscle tissue post-cardiotoxin (CTX) injury were detected, and the number of MuSCs isolated from FOP mice were comparable to that from WT mice. We next investigated the ability of WT and FOP MuSCs to differentiate. We cultured isolated WT and FOP MuSCs in myogenic fusion media and while WT MuSCs differentiate normally to form branching myofibers (high fusion index), FOP MuSCs form underdeveloped fibers that fail to fuse (low fusion index) (Figure One). These data indicate that the *Acvr1*^{R206H} mutation does not alter MuSC proliferation but has a negative impact on their ability to undergo myogenesis. On-going *in vivo* experiments will further elucidate the role of the MuSCs in response to the *Acvr1*^{R206H} mutation during muscle regeneration in response to tissue injury.

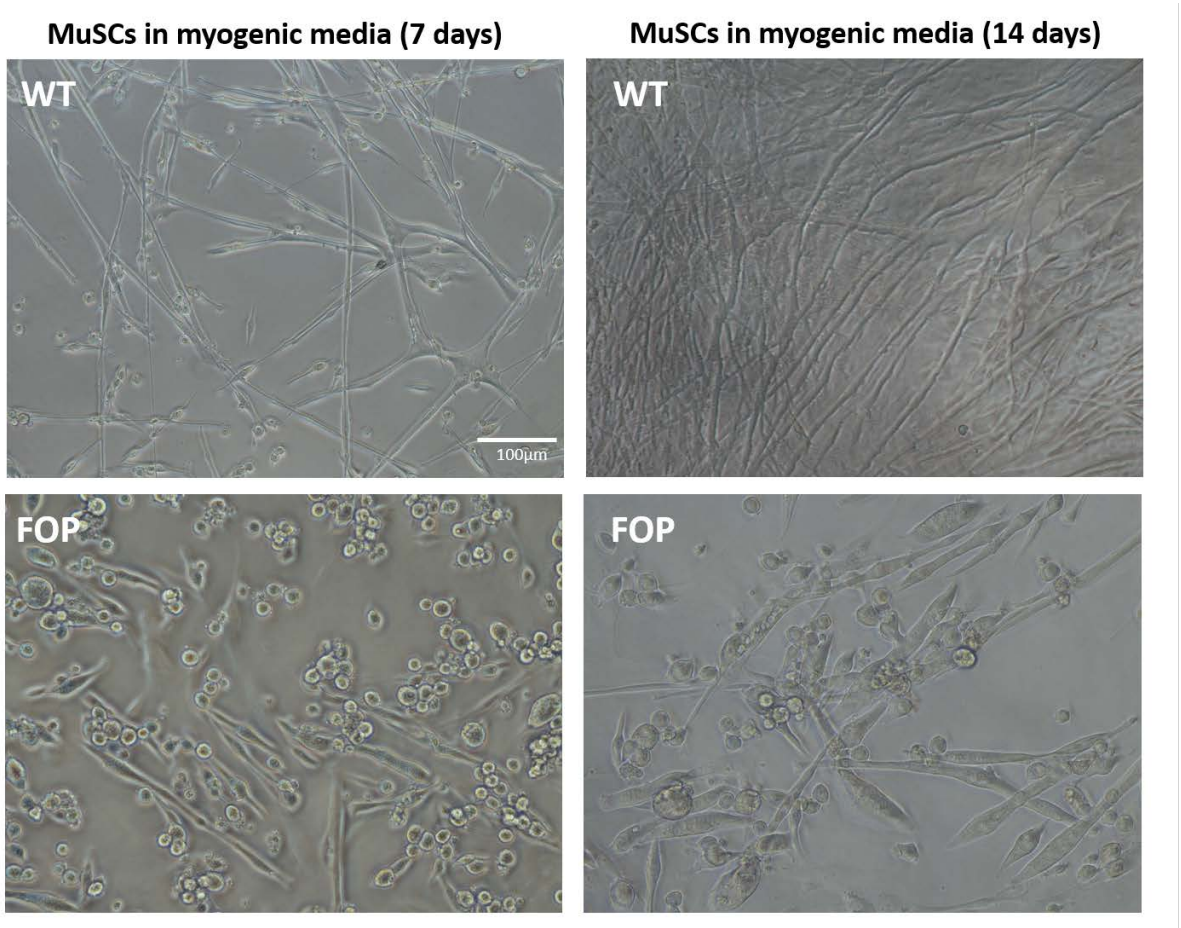

Figure 1. FOP MuSCs fail to form fused myofibers. *MuSCs from WT skeletal muscle tissue form normal myofibers that fuse into myotubes after 14 days in fusion media (5% HS in DMEM), while MuSCs from FOP skeletal muscle tissue do not differentiate into normal myofibers, nor fuse together in vitro; n= 6 for each genotype.*

Gnas inactivation alters adipose tissue properties during progression to heterotopic ossification

Niambi Brewer, John T Fong, Deyu Zhang, Frederick S Kaplan, Robert J Pignolo, Eileen M Shore

Heterotopic ossification (HO) is a common physiological response to severe tissue trauma such as combat blast injuries, high impact trauma, and hip replacements. The investigation of rare genetic disorders provides insight into the aberrant mechanisms that cause HO formation and leads to identification of targets for pharmacological intervention in both genetic and non-genetic forms of HO. HO in the rare genetic disorder, Progressive Osseous Heteroplasia (POH), initiates in subcutaneous soft tissues then progresses into deeper connective tissues. POH is caused by inactivation of *GNAS*, a gene that encodes the alpha stimulatory subunit of G proteins (Gsα). Our previous work demonstrated that adipose derived stromal cells (ASCs) from *Gnas*$^{p\text{-}KO}$ mice exhibit enhanced osteogenic and impaired adipogenic potential *in vitro*, supporting that osteogenesis and heterotopic bone in POH occurs at the expense of adipogenesis, however, the pathophysiology of POH remains poorly understood. To examine the mechanisms and signals that lead to initiation of heterotopic bone caused by *GNAS* inactivation in osteogenic progenitor cells, we developed an *in vivo* HO model using *Gnas*-null mice (*Gnas*$^{fl/fl}$*;Cre-ER*^{T2} or *Gnas*$^{fl/fl}$*;Ai9*$^{fl/fl}$*;Cre-ER*^{T2}) that consistently and reliably induces spontaneous HO. Through microCT, histologic, and immunohistochemistry analyses in cross-sectional and longitudinal studies, this model initiates HO within subcutaneous adipose tissues with progressive expansion over time. Using the same model and methods, we investigated the tissue changes that precede HO formation and identified increased extracellular matrix content, as well as a shift from white to beige adipose tissue, including UCP1 expression and decreased adipocyte size and lipid content. Cell implant studies showed that fluorescent-labeled Gnas-null ASCs form HO when implanted within Gnas-null adipose tissue, as expected. However, wildtype (WT) ASCs also induce HO in a Gnas-null background, although less robustly than mutant ASCs, suggesting that the tissue microenvironment strongly influences cell fate. Further, neither WT nor Gnas-null ASCs implanted into a control background formed HO, supporting that the mutant osteogenic progenitor cells are insufficient to induce HO. These data highlight the importance of the microenvironment within the adipose tissue in supporting ectopic bone formation by Gnas inactivation and provide insights into the pathophysiology of POH and other *GNAS*-related disorders.

Prolonged Release of Ibuprofen from a Nanofibrous Delivery System Under Physiological Conditions

Brittany L. Taylor[1,2], Dong Hwa Kim[1,2], Corinne N. Riggin[1,2] , Julianne Huegel[1,2], Andrew F. Kuntz[1,2], Louis J. Soslowsky[1,2], Robert L. Mauck[1,2], and Joseph Bernstein[1,2]

[1]McKay Orthopaedic Research Laboratory, University of Pennsylvania, Philadelphia, PA, [2]Philadelphia VA Medical Center, Philadelphia, PA

Disclosures: Brittany L. Taylor (N), Dong Hwa Kim (N), Corinne N. Riggin (N), Julianne Huegel (N), Andrew F. Kuntz (N), Louis J. Soslowsky (5; Orthofix, DJO), Robert L. Mauck (N), Joseph Bernstein (7; CORR)

INTRODUCTION: Using non-steroidal anti-inflammatory drugs (NSAIDS) to mitigate inflammation may represent a promising approach to modulate the tendon healing environment. In particular, biodegradable nanofibrous delivery systems offer an optimized architecture and surface area for cellular attachment, proliferation, and infiltration while releasing soluble factors to promote tendon regeneration [1–3]. Previous work confirmed the sustained release of ibuprofen (IBP) from Labrafil-modified poly(lactic-co-glycolic) acid (PLGA) microspheres *in vitro* in PBS and characterized a bilayer delivery system (BiLDS) incorporating these microspheres for localized delivery of therapeutics [4]. Nonetheless, the behavior of ibuprofen-releasing BiLDS in more physiologically relevant conditions and their influence on tenocytes *in vitro* is unknown. Therefore, the objective of this study was to evaluate the release profile of IBP from both PLGA microspheres alone and within BiLDS in serum and to elucidate their effect on primary tenocytes. We hypothesized that IBP would release at a faster rate from both the free microspheres and the BiLDS in serum than in PBS and the direct and indirect delivery of IBP *in vitro* would not have an adverse effect on cellular viability or morphology.

METHODS: *Microsphere and BiLDS Fabrication:* PLGA microspheres with varying concentrations of Labrafil® M1944CS oil ranging from 0 to 600 µL (P0, P30, P300 and P600) and 30mg/mL of IBP were created using an oil-in-water emulsion technique with an external phase of 1% poly(vinyl alcohol). The microsphere solution was stirred for 4 hours at room temperature. The BiLDS were created by entrapping 10mg of the P300 microspheres, without and with IBP (BiLDS_MS and BiLDS_IBP), between two sintered 6 x 8mm electrospun poly(ε-capalactone) (PCL) scaffolds. The microspheres and BiLDS were then SEM imaged for morphological analysis. *In Vitro Release Studies:* In the first release study, 20 mg of free microspheres were submerged in 5mL of normal rat serum or PBS and incubated at 37°C. The quantity of total IBP released (µg/mL) was measured over 14 days using a competitive ELISA assay and UV spectrophotometer (λ= 223nm). In the second release study, BiLDS_MS and BiLDS_IBP were incubated on a shaker at 37°C in 5mL serum up to 14 days. In the one group, BiLDS_IBP and BiLDS_MS, the total 5mL of serum was collected at 0.5, 3, 7, 14 days and in the 'continuous' groups (BiLDS_MS_C and BiLDS_IBP_C), 2mL of serum was collected at the same time points and replaced with fresh serum to assess the effect fresh serum had on the release of IBP from the BiLDS over time. *In Vitro Cell Study:* Primary Achilles tenocytes were isolated from Sprague-Dawley rats and cultured in DMEM with 10% FBS and 2X penicillin-streptomycin (P/S) for one week. The tenocytes (passage 1) were seeded at 5 x 10^3 per construct on empty BiLDS (BiLDS), BiLDS_MS and BiLDS_IBP for the direct cell study. The cells were maintained in media with 1% FBS. For the indirect study, the same BiLDS groups were submerged in culture media for one week and the conditioned media was then added to cells cultured on TCP at 5 x 10^3 cells per well. Tenocytes were cultured with normal culture media as the control. MTT cell proliferation assay and Alexa Fluor 488 phalloidin fluorescence staining for actin were used to quantify metabolic activity and visualize cell morphology over 14 days for both studies. *Statistics:* Comparisons between groups at each time point were assessed using two-way ANOVAs with post-hoc Bonferroni tests. Significance of differences was set at $p<0.05$.

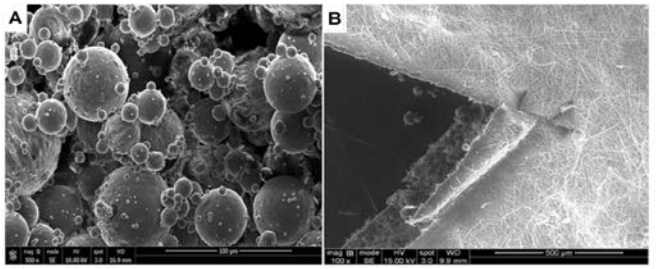

Fig. 1. SEM images of (A) P300 microspheres at 500x and (B) the cross-section of a BiLDS at 100x.

RESULTS: Qualitatively, the microspheres in each group were consistent in morphology and similar to the representative image of P300 microspheres in **Figure 1A**. SEM images of the BiLDS confirmed the presence of microspheres between the two nanofibrous scaffolds (**Fig.1B**). The IBP released in a linear manner from all the microsphere groups in serum (**Fig. 2A**), whereas there was an initial burst in release in PBS (**Fig. 2B**). Furthermore, the P0 microspheres released 74% more IBP than the P600 microspheres through Day 14, indicating the total amount of IBP released was inversely related to the concentration of Labrafil oil used to create the microspheres. At Day 14, 165 µg/ml of total IBP was released from the BiLDS in serum, which was about 70% less than the free P300 microspheres in serum. The BiLDS with IBP in the continuous group, BiLDS_IBP_C, had a significant increase in total IBP released from Day 7 to Day 14 (**Fig. 2C**). There were no differences in cell viability over 14 days for all the BiLDS groups in the direct cell study (data not shown). However, when the cells were cultured in conditioned media for the indirect cell study, there was a significant increase in cellular viability at Day 1, 10 and 14 for the BiLDS and BiLDS_IBP groups and at Day 3 for all the groups in comparison to the cells cultured in control media (**Fig. 2D**).

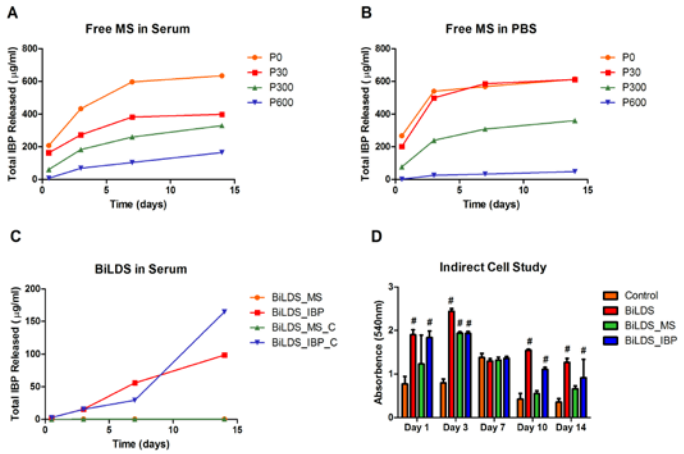

Fig. 2. Release of IBP from free microspheres in (A) serum and (B) PBS over 14 days.(C) Release of IBP from the BiLDs in serum over 14 days. (D) MTT cell proliferation assay results of primary Achilles tenocytes cultured in conditioned medium from control (TCP), BiLDS alone, and BiLDS with and without IBP. #:P <0.05 in comparison to the control.

DISCUSSION: Similar to previous studies, the addition of Labrafil oil slowed the release of IBP over time. The release of the ibuprofen was delayed and sustained from the P300 microspheres enclosed in the bilayer scaffold design in serum, confirming the prolonged behavior of the microspheres in physiologically relevant conditions. This is a desirable characteristic in modulating inflammation during the tendon healing phase *in vivo*. Also, the addition of fresh serum over time, resembling *in vivo* conditions of exchange of serum, increased the release of IBP from the BiLDS. This could be due to the frequent pH changes in the environment affecting the scaffold degradation or release kinetics [5]. *In vitro* biological assessment proved that all the components of the BiLDS were biocompatible. Furthermore, the concentration of IBP released did not have any detrimental effects on cellular viability or morphology. Future studies will investigate the regenerative effects of the BiLDS using an *in vitro* inflammation model.

SIGNIFICANCE: This study identifies the therapeutic potential of a biocompatible nanofibrous bilayer delivery system for prolonged and continued released of ibuprofen to mitigate inflammation during tendon healing.

REFERENCES: [1] Huang et al. J. Hand Surg. Am., 31:693–704, 2006. [2] Sahoo et al. Tissue Eng., 12:91–99, 2006. [3] Reverchon et al. Muscles. Ligaments Tendons J., 2:181–6, 2012. [4] Kim et al. ORS, 2017. [5] Riggin et al. Ann. Biomed. Eng., 1–12, 2017 (epub).

ACKNOWLEDGEMENTS: This study was supported by VA Merit Grant (O0979-R), Penn Center for Musculoskeletal Disorders (NIH/NIAMS P30 AR069619), and a fellowship for B. Taylor through the University of Pennsylvania's Office of the Vice Provost for Research.

Time-dependent Changes in Synovial Macrophage and Dendritic Cells in a Murine Model of Osteoarthritis

Cheng Zhou[1, 2], Vu Nguyen[1, 2], Nisha Sambamurthy[1, 2], De'Broski R. Herbert[3], George R. Dodge[1, 2], Carla R. Scanzello[1, 2]
[1]Translational Musculoskeletal Research Center, Corp. Michael J. Crescenz VA Medical Center, [2]Perelman School of Medicine and [3]School of Veterinary Medicine University of Pennsylvania, Philadelphia, PA

INTRODUCTION: Macrophage infiltration in the synovial membrane (SM) and intra-articular fat pads (FP) is common in osteoarthritis (OA) development, and can contribute to catabolic and anabolic cytokine and protease production, which contributes significantly to OA symptoms. However, whether macrophages are appropriate targets for therapy in OA is unclear, as macrophages can also promote tissue repair. The purpose of this study is to characterize the timeline and phenotype of macrophages in SM and FP in a translationally relevant murine model of post-traumatic OA. We hypothesized that by analyzing macrophage populations by two separate approaches, cellular phenotype and gene expression analysis, we could confirm the precise temporal role and characteristics of infiltrating macrophages while OA is developing.

METHODS: All animal research was conducted with IACUC approval from the University of Pennsylvania and the CMC VA Medical Center. C57BL/6 male mice (10-12 wks old) were subjected to destabilization of medial meniscus (DMM) on the right hind leg, and the left hind leg was un-operated. Mice were sacrificed 4 and 8 weeks post-surgery, and SM/FP dissected for cellular analysis. Tissues from 4 knees were pooled, cells isolated enzymatically, and stained with the Live/Dead™ Fixable Violet Dead Cell Stain Kit (Invitrogen) and the following antibodies: CD45-PerCP Cy5.5, CD11c-Super Bright 645, F4/80-APC, iNOS-Alexa Fluor 488, CD206-PE. Multicolor flow cytometry was performed and data analyzed with FlowJo software. After gating on single live cells, F4/80$^+$ (general macrophage marker) and CD11c$^+$ (expressed by dendritic cells, monocytes and macrophages) cells were expressed as percent of the CD45$^+$ population. iNOS (expressed by M1-type inflammatory macrophages) and CD206 (expressed by M2 reparative macrophages) expression was then characterized on F4/80 and CD11c expressing cells. To determine whether gene expression of macrophage-related transcripts reflects cytometric analysis, additional groups of mice were sacrificed pre-DMM (baseline), and post-DMM at 4 and 8 weeks. SM/FP tissues from 4 knees were dissected and pooled for each sample to obtain adequate mRNA. cDNA was synthesized by routine methods, and mRNA transcripts amplified using the QX200TM Droplet Digital PCR System (BioRad). Primers for macrophage markers (CD68, F4/80 and CD11c) as well as M1 (iNOS, CCR7) and M2 macrophage products (CD206 and CD163) were used, and transcript levels expressed relative to TATA-Box binding protein (TBP) transcript numbers.

RESULTS: Gating on the CD45$^+$ population, two main populations of cells were defined by F4/80 and CD11c expression: A CD11c$^+$ F4/80$^-$ population (reflective of dendritic cell phenotype), and a CD11c$^+$ F4/80$^+$ population (reflective of macrophage phenotype). Percentages of both populations were significantly increased in DMM-operated compared to un-operated joints at 4 weeks but not at 8 weeks (Fig 1A&B, F4/80$^-$ CD11c$^+$, DMM: 11.84±1.46, un-operated: 4.55±0.98, p=0.009. F4/80$^+$ CD11c$^+$, DMM: 15.28 ± 2.55, un-operated: 4.66±2.06, p=0.017). Compared to the un-operated side, CD206$^+$ macrophages (F4/80$^+$ CD11c$^+$) and dendritic cells (F4/80$^-$ CD11c$^+$) were significantly lower proportionally in DMM-operated limbs at 4 weeks, and this trend was sustained at 8 weeks in the F4/80$^+$ CD11c$^+$ population (Fig 1C). Percentage of iNOS + cells were slightly elevated in the F4/80$^+$ CD11c$^+$ macrophage population at 8 weeks (p=0.02) post-DMM, but overall numbers of cells were small. We next tested whether similar phenotypic changes post-DMM could be detected at the mRNA level. We measured multiple markers of macrophage lineage (F4/80, CD68, and CD11c) and phenotype (M1: iNOS, CCR7; M2: CD206, CD163) by qPCR. CD11c and CD68 expression levels were increased on the DMM-operated side at 4 weeks post-DMM compared to the un-operated side (CDllc: 9.8-fold higher; CD68: 9.7-fold higher than un-operated, all p<0.05), and CD68 remained elevated (3.3-fold higher, p<0.05) at 8 weeks post-DMM. Of the M1-markers, mRNA levels for iNOS and CCR7 did not differ between DMM- and un-operated sides at 4 or 8 weeks. However, levels of iNOS were highly upregulated compared to baseline at 4 weeks (2000-fold higher, p<0.05), while levels of CCR7 mRNA were upregulated compared to baseline at both 4 (6.6-fold) and 8 weeks (7-fold). Transcripts for the M2 marker CD163 were lower on the DMM-operated side at 4 weeks (30-fold lower) and 8 weeks (35-fold lower than un-operated, both p<0.05), but no difference in levels of CD206 mRNA were observed at any time point.

DISCUSSION: Interestingly, time-dependent increases in both F4/80$^+$CD11c$^+$ macrophages and F4/80$^-$CD11c$^+$ dendritic cells can be detected in SM/FP tissues after DMM surgery, peaking at 4 weeks. These changes in cell proportions were reflected by changes at the transcriptional level of select but not all macrophage markers. Overall proportions of CD206+ cells were much higher in the macrophage population than iNOS$^+$ cells. Significant decreases compared to the un-operated side at 4 and 8 weeks post-DMM in macrophages expressing CD206 suggest early and sustained suppression of the M-2 macrophage phenotype. Although iNOS expressing macrophages were slightly increased at 8 weeks post-DMM, this reflected expression on very small proportions of cells. Importantly, not all phenotypic markers measured at the mRNA level reflected changes in these markers on macrophage and dendritic cell populations. Specifically, F4/80 and CD206 transcripts were not modulated despite clear differences in proportions of cells expressing these markers, while iNOS mRNA expression was highly upregulated more than other markers despite minimal expression on measured cells. It is possible that iNOS mRNA changes reflect other unmeasured cells in these tissues, or that post-transcriptional or translational mechanisms are more important in controlling cellular expression of this gene. It is quite revealing that mRNA levels of other M1 and M2 phenotypic markers, specifically CCR7 and CD163, more closely reflected phenotypic changes to macrophage populations detected by cytometry in this model. These discrepancies point to the importance of confirming transcriptional analysis at the cellular level and demonstrate that conclusions cannot be drawn solely from one measurement of gene expression.

SIGNIFICANCE/CLINICAL RELEVANCE: This study demonstrates clearly divergent macrophage signatures in the early stages of OA development in the DMM model, and is the first to document suppression of M2 macrophage proportions post-DMM. These observations will be insightful to plan timing of interventions to better understand the pathologic roles of macrophage subtypes in OA. Specifically, this data suggests that enhancement of M2-reparative macrophage responses, rather than blockade of M1-inflammatory macrophages, could be a novel therapeutic strategy for treatment of post-traumatic OA.

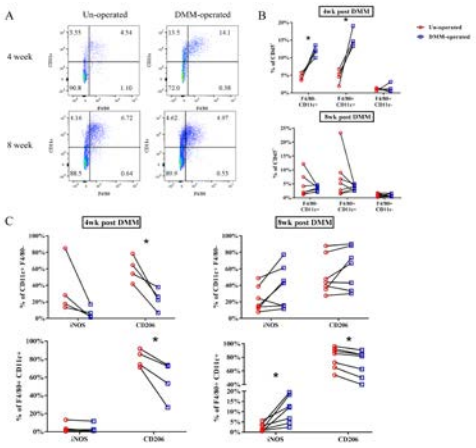

Figure 1 (left). Flow cytometry analysis of SM/FP tissue **A)** Representative CD11c and F4/80 expression gated on CD45. **B)** Quantification of F4/80$^+$ & CD11c$^+$ cells as % of CD45$^+$ gate. **C)** iNOS$^+$ and CD206$^+$ cells in the CD11c$^+$ F4/80$^-$ & CD11c$^+$ F4/80$^+$ populations at 4- & 8-weeks.

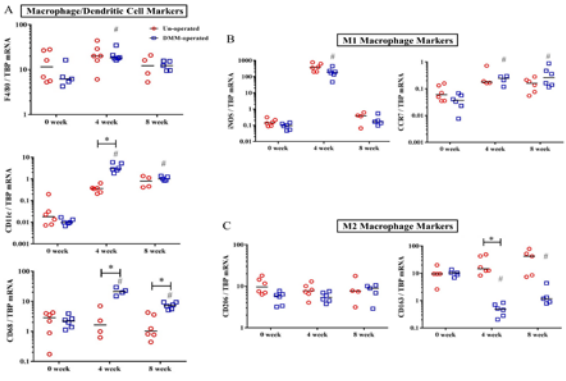

Figure 2 (right). mRNA expression analysis of **A)** macrophage and dendritic cell markers, **B)** M1, and **C)** M2 markers at 4- & 8-week post DMM.

Stem Cell Regulation in Muscular Dystrophy

Elisia D. Tichy[1], David Sidibe[1], Jacob Kocan[1], Delia Chen[1], and Foteini Mourkioti[1, 2, 3]

[1]Department of Orthopaedic Surgery, McKay Laboratory, Perelman School of Medicine, University of Pennsylvania, Philadelphia, PA 19104.

[2]Department of Cell and Developmental Biology, Perelman School of Medicine, University of Pennsylvania, Philadelphia, PA 19104.

[3]Penn Institute for Regenerative Medicine, Musculoskeletal Regeneration Program, Perelman School of Medicine, University of Pennsylvania, Philadelphia, PA 19104.

In many muscle disorders, including Duchenne muscular dystrophy (DMD), the repeated cycles of muscle damage and repair leads to stem cell dysfunction. We and others have previously shown that the muscle stem cell (MuSC) pool becomes less efficient at repairing damage in dystrophic mouse models. However, the underlying cause of stem cell failure in the repair process is not fully known. By developing a single cell imaging technique, we recently demonstrated that telomere shortening is a district feature of dystrophic muscle stem cells in both mice and DMD patients already at a very young age (Tichy et al. *Stem Cell Reports,* 2017). The premature telomere shortening observed in DMD boys implies a limited window of effectiveness before critical telomere shortening triggers replicative senescence and regenerative failure in DMD muscles. To identify key pathways involved with early MuSC function in muscular dystrophy, we analyzed signaling dynamics in dystrophic MuSCs and found aberrant activation of NF-κB signaling pathway during the progression of the disease. To better understand the role of NF-κB in muscle telomere biology of stem cells, we targeted the pathway specifically in MuSCs ($IKK2^{CA}$ mice). In steady state conditions, MuSCs of these mice do not exhibit any telomere shortening. Interestingly, in chronic, multiple injuries, telomere shortening became apparent in the I $IKK2^{CA}$ MuSCs. We have crossed the $IKK2^{CA}$ mouse with mdx mice, and we have found that the double mutant mice display hallmarks of the DMD process at a much earlier time than mdx mice alone, including kyphosis, high levels of circulating creatine kinase, and muscle weakness. Furthermore, our molecular analyses show that NF-κB induces telomere shortening in a proliferation-independent manner. These findings expand the fundamental knowledge of MuSC biology in diseased muscles and reveal the molecular players by which persistent NF-κB activation in MuSCs leads to their rapid telomere shortening and stem cell dysfunction under multiple injury conditions.

Craniofacial MRI Using Dual-RF, Dual-Echo 3D Ultrashort Echo Time With View-Sharing

Hyunyeol Lee[1], Xia Zhao[1], Hee Kwon Song[1], Rosaline Zhang[2], Scott P Bartlett[2], Felix W Wehrli[1]

[1]Department of Radiology, University of Pennsylvania, Philadelphia, PA

[2]Department of Plastic Surgery, University of Pennsylvania, Philadelphia, PA

Introduction Computed tomography (CT) enables 3D visualization of cortical bone structures with high spatial resolution, and thus has been the gold standard method for evaluation and diagnosis of craniofacial skeletal pathologies. However, ionizing radiation, and in particular, repeated scanning with this modality in pre- and post-surgery, is of concern when applied to infants and young children. As an alternative, Eley et al(1) proposed a 'black-bone' MRI method in which low flip-angle 3D GRE imaging yields proton-density weighted contrast, thereby facilitating discrimination between bone and soft-tissue. However, in this approach bone appears with near background intensity (i.e. 'black') due to very short T_2 relaxation times and relatively low proton density, making it challenging to distinguish between bone and air. Solid-state MRI methods via ultrashort echo time (UTE) (2) or zero TE (3), capable of imaging spins with very short T_2 relaxation times, are thus promising alternatives. Wiesinger et al (4) demonstrated a feasibility of a low flip-angle, short TR ZTE sequence in identifying skull bone structures via histogram-based post-processing. As an another approach to bone-specific imaging, a dual-RF based UTE method, which exploits sensitivity of bone signals to variable RF pulse widths, has recently been introduced (5). In this work, we developed a dual-RF, dual-echo 3D UTE sequence and accelerated imaging time via view-sharing. Its feasibility in producing accurate 3D renderings of the human skull was investigated in comparison to CT.

Methods *Imaging technique*: Figure 1a shows a diagram of the dual-RF, dual-echo 3D UTE pulse sequence, wherein two RF pulses (RF_1, RF_2) differing in duration and amplitude (but equal nominal nutation angle) are alternately applied in successive TR periods along the pulse train while within each TR two echoes are acquired at short and long TEs (TE_1, TE_2), respectively, from the beginning of gradient ramp-up. Thus, four echoes are obtained: $ECHO_{11}$, $ECHO_{12}$, $ECHO_{21}$, and $ECHO_{22}$. Here, the subscripts represent RF and TE indices in this order (Fig. 1a). Bone proton magnetization (pertaining to bound water), due to its very short T_2 relaxation time, exhibits a substantial level of signal decay during the relatively long duration of RF_2, while soft-tissue retains nearly the same level of signal intensities over all echoes. Thus, subtraction of $ECHO_{22}$ from $ECHO_{11}$, when compared to the difference between $ECHO_{11}$ and $ECHO_{12}$, further enhances bone contrast (5). In distinction to the approach in ref. 5, in the proposed method two additional signals, $ECHO_{12}$ and $ECHO_{21}$, are collected while radial view angles are varied every TR (instead of every two TRs as in ref. 5), leading to a two-fold increase in imaging efficiency via view-sharing. Echoes at the same TEs are combined to produce two k-space sets (k_1, k_2), in which central regions are composed only of $ECHO_{11}$ and $ECHO_{22}$ views to retain the highest and lowest bone signals, respectively, thereby maximizing bone signal specificity upon subtraction. *Data acquisition/processing*: Data were acquired in two subjects in vivo at 3 T field strength (Siemens Prisma) using the proposed dual-RF, dual-echo 3D UTE sequence. Imaging parameters: $TR/TE_1/TE_2$ = 7/0.06/2.46 ms, RF_1/RF_2 durations = 40/520 μs, flip angle = 12°, matrix size = 256^3, field-of-view = 280^3 mm^3, voxel size = 1.1 mm isotropic, number of radial spokes = 25,000, and scan time = 6 min. Additionally, a calibration scan was performed using the method in ref. 6 to determine gradient timing delays and subsequent correction for k-space trajectory errors. Images for k_1 (I_1) and k_2 (I_2) were reconstructed using a conventional gridding algorithm. Bone images (I_{bone}) with minimal soft-tissue contamination were then obtained as $I_{bone}=(I_1-I_2)/(I_1+I_2)$. Given the three sets of images (I_1, I_2, I_{bone}), segmentation of bone voxels was performed using ITK-SNAP (7) in a semi-automatic fashion, leading to 3D renderings of the skull.

Results and Discussion Figure 2 shows the effectiveness of the proposed view-sharing approach in accelerating the imaging time by a factor of two. Compared with full sampling[5], the view-sharing scheme exhibits no appreciable loss in image quality. Figure 3 displays in vivo head images in two subjects: I_1, I_2, I_{bone}, and 3D rendering. In I_{bone} images, bone voxels as well as inner table of the cranium are clearly visualized, and cranial and spinal bone structures are well depicted in the 3D renderings. Still, some voxels erroneously included or excluded in the renderings will require further improvement in post-processing.

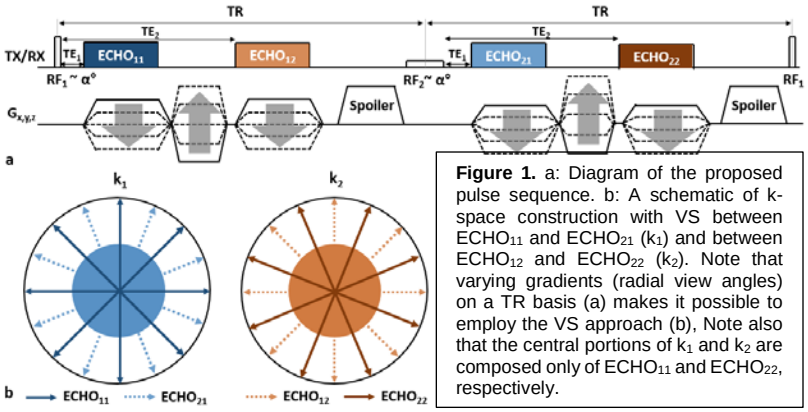

Figure 1. a: Diagram of the proposed pulse sequence. b: A schematic of k-space construction with VS between $ECHO_{11}$ and $ECHO_{21}$ (k_1) and between $ECHO_{12}$ and $ECHO_{22}$ (k_2). Note that varying gradients (radial view angles) on a TR basis (a) makes it possible to employ the VS approach (b), Note also that the central portions of k_1 and k_2 are composed only of $ECHO_{11}$ and $ECHO_{22}$, respectively.

Conclusions The proposed MRI-based skull imaging method, along with optimized post-processing, shows promise as a non-invasive alternative to CT for visualization of craniofacial architecture.

References 1. Eley et al, Br J Radiol 2012; 85(1011): 272-278; 2. Robson et al, J Comput Assist Tomogr 2003;27:825-846; 3. Grodzki et al, Magn Reson Med 2012;67(2):510-518; 4. Wiesinger et al, Magn Reson Med 2016;75(1):107-114; 5. Johnson et al, Magn Reson Med 2017;77:684-695; 6. Herrman et al, PLoS ONE 2016;11(3):e0140371; 7. Yushkevich et al, Neuroimage 2006;31(3):1116-1128.

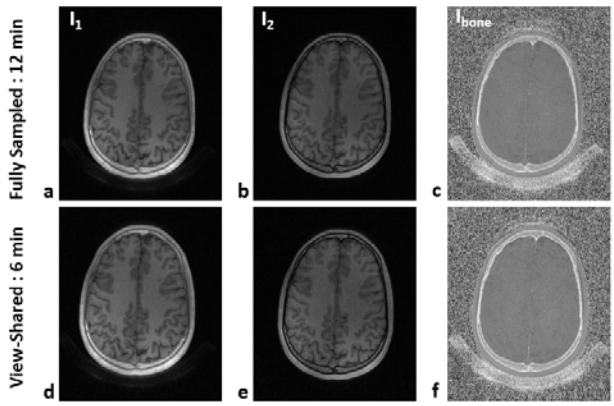

Figure 2. Images acquired using dual-RF 3D UTE with full sampling (top) and with view-sharing (bottom): I_1 (a,d), I_2 (b,e), and I_{bone} (c,f). Note that the view-sharing method (bottom), when compared with the parent technique (top), halves scan time without visible loss of image quality.

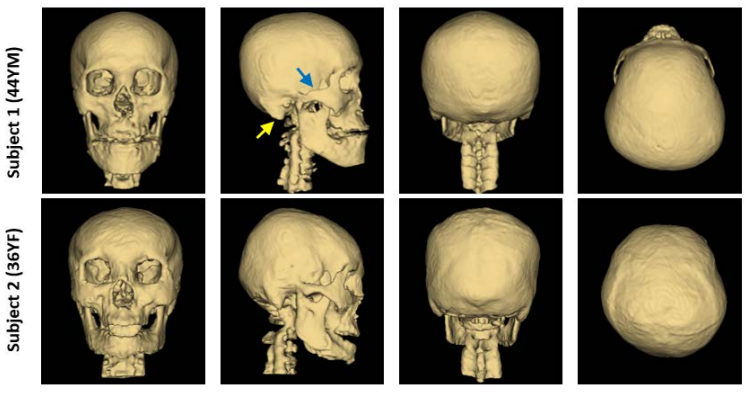

Figure 3. 3D renderings of the skull in two subjects in anterior, lateral, posterior, and superior views. Note the expected anatomic structures such as mandible and upper portion of cervical spine. More subtle structures including zygomatic arch and mastoid process (blue and yellow arrows) are pointed out as well.

Alterations in Fibrous Network Topography Regulates Onset of Fibrotic Phenotypes in Annulus Fibrosus Cells

Edward Bonnevie[1], Sarah Gullbrand[1], Beth Ashinsky[1,2], Tonia Tsinman[1], Dawn Elliott[3], Harvey Smith[1], Robert Mauck[1]
[1]University of Pennsylvania and CMC VA Medical Center, Philadelphia, PA, [2]Drexel University, Philadelphia, PA, [3]University of Delaware, Newark, DE
edbon@pennmedicine.upenn.edu

Disclosures: Bonnevie (2, Fidia Pharma USA), Mauck (8, JOR Spine), no other disclosures.

INTRODUCTION: Cells respond to local mechanical and topographic cues to regulate their phenotype[1,2], with 'stiff' environments driving a fibrotic phenotype[3]. In the context of disc degeneration, loss of nucleus pulposus swelling and residual strains in the annulus fibrosus likely alter the mechanics and organization of the cellular microenvironment[4]. Here, we used in vivo and in vitro models to test the hypothesis that altered fiber organization in the annulus fibrosus regulates the emergence of fibrotic phenotypes seen in the context of intervertebral disc injury and subsequent degeneration.

METHODS: New Zealand White rabbits were subjected to annulus puncture[5] with a 16-gauge needle to 5 mm depth, with 2-, 4-, and 8-week survival. The annulus fibrosus was assessed via second harmonic generation imaging and staining for alpha smooth muscle actin (αSMA). In vitro, bovine annulus cells were seeded onto electrospun PCL scaffolds, and a tensile stretching device was use to apply pre-strain to scaffolds prior to cell seeding (9% prestrain) for 24 hours. Both aligned and nonaligned prestrained and free swelling scaffolds (NE, NF, AE, AF) were assessed for fiber organization (angular spread), focal adhesions, YAP/TAZ nuclear localization, and αSMA+ stress fibers. Angular spread is reported as the standard deviation of the fiber angle distribution.

RESULTS: In the in vivo model, release of residual strains via needle puncture resulted in progressive disorganization of the AF (**Fig 1ab**) and the emergence of fibrotic phenotypes (i.e., αSMA expressing cells) after 2 weeks; these fibrotic signatures remained elevated through 8 weeks (**Fig 1ac**). In the in vitro model, both baseline organization and prestrain dictated fiber organization at the cellular length scale (**Fig 1f**). This organization had a significant effect on cell spreading (aspect ratio and spread area, **Fig 1gh**), with aligned microenvironments promoting elongation and minimizing spread area. These organized, pre-strained fiber environments limited focal adhesion area and maintained nuclear levels of YAP/TAZ at a low level (**Fig 1de,ij**), outcomes representative of cells interpreting the environmental cues as 'soft'[2]. Likewise, incorporation of αSMA into stress fibers was dependent on the organizational and prestrained state of fibrous environments, with aligned prestrained scaffolds reducing the fibrotic phenotype compared to nonaligned free swelling scaffolds (**Fig 1kl**). Thus, the contact-guidance provided by fiber organization inhibited the fibrotic phenotypes expected in stiff environments[3].

DISCUSSION: Our findings suggest that fibrotic phenotypes emerge with the release of residual strains in the annulus of injured discs. This patho-mechanobiologic event was replicated by an in vitro scaffold system, where cellular perception of the local environment was dictated by both baseline and strain-mediated fiber organization. Fiber organization provided cues (contact guidance) in aligned environments to modulate cell shape and size such that YAP/TAZ remained largely cytosolic, which in turn, suppressed incorporation of αSMA into stress fibers and the development of a fibrotic phenotype[3]. Continuing work is focused on using this scaffold-based system to evaluate pharmacologics that might inhibit this fibrotic remodeling response after injury.

SIGNIFICANCE: This study shows that the emergence of fibrotic phenotypes in annulus fibrosus cells is governed by local fiber organization, providing new directions for the development of therapeutics that can attenuate disease progression after fibrous tissue injury.

REFERENCES: [1] Engler+ 2005, [2] Dupont+ 2011, [3] Li+ 2017, [4] Michalek+ 2012, [5] Masuda+ 2005

ACKNOWLEDGEMENTS: This study was supported by NIH F32AR072478, R01EB02425, T32AR53461, P30AR050950, and VA I01RX002274.

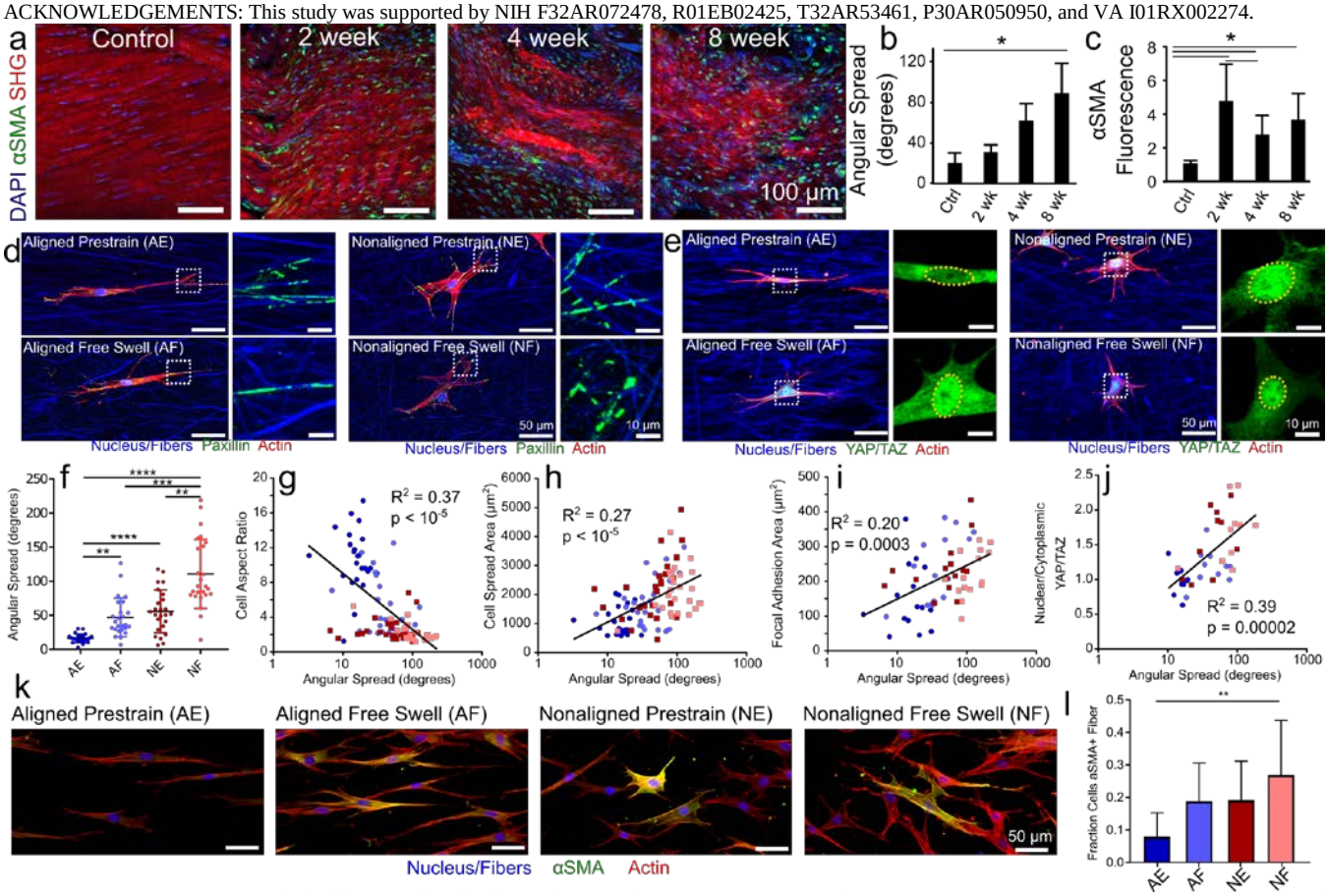

Figure 1: (a) SHG imaging coupled with αSMA localization and DAPI of injured native annulus fibrosus tissue. (b) Angular spread (standard deviation of fiber angle distribution) and (c) αSMA increased following puncture injury (n = 3 rabbits/group). (d) angular spread on scaffolds predicted (e) cellular morphology and spread area (f) (n = 100 cells/correlation), as well as (g, i) focal adhesion (i.e., paxillin) area per cell and (h. j) YAP/TAZ localization (n = 60 and 40 cells/correlation, respectively). (k, l) Fiber organization modulated αSMA+ expression and localization to stress fibers (n = 6 scaffolds/group) (*p<0.05, **p<0.01, ***p<0.001, ****p<0.0001).

Non-Invasive Imaging of Therapeutic Cells Delivered Percutaneously to the Mouse Intervertebral Disc

Chenghao Zhang[1], Sun H. Peck[1], Justin R. Bendigo[1], Yian Kai A. Lau[1], Neil R. Malhotra[1], Lachlan J. Smith[1]
[1]Departments of Neurosurgery and Orthopaedic Surgery, University of Pennsylvania, USA
chenghao.zhang@pennmedicine.upenn.edu

Disclosures: C. Zhang (N). S.H. Peck (N). J.R. Bendigo (N). Y.A. Lau (N). N.R. Malhotra (N). L.J. Smith (5-Ultragenyx; 9-ORS Spine Section).

INTRODUCTION: Intervertebral disc degeneration is strongly implicated as a cause of low back pain, and cell-based therapies hold significant promise for disc regeneration [1]. While large animal models are a requisite preclinical step prior to clinical translation of cell-based disc therapies, mouse models represent an important intermediate *in vivo* platform, as genetic manipulation permits mechanistic studies of cell-mediated regeneration. The small size of the mouse disc, however, poses technical challenges with respect to surgical technique and, consequently, experimental reproducibility. Our group recently described a percutaneous needle-injury model of moderate severity disc degeneration in the mouse caudal spine suitable for evaluating cell-based regenerative therapies [2]. As a prerequisite for using this model in studies of cell-based disc regeneration, the objectives of the current study were to: 1) Establish a technique for percutaneous delivery of therapeutic cells to the mouse caudal disc; and 2) Validate a technique for non-invasive quantitative tracking of injected cells.

METHODS: With institutional IACUC approval, mesenchymal stem cells (MSCs) were isolated from the bone marrow of adult C57BL/6 mice using established techniques [3], expanded through 3 passages, and labeled with cell tracker red (Thermo Fisher). Using standard aseptic technique and under general anesthesia, and ~2-5x10^4 MSCs were suspended in saline were injected percutaneously into the nucleus pulposus (NP) of 3 caudal discs (C7-8, C9-10 and C11-12) of 5 adult male C57BL/6 mice (15 discs total) using a 33G needle under fluoroscopic guidance. Mice were euthanized at 1, 3, 5, 7 and 14 days post-injection. As a negative control, 1 additional mouse received injection of unlabeled MSCs into 3 caudal discs, while another served as an un-injected control, both euthanized after 1 day. Immediately following euthanasia, intact tails were imaged using an IVIS Spectrum (Perkin Elmer) imaging system. Mean fluorescence intensity was calculated for each injected disc for a 4mm diameter region of interest centered on the point of peak fluorescence intensity. Whole discs were isolated via sharp dissection and stained with Hoechst to visualize cell nuclei. Discs were then imaged through their complete thickness in the axial plane using confocal microscopy to assess both total cells (blue fluorescence) and injected cells (red fluorescence) in the NP. The NP boundary was identified using Photoshop (Adobe) and the relative area occupied by injected (red) cells was then determined using ImageJ (NIH) on a z-projection image. Linear correlation between the mean fluorescence intensity for each disc as determined via IVIS imaging, and NP area occupied by injected cells determined via confocal microscopy was evaluated ($p<0.05$).

RESULTS: All animals successfully underwent surgery and survived to the study endpoints. MSCs labeled with cell-tracker could be detected using IVIS imaging (Figure 1) at all time points post injection, with mean fluorescence intensities for injected discs ranging from 0.50 to 6.02 x 10^7. No fluorescence signal was evident for either discs injected with unlabeled MSCs, or un-injected control discs (Figure 1). Confocal imaging clearly demonstrated the presence of injected MSCs in the NP (red fluorescence; Figure 2). The area occupied by injected MSCs ranged from 3.0 to 33.5% of the total NP area. There was a moderate, significant correlation between mean fluorescence intensity of injected MSCs measured non-invasively using IVIS imaging, and area occupied by injected MSCs measured using confocal microscopy ($r = 0.65$, $p = 0.008$; Figure 3).

DISCUSSION: The small size of the mouse intervertebral disc makes surgical delivery of cells extremely challenging. The percutaneous technique applied here does not require an open incision and therefore minimizes local inflammation and scar tissue formation that could confound results. The non-invasive imaging technique validated here to track cells post-injection can be used to account for a variable number of cells injected by establishing a baseline against which longitudinal changes in cell survival and localization can be compared. Further, non-invasive imaging that does not require animal sacrifice may facilitate a reduction in animals required for *in vivo* experimentation. Ongoing studies will apply these techniques to evaluate the regenerative effects of therapeutic cell types including MSCs and notochordal progenitor cells.

SIGNIFICANCE/CLINICAL RELEVANCE: This study establishes techniques for percutaneous delivery of therapeutic cells to the mouse intervertebral disc and for subsequent non-invasive imaging of those cells. These techniques can be applied to conduct mechanistic studies of cell-based intervertebral disc regeneration in mice.

ACKNOWLDEGMENTS: Funding was received from the NIH (R21AR070959).

REFERENCES: [1] Tong+ Transl Res 2017; [2] Piazza+ J Orthop Res 2018; [3] Soleimani+ Nat Protoc 2008.

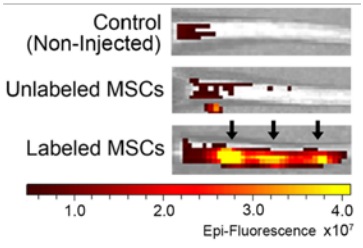

Figure 1. Non-invasive assessment of cell tracker-labeled MSCs delivered to the C7-8, C9-10 and C10-11 (arrows) mouse caudal intervertebral discs using the IVIS imaging system 1 day post-injection. No fluorescent signal is evident for control (non-injected) discs or discs injected with unlabeled MSCs.

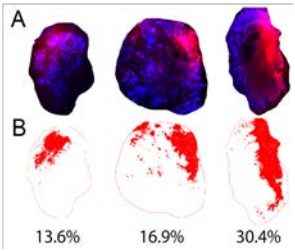

Figure 2. Nucleus pulposus area occupied by MSCs as determined by confocal microscopy of whole, isolated mouse intervertebral discs. **A.** Representative confocal images showing all cells (Hoechst, blue) relative to injected MSCs (cell tracker, red). **B.** Relative area occupied by injected cells determined using ImageJ.

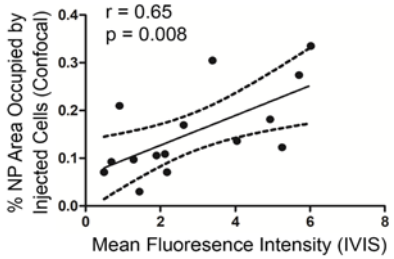

Figure 3. Correlation between mean fluorescence intensity of injected MSCs measured non-invasively using IVIS imaging, and NP area occupied by injected MSCs measured using confocal microscopy.

Modulation of Covalently Crosslinked 3D Collagen Hydrogels Regulate Metabolic and Fibrotic Gene Expression

Nikolas Di Caprio[1], Evangelia Bellas[1], Ph.D.
[1]Department of Bioengineering, Temple University, Philadelphia, PA

Introduction: Obesity is a prevalent disease that affects more than 1 in 3 U.S. adults and increases the risk of major comorbidities, such as type II diabetes, cardiovascular disease, stroke and some cancers. In obesity, hypertrophic adipocytes cause the tissue to become hypoxic. Hypoxia results in Hypoxia Inducible Factor 1α (HIF1α) nuclear localization, where it upregulates pro-fibrotic and pro-inflammatory factors, resulting in stiffening of the extracellular matrix (ECM). Whether substrate stiffness affects adipocyte dysfunction remains poorly understood. In this study, we aim to investigate the effects substrate stiffness on adipocytes in 3D to better understand its role in adipose tissue fibrosis.

Materials and Methods: Collagen type I (2mg/mL) was used to encapsulate human adipocytes (8 million/mL). Collagen hydrogels were placed in incubator and gelled at 37°C for 30 minutes . The gels were tuned to different stiffnesses by covalent crosslinking, using varying mass ratios of polyethylene glycol disuccinimidyl ester (PEGDS) to collagen. After 5 days in culture, the 3D gels were fixed, stained for lipid accumulation (Bodipy), F-actin polymerization (Phalloidin) and the nucleus (Hoechst) and imaged using confocal microscopy. Gene expression by qPCR was also performed at day 5 to observe changes in adipocyte, metabolism and ECM related gene activity.

Results and Discussion: When adipocytes were encapsulated in 0.33% PEGDS:collagen 3D hydrogels for 5 days, qPCR results revealed statistically significant upregulation in extracellular gene expression (COLA1/3, LOX) and a downregulation in adipocyte and metabolism gene expression (PPARγ, ADIPOQ) compared to the collagen control **(Fig. 1C)**. Confocal microscopy was used to visualize actin stress fiber formation. Adipocytes encapsulated in PEGDS:collagen hydrogels revealed more apparent cytoskeletal tension and less lipid droplet accumulation in contrast to control adipocytes **(Fig. 1A & B)**.

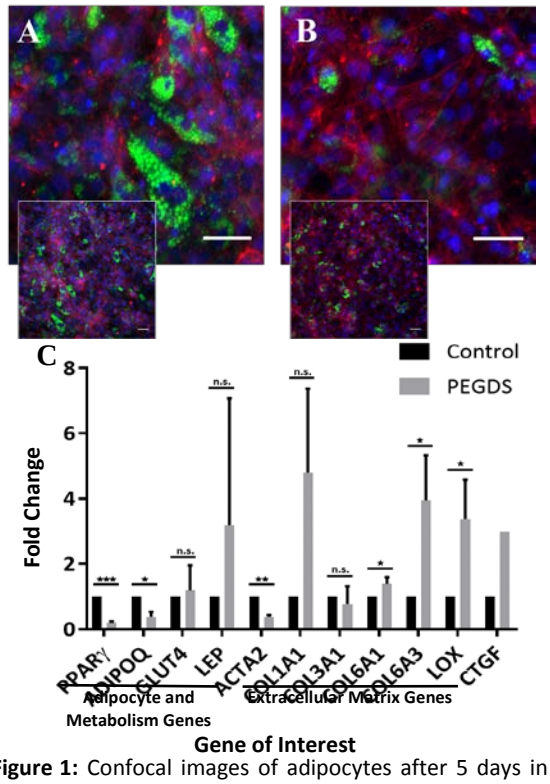

Figure 1: Confocal images of adipocytes after 5 days in control collagen 3D culture **(A)** and 0.33% PEGDS:collagen 3D culture **(B)**. Adipocytes were stained for F-actin (Red, Phalloidin), lipid accumulation (Green, Bodipy), and the nucleus (Blue, Hoescht). Scale Bar: 50µm.Adipocyte gene expression fold change after 5 days in control collagen 3D culture and 0.33% PEGDS:Collagen 3D culture **(C).** N=3, except CTGF N=1. Student t-tests were performed for each gene of interest. 3 stars: p< 0.0001, 2 stars: p< 0.001, 1 star: p< 0.05.

Conclusion: Based on these preliminary results, we have shown that modulation of ECM stiffness independently of collagen concentration can regulate adipocyte metabolic and fibrotic gene expression towards dysfunction.

Acknowledgements: We would like to acknowledge funding support from Dr. Bellas' startup funds from Temple University College of Engineering and the NIH NIDDK Diabetic Complications Consortium DK07616 and DK115255 grants (to EB) for their financial support towards this project.

A Microphysiological Model of Adipose Tissue for High-Throughput Applications

Michael Struss, B.S. Evangelia Bellas, Ph.D.
Department of Bioengineering, Temple University, Philadelphia, PA, United States

Adipose tissue (AT) is a highly vascularized endocrine organ that maintains whole body metabolic homeostasis. AT communicates with other tissues, like those of the musculoskeletal system, via vasculature to regulate metabolism and function. When AT is impaired as with obesity, musculoskeletal tissues can be negatively affected (e.g. osteoarthritis, ectopic lipid formation in muscle). However, the direct crosstalk between these tissues is not well studied. To model adipose tissue with appropriate spatial and temporal control, we developed a microphysiological adipose tissue (μAT) model with a vascular component to ultimately interface with other tissues. Here, we introduce a novel, miniaturized AT model compatible with standard culture ware, amenable to high-throughput platforms and capable of being integrated with other tissue types.

To accommodate high-throughput culture plates, the miniaturized μAT device is 6 mm in diameter and 750 microns in height. The μAT device includes a central hydrogel reservoir, containing adipocytes, fed by an endothelialized microchannel and two media reservoirs. To fabricate these devices, polydimethylsiloxane (PDMS) is casted from a 3D printed template and bonded to a glass coverslip. Human mesenchymal stem cells (hMSCs) are differentiated into adipocytes, encapsulated within collagen type I, and injected into the central reservoir. A microchannel, fabricated via subtractive molding, is seeded with human umbilical cord vascular endothelial cells (HUVECs) to form the blood vessel.

To validate the cell organization within the μAT model we performed confocal imaging. We verified the adipocytes are evenly distributed in collagen type I hydrogel by Bodipy (a lipid droplet stain). The blood vessel formation was visualized by immunofluorescence staining for CD31 (an endothelial cell junction marker). The CD31 staining demonstrated clear cell-cell junctions between endothelial cells and an open lumen cross-section through the vessel.

Activin A Heparin Binding Domain Identification and Expression in Human Tissues

Evan Yang, Christina Mundy, Eric Rappaport, Maurizio Pacifici and Paul Billings

Activins, members of the TGFβ superfamily of signaling molecules, were originally purified from gonadal fluids based on their ability to control release of pituitary follicle stimulating hormone (FSH). It is now known that Activins have many other functions including effects on differentiation, apoptosis, metabolism, homeostasis, immune response, wound repair, endocrine functions and pathological conditions such as cancer and heterotopic ossification. Activins are synthesized as large precursors, proteolytically processed and secreted as a large complex containing the pro-protein and a non-covalently associated, mature disulfide-linked ligand. Following secretion, the complexes are believed to associate with heparan sulfate proteoglycans (HSPGs) in the extracellular matrix (ECM), such as Perlecan. These interactions serve to create a reservoir of Activn ligands that when needed, are released from the prodomain to exert their biological activity.

Activins signal by binding to cell surface type I and type II membrane receptor serine-threonine kinases. Following ligand binding, heterodimeric receptor complexes subsequently bind and phosphorylate receptor Smad2/3 proteins which form complexes with co-Smad 4, translocate to the nucleus activating target genes. Recently, it has been shown that Activin A (ActA) plays a key role in the pathogenesis of Fibrodysplasia Ossificans Progressiva (FOP), a rare pediatric genetic condition characterized by progressive heterotopic ossification (HO) of muscles and tendons, impairing movement and body functioning. FOP is caused by mutations in the intracellular domain of the bone morphogenetic protein (BMP) type I receptor, ACVR1 (ALK2). The most common mutation found in FOP patients is an R206H mutation within the glycine-serine domain just upstream of the kinase domain, rendering mutant ACVR1 responsive to Act A. The onset of HO is often preceded by flare-ups, which can be triggered by physical trauma and eliciting local inflammation. This suggests that following trauma, ActA is released from ECM deposits or infiltrating monocytes and/or macrophages and once released, would be free to bind ACVR1, promoting ectopic endochondral ossification. Although the biological actions of mature ActA ligand has been widely studied, little information is available about the expression of full-length ActA by human cells. In addition, very little is known about the domain(s) in ActA mediating its interactions with HSPGs in the ECM. The goals of the present study were to address these key questions.

Bacterial aggregation in equine synovial fluid shows similarities to traditional biofilms and increased antimicrobial recalcitrance *in vitro*

Jessica M. Gilbertie[1,2], Lauren V. Schnabel[2], Thomas P. Schaer[1]
[1]University of Pennsylvania, School of Veterinary Medicine, Kennett Square, PA
[2]North Carolina State University, College of Veterinary Medicine, Raleigh, NC

Bacterial colonization of synovial structures can cause infections that are difficult to treat complicating veterinary and human clinical practice. It has recently been shown that antimicrobial recalcitrance in synovial fluid (SynF) could be due to bacterial clumping or aggregation leading to the formation of free-floating biofilms termed biofloats (Dastgheyb et al., 2015; Perez and Patel 2015). We now report the microscopic characteristics of free-floating bacterial aggregates (biofloats) formed in equine SynF from several bacterial species. SynF was aseptically collected from six healthy horses euthanized at our clinic for reasons other than orthopedic disease. Several isolates from clinical infectious arthritis cases were collected: *Staphylococcus aureus*, *Streptococcus zooepidemicus*, *Enterococcus faecalis*, *Pseudomonas aeruginosa*, and *Escherichia coli* and inoculated into SynF. The infected SynF was incubated overnight on a shaker at 37°C. The ultrastructural architecture of the biofloats was studied using scanning electron microscopy (SEM) and multiphoton confocal microscopy using wheat germ agglutinin (blue)/FilmTracer (red) to stain sugar/protein within the extracellular matrix and a nucleic acid stain (Syto 9) for the bacterial component. For antimicrobial testing, each bacteria had antimicrobial susceptibility testing performed to evaluate the minimum inhibitory concentration (MIC) of Amkacin. Synovial fluid was inoculated with each bacteria at $1x10^6$ CFU/mL and incubated for overnight to allow bacterial clumping. The bacteria were subsequently treated with 1x, 10x and 100x MIC of Amikacin for 24 hours. Bacteria were also pre-treated with hyaluronidase or proteinase K for 1 hour prior to addition of Amikacin. Bacterial load after 24 hours of treatment was determined with serial dilutions and colony plate counting. Macroscopic biofloat formation in synovial fluid was observed in all clinical isolates 18 hours post-infection. Similar conformation of the extracellular matrix (ECM) and bacterial cells was shown amongst the different bacterial species; however, the abundance of the ECM varied with the bacterial species. All the clinical isolates showed significant antimicrobial recalcitrance *in vitro*. Each clinical isolate was able to be eradicated when grown in tryptic soy broth (TSB) but had a negligible decrease in CFU/mL in synovial fluid treated with Amikacin even at concentration 100x MIC. Hyaluronidase pre-treatment had a minor effect on bacterial load; however, proteinase K pre-treatment restored antimicrobial efficacy of Amikacin, indicating that one important structural component of biofloats are proteinaceous in nature. A biofilm extracellular polymeric matrix (EPS) allows bacteria to avoid immune clearance and exhibit increased resistance to antimicrobials. Biofloats that form in synovial fluid have similar morphological characteristics and structure when compared to biofilm communities. This allows for their persistence in septic synovial structures making septic arthritides difficult and costly to treat. Our findings may direct future studies towards investigating the complexity of the proteins within the EPS of these aggregates to identify potential drug targets. Exploring the microbial-host interactions of biofloats or bacterial aggregates *in vivo* are currently underway using an infectious arthritis model of the tarsocrural joint in the horse.

Use of platelet-rich plasma lysate improves bacterial load and outcomes of *S. aureus* infectious arthritis in horses

Jessica M. Gilbertie[1,2], Lauren V. Schnabel[2], Thomas P. Schaer[1]
[1]University of Pennsylvania, School of Veterinary Medicine, Kennett Square, PA
[2]North Carolina State University, College of Veterinary Medicine, Raleigh, NC

Introduction: Infectious arthritis is a challenging condition that can lead to persistent infection necessitating euthanasia or to degenerative joint disease in patients that survive. Our group has recently shown that several arthrotropic pathogens, including *Staphylococcus aureus*, aggregate within equine synovial fluid to form free-floating biofilms, termed "biofloats". These biofloats are extremely difficult to eradicate and show antimicrobial resistance even when treated with antimicrobials at 100x the minimum inhibitory concentration (MIC). Our group has also shown that highly concentrated platelet-rich plasma lysate (PRP-L), pooled from multiple donors and with the anionic fraction removed, has a potent bactericidal effect on *S. aureus* biofloats. **Hypothesis**: The combination of PRP-L and amikacin will decrease bacterial burden and improve outcome parameters in an equine *S. aureus* infectious arthritis model compared to horses treated with amikacin alone. **Methods:** Highly concentrated pooled PRP-L was generated from 8 healthy donor horses and processed to have the anionic fraction, removed. Bactericidal efficacy was confirmed *in vitro* prior to use in the current study. Study horses (n=12; 7 mares, 4 geldings, 1 stallion; ages 2-14 years; multiple breeds) with normal physical examinations, bloodwork, and tarsocrural radiographs were randomly allocated into treatment or control groups. On day 0, epidural analgesia (buprenorphine and detomidine) was administered under standing sedation. *S. aureus* at $1x10^6$ CFU in 1mL sterile saline was then introduced via intra-articular injection into one randomly assigned tarsocrural joint. Twenty-four hours post-infection, horses were treated with PRP-L (5mL) and 500mg amikacin (treatment; n=6) or 500mg of amikacin and sterile saline (5mL) (control; n=6) daily for 7 days. All horses received systemic antimicrobials (potassium penicillin and gentamicin) for 10 days post-infection as well as a tapering course of phenylbutazone for the duration of the study. Physical examinations were performed daily and pain scores based on lameness, hock swelling, distal limb swelling, pain to palpation, and presence of heat were calculated at days 0-7, 14 and 21. Ultrasound exams were performed on days 0, 1, 7, 14 and 21. Blood was collected on days 0-7, 14, and 21 for complete blood count, fibrinogen, D-Dimer and serum amyloid A (SAA) analyses. Synovial fluid (SynF) was collected on the same days for total protein (TP), total nucleated cell count (TNCC), cellular differential, and bacterial load determination, as well as biomarker analysis (EMD Millipore MILLIPLEX MAP Equine Cytokine/Chemokine Magnetic Bead Panel). Standing digital orthogonal radiographs were performed on day 21. At end-term on day 24, horses were euthanized, and synovium and cartilage samples were collected for histopathology and tissue bacterial load determination in the infected tarsocrural joint. Data were analyzed with ANCOVA, with horse as a covariate, when normally distributed or with Wilcoxon Signed Rank Test when not normally distributed. Statistical analysis was performed using JMP Pro 11.0 software (SAS Institute Inc., Cary, NC); $p<0.05$ was considered statistically significant. **Results:** All horses completed the study and maintained an acceptable comfort level. Tarsocrural joint sepsis was clinically evident in all horses following inoculation with *S. aureus* and SynF TNCC increased from a mean of 133±77 cells/µL on day 0 to a mean of 38,989±13,276 cells/µL on day 1. Horses treated with PRP-L had lower pain scores at days 4-7, 14, and 21 ($p<0.003$) with most notable differences in hock and distal limb swelling. PRP-L treatment also substantially improved joint appearance on grey scale ultrasound imaging. Systemic fibrinogen was significantly lower in PRP-L treated horses at days 6 and 7 ($p<0.0003$) as was D-dimer concentration at days 3-7, 14 and 21 ($p<0.001$). Serum amyloid A concentrations were not significantly different between PRP-L treated and control horses. SynF samples were obtained from all horses at sufficient volume for analyses from days 0-7 only and therefore days 14 and 21 were excluded from analyses. Although no differences in SynF TNCC or TP were appreciated between treated and control horses, PRP-L treated horses had a lower percentage of neutrophils ($p<0.02$) and higher percentage of mononuclear cells ($p<0.01$) at day 7 compared to control horses. Additionally, SynF from PRP-L treated horses had lower concentrations of IL-18 ($p<0.001$), IL-4 ($p<0.0008$), IL-5 ($p<0.02$), IL-8 ($p<0.03$), and G-CSF ($p<0.05$) from days 2-7; lower concentrations of MCP-1 ($p<0.03$) and IL-1β ($p<0.02$) from days 4-7; and lower concentrations of IFNγ ($p<0.02$) from days 6-7. No differences in concentrations of TNF-α or IL-6 were appreciated. Importantly, PRP-L treated horses had significantly lower concentrations of bacteria in SynF at days 3-7 ($p<0.006$) and significantly less bacteria within the synovial tissue at end-term (2.06±4.86 CFU/g tissue) compared to horses treated with amikacin alone (80.95±58.77 CFU/g tissue) ($p<0.009$). **Discussion:** The findings of this *in vivo* study to date strongly support the use of PRP-L in combination with antimicrobials to treat *S. aureus* infectious arthritis. Safety testing is required, before moving this allogeneic product into clinical use. Although acellular in nature, removal of immunoglobulins and major histocompatibility complex (MHC) fragments must be confirmed and donor horses must be screened for viral diseases which can be transmitted through biologics. We plana clinical safety trial followed by a field trial to demonstrate clinical efficacy in the near future. **Main study limitations:** This *in vivo* study evaluated the effect of PRP-L on acute experimental infectious arthritis model using *S. aureus*. It is unknown, if PRP-L will display similar efficacy against other pathogens *in vivo* and thus replication our previous *in vitro* findings. Although we have anecdotal data of a successive resolution in one horse that presented with a chronic history of bacterial arthritis, the efficacy of PRP-L for chronic infections (>24 hrs.) has yet to be established. **Scientific or clinical relevance:** Despite a need for antimicrobials that can effectively target antimicrobial tolerant bacteria within biofilms/biofloats, there are no FDA-approved drugs that exhibit these properties. PRP-L may present as one putative therapeutic strategy against antimicrobial tolerant infections and in combination with existing antimicrobials restore their efficacy in the treatment of infected joints and even of implant associated biofilm infections.

Discovery of Plasma Biomarkers in a Rabbit Periprosthetic Joint Infection Revision Model

Jessica Gilbertie, Meoghan MacPherson, Zosia Zawacki, Aubry Vena, Javad Parvizi, Thomas Schaer

INTRODUCTION: The lack of a definitive test in the diagnosis of PJI makes the evaluation of a painful joint following total joint arthroplasty difficult. A battery of tests is used in concordance with clinical presentation to allow the clinician to make the best diagnosis. The "gold standard" treatment for PJI is the two-stage exchange arthroplasty. The first stage is a resection of the infected implant and insertion of an antibiotic impregnated cement spacer. An interim of 4-8 weeks is then given during which intravenous antibiotics are given before the second stage, resection of the antibiotic spacer and reimplantation of new prosthesis. The role of synovial fluid inflammatory markers has proven efficacious in the initial diagnosis of PJI but the role in reimplantation is still unclear. Surgeons are left relying on the efficacy of the treatment modality and intraoperative assessment of the soft tissues and joint space to determine if the patient is fit for reimplantation or should undergo a spacer exchange. Numerous animal models of PJI have attempted to fill this void. In this study we propose and evaluate an animal model for PJI that is amenable to a two-stage revision procedure, along with serum inflammatory marker measurements that allow for clinically relevant assessment of infection as well as infection eradication. **METHODS:** A periprosthetic joint infection model was induced in the right stifle joints of 16 rabbits using a stainless steel screw in combination with a UHMPE washer placed in the intercondylar fossa of the distal femur extending 1/3 into the medullary canal of the femur. Ten days later the right femorotibial joint was inoculated with 0.1ml containing $1x10^4$ *Staphylococcus aureus*. Following a six to ten day incubation period, a revision treatment protocol was implemented consisting a two-stage implant exchange using standard clinical care. Briefly, the first revision stage consistent of implant removal, irrigation and debridement followed by a cement spacer. Rabbits in the control cohort were not treated with any antimicrobials whereas rabbits in the treatment cohort received antimicrobials added to the irrigation solution and the PMMA spacer. The cement spacer was prepared by mixing 8g of powdered cement polymer mixed with antimicrobials (130mg tobramycin, 200mg vancomycin) and methylmethacrylate. Postoperatively, rabbits were monitored and scored for signs of pain and appetite for 28 days. No systemic antimicrobials were given at any time. Blood samples were collected and analyzed for cytokine and chemokine biomarkers and data from days 3, 4 and 28 were quantitatively examined using a multiplex assay instrument, MAGPIX (Luminex Corporation). Twenty-eight days after revision surgery rabbits were sacrificed and *ex vivo* analyses consisted of bacteriology, imaging of the implant surface topography using confocal microscopy and scanning electron microscopy. Data were analyzed with ANCOVA, with rabbit as a covariate, when normally distributed or with Wilcoxon Signed Rank Test when not normally distributed. Statistical analysis was performed using JMP Pro 11.0 software (SAS Institute Inc., Cary, NC); $p<0.05$ was considered statistically significant. **RESULTS:** Surgical procedures were uneventful and all rabbits recovered from general anesthesia and surgical procedures. Rabbits were supported with Nutri-cal and fresh Kale throughout the study. One rabbit in the control cohort was euthanized after revision surgery due progressive clinical deterioration. Clinically all rabbits exhibited fever, lethargy and hyperfibrinogenemia following intra-articular inoculation with *S. aureus* which persisted until revision surgery. Rabbits undergoing revision surgery in combination with antimicrobials demonstrated an immediate and remarkable clinical improvement (body weight and pain score; Fig.1) following recovery from general anesthesia which persisted throughout the remainder of the study. Conversely, rabbits not receiving antimicrobials continued to exhibit lethargy and decreased appetite. All rabbits in the treatment cohort were negative on microbial culture while 7 out 8 of the control rabbits were culture positive (Fig. 1). The clinical observations were further corroborated by decreased systemic serum concentrations of fibrinogen and D-Dimer in rabbits treated with antimicrobials during revision surgery ($p<0.001$). Moreover, rabbits in the control group were consistent with increased inflammation and infection exhibiting elevated serum levels of fibrinogen and D-Dimer ($p<0.001$). Rabbits undergoing revision surgery using antimicrobials resulted in significantly decreased bacterial load in the in the femorotibial joints when compared to control rabbits determined by synovial tissue homogenate at time of sacrifice ($p<0.0001$). **DISCUSSION:** Culture negative PJI is a mysterious and uncomfortable scenario and causes uncertainty for diagnosis and treatment decisions in terms of type of antimicrobial(s), the duration of therapy, and the appropriate time for re-implantation in a 2-stage arthroplasty strategy. In a recent retrospective comparative study, culture negative PJI consisted 23 % of all PJI cases and prior antibiotic and surgical therapy were reported as risk factors for such an infection. Curiously, culture negative infections were associated with more successful outcomes, which could be because of more aggressive antibiotic and surgical treatment commonly applied for this scenario. Our findings in this proof-of-concept animal study are consistent with the cardinal signs of periprosthetic joint infection. Interestingly, D-Dimer serum concentration was the only biomarker in this study so far indicating a strong correlation between culture positive and culture negative animals. Clinicians have been searching for reliable serum biomarkers and a recent study by one of the co-authors indicates the D-Dimer serum concentration levels may be a reliable test for diagnosis of periprosthetic joint infection (PJI) and, most importantly, for determining the optimal timing of reimplantation for patients undergoing two-stage exchange arthroplasty. D-dimer is a fibrin degradation product and the serum levels indicate fibrinolytic activities. Several studies have demonstrated fibrin deposits in joints following an inflammatory reaction, mainly due to an increase in the permeability of the inflamed synovium and local extravasation of plasma fibrinogen. The model described here may provide a platform to assess revision arthroplasty strategies that aim at improving the optimal timing for re-implantation.

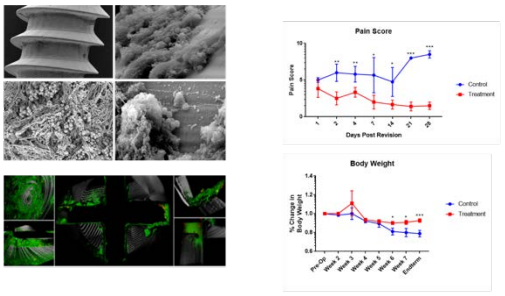

	#Rabbits	Culture neg.	Culture pos.
Control: Saline/PMMA	8	1	7
Treatment: TAO/PMMA +Abx	8	8	0

Figure 1. SEM of explanted hardware demonstrated consistent thick carpets of biofilm on screw head (exposed to joint) and shaft (intramedullary) consistent with findings on confocal microscopy. Clinical scores (pain and body weight) further support the microbiological culture results.

Extent and Type of Modification of Hyaluronic Acid Influence CD44 Binding in Soluble and Hydrogel Forms

Mi Y. Kwon[1], Chao Wang[2], Lin Han[2], Jason A. Burdick[1]
[1]Department of Bioengineering, University of Pennsylvania, Philadelphia, PA
[2]School of Biomedical Engineering, Drexel University, Philadelphia, PA

Statement of Purpose: Hyaluronic acid (HA) is a polysaccharide of D-glucuronic acid and N-acetyl-D-glucosamine repeat units that binds to cells via surface receptors, primarily CD44[1]. Modified HA has been used in the fabrication of glycomaterials such as hydrogels[2], including for mesenchymal stromal cell (MSC) chondrogenesis[3]. Despite the potential importance on material design, the influence of the extent and type of HA modification on its binding to CD44 is not well understood. Thus, we modified HA with either norbornenes (NorHA) or methacrylates (MeHA) and characterized their binding to CD44 in various contexts.

Methods: NorHA was synthesized by reacting HA tert-butyl ammonium salt with 5-norbornene-2-methylamine, coupling to either the carboxylic acid (NorHA 1) or primary hydroxyl (NorHA 2). MeHA was synthesized via addition of methacrylic anhydride to HA at the primary hydroxyl. NorHA/MeHA modifications were assessed with ^{1}H NMR. HA concentration was maintained in all studies. Modified HA binding to human CD44 was confirmed by a CD44-Fc chimera plate assay with FITC-tagged polymer, with FITC-PEG as a control. For cell-binding studies, hMSCs were treated with 200 ug/mL FITC-tagged polymer for 30 minutes on ice, washed, and analyzed for bound FITC signal by flow cytometry. For adhesion force analysis, atomic force microscopy (AFM) was performed on hydrogels with matched properties (elastic modulus, mass swelling, diffusivity for all gels including PEG control; data not shown) using polystyrene beads covalently conjugated with CD44-Fc. The max adhesion force was quantified as the greatest change from the baseline of the retraction curve post-indentation.

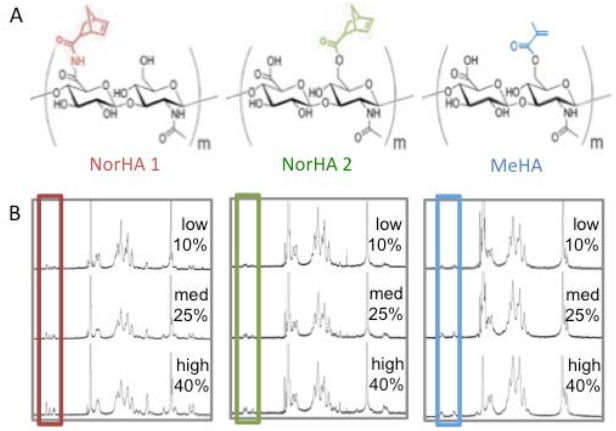

Figure 1. A) Structures and B) ^{1}H NMR of norbornene- (NorHA) or methacrylate-modified HA (MeHA).

Results: HA macromers with ~10, 25, and 40% (indicated as low, med, high) of repeat units modified with either norbornenes or methacrylates were synthesized (Fig. 1). Binding studies with human CD44 on surfaces showed differential binding of FITC-labeled macromers depending on the type of modifying group (hydrophobicity: NorHA vs MeHA, charge: -OH vs –COOH modified) and extent of modification, indicating altered avidity to CD44 based on HA synthesis (Fig. 2A). Binding studies directly to hMSCs (that present CD44, not shown) showed similar differential binding of FITC-labeled macromers based on the type and extent of modification (Fig. 2B). These findings are expected based on minimum repeat units for CD44 binding[4]. Lastly, AFM (with CD44-modified beads) of hydrogels fabricated from modified macromers also showed decreased adhesion forces with increased extent and hydrophobicity of modification (Fig. 2C). Since the hydrogels were designed to have otherwise similar properties, CD44 adhesion to hydrogels from modified HA depends on the extent and type of HA modification.

Figure 2. FITC-tagged modified HA binding to A) CD44

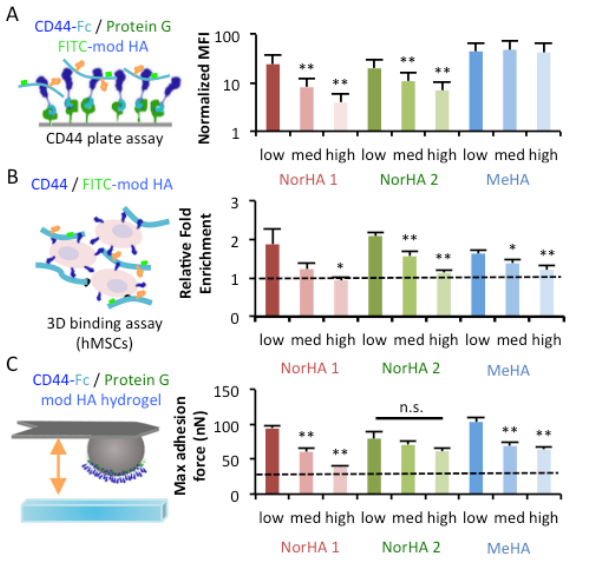

coated surfaces (MFI relative to FITC-PEG) or B) hMSCs (dotted line FITC-PEG). C) AFM with CD44 coated beads to measure CD44-hydrogel adhesion (dotted line PEG gel). *p<0.05, **p<0.01 to respective low groups.

Conclusions: Modified HA binding to CD44 is influenced by the extent and type of its modification, where increased modification (here, up to 40%) decreases binding. Thus, HA modification should be considered when designing glycomaterials for use as biomaterials. Ongoing work is evaluating the effect of modification on hMSC chondrogenesis within HA hydrogels from these same macromers and PEG hydrogel controls.

References: 1. Aruffo A. Cell. 1990; 61:1303-1313. 2. Burdick JA, Prestwich GD. Adv Mater. 2011; 23:H41-H56. 3. Kim IL. Biomaterials. 2011; 32:8771-8782. 4. Teriete P. Molec. Cell 2004; 13:483-496.

Gli1 identifies osteogenic progenitors for bone formation and fracture repair

Yu Shi, Guangxu He, Wen-Chih Lee, Jennifer A. McKenzie, Matthew J. Silva & Fanxin Long

Bone formation in mammals requires continuous production of osteoblasts throughout life. A common molecular marker for all osteogenic mesenchymal progenitors has not been iden- tified. Here, by lineage-tracing experiments in fetal or postnatal mice, we discover that $Gli1^+$ cells progressively produce osteoblasts in all skeletal sites. Most notably, in postnatal growing mice, the $Gli1^+$ cells residing immediately beneath the growth plate, termed here “metaphyseal mesenchymal progenitors” (MMPs), are essential for cancellous bone for- mation. Besides osteoblasts, MMPs also give rise to bone marrow adipocytes and stromal cells in vivo. RNA-seq reveals that MMPs express a number of marker genes previously assigned to mesenchymal stem/progenitor cells, including CD146/Mcam, CD44, CD106/ Vcam1, Pdgfra, and Lepr. Genetic disruption of Hh signaling impairs proliferation and osteoblast differentiation of MMPs. Removal of β-catenin causes MMPs to favor adipogen- esis, resulting in osteopenia coupled with increased marrow adiposity. Finally, postnatal $Gli1^+$ cells contribute to both chondrocytes and osteoblasts during bone fracture healing. Thus Gli1 marks mesenchymal progenitors responsible for both normal bone formation and fracture repair.

Biophysical Regulation of Histone Modification and Nano-Scale Chromatin Organization in Mesenchymal Stem Cells

Su Chin Heo[1], Shreyasi Thakur[1], Kiera Yankson[1], Boao Xia[1], Kwang Hoon Song[1], Jason Burdick[1], Melike Lakadamyali[1], Robert Mauck[1]
[1]University of Pennsylvania, Philadelphia, PA

INTRODUCTION: Exogenous biophysical cues [i.e. substrate stiffness (SS), dynamic compressive and tensile loading (DL), and fluid-induced shear stress (FSS)] can direct the lineage specification of mesenchymal stem cells (MSCs), a promising cell source for regenerative therapies [**1, 2, 3**]. For instance, we recently showed that dynamic tensile loading causes rapid chromatin reorganization in MSC nuclei [**4**], as well as changes in gene expression over time. These changes in chromatin organization and gene expression are regulated by histone modifications, including histone acetylation and methylation [which result in chromatin relaxation (transcriptional activation) and condensation (transcriptional repression), respectively] [**5**]. Consistent with this paradigm, we reported that fibro-chondrogenic differentiation of MSCs by soluble growth factors or mechanical loading increased the tri-methylation of H3K27 (H3K27me3) [**3**]. Here, we assessed how SS and FSS altered histone acetylation and methylation in MSCs. Further, we revaluated the early reorganization of histone-H2B (H2B) in response to FSS at nanoscale resolution, using a super-resolution microscopy [i.e. stochastic optical reconstruction microscopy (STORM)].

METHODS: MSCs were isolated from juvenile (~3 months) bovine femoral bone marrow. To investigate the effects of SS, cells were seeded on 5, 15, or 55 kPa polyacrylamide (PA) gels (3,000 cells/cm^2) [**6**] followed by 2 days of culture in basal growth media. Cells were fixed and immunostained for tri-methyl-histone H3 (Lys27) (H3K27me3, Thermo) or acetyl-Histone H3 (Lys9) (Ac-H3K9, Thermo). To investigate the effects of FSS, a custom-PDMS microfluidic chamber was developed to impose fluid-induced shear stress (**Fig. 2A**, FSS, 2 dyne/cm^2, 30 mins) on MSCs seeded on a chambered cover glass (100 cells/mm^2). After flow, cells were fixed and immunostained for H3K27me3, H3K9me3 (Thermo), AC-H3K9, and RNA polymerase-II (Pol-II, Thermo). Images were acquired by confocal microscopy (Nikon), and fluorescent intensity was measured using ImageJ. To assess chromatin condensation, nuclei (visualized by DAPI) were scanned across their mid-section, and the chromatin condensation parameter (CCP) in individual nuclei was calculated using a gradient-based Sobel edge detection algorithm in MATLAB [**2, 3**]. Additionally, the organization of histone H2B (abcam) at the nano-scale was determined using super-resolution microscopy, specifically stochastic optical reconstruction microscopy (STORM). STORM images were analyzed using custom-written software (Insight3) [**7**], and Voronoi diagram-based clustering algorithms in MATLAB [**8**]. Statistical analysis was performed using ANOVA (with Tukey's post hoc) or by Student's t-test ($p<0.05$).

RESULTS: We found that, as the stiffness increased (5kPa → 55kPa) the levels of both repressive (H3K27me3) and activating (AC-H3K9) histone modifications increased (**Fig. 1 A, B**). Conversely, MSCs exposed to FSS increased repressive (H3K27me3 or H3K9me3) marks and decreased activating (AC-H3K9 or Pol-II) marks (**Fig. 2 B-E**). Similarly, FSS increased the visible edges in DAPI stained nuclei and the quantified CCP (**Fig. 3**). STORM imaging showed dramatic histone reorganization in MSCs after FSS(**Fig. 4A**). Voronoi-based clustering analysis indicated an increased number of localization per histone cluster and increases in cluster size with FSS (**Fig. 4B-D**).

DISCUSSION: In this study, we explored how biophysical cues regulate histone modifications and chromatin reorganization in MSC nuclei. Our findings showed that substrate stiffness increased both repressive and activating histone modifying marks. Conversely, FSS increased repressive histone modifying marks and decreased histone modifying marks. FSS also caused rapid chromatin condensation and histone reorganization, at both the micro- (CCP) and nano-scale. Taken together these data suggest that mechanical perturbation regulates chromatin organization through histone modifications in MSCs. Ongoing studies are focused on elucidating the molecular mechanism mediating these changes, and linking these chromatin modifications to longer term changes to gene expression.

SIGNIFICANCE: Here, we show that biophysical cues regulate histone modification and chromatin organization. Fluid shear stress resulted in rapid reorganization of histone H2B at the nano-scale. These studies improve our understanding of the epigenetic mechanisms regulating stem cell differentiation, with the goal of enhancing stem cell activity for tissue engineering and regenerative medicine applications.

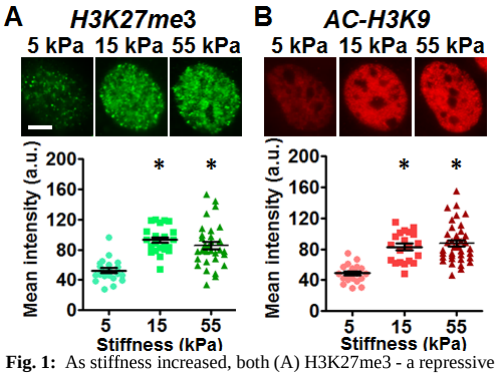

Fig. 1: As stiffness increased, both (A) H3K27me3 - a repressive mark - and (B) AC-H3K9 - an activating mark, increased (bar = 3μm, *p<0.05 vs. 5 kPa).

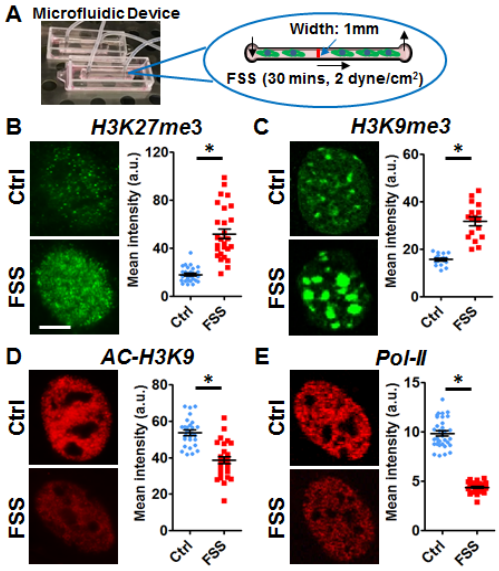

Fig. 2: (A) Schematic of microfluidic FSS device. Cells exposed to FSS for 30 mins increased H3K27me3 and H3K9me3, and decreased in AC-H3K9 and Pol-II (bar = 3μm, *p<0.05 vs. Ctrl).

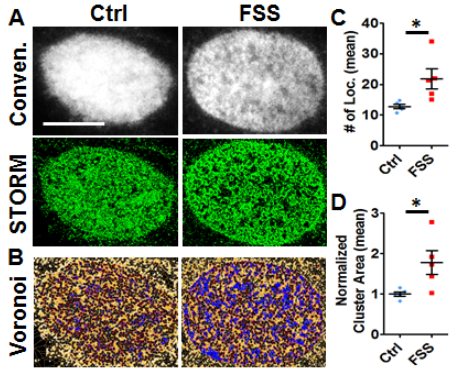

Fig. 4: (A) Conventional and STORM images of H2B localizations in MSC nuclei (bar = 5μm). (B) Voronoi clustering analysis to quantify the number of H2B localization in a cluster (C) and the mean cluster area (D). (n = 5, *p<0.05 vs. Ctrl).

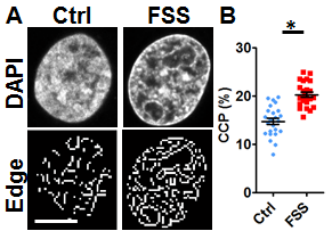

Fig. 3: (A) DAPI images and edge detection (bar = 5μm) of MSC nuclei. (B) Quantification of chromatin condensation parameter (CCP) (n = ~23 cells, mean ± SEM, *p<0.05 vs. Ctrl.)

REFERENCES: [1] Pittenger+, Science 1999; [2] Heo+, Sci Rep 2015; [3] Heo+, eLife 2016; [4] Heo+, Biophys J 2016; [5] Bannister+, Cell Res 2011; [6] Cosgrove+, Nat Mater 2016; [7] Ricci+, Cell 2015, [8] Andronov+, Sci Rep 2016.

ACKNOWLEDGEMENTS: This work was supported by the National Institutes of Health (R01 AR056624) and the National Science Foundation (CMMI-1548571).

Osteoclast Notch signaling suppression improves fracture healing

Peeyush N Goel[1,2], Yasaman Moharrer[1,2], John H Hebb[1,2,3], Alexander J Egol[1,2], Gurpreet Kaur[4], Kurt D Hankenson[5], Jaimo Ahn[1,2*], Jason W Ashley[6**]

[1]University of Pennsylvania, Philadelphia, PA; [2]Corporal Michael J. Crescenz VA Medical Center, Philadelphia, PA; [3]Georgetown University School of Medicine, Washington D.C; [4]University of the Sciences, Philadelphia, PA; [5]University of Michigan, Ann Arbor, MI; [6]Eastern Washington University, Cheney, WA

** Corresponding Author; *Co-corresponding Author

The pathologic dysregulation of osteoblasts (bone forming) and osteoclasts (bone resorbing and remodeling) produces disease states such as age-dependent bone loss while its optimization results in increased bone quantity and quality. Notch signaling plays a crucial role in both osteoblast and osteoclast maturation and function. To elucidate the influence of the Notch pathway in bone physiology, we genetically inhibited the Notch signaling pathway in osteoclast precursors, using a dominant negative form of MAML (dnMAML) involved in downstream Notch signaling. Osteoclasts derived from dnMAML mice showed no significant differences in early osteoclastic gene expression compared to the wild-type (WT). Further, these demonstrated significantly lowered resorption activity using bone surfaces while retaining their osteoblast stimulating ability using *ex vivo* techniques. Using *in vivo* approaches, we detected significantly higher bone formation rates and osteoblast gene expression in dnMAML cohorts. Further, these mice exhibited increased bone/tissue mineral density compared to WT with improved fracture healing. These observations suggest that therapeutic suppression of osteoclast Notch signaling could reduce, but not eliminate, osteoclastic resorption without suppression of restorative bone remodeling and, therefore, presents a balanced paradigm for increasing bone formation, regeneration, and healing.

A high resolution Capture-C promoter ‘interactome’ implicates causal genes at BMD GWAS loci

A. Chesi [1]; Y. Wagley [2]; M.E. Johnson [1]; M. Manduchi [1,3]; C. Su [1]; S. Lu [1]; M.E. Leonard [1]; K.M. Hodge [1]; J.A. Pippin [1]; K.D. Hankenson [2]; A.D. Wells [1,4]; S.F.A. Grant [1,5,6,7]

Affiliations:

[1)] Center for Spatial and Functional Genomics, Children's Hospital of Philadelphia, Philadelphia, PA;
[2)] Department of Orthopaedic Surgery, University of Michigan Medical School, Ann Arbor, MI;
[3)] Institute for Biomedical Informatics, University of Pennsylvania Perelman School of Medicine, Philadelphia, PA;
[4)] Department of Pathology and Laboratory Medicine, University of Pennsylvania Perelman School of Medicine, Philadelphia, PA;
[5)] Department of Pediatrics, University of Pennsylvania Perelman School of Medicine, Philadelphia, PA;
[6)] Divisions of Genetics and Endocrinology, Children's Hospital of Philadelphia, Philadelphia, United States;
[7)] Department of Genetics, University of Pennsylvania Perelman School of Medicine, Philadelphia, PA

Osteoporosis is a devastating disease with an essential genetic component. Genome wide association studies (GWAS) in both children and adults have discovered genetic variants robustly associated with bone mineral density (BMD); however, they only report genomic signals and not necessarily the precise localization of culprit effector genes. Therefore, we sought to carry out physical and direct ‘variant to gene mapping’ in a relevant primary human cell type. Given the notable paucity of genomic data available on bone in the public domain, and to improve upon the low resolution of typical Hi-C approaches, we developed a massively parallel, high-resolution Capture-C based method, SPATIaL-seq (genome-Scale, Promoter-focused Analysis of chromaTIn Looping), to characterize the genome- wide interactions of all human promoters in human mesenchymal progenitor cell-derived osteoblasts - facilitated by a custom Agilent SureSelect RNA library targeting *DpnII* restriction fragments overlapping 36,691 promoters of protein-coding, noncoding, antisense, snRNA, miRNA, snoRNA and lincRNA genes. We also generated ATAC-seq open chromatin maps from the same MSC-derived osteoblast samples to determine informative proxy SNPs residing in open chromatin for each of the 110 independent BMD GWAS signals at 107 candidate loci. By intersecting our SPATIaL-seq and ATAC- seq data, we observed consistent contacts between candidate causal variants and putative target gene promoters in open chromatin for ~30% of the loci investigated. In order to validate our findings, we targeted the expression of implicated genes using siRNA at two key loci in primary human MSC-derived osteoblasts from multiple donors: *CPED1* and *ING3* at the ‘*WNT16-CPED1*’ locus, and *EPDR1* and *SFRP4* at the ‘*STARD3NL*’ locus. Knockdown of either *ING3* or *EPDR1* yielded pronounced inhibitory effects on osteoblastogenesis, as assessed by staining for alkaline phosphatase and Alizarin red S. In summary, knockdown of two novel genes not previously associated with BMD but implicated by our combined ATAC-seq and SPATIaL-seq approach revealed strong effects on osteoblast differentiation (decreased ALP expression and absence of calcium phosphate mineral deposition), suggesting an important role for *ING3* and *EPDR1* in bone biology. Our approach therefore aids target discovery in osteoporosis and can be applied to other common genetic diseases.

The Effect of Fibroblasts on Extracellular Remodeling in Obese and Healthy Adipose Tissue

Golnaz Anvari, M.S.; Evangelia Bellas, Ph.D
Department of Bioengineering, College of Engineering, Temple University, Philadelphia, PA, United States

Obesity is a global epidemic and a risk factor for many major diseases such as type II diabetes, cardiovascular disease, stroke and cancer. Furthermore, obesity plays a role in development and progression of variety of musculoskeletal disorders such as osteoarthritis, back pain and osteoporosis but the mechanisms underlying this relation is not yet clear therefore it is critical to study adipose tissue at the cellular level to find out how changes in obese adipose tissue microenvironment can ultimately affect the musculoskeletal system. In simplest terms, obesity is defined as excess adipose tissue. Although white adipose tissue (WAT) was once known as a static organ that plays a vital role in energy storage, we know now that it is a complex endocrine organ which can regulate a variety of processes in our body. Under healthy expansion conditions, adipocytes grow in number (hyperplasia) and size (hypertrophy) by degrading their local matrix (matrix remodeling) and taking up dietary fatty acids to maintain normal function, however this process of remodeling is disrupted during obesity, where the hypertrophy occurs too rapidly leading to WAT hypoxia, fibrosis and inflammation. *Therefore, it is critical to study the healthy WAT microenvironment and how this microenvironment is altered during obesity.* A better understanding of how the microenvironment impacts metabolic functions at the cellular level plays an important role how we can target new obesity treatments.

Fibroblasts play a supporting role in adipose tissue but their contribution to fibrosis and disease progression is unknown. To evaluate the role of fibroblasts, a 3D in vitro model of WAT is developed by incorporating human adipocytes with or without human primary fibroblasts in a type I collagen matrix. These hydrogels were kept in either normoxic condition or hypoxic condition to mimic the early stage of obesity. Gene expression and organization of collagen fibers were studied by performing q-PCR and confocal microscopy respectively.

Preliminary data indicate that in the normoxic condition there is no significant difference in the expression of ECM related proteins and remodeling genes comparing mono-culture and co-culture. however, under hypoxic condition confocal reflection microscopy demonstrates an increase in collagen fiber clustering and density in hypoxic conditions. We expect that when inducing obese cues like hypoxia, activated fibroblasts will further alter extracellular matrix architecture by enhancing collagen deposition. This stiffer matrix could affect adipocyte gene expression through changes in integrin binding and cytoskeletal remodeling resulting in chronic overexpression of ECM related genes and fibrosis.

Novel BMP-Smad1/5 signaling interactions revealed in a zebrafish model of FOP

Allen, Robyn S., Eileen M. Shore, and Mary C. Mullins

Fibrodysplasia ossificans progressiva (FOP) is a rare and debilitating human genetic disorder that perturbs skeletal development and induces heterotopic ossification. Classical FOP is caused by a single nucleotide substitution in the BMP/TGFβ cell surface receptor, Acvr1 (617G>A, R206H). This mutation results in over-activation of BMP receptor signaling through the Phospho-Smad1/5 (pSmad1/5) pathway. To investigate the still uncertain mechanism by which FOP-Acvr1 enhances BMP signaling activity, we assayed for signaling activity using zebrafish embryonic DV patterning, which is established by a gradient of BMP-pSmad1/5 signaling. Perturbations to BMP-pSmad1/5 signaling directly correlate with a series of distinct dose-dependent phenotypes in the developing zebrafish embryo. Misexpression of hAcvr1-R206H, as well as several less studied variant FOP-Acvr1 mutations, causes increased pSmad1/5 signaling and ventralization of zebrafish embryos. Recent studies suggest that FOP-Acvr1 may have altered ligand responsiveness compared to WT-Acvr1. We confirmed that BMP ligand enhances pSmad1/5 signaling through Acvr1-R206H. Surprisingly, Activin A, a ligand that normally binds Acvr1b and signals through pSmad2/3, also enhances pSmad1/5 signaling by Acvr1-R206H. However, we found ACVR1-R206H does not require its ligand binding domain to over-activate BMP signaling, suggesting that while the mutant receptor responds to ligand, it does not require ligand. We then examined if other BMP receptors are required by FOP-ACVR1 to signal. We found that Bmpr1, a type I BMP receptor normally required for pSmad1/5 signaling and DV patterning in the zebrafish, is not required for pSmad1/5 over-activation by Acvr1-R206H or the variant mutant Acvr1-G328R. These data suggest that the mechanism by which FOP-Acvr1 signals is not bound by the same receptor and ligand partner requirements as WT-Acvr1. We found that the small molecule Acvr1 inhibitor, LDN214117, rescues zebrafish embryos injected with either Acvr1-R206H or Acvr1-G328R to a WT phenotype. These results show that the kinase activity of FOP-Acvr1 is required for its pathology and demonstrate the promising potential of a zebrafish development model for high-throughput screens of FOP treatments. These and further studies of the mechanism by which FOP-ACVR1 over-activates BMP signaling will help to identify additional therapeutic targets and provide unique insight into how this fundamental cell signaling pathway functions in development.

Funding Sources: NIH R01 GM56326, Cali Grant

Rerouting the glucose metabolism during the primary osteoblast differentiation

Wen-Chih Lee and Fanxin Long

Translational Research Program in Pediatric Orthopaedics, Division of Orthopaedic Surgery, Children's Hospital of Philadelphia

Osteolineage cells exert diverse functions to support the functions of bone as the supporting, mineral storage, and endocrine organ. To fulfill varied demands at different stages, we purposed the osteolineage cells acquires distinct nutrient metabolic profiling. In this study, we reported a robust 7 day calvarial osteoblast differentiation and assay protocol to facilitate the metabolism studies. Glucose metabolism was identified as the major source for ATP production, but not glutamine or fatty acid. Not only increased in glucose consumption during osteoblast differentiation, blocking glucose metabolism by 2-DG abolishes this process. These data demonstrated glucose is the most important nutrient for osteoblast differentiation. For the usage of glucose, aerobic glycolysis is the preferred route for glucose metabolism and highly upregulated during the osteoblast differentiation process. Although ATP production from mitochondria contributes less to aerobic glycolysis, inhibition of mitochondrial ATP production by oligomycin completely inhibits the osteoblast differentiation. Moreover, glucose consumption and aerobic glycolysis are both upregulated upon oligomycin treatment, suggesting an energy independent role for mitochondrial ATP production during osteoblast differentiation. Ongoing experiments are designed to determine the regulatory roles of mitochondria. Our studies demonstrates that glucose metabolism is upregulated and rerouted during osteoblast differentiation, and functions as the major route for ATP production.

Discovery of a unique bi-partite mechanism of transcriptional activation for SOX9, a key cell fate determinant in chondrogenesis

Abdul Haseeb and Véronique Lefebvre

Translational Research Program in Pediatric Orthopaedics, Division of Orthopaedic Surgery, The Children's Hospital of Philadelphia, Philadelphia, PA 19104

SOX9 is a master regulator of chondrogenesis and it is also involved, together with the other members of the SOXE group – SOX8 and SOX10 – in cell lineage fate specification and differentiation in a variety of other processes. Despite wide recognition of these important roles, the functional properties and modes of regulation of SOXE proteins are not completely understood, limiting our insight into disease mechanisms and discovery of effective therapies. To fill these knowledge gaps, here we employed complementary computational and biochemical tools to carry out an in-depth search for the protein domains that mediate the potent ability of SOXE proteins to activate transcription. We found that SOX9 and its relatives have conserved a high degree of identity in a centrally located domain, in addition to their homodimerization, DNA-binding and C-terminal transactivation domains. We uncover that both this middle domain (which we refer to as TAM) and the C-terminal domain (which we refer to as TAC) have transactivation capability when tested as fusion proteins with a GAL4 DNA-binding domain, but that both are required for efficient transactivation by the SOXE proteins, revealing a novel bi-partite transactivation mechanism. The activity of TAM relies on two amphipathic □-helices overlapping with a critical FDQYL motif that matches the FXX□□ consensus for the transactivation core domain of other potent transcription factors, including p53, p65 and VP16. Analysis of missense variants identified in SOXE proteins in the general human population supports the importance of harboring an intact FDQYL motif for normal development. Together, these novel findings add depth to our understanding of the modes of action of SOX9 and other SOXE proteins and will help further dissect the molecular networks whereby these proteins activate specific genetic programs in various developmental processes and human diseases.

Effects of Valporic acid on tenogenic gene expression in equine induced pluripotent stem cells and bone marrow derived mesenchymal stem cells

Feikun Yang, Aiwu Zhang, Dean W. Richardson

Department of Clinic Studies at New Bolton Center, University of Pennsylvania, 382 West Street Road, Kennett Square, PA 19348

Abstract

Cell-based therapeutic strategy affords potential advantages in repair of injured tendon in both human and horses. Although bone marrow derived mesenchymal stem cells (BMSCs) have commonly used, generation of induced pluripotent stem cells (iPSCs) from differentiated somatic cells expands the cell source and holds great potential for cell therapy and tissue engineering in tendon repair. As epigenetic modifications play essential roles in controlling cellular differentiation, the effects of valporic acid (VPA), a histone deacetylase inhibitor (HDACi), on tenogenic gene expression of BMSCs and tenocyte-derived iPSCs (teno-iPSCs) were investigated in this study. Compared to vehicle treatment, VPA (2mM) promoted the proliferation of BMSCs and inhibited the cluster formation induced by transforming growth factor β3 (TGF-β3) or by extended cultivation during *in vitro* differentiation. On the other hand, upon VPA treatment, teno-iPSC colonies lost their typical appearance such as distinct borders and clear edges, and shifted from colony morphology into an expanded monolayer appearance. Quantitative real-time PCR revealed that VPA treatment upregulated the expression of tenogenic transcription factors Mohawk and Egr1 as well as several matrix genes (Collagen I, Collagen XIV, Decorin, Elastin, Tenascin C, Thrombospondin 4) in both BMSCs and teno-iPSCs. Interestingly, the expression of scleraxis, another tenogenic transcription factor, was repressed by VPA in both type of stem cells. This effect was slightly weakened by the addition of TGF-β3, which has been reported to activate scleraxis expression. Collectively, our data suggest that the morphology and tenogenic differentiation capacity of BMSCs and teno-iPSCs can be regulated by epigenetic modifier HDACi.

Effects of Aging on the Molecular Profile of Cultured Tendon Cells

Carrie E. Barnum, Julianne Huegel, Louis J. Soslowsky, Andrew F. Kuntz
McKay Orthopaedic Research Laboratory, University of Pennsylvania, Philadelphia, PA

DISCLOSURES: Barnum C (N), Huegel J (N), Soslowsky LJ (N), Kuntz AF (N)

INTRODUCTION: Rotator cuff tears affect millions of individuals each year, with a higher incidence in the elderly. Although surgical repair can improve function and reduce pain, rotator cuff repair failure is common [1]. To improve surgical outcomes, biologic augmentation via delivery of cells or growth factors has been investigated [2-4]. Recently, autologous biceps cells delivered via nanofibrous scaffold to the repair site during supraspinatus repair were shown to improve healing in juvenile and aged rats, but did not affect healing in adult rats [5]. However, the molecular mechanisms behind these differential effects are not well understood. Therefore, the objective of this study was to determine the differences in the RNA signature of primary tendon-derived cells cultured from the long head of the biceps of juvenile, adult, and aged animals. Our hypotheses were: 1) tendon-derived cells from juvenile animals would exhibit a molecular profile more characteristic of stem cells than tendon-derived cells from adult or aged animals, and 2) tendon-derived cells from aged rats would have increased expression of genes associated with tendon homeostasis and differentiation compared to cells derived from juvenile or adult rats.

METHODS: 27 Fisher (F344) rats were used (IACUC approved) across three age groups: juvenile (4 weeks), adult (8 months), and aged (16 months) (n=9/age group). Animals were sacrificed and the intra-articular biceps tendons were collected. *Cell Culture*: Biceps tendon cells were harvested from the tissue via morselization and cell migration. Cells were expanded in culture using basal media and split at confluence. Subcultured (P1) cells were allowed to reach 75-85% confluence (average 12 days in culture) at which time they were lysed and homogenized in TRIzol. *RNA Isolation*: RNA was isolated using the TRIspin method and processed via RNA Clean & Concentrator 5 columns (Zymo Research). *Rat Transcriptome Array and Bioinformatics Analysis*: cDNA made with 250ng of RNA using the Affymetrix WT PLUS Kit and was run on a Clariom™ D Rat Transcriptome Array 1.0 (Applied Biosystems, n=5/age group). Bioinformatics processing was performed using Transcriptome Analysis Console Software and DAVID analysis (cut-offs set at |FC|>2 and $p<0.05$ for all pair-wise age comparisons). *qRT-PCR*: Reverse transcription was performed using a High Capacity cDNA Reverse Transcription Kit (Applied Biosystems). To validate microarray results, qPCR was run in quadruplicate using TaqMan Assays on a QuantStudio 12K Flex Real-Time PCR system (ThermoFisher, n=8/age group). Data was analyzed using the ΔΔCt method, and expression levels were compared between age groups with one-way ANOVAs and post-hoc Tukey tests. *Cell Staining*: At 50% confluence, P1 cells were fixed, permeabilized, and stained with Alexa Fluor 488 Phalloidin and DAPI. Slides were imaged with a Leica TCS SP8 Multiphoton Confocal.

RESULTS: Principle component analysis demonstrated that cell expression profiles grouped into distinct regions by age (Fig. 1). The majority of gene expression clustered into six distinct patterns when comparing between ages (data not shown). The majority of differential gene expression exists between juvenile and aged cells (640 genes significantly decreased, 531 increased), while the fewest differences exist between adult and aged cells (54 genes significantly decreased, 101 genes increased). Comparison of juvenile cells to adult cells identified 216 significantly increased genes and 203 significantly decreased genes. No qualitative differences were observed in cell morphology between age groups (data not shown). Gene ontology identified differences in genes related to: 1) cell adhesion, wound healing, and chondrocyte differentiation between juvenile and adult cells, 2) cell division and cell adhesion between juvenile and aged cells, and 3) wound healing and vasculogenesis between adult and aged cells. qPCR confirmed that genes associated with stemness are downregulated with age, including *Postn*, *Fgf10*, *Osr1*, and *Gpmnb* (Fig. 2). Additionally, genes related to inflammation are differentially expressed with age, including increased *Cd28* and *Cd200* expression and decreased *Il6* and *Il6st* expression (Fig. 3).

DISCUSSION: Results demonstrate distinct molecular profiles for juvenile, adult, and aged biceps tendon-derived cells. Juvenile cells showed increased expression of genes associated with mesenchymal stem cells, such as *Postn and Fgf10*, supporting our first hypothesis. Furthermore, although stem cell associated markers are present in both juvenile and adult cells, they are significantly decreased in aged cells, suggesting that a greater population of aged tendon cells may have terminally differentiated. However, contrary to our second hypothesis, there were no consistent increases in the expression of tendon markers in aged cells, suggesting that there may be significant population heterogeneity. Interestingly, aged cells demonstrate a decreased pro-inflammatory signature, including decreased expression of pro-inflammatory cytokine *Il6* and its signaling receptor *Il6st*, as well as an increased anti-inflammatory milieu, including increases in both *Cd28* and *Cd200* expression compared to juvenile cells. Previous work demonstrated that Il6-null mice (simulating an aged phenotype) have increased native tendon mechanical properties [6], but show a similar healing response as WT mice [7], suggesting a role for this cytokine in how delivered cells integrate into and contribute to new tendon formation. This study specifically explored RNA level changes in biceps tendons in culture, and we have not yet shown that these findings relate to changes at the protein level. However, these age-specific expression signatures can begin to uncover the mechanisms behind functional differences previously shown between age groups after cell delivery [5]. Future research will investigate protein level changes as well as how these changes relate to functional differences in tendon healing with age. It will be important to discern how both population heterogeneity and inflammation affect the contribution of scaffold-delivered biceps cells for rotator cuff repair.

SIGNIFICANCE/CLINICAL RELEVANCE: We previously demonstrated age-specific differences in supraspinatus healing after autologous biceps cell delivery [5]; the current study demonstrates that these cell populations display distinct molecular differences. These differences should be considered when addressing musculoskeletal regenerative medicine, particularly in the context of augmented tendon repair. Furthermore, modulating the molecular profile of adult or aged cells may further improve tendon repair.

REFERENCES: [1] Galatz LM et al. J Bone Joint Surg Am, 2004. [2] Hernigou P et al. Int Orthop, 2014. [3] Chen JM et al. Tissue Eng, 2007. [4] Longo UG et al. Br Med Bull, 2010. [5] Huegel J et al. J Orthop Res. 2017. [6] Lin TW et al. J Biomech. 2005. [7] Lin TW et al. J Biomech. 2006.

ACKNOWLEDGEMENTS: This study was supported by the American Shoulder and Elbow Surgeons Research Grant. We would like to thank Dr. Snehal Shetye for his help with the cluster analysis.

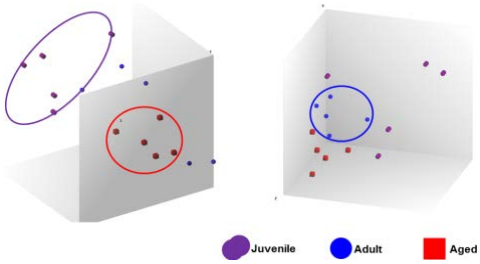

Figure 1.Two Principle Component Analysis plots from Rat Transcriptome Analysis. Juvenile cells shown as purple cylinders, adult cells are shown as blue spheres, and aged cells are represented as red cubes. Age groups are circled to demonstrate distinct clusters.

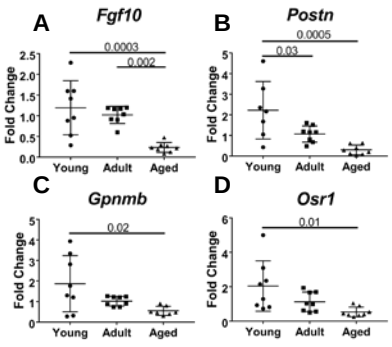

Figure 2. Decreased expression of stem related mRNAs measured via qPCR. (A) *Fgf10* (B) *Postn* (C) *Gpnmb* and (D) *Osr1* expression decreased with aging. Significance is denoted with solid lines (n=8/group).

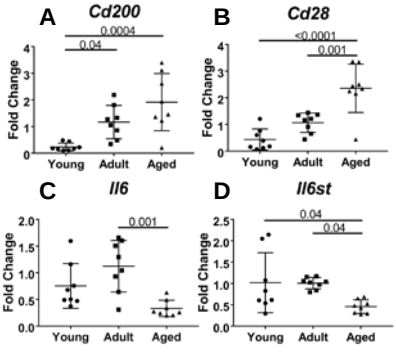

Figure 3. qPCR confirms changes in inflammatory response with age. (A) *Cd200* and (B) *Cd28* increased with age, while (C) *Il6* decreased in aged cells only and (D) *Il6st* decreased with aging. Significance is denoted with solid lines (n=8/group).